Structural and Functional Studies of Large-Pore Channels of the CALHM Family

Dissertation

zur

Erlangung der naturwissenschaftlichen Doktorwürde
(Dr. sc. nat.)

vorgelegt der

Mathematisch-naturwissenschaftlichen Fakultät

der

Universität Zürich

von

Katarzyna Drożdżyk

aus Polen

Promotionskommission

Prof. Dr. Raimund Dutzler (Leitung und Vorsitz)

Prof. Dr. Christiane Albrecht

Prof. Dr. Martin Jinek

Zürich, 2023

Acknowledgements

I would like to express my gratitude to the people whose help and support have been crucial in bringing this project into its final form as this thesis.

First and foremost, I would like to thank my supervisor, Prof. Raimund Dutzler, for his guidance over the past nearly five years. I have learned a lot under his mentorship, and I am grateful to have been a part of his research group.

I would also like to extend a special thank you to Prof. Christiane Albrecht for her invaluable insights. I appreciate the broader perspective I gained on this project through our collaboration.

I extend my appreciation to Prof. Martin Jinek, a member of my PhD committee, for his input during the committee meetings.

I am grateful to the many people who were directly involved in this project. Dawid, thank you for introducing me to the project and the lab. Marta, your great contributions to the structural aspects of this work and your expertise in cryo-EM have been invaluable. Marisabel, I am grateful for your contributions to the functional studies and for teaching me about electrophysiology. Jonas, thank you for your dedicated work on the placental part and for sharing your knowledge.

I would also like to express my thanks to Martina for her work in her master's project. Your contributions were invaluable and working with you was the best!

I extend my gratitude to all past and present members of the Dutzler group. I would like to express my special appreciation to a remarkable group of people: Monique, Sonja, Dave, Marton, Anastasiia, Melanie, Kyoko, Elena, and Mengting. I have learned a lot from each of you, and I am truly impressed with your work! Thank you for all your help and all the laugh we shared!

Lastly, I would like to thank my family and friends for all the support and interest in my work. This made it a little bit easier to live far away from you.

Table of Contents

List of figures and tables

Abstract

A cell relies on proteins, termed ion channels, that facilitate the passage of ions across its membranes. These channels contain pores that activate in response to certain stimuli, allowing ion flow in their open state. Previous research has predominantly focused on ion channels with narrow and selective pores, which permit only certain types of inorganic ions to cross the membrane. However, there is increasing interest in proteins that form channels with wider pores that facilitate the permeation of larger substrates. These large-pore channels play various biological roles by allowing signaling molecules such as ATP to cross the membrane. One family of large-pore channels is the recently discovered calcium homeostasis modulators (CALHM) family, which contains six paralogs in humans. CALHM1 has been shown to form ion channels that are activated by voltage and the decrease of extracellular calcium. It pairs with CALHM3 to form heteromeric channels with improved activation properties. CALHM1 and 3 have been found in primate taste buds, and their role in perceiving sweet, bitter, and umami tastes through ATP efflux and subsequent purinergic signaling has been demonstrated. Despite these breakthroughs, the mechanisms underlying ion permeation and gating of CALHM channels, and the function of other family members have remained elusive.

In this thesis project, I aimed to study the functional and structural features of human CALHM proteins, with a particular focus on uncharacterized members of the family. To achieve this goal, I have identified biochemically stable constructs of CALHM2, CALHM4, and CALHM6 and used cryo-electron microscopy to characterize their detailed three-dimensional structures. These findings provided the first structures of CALHM4 and CALHM6, revealing their unique features to assemble as large channels composed of ten or eleven subunits with a central pore. Strikingly, I observed two different conformations between the homologues that significantly impacted pore size and geometry, potentially suggesting a gating mechanism. In one conformation, the pore-lining α-helix 1 runs parallel to the pore axis, creating a wide-open cylindrical pore, while in the other conformation, the same elements lifts to form a conical pore, which narrows towards the cytoplasm. Additionally, the CALHM4 structure exhibited extra bilayer-like density inside the pore, which likely either originates from detergents used in the purification or co-purified lipids, indicating a potential role of lipids in the regulation of channel activity. Although the physiological relevance of observed features remains unclear, the described work has provided valuable insight into the general architecture and potential activation mechanisms of the CALHM channels.

Complementary functional studies of CALHM2, CALHM4, and CALHM6 by electrophysiology and *in vitro* transport assays did not show any activity under conditions that activate CALHM1, suggesting a distinct mechanism of activation. Transcript analysis demonstrated that all three homologues are highly enriched in the placenta, prompting the investigation of mutual interactions *in vitro*. I could show that CALHM2 and CALHM4 interact to form heteromeric CALHM channels, similar to the previously reported CALHM1/3 heteromers. However, functional studies did not show any activity in cells co-expressing CALHM2 and CALHM4, in contrast to the altered phenotype of

CALHM1/3 heteromers and similar to the lack of activity that was previously observed in homomeric CALHM2, 4 and 6 channels. Despite the observed lack of activity, I pursued the structural characterization of heteromeric CALHM2/4 complexes in the hope to uncover structural features that facilitate the comprehension of CALHM function.

To overcome the challenge of identifying structurally similar subunits in a heteromeric channel, I have generated specific sybodies to each of the two homologues to facilitate their distinction during reconstruction. Before structure determination of heteromeric channel complexes, I first characterized the homomeric CALHM paralogs in complex with their respective sybodies, which identified their respective binding sites. These efforts also yielded a structure of CALHM2, which was prevented in case of the apo-protein due to the preferred channel orientation on cryo-EM grids. CALHM2, like CALHM4 and 6, form large channels and its pore conformation is similar as observed for CALHM6. The structure of CALHM2/4 complexes revealed heteromeric channels with broad distribution of oligomeric states, ranging from decamers to dodecamers, with varying subunit stoichiometries. The high-resolution structure of a predominant population showed a heteromeric channel with an excess of CALHM2 subunits that are arranged in a cluster and a group of two to three CALHM4 subunits. While most subunits reside in the preferred conformation defined in homomeric structures, the conformation of a CALHM2 subunit, located in the neighborhood of CALHM4, differed in conformation, aiding the understanding on the conversion of states. Intriguingly, similar to the CALHM4 structure, extra density was observed in a section of the pore close to the subunits residing in cylindrical conformations. This further supports the notion that the pore-lining α-helix and lipids may play a crucial role in the gating of CALHM channels, which likely employ complex regulatory mechanisms that may be distinct for different members of the family.

1. Introduction

1.1 Homeostasis across the membrane

Cells, as the smallest unit of life, maintain their autonomy and integrity through the presence of membranes that separate their interior and that of intracellular membrane-enclosed compartments from the environment[4]. Controlled exchange with the environment is achieved by a universal feature of biological membranes, known as semipermeability[5,6]. Membranes are composed of phospholipids, with their hydrophilic heads facing the inside and outside of the cell, and hydrophobic acyl chains forming the interior of the membrane[4]. While hydrophobic and small polar molecules can diffuse through the membrane, larger and charged molecules encounter a barrier due to the presence of the hydrophobic core[4,7]. Despite its poor permeability, cells have evolved mechanisms to exchange signals and molecules with their environment and between compartments[6,7]. In addition to endocytic and secretory pathways, this is made possible by a multitude of specialized proteins residing in the membranes, which serve as the first line of response to changing conditions and cellular requirements[6].

The interplay between cellular processes and membrane proteins contributes to cell homeostasis, including the distribution of ions across the membrane[4,8]. The specific ion imbalance, which is fundamental for cell homeostasis, is maintained through active transport mechanisms and the selective permeability of the cell membrane[4,6]. Active transport mechanisms, such as the sodium-potassium pump, use ATP energy to actively transport ions[4,6,7]. As a result of this activity, the concentration of potassium ions (K^+) is higher inside the cell, while the concentration of sodium ions (Na^+) is higher on the outside, creating an electrochemical gradient[4,6] In addition to sodium and potassium ions, other ions contribute to the difference in ion concentration[4,6]. The interior of the cell is enriched in organic anions, while the concentration of chloride and calcium is generally higher in their extracellular environment[4,6]. In fact, among ions, calcium has the highest concentration difference across the membrane[4,6]. Such ion distribution is fundamental for the creation of an electrochemical potential across the cell membrane which is known as the resting membrane potential[9]. The exact ion concentrations vary between cell types, resulting in different resting membrane potentials typically ranging from -10 to -100 mV in different cells, and it is usually set by K^+ and Cl^- gradients[10,11]. This membrane potential, is used by cells for transport processes, and to receive, transmit and amplify signals[4,11]. Among the many different types of membrane proteins, ion channels play an important role in performing all of these functions[4,6,12]. As their name suggests, ion channels are pore-forming membrane proteins that allow ions to move across the membrane[12]. Ion movement occurs by passive diffusion, driven by the transmembrane electrochemical potential, which includes components of the membrane potential and the concentration gradient of the substrate ions, and determines the direction of ion flow[12].

1.2 Ion channels

Although limited to facilitating passive transport, ion channels are not simply large open pores in the membrane that allow ions to diffuse freely in and out of the cell since any uncontrolled opening of channels would be detrimental to cellular homeostasis[12]. Instead, a typical ion channel is composed of multiple subunits that come together to form a tightly regulated conduit for ions[12]. At its narrowest part, the typical diameter of a conducting pore measures few angstroms, barely larger than the size of their conducted substances[12,13]. Tight regulation implies that this passage opens only under specific conditions in a process called gating and that the open channel exhibits selectivity for specific substrates. To date, more than hundreds of ion channels have been described, reflecting the diversity of molecular mechanisms[12]. Despite this diversity, the majority of ion channels share common features and their general modes of action are similar[12,14].

The typical ion channel substrate is a monoatomic ion, and selectivity for a particular ion is primarily conferred by a specialized region called the selectivity filter[13,14]. The selectivity filter is a narrow structure within the pore that discriminates between ionic substrates based on their size, charge, and hydration properties[13]. They are formed by specific arrangements of amino acids that set the charge and size requirements for ion passage, allowing only certain substrates to pass[13]. It is worth noting that selectivity is often not conferred by the selectivity filter alone as other regions, including the wider channel entrances, can also contribute to shaping selectivity through long-range electrostatic interactions with permeating ions[13].

Channels open and close in a process known as 'gating'[14]. Gating involves a series of conformational changes that result in either pore expansion or constriction, thereby allowing or restricting ion flow[14]. The gate can be steric, electrostatic, hydrophobic or a combination of those[12,15,16]. Gating follows a general scheme involving closed, open and inactivated states[12]. However, within this scheme, there may be multiple substates, and some channels may inactivate from the closed state or have multiple open states[12]. Various mechanisms have been discovered that regulate ion channels, including voltage gating, ligand binding, pH modulation, post-translational modifications, mechanical force, photon activation, and temperature sensitivity[12,17-19]. These different stimuli alter the distribution of states the channel resides in[12]. In electrophysiological experiments, these states can be identified by the absence, presence or decrease of currents mediated by the flux of charged particles through the pore[12].

1.3 Large-pore channels

Although the described general properties apply to the majority of ion channels, there are proteins that defy the definition of a canonical ion channel. These include connexins, innexins, pannexins and leucine rich repeat containing protein 8 (LRRC8), which together form a diverse group known as 'large-pore' channels[20-22]. The name reflects the main feature that distinguishes them from typical ion channels, as they form a large pore with a functional diameter of more than 10 Å, significantly larger than that of common channels[21,22]. This versatile group allows the transport of small molecules (including second

messengers, metabolites, hormones and cytokines) in addition to the transport of monoatomic ions and it shows a complex activation mechanism that appears to go beyond the sensing of a single specific stimulus[20,22-25]. Although evolutionarily unrelated, members of the families are predicted to share a similar topology of the membrane region (**Figure 1**)[3]. Structural studies of connexins, innexins and LRRC8 proteins revealed that in all families, the channels are formed by high oligomeric assemblies of protomers surrounding a large central pore[22,26-29]. The topologies of the protomers are similar, each consisting of four transmembrane helices, two extracellular loops and intracellular C- and N-terminal domains[27-30].

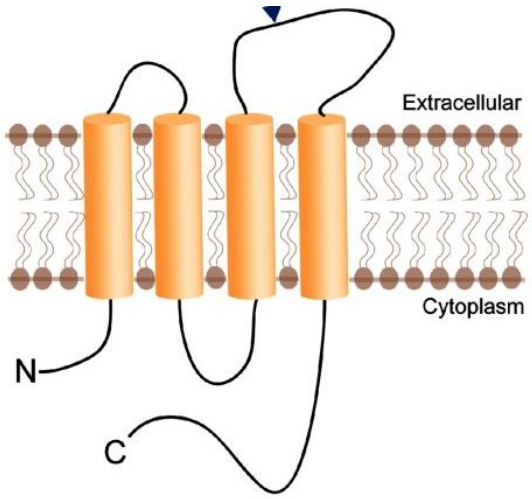

Figure 1. Membrane topology of large pore channels. Schematic representation of the topology of membrane-spanning regions of large pore channels. Figure from [3]

Connexins form gap junction channels that allow direct communication and exchange of ions and small molecules between neighbouring cells[20]. They are activated by voltage, pH and extracellular calcium[20,25]. Innexins are the invertebrate homologues of connexins and are activated by voltage and mechanical stress[21,24,31]. In both cases it has been shown that hemichannels can also act as gated channels connecting the cytoplasm to the outside of the cell[25,32]. Connexins form hexamers and innexins octamers, both docking through their extracellular regions[27,30,33]. Pannexins, like connexins and innexins, are involved in intercellular communication but do not form gap junctions[24]. These channels can be activated by various stimuli, including voltage, mechanical stress and changes in intracellular calcium levels or cleavage of their C-terminal amino acids[23]. Pannexins are known for their role in the release of signaling molecules such as ATP, which plays an important role in cell signaling and immune responses[34]. At the start of the project, the structure of pannexins had not been reported, but they were predicted to form hexamers[23]. Finally, LRRC8 proteins form volume-regulated anion channels (VRACs), which are involved in cell volume regulation and play a crucial role in maintaining cellular homeostasis by allowing the efflux of chloride ions and other anions when cells undergo swelling[22]. These heteromeric proteins are formed by hexameric assemblies of LRRC8 proteins[22].

1.4 The family of CALHM proteins

Another family of large-pore channels is constituted by the calcium homeostasis modulator (CALHM) proteins[35]. The *CALHM* gene family is conserved across vertebrates and is predicted to encode membrane proteins of approximately 330 amino acids[1,35]. To date six members of the family, CALHM1-6, have been discovered and no significant sequence homology to other characterized genes has been recognized. Formerly named the FAM26 family, which reflects the low sequence identity of the family, its members are clustered on two chromosomes (**Figure 2**)[1,35]. While CALHM1 (FAM26C) is located on chromosome 10 together with CALHM2 (FAM26B) and CALHM3 (FAM26A), three other homologues CALHM4 (FAM26D), CALHM5 (FAM26E) and CALHM6 (FAM26F) are located on chromosome 6[1]. Sequence alignment of the human CALHM paralogs is found in Appendix A.

	1	2	3	4	5	6
1	100	25.48	45.86	24.75	22.22	24.92
2	25.48	100	29.45	32.89	31.62	30.69
3	45.86	29.45	100	23.05	22.15	24.75
4	24.75	32.89	23.05	100	30.1	29.86
5	22.22	31.62	22.15	30.1	100	38.28
6	24.92	30.69	23.05	29.86	38.28	100

Figure 2. Sequence identity matrix of human CALHM homologues. Matrix showing the sequence identity (%) of CALHM 1-6 homologues. Numbers indicate the homologue.

1.4.1 Identification

The CALHM family was identified in 2008 resulting from efforts to identify a gene associated with late-onset Alzheimer's disease[35]. The P86L polymorphisms of its member CALHM1 was linked to this disease. Soon after the association was refuted by groups, who attempted to replicate these results and reported that no such association was observed[36-39]. Later, two meta-analyses studies showed the association between the polymorphism and the disease with the caveat that the association is restricted to the Caucasian population[40,41]. Although this may partially explain reported discrepancies, there is still no clear link between the protein and the disease. Nevertheless, the gene has attracted interest, with studies revealing the unique characteristics of the encoded protein.

When CALHM1 was investigated in the context of Alzheimer's disease, topology predictions showed that this small protein is a membrane protein with four membrane-spanning segments, similar to large pore channels[35]. Experimental data further confirmed the cell surface localization and revealed that CALHM1 homo-oligomerizes to form hexameric complexes[3,35]. As it was predicted to contain structural motifs similar to the selectivity filters of the calcium conducting channels (NMDA receptors and Orai1), its role in calcium homeostasis was investigated[1,35,36]. A variety of methods showed that CALHM1

controls cytosolic Ca^{2+} concentration, as a sustained increase in intracellular calcium was observed after calcium repletion in previously depleted cells[35,42]. Taken together, the predicted topology, its oligomeric state and plasma membrane localization and the observed control of the cytosolic calcium concentration led to the proposal that CALHM proteins form a novel family of ion channels with similar properties as other large pore channels[2,3,36].

1.4.2 Functional properties of CALHM1 channels

Since the predicted topology of CALHM1 was similar to that of connexins, it was investigated whether CALHM1 forms gap junctions[3]. However, dye permeation studies showed no evidence that CALHM1 would form intercellular channels[3]. This property might be hindered by glycosylation found in CALHM1 channels, a post-translational modification that was also found in pannexins, which do not form gap junctions either[3]. The initially proposed functional similarity to calcium channels was later also refuted by mutational studies[2]. Instead, CALHM1 was shown to function as plasma membrane ion channel with unique properties[2].

Functional studies in oocytes and mammalian cells have shown that the heterologous expression of CALHM1 evokes currents modulated by voltage and extracellular calcium (**Figure 3-A and E**)[2,35,43]. Under near-physiological conditions, slowly activating outward currents were observed upon membrane depolarization which deactivate at negative voltages (**Figure 3-A**)[2,44,45]. Selectivity studies showed that CALHM1 exhibits weak ion selectivity with a preference for calcium ions and a higher permeability for monovalent cations over chloride (P_{Ca}:P_{Na}:P_K:P_{Cl}:11:1:1.17:0.56)[2]. Further permeation studies, including an optical analysis with fluorescent probes of various sizes and charges, estimated a pore diameter of 14 Å[3]. The origin of the rectification was investigated and systematic exclusion of a divalent cation effect showed that the voltage-sensitivity is intrinsic and CALHM1 can thus be classified as weakly voltage-gated ion channel[2,43]. Studies of the N-terminal region, predicted to line the pore of the channel, showed that this region modulates the voltage dependence of CALHM1[43]. However, it appears not to be the sole voltage sensor, as neither mutations nor significant truncations and extensions of the N-terminus abolished the observed voltage dependence[43]. As second stimulus for activation, the depletion of extracellular calcium evokes currents even at negative voltages with half maximal inhibitory Ca^{2+} concentration of ~220 µM and a Hill coefficient ~2 (**Figure 3-B and C**)[2]. A similar response was observed upon Mg^{2+} depletion but with a lower potency (IC_{50}: 3.3 mM)[2].

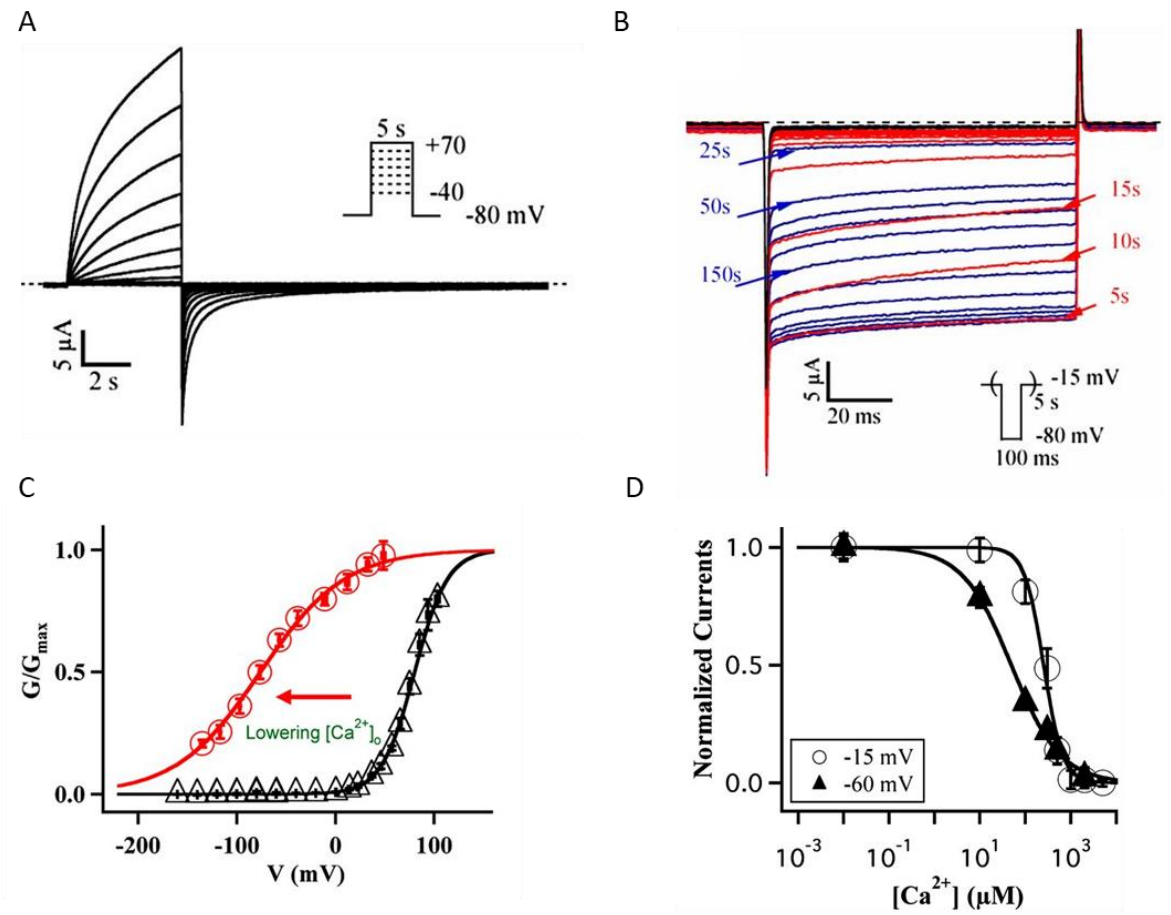

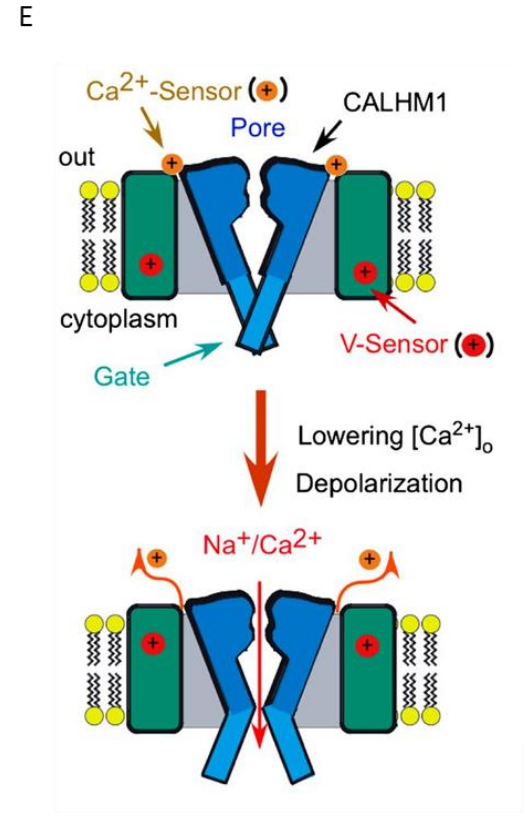

Figure 3. Functional properties of murine CALHM1. (**A**) Currents in a CALHM1-expressing oocyte in response to voltage pulses from holding potential of -80 mV in solution containing 2 mM Ca^{2+} and 1 mM Mg^{2+}. (**B**) CALHM1 currents measured in oocytes every 5 s increase during continuous perfusion (blue) with divalent cation-free solution and reverse to control levels after perfusion with 5 mM Ca^{2+} (red). The recording protocols are shown. (**C**) Lowering $[Ca^{2+}]_o$ shifts the conductance–voltage relations of CALHM1 channels by −150 mV (**D**) Hyperpolarization shifts IC_{50} of $[Ca^{2+}]_o$ to lower values. (**E**) Schematic depiction of the putative CALHM1 mechanism of action. The CALHM1 channel contains a voltage sensor and a Ca^{2+} sensor that detects the extracellular Ca^{2+} concentration ($[Ca^{2+}]_o$). (*Top*) The CALHM1 channel gate is closed by physiological $[Ca^{2+}]_o$ and hyperpolarized voltages. (*Bottom*) Lowering $[Ca^{2+}]_o$ and/or depolarization can open the gate, allowing Na^+ and Ca^{2+} influx and causing membrane depolarization. Figures from[2]

Activation by the two mechanisms is coupled [2]. Removal of divalent cations causes a leftward shift in the conductance-voltage relationship, allowing CALHM1 channels to open at hyperpolarized voltages (**Figure 3-C**)[2]. Interestingly, calcium removal also decreases the sensitivity of CALHM1 to voltage changes, suggesting an allosteric modulation of its voltage gating by $[Ca^{2+}]_o$ (**Figure 3-C**)[2]. Membrane voltage also affects the sensitivity of the channel to inhibition by extracellular calcium (**Figure 3-D**)[2]. Hyperpolarization significantly increases the apparent Ca^{2+} affinity, indicating that regulation by extracellular Ca^{2+} is strongly voltage dependent (**Figure 3-D**). At present, neither a voltage sensor nor a calcium-binding site have been identified in CALHM1 and the structural basis of its activation remains unknown[1,43].

1.4.3 Functional properties of CALHM1/3 channels

To date CALHM3 has not been shown to act as an ion channel itself, but it was instead demonstrated that it modulates the gating properties and activation kinetics of CALHM1 channels (**Figure 4-A and B**)[44]. Biochemical and colocalization studies of heterologously expressed CALHM1 and CALHM3 showed that the two proteins interact in vitro and in vivo[44,46]. Electrophysiological studies in both, *X. laevis* oocytes and mammalian cells showed that these subunits interact to form single heteromeric channels. CALHM1/3 channels are voltage gated and activate 50 times faster than homomeric CALHM1 channels (**Figure 4-A and B**)[44]. Additionally, their voltage dependence is shifted towards more hyperpolarized voltages compared to homomeric CALHM1 (**Figure 4-B**)[44]. Heteromeric CALHM channels retain the extracellular calcium sensitivity and permeability properties of CALHM1 channels[44].

1.4.4 ATP permeability and pharmacology of CALHM channels.

Studies in cultured cells heterologously expressing CALHM channels showed that CALHM1 mediates ATP release (**Figure 5**)[45]. The regulation of ATP release is similar to the gating of CALHM1 channels as it was triggered by the depletion of extracellular Ca^{2+} and membrane depolarization induced by high extracellular K^+ (**Figure 5**)[45]. In agreements with electrophysiological studies, CALHM3 does not mediate ATP efflux by itself, but enhances ATP release through CALHM1 channels (**Figure 5**)[44]. The pharmacology of CALHM1 channels differs from that of other ion channels[2]. Inhibition is observed in the presence of non-selective inhibitors, including Gd^{3+}, Zn^{2+} and ruthenium red[2,44,45]. Currents from CALHM1/3 channels were inhibited by carbenoxolone (CBX), an inhibitor of pannexins and connexin hemichannels. Other inhibitors specific for voltage-gated K^+ channels, Na^+ channels, NMDA receptors, pannexins and connexins had no effect on CALHM1[44,45].

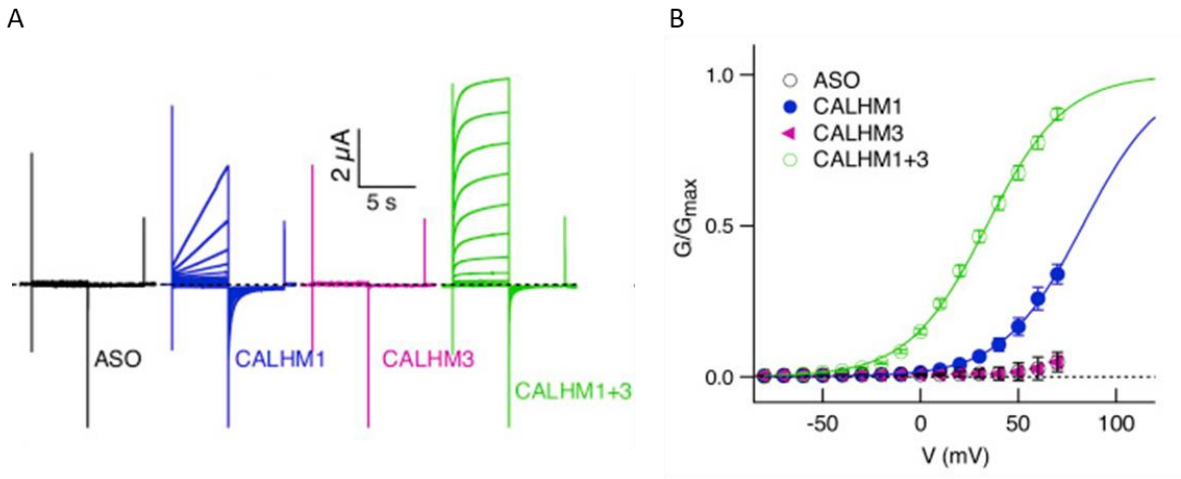

Figure 4. Functional properties of murine heteromeric CALHM1/3 channels. (**A**) Currents in control oocytes (ASO) and oocytes expressing either CALHM1 or CALHM3 or both CALHM1 and CALHM3 in response to a 5s voltage pulses stepping to voltages between -80 and 70 mV from a holding potential of -40 mV. (**B**) Comparison of the conductance-voltage relationship of CALHM1, CALHM3 and CALHM1/3 currents. Figure from [44].

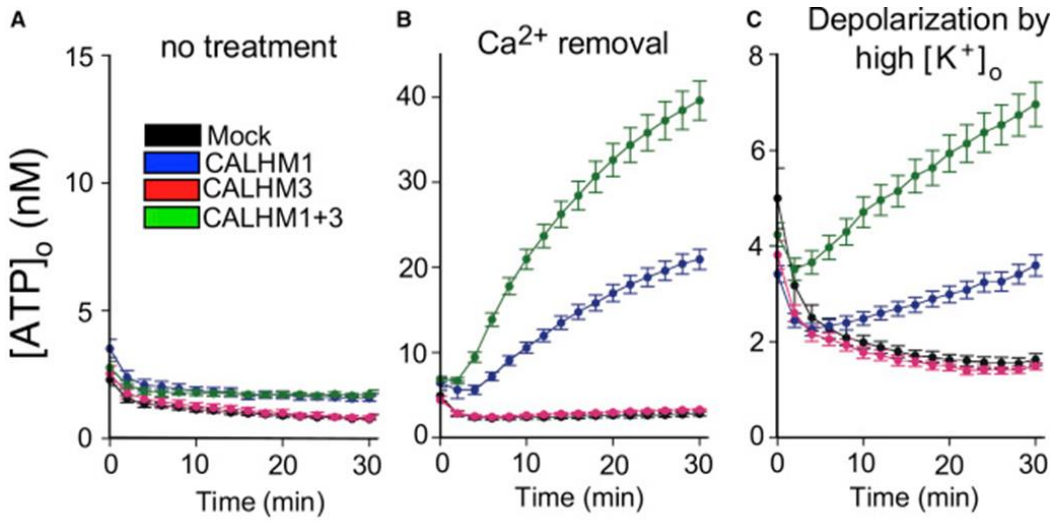

Figure 5. CALHM mediated ATP release. Time course of ATP efflux from HeLa cells transfected with vector only (mock) or CALHM1 or CALHM3 or both CALHM1 and 3 (**A**) without treatment (**B**) after extracellular calcium removal (**C**) after extracellular potassium increase. Figure from [44].

1.4.5 Biology of CALHM channels

So far, two physiological roles have been proposed for CALHM1 or CALHM1/3 channels[2,44,45]. At the transcript level, CALHM1 is highly enriched in brain tissue[35]. The excitability of cortical neurons is known to be enhanced by extracellular Ca^{2+} depletion, but the identity of the proteins involved in this phenomenon and the full mechanism of the enhancement remained unknown [47,48]. Knock-out studies of CALHM1 in mice resulted in altered electrophysiological properties of their cortical neurons. In contrast to wild-type neurons, neurons lacking CALHM1 were unable to reduce the input resistance and induce their excitatory response at low extracellular Ca^{2+} concentrations[2]. These data suggest that CALHM1 contributes to enhanced neuronal excitability in response to low external Ca^{2+2}.

A more extensively studied role of CALHM channels is their role in taste perception[44,45]. Type II taste bud cells are responsible for sensing sweet, bitter and umami tastes [45,46]. Sensation is mediated by a signaling cascade that begins with the activation of specific GPCR receptors upon tastant binding (**Figure 6**)[44,45]. This leads to an increase in intracellular calcium, which in turn activates TRPM5 channels[44,45]. As a result of their activation, membrane depolarization occurs, which triggers action potential firing resulting in non-vesicular ATP release through voltage-gated channels and the released ATP serves as a neurotransmitter for gustatory nerves[44,45]. The identity of the channels that mediate this release has long been unknown and awaited.

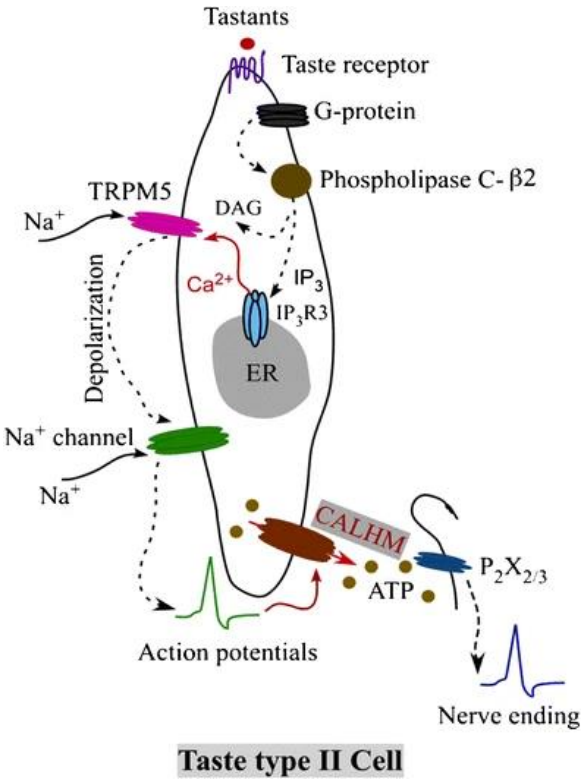

Figure 6. Sweet, bitter and umami taste perception signaling cascade. Tastants bind to GPCR taste receptors in the apical membranes of type II taste cells. Activation of the receptor activates phospholipase C-β2, resulting in increased cytoplasmic calcium. This activates TRPM5 channels, which depolarize the membrane, triggering Na^+ action potential which activates CALHM1/3 channels to release ATP. ATP binds to P2X2/3 receptors on afferent taste nerves to further transmit the information to the brain. Figure from [1].

Studies in animal models, as well as biochemical and biophysical studies, have shown that it is the CALHM1/3 channels that mediate this release[44]. Genetically modified mice lacking CALHM1 or CALHM3 expression lose the ability to perceive sweet, bitter and umami tastes[44,49]. Enrichment of CALHM1 and CALHM3 transcripts has been found in type II taste bud cells, and CALHM1 proteins have been shown to localize to the contact sites of receptor cells and taste nerve fibres[44,45,50]. The CALHM1/3 channels are permeable to ATP and currents evoked in type II taste bud cells at positive voltages resemble those of CALHM1/3 channels in their kinetics, morphology and pharmacology[44]. All this has established heteromeric CALHM1/3 channels as part of the signaling cascade of sweet, umami and bitter taste perception[44].

CALHM1 has also been shown to colocalize with pannexins in nasal epithelial cells and porcine bladder[49,51]. Both channels have been implicated in mediating ATP efflux in these tissues. Knockout of either one or both proteins in airway epithelial cells significantly reduced ATP release upon mechanical stimulation[49]. In porcine bladder cell cultures, specific blockers of pannexins and CALHM1 reduced ATP release on stretch[52]. In *C.elegans*, CLHM-1, the only homologue of the CALHM family, which shares 16% sequence identity with human CALHM1, is expressed in sensory neurons and body wall muscles[53]. Knockout of the gene results in impaired locomotion[53]. The phenotype can rescued by expression of human CALHM1, whose invertebrate isoform has similar biophysical properties[53]. The molecular mechanisms underlying these observations are still unknown.

1.4.6 Uncharacterized CALHM homologues

The localization, expression and function of other members of the CALHM family remain unknown or poorly characterized. One study suggested a role for CALHM2 in ATP release in astrocytes[54]. In this study low levels of ATP efflux were observed in cell-derived vesicles heterologously expressing CALHM2[54]. Notably, ATP release appeared to be potentiated by an increase in extracellular calcium, in contrast to observations with CALHM1/3 channels[54]. Knocking out the CALHM2 gene resulted in reduced ATP release from astrocytes, impaired neuronal function and depressive-like behaviors in KO mice[54]. The symptoms could be ameliorated by ATP administration[54]. CALHM6 has been proposed to be involved in the immune responses of NK cells[55,56]. Its expression was induced in activated macrophages and dendric cells and it was required to induce IFN-γ secretion, but not cytotoxicity, from NK cells[55]. Consequently, CALHM6 deficiency resulted in poor anti-tumor immunity against IFN-sensitive metastatic tumors and reduced efficacy of IFN-dependent, poly(I:C)-based immunotherapy[56]. The physiological role and functional properties of CALHM4 and CALHM5 paralogues remain unknown.

1.5 Aim

Despite the breakthrough studies, which revealed the unique functional properties of CALHM1 and CALHM1/3 ion channels, it remained unknown how these channels integrate electrical and chemical signals to catalyze the membrane permeation of large substrates. In addition, the biology and molecular function of most CALHM family members remained elusive.

To address these gaps in the comprehension of the CALHM family, this work aimed to characterize family members at the functional and structural level. Given the importance of CALHM1 and CALHM1/3 channels, and large-pore channels in general, in physiological processes, it was essential to investigate the structure of the CALHM family members. The structural characterization of large-pore channels by crystallography, has been challenging. However, the emergence of cryo-electron microscopy revolutionized this field, and I thus decided to employ this technique for structural studies of the CALHM family. Moreover, since the knowledge of the biology and molecular function of the majority of CALHM family members has remained elusive, a closer look on these poorly characterized paralogs was warranted. For functional studies, electrophysiology and *in vitro* assays using reconstituted proteins provide powerful methods for the characterization of ion channels. Furthermore, I attempted to gain initial insight into the biology of these proteins studying their expression patterns and investigating their interactions in native tissues.

2. Results

2.1 Structural studies of homomeric CALHM channels

The CALHM family has been largely unexplored in terms of structural studies, with no reported structures of any family members at the beginning of this thesis project. Consequently, my primary aim was to identify biochemically stable homologues within the family, enabling me to characterize their structural properties and gain insights into the mechanistic basis of their function as large-pore channels.

2.1.1 Screening of CALHM proteins

Structural studies of recombinant proteins require their preparation comprising over-expression, extraction and purification and all these steps need to work optimally to result in a sample of a stable protein at a sufficient yield for subsequent investigations. In order to identify members of the CALHM family exhibiting suitable biochemical features required for structural studies, small scale expression and detergent extraction tests have been performed. As an expression host, HEK293T cells have been chosen, accounting for their broad use for eukaryotic membrane proteins production. To monitor expression and extraction, a fluorescent protein has been genetically fused to the C-terminus of the respective CALHM paralog to act as a reporter in fluorescence-based analysis. **Figure 7-A** shows the scheme of expression constructs comprising sequences of a human *CALHM* gene followed by sequences coding for a 3C protease cleavage site, venus-YFP (vYFP), Myc and Streptavidine-Binding Peptide (SBP) tags. Such constructs of all CALHM homologues were transiently expressed in adherent cultures of HEK293T cells and their expression, localization and folding quality were monitored by fluorescence microscopy. **Figure 7-B** shows fluorescence-microscopy images taken after 36 h of expression. Fluorescent signals detected in the images indicate that all human CALHM homologues are expressed in HEK293T cells. However, for different constructs I found a variable strength of the signal corresponding to protein expression levels and localization. CALHM1 and 3 proteins exhibit low expression levels and predominant intracellular localization with marginal surface expression (**Figure 7-B**). Notably, detached cells expressing strong fluorescence signals are abundant in images obtained for these homologues indicating misfolding or toxicity of CALHM1 and 3 proteins during overexpression in HEK293T cells (**Figure 7-B**). The reverse trend is observed for CALHM2 and 4-6 homologues, for which higher expression and enriched surface localization is observed as well as apparent lower ratio of dead to alive cells in comparison to CALHM1 and 3 (**Figure 7-B**).

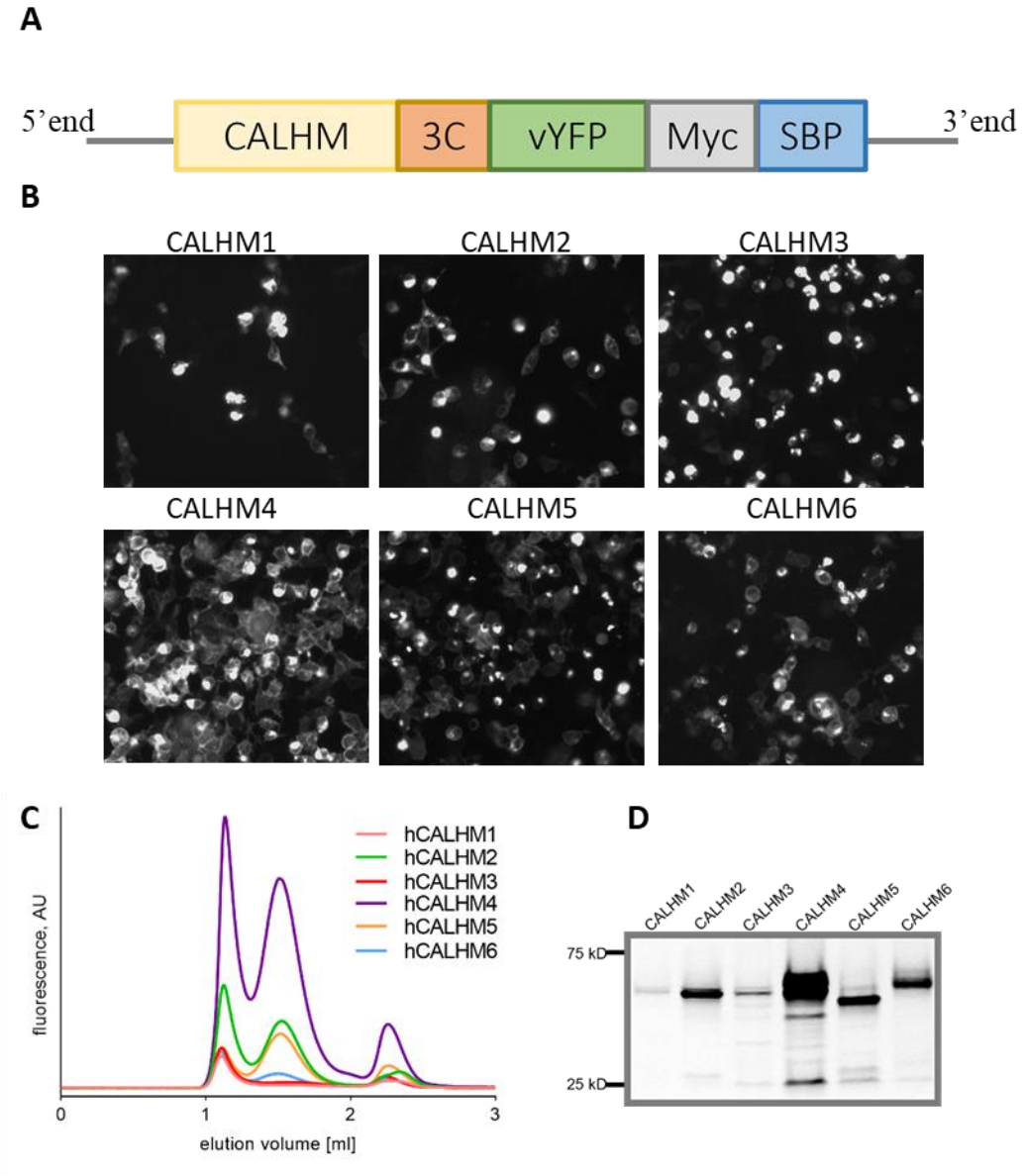

Figure 7. Expression of human CALHM proteins in adherent HEK293 cell cultures. (A) Schematic depiction of the genetic CALHM construct expressed in HEK cells. The sequence of the CALHM gene is followed by sequences of 3C protease cleavage site, vYFP, Myc and SBP tags. **(B)** Fluorescence-microscopy images of HEK293 cells transfected with different *CALHM* constructs. **(C),** Superose 6 FSEC profiles and **(D)** in-gel fluorescence of extracted fluorescently tagged CALHM proteins showing the yields of extracted CALHM proteins.

With respect to its properties, CALHM4 stands out showing high expression and an unambiguous enriched plasma membrane fluorescence, distinguishing it as the most promising candidate for structural studies (**Figure 7-B**). To assess whether the observed expression pattern extends towards the stability of the proteins in vitro, I proceeded with extraction tests. The conventional way of extracting membrane proteins utilizes solubilization with a detergent, which amphipathic character mimics the native environment of a lipid bilayer and thus preserves their native state. For the extraction of CALHM proteins from HEK cells, I decided to use the mild nonionic glyco-diosgenin (GDN) detergent,

accounting for its successful use in numerous membrane proteins studies. After treatment with GDN, HEK cells extracts were analyzed by size-exclusion chromatography and SDS-PAGE analysis utilizing fluorescence detection in order to selectively monitor the vYFP-tagged constructs. **Figure 7–C** shows resulting fluorescence chromatography profiles on a Superose S6 column of extracted CALHM-3C-vYFP-Myc-SBP proteins. As anticipated based on imaging results, different behaviors were observed between homologues, however, a certain degree of aggregation reflected in a peak eluting at the void volume of the column, is common for all homologues (**Figure 7-C**). To assess the fraction of CALHM proteins residing in their native state I focused on the size and monodispersity of the main peaks of the profiles at the expected elution volume of a oligomeric CALHM channel. Based on marker proteins, on a Superose 6 column, the monomeric ~36 kDa CALHM protein would elute at an approximate volume of 2 ml. However such peaks are not observed in any of the recorded chromatograms. Instead, relatively large monodisperse peaks at elution volumes of approximately 1.5 ml are observed for CALHM2 and 4-6 proteins (**Figure 7-C**). This elution volume corresponds to approximately 700 kDa and, after correcting for the mass contribution of the fusion tag and the detergent micelle, it indicates high oligomeric assemblies of extracted CALHM2 and 4-6 proteins as expected from previous studies on CALHM proteins[35,44]. In contrast, no peak corresponding to stable proteins is observed for CALHM1 and 3 constructs, which agrees with the observations in fluorescence microscopy images showing low expression of those homologues (**Figure 7-C**). Finally, a small peak eluting around 2.3 ml corresponding to a mass of about 20 kD is observed for all constructs and is suspected to be a consequence of protein degradation releasing the C-terminal 3C-vYFP-Myc-SBP fusion tag (**Figure 7-C**).

To investigate the molecular masses of the monomeric components, the samples of the whole-cell extracts were subjected to SDS-PAGE monitoring the in-gel fluoresce (**Figure 7-D**). All constructs were expected to show bands within the range of 60-70 kD corresponding to the mass of a fusion CALHM construct. Indeed, for all constructs, fluorescing bands in this MW range are observed. The strongest band intensities were found for CALHM4 followed by CALHM2, 5 and 6 (**Figure 7-C**). Weak narrow bands are observed for CALHM1 and 3, which agrees with observations from fluorescence microscopy and FSEC experiments, together indicating poor expression of these constructs in HEK cells (**Figure-7-C**).

In conclusion, the analysis revealed the high expression and extractability of CALHM4, moderate expression and extraction of CALHM2, 5 and 6 and low expression and essentially no extraction of CALHM1 and CALHM3. Additionally, FSEC experiments revealed the elution of well-extractable CALHM proteins at volumes corresponding to high oligomeric assemblies, distinguishing them as promising candidates for cryo-electron microscopy studies. Due to their low expression and unsuccessful extraction CALHM1 and 3 were not considered for further analysis.

2.1.2 Biochemical characterization and purification of CALHM proteins

Note: negative staining sample and data collection of CALHM4 was performed by Dr. Marta Sawicka

In order to examine the stability of the isolated proteins I proceeded with the purification of CALHM2 and CALHM4-6 proteins. Constructs of CALHM-3C-vYFP-Myc-SBP were transiently expressed in HEK293 cells in suspension culture allowing for an easier handling of larger expression volumes in comparison to adherent HEK cells. All proteins were purified by a two-step procedure including affinity chromatography followed by gel-filtration. **Figure 8** shows obtained gel-filtration chromatography profiles and corresponding SDS-page gels.

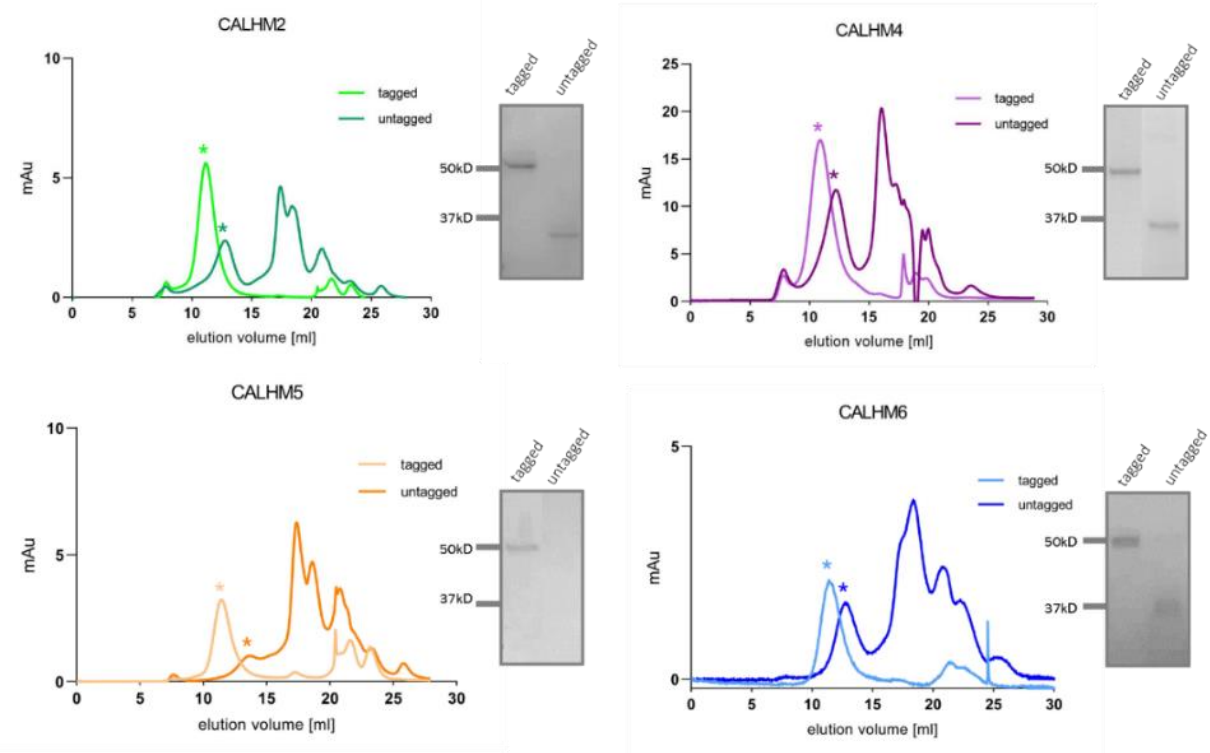

Figure 8. Small scale purification and stability test upon tag cleavage of CALHM2, 4, 5 and 6. Overlayed Superose S6 SEC profiles allow comparison of yield and dispersity of affinity purified CALHM proteins before and after tag cleavage. Shown is the absorption at 280 nM plotted against elution volumes. Respective CALHM peaks are marked with the asterisks. Coomassie stained SDS-PAGE gels show shifts of purified CALHM proteins to lower masses after tag cleavage.

Consistent with FSEC studies, all purified fusion constructs elute as monodisperse symmetric peaks (**Figure 8**). However, the goal of the experiments was to obtain pure samples of untagged CALHM proteins, as the flexible nature of the tag could preclude structural characterization efforts. For this purpose, a proteolytic cleavage step has been introduced prior a gel filtration for half of the sample and the peak profiles were compared. Upon tag cleavage, the main peaks shift towards the higher elution volumes and corresponding SDS-PAGE bands towards lower molecular masses, which confirms the successful proteolysis (**Figure 8**). The peaks maintain their morphology, indicating the stability of the untagged CALHM proteins with the exception of CALHM5 (**Figure 8**). In this case, a broad asymmetric peak is observed upon removal of the fusion tag, suggesting an increasing instability of the CALHM5 protein, a phenomenon that is frequently observed for proteins upon cleavage of stable and soluble tags (**Figure 8**). Interestingly, differences in elution volumes are observed between the three well-behaved homologues (**Figure 8**). To exclude artifacts from gel-filtration runs on the used column, large scale purifications have been performed for the three well behaved homologues.

Figure 9-A shows a comparison of elution volumes in gel filtration chromatograms of large-scale purifications of CALHM2, 4 and 6. The highest elution volume is observed for CALHM6, a similar but slightly lower volume for CALHM2 and the smallest volume for CALHM4, thus hinting towards distinct oligomeric organizations of the three proteins with CALHM4 forming larger complexes than CALHM2 and 6 (**Figure 9-A**). To investigate the heterogeneity of the CALHM samples with respect to their oligomeric organization, the proteins were analyzed by negative-stain EM. In the process of negative staining, the dye surrounds the immobilized molecules, allowing the visualization of their surface and producing bright images of molecules on a dark background. CALHM2, 4 and 6 grids stained with uranyl acetate were analyzed using a transmission electron microscope. **Figure 9-B** shows obtained images exhibiting a homogenous sample of large channel-like assemblies as expected from gel filtration experiments and previous reports on CALHM proteins. However, one striking result was the presence of CALHM2 and CALHM4 channel dimers (**Figure 9-B**). In case of the latter, exclusively dimers of channels were observed, whereas in case of CALHM2 also single channels are present (**Figure 9-B**). In contrast to those two samples, CALHM6 channels adopt a preferred top-view orientation, which generally precludes the identification of dimeric assemblies. In this case, rare side-views hint towards single channel assemblies in agreement with the gel-filtration profile.

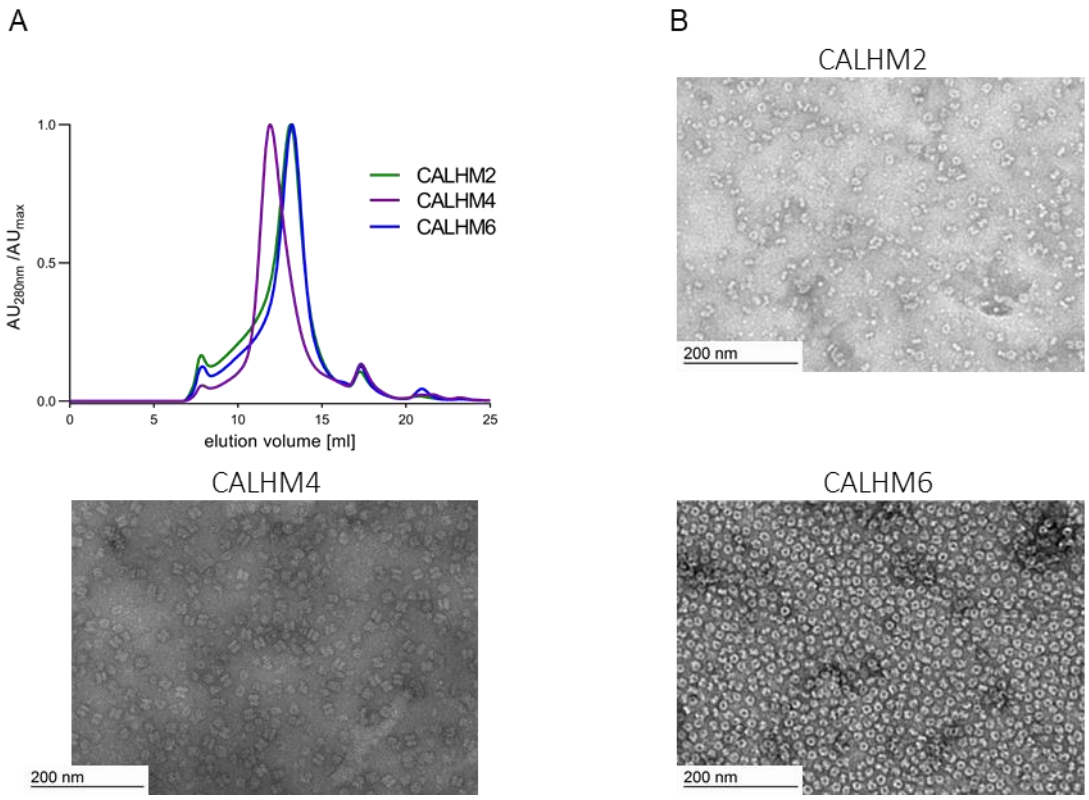

Figure 9. Large scale purification and biochemical characterization of CALHM2, CALHM4 and CALHM6. (A) Overlayed Superose S6 SEC profiles of the three CALHM homologues.
(B) Representative negative staining micrographs containing purified CALHM proteins of the three homologues.

2.1.3 The attempted structure determination of CALHM2 channels

Note: Chapters 2.1.3 - 2.1.8 include a slightly modified part of the publication (Cryo-EM structures and functional properties of CALHM channels of the human placenta)[57]. The author of the thesis shared joint first authorship with Dr. Marta Sawicka and was responsible for construct generation, screening, sample preparation, assistance in cryo-EM data processing, model building and refinement, and the analysis of the lipidomic data.

For the structure determination of CALHM2 channels, purified protein was prepared in GDN in the presence of Ca^{2+}. The sample was plunge-frozen in a liquid mixture of propane and ethane and 2 065 images were collected on a Tecnai G^2 Polara cryo-electron microscope equipped with a K2 camera. **Figure 10** shows details of the processing strategy. Details of cryoEM data processing and model building can be found in the figure legend as well as in the Method section. In brief, 417 612 particles were picked, extracted and iteratively sorted by 2D classification. As revealed by classes viewed along the pore axis, which clearly display the number of individual CALHM2 subunits, channels exhibit undecameric and dodecameric assemblies in a particle ratio of 2:1 (**Figure 10-B)**. In addition, we observe paired and non-paired channel assemblies with a predominance of the latter constituting 2/3 of all the particles (**Figure 10-B)**. Although we attempted to further sort the particles by 3D classification, the strong preferential orientation of CALHM2, resulting in a predominance of views along the pore axis, prohibited the reconstruction of a high-resolution cryoEM map, which limited the processing workflow to 2D classification (**Figure 10-B)**.

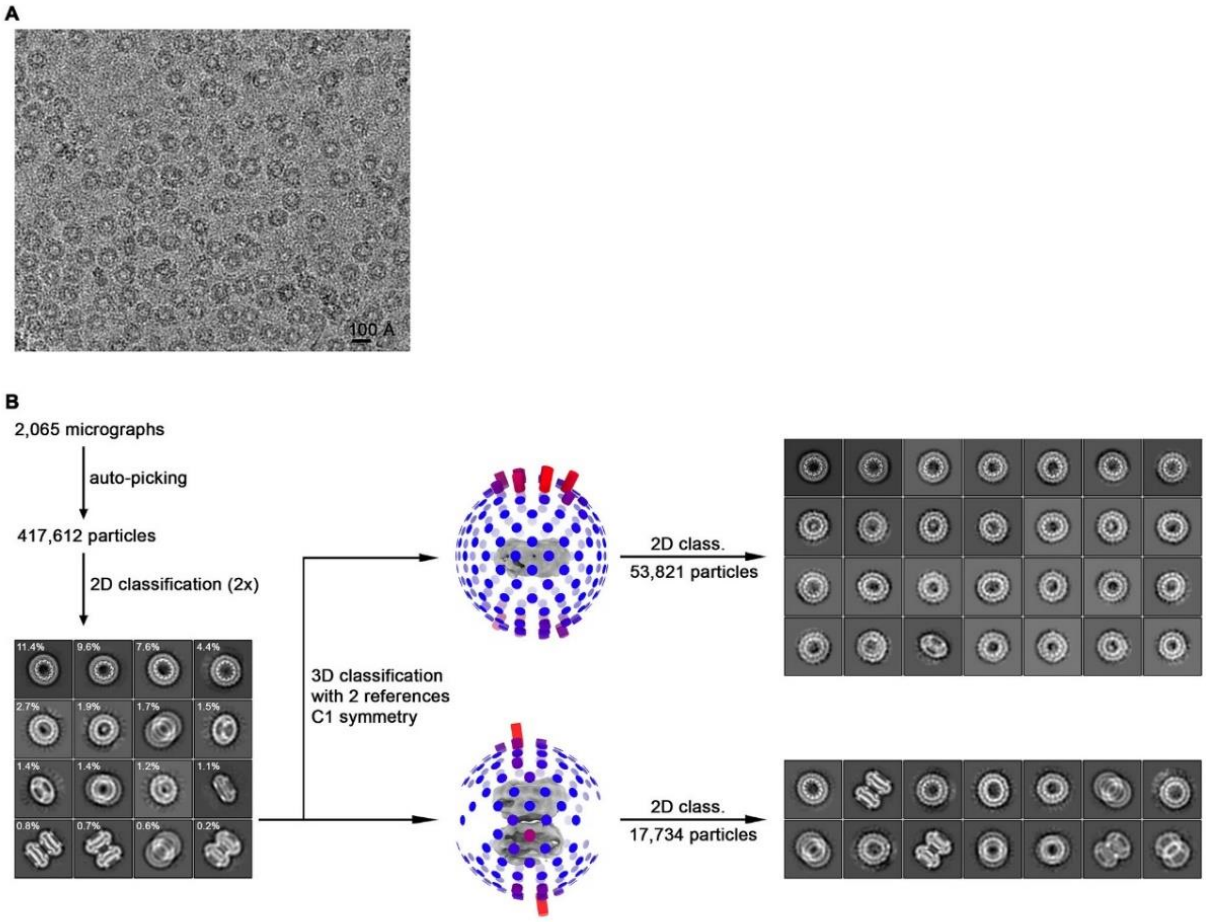

Figure 10. Cryo-EM reconstruction of CALHM2. (**A**) Representative cryo-EM micrograph acquired with a Tecnai G^2 Polara microscope equipped with a K2 camera. (**B**) Data processing workflow. Non-symmetrized 3D classification with two reference models representing monomeric and dihedrally-related dimeric architectures allowed to separate CALHM2 particles into respective subsets. However, preferential orientation of the particles on a grid together with the presence of compositional heterogeneity in form of undecameric and dodecameric assemblies within each subset hindered generation of a high-resolution 3D reconstruction. 2D class averages calculated separately from monomeric and dimeric subsets highlight the predominance of views from the extracellular side.

2.1.4 Structure determination of CALHM4 channels

For the structure determination of CALHM4 channel, samples were prepared like for CALHM2 except that in this case samples in the presence and absence of Ca^{2+} have been prepared. **Figure 11** and **12** show details of the processing strategy for samples in the presence and absence of Ca^{2+} respectively. More explicit details of cryoEM data processing and model building can be found in the figure legend as well as in the Method section. In brief, 422 281 particles were picked and subjected to repeated iterative rounds of 2D and 3D classification and further 3D and post-processing refinement steps with C10 or C11 symmetry imposed (**Figure 11 and 12**). This approach yielded maps at 3.92 Å and 4.07 Å for undecameric and decameric assemblies of CALHM4 in the presence of Ca^{2+} and 3.69 Å and 4.07 Å for decameric and undecameric assemblies in the absence of Ca^{2+} (**Figure 11-C and D and Figure 12-C and D**) The obtained maps permitted the unambiguous interpretation by an atomic model. **Figure 13** shows representative cryo-EM densities. Details on model building can be found in the Method section.

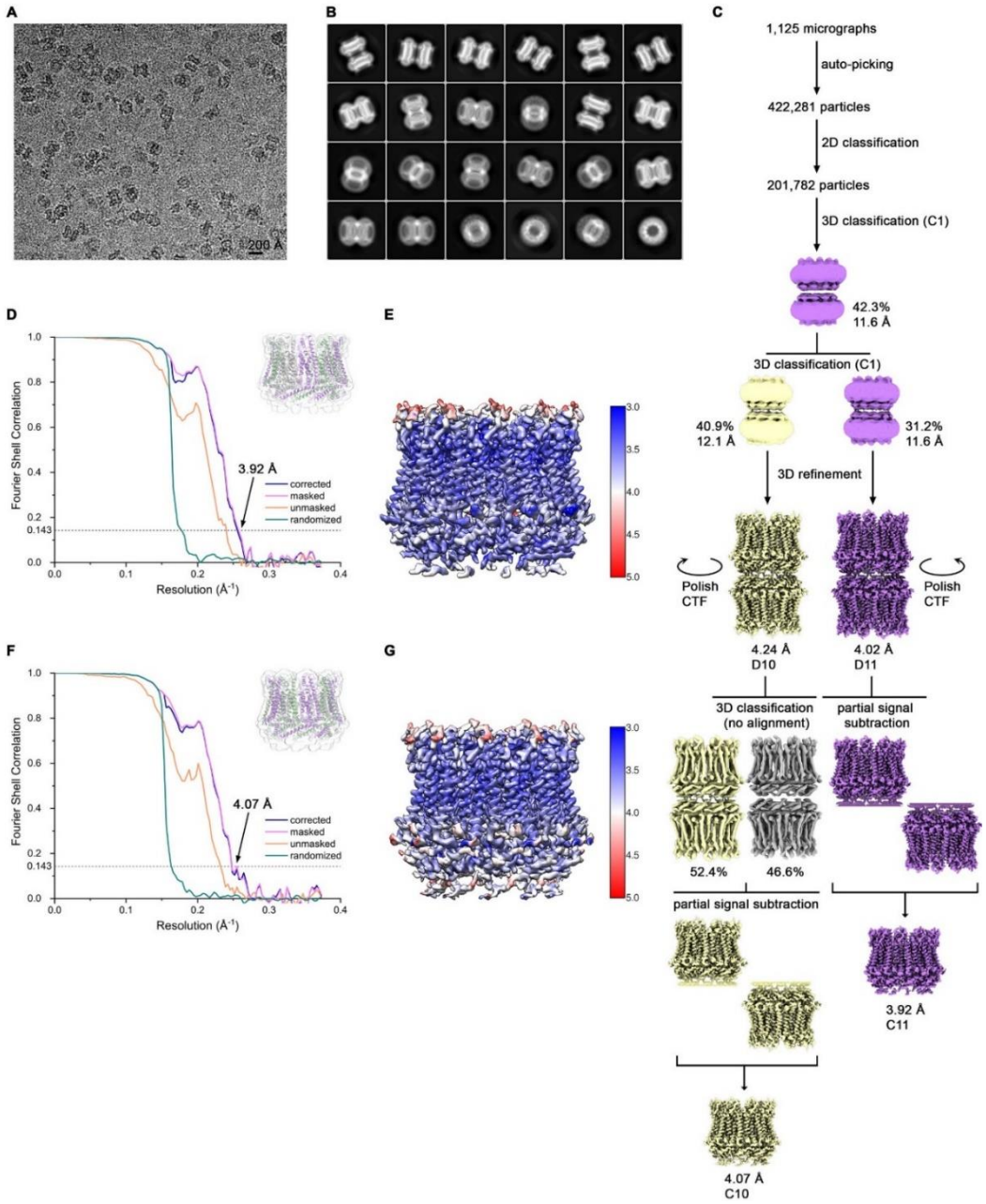

Figure 11. Cryo-EM reconstruction of CALHM4 in the presence of Ca^{2+}. (**A**) Representative cryo-EM micrograph acquired with a Tecnai G^2 Polara microscope equipped with a K2 camera. (**B**) 2D class averages of CALHM4 in presence of Ca^{2+}. (**C**) Data processing workflow. Two rounds of non-symmetrized 3D classification allowed to isolate two populations representing decameric and undecameric assemblies. The particles were further refined with either D10 or D11 symmetry imposed. After performing per-particle CTF refinement and Bayesian polishing, the remaining structural heterogeneity in decamers was segregated by performing a final round of 3D classification, where the orientations were kept fixed as in the consensus model. To further improve the resolution of each reconstruction, partial signal subtraction followed by 3D refinement was applied. Particles with the symmetry relaxed to either C10 or C11 were merged and subjected to a final round of auto-refinement. The distribution of all particles (%) and the resolution of each class is indicated. (**D**) FSC plot of the final refined undecameric unmasked (orange), masked (pink), phase-randomized (green) and corrected for mask convolution effects (blue) cryo-EM density map of CALHM4. The resolution at which the FSC curve drops below the 0.143 threshold is indicated. The inset shows the atomic model within the mask that was applied for calculations of the resolution estimates. (**E**) Final 3D reconstruction of undecameric CALHM4 colored according to local resolution. (**F**) FSC plot of the final refined decameric unmasked (orange), masked (pink), phase-randomized (green) and corrected for mask convolution effects (blue) cryo-EM density map of CALHM4. The resolution at which the FSC curve drops below the 0.143 threshold is indicated. The inset shows the atomic model within the mask that was applied for calculations of the resolution estimates. (**G**) Final 3D reconstruction of decameric CALHM4 colored according to local resolution.

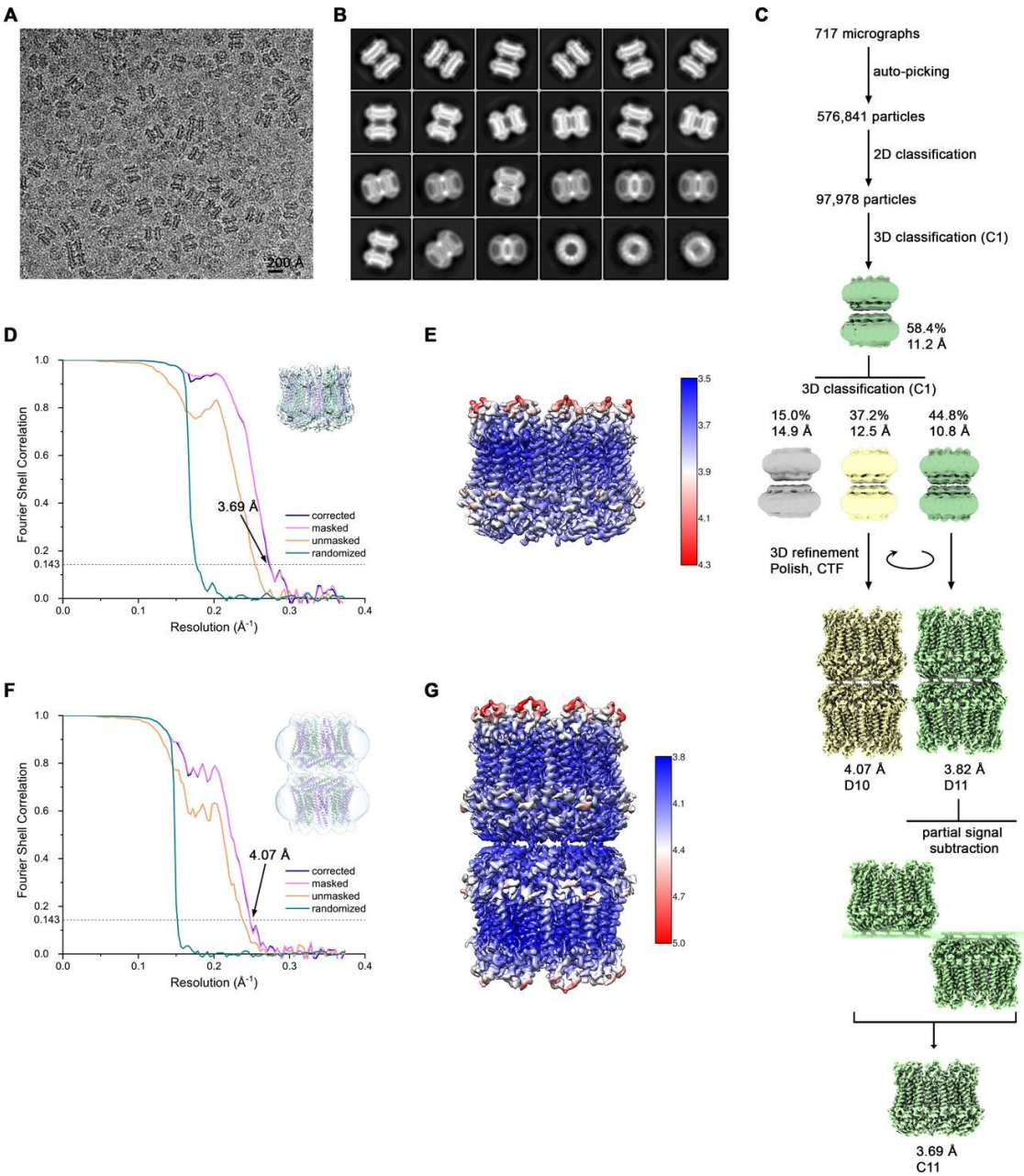

Figure 12. Cryo-EM reconstruction of CALHM4 in absence of Ca^{2+}. (**A**) Representative cryo-EM micrograph acquired with a Tecnai G^2 Polara microscope equipped with a K2 camera. (**B**) 2D class averages of CALHM4 in absence of Ca^{2+}. (**C**) Data processing workflow. Two rounds of non-symmetrized 3D classification allowed to isolate two populations representing decameric and undecameric assemblies. The particles were further refined with either D10 or D11 symmetry imposed and iterative per-particle CTF refinement and Bayesian polishing. The distribution of all particles (%) and the resolution of each class is indicated. (**D**) FSC plot of the final refined undecameric unmasked (orange), masked (pink), phase-randomized (green) and corrected for mask convolution effects (blue) cryo-EM density map of CALHM4. The resolution at which the FSC curve drops below the 0.143 threshold is indicated. The inset shows the atomic model within the mask that was applied for calculations of the resolution estimates. (**E**) Final 3D reconstruction of undecameric CALHM4 colored according to local resolution. (**F**) FSC plot of the final refined decameric unmasked (orange), masked (pink), phase-randomized (green) and corrected for mask convolution effects (blue) cryo-EM density map of CALHM4. The resolution at which the FSC curve drops below the 0.143 threshold is indicated. The inset shows the atomic model within the mask that was applied for calculations of the resolution estimates. (**G**) Final 3D reconstruction of decameric CALHM4 colored according to local resolution.

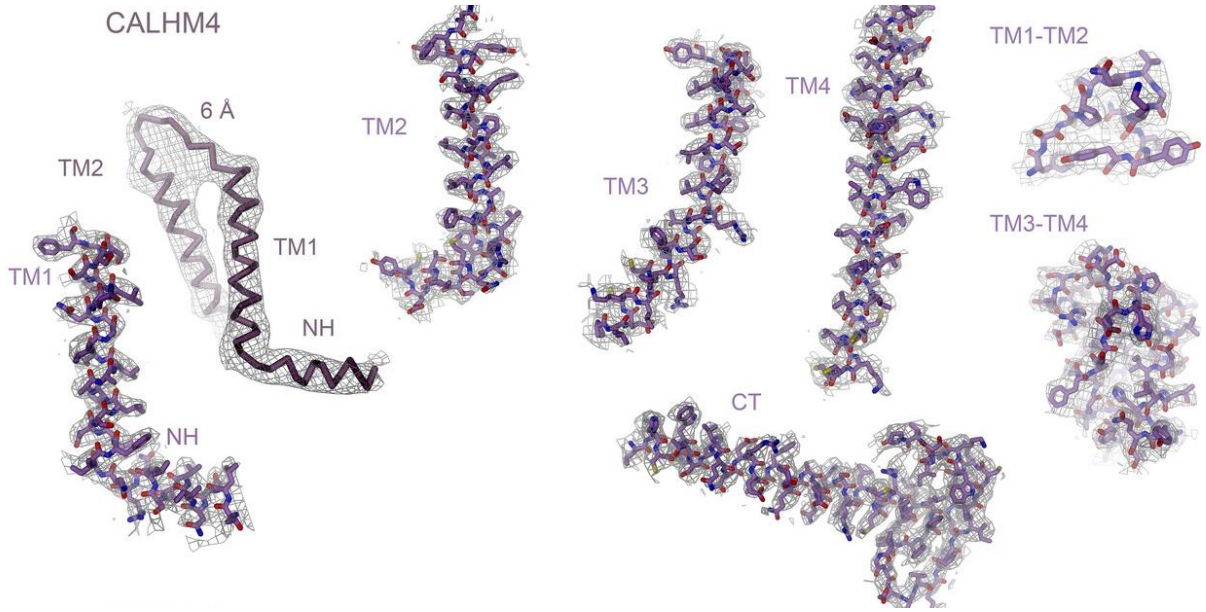

Figure 13. Cryo-EM density of CALHM4. (**A**) Cryo-EM density at 3.7 Å of selected regions of the undecameric CALHM4 structure recorded from a sample obtained in the absence of Ca^{2+} superimposed on the model. Structural elements are indicated, '6 Å' marks cryo-EM density low-pass filtered to 6 Å superimposed on a Cα trace of NH and TM1.

2.1.5. General architecture of CALHM4 channels

Regardless of the presence or absence of Ca^{2+}, we observed about equal distributions of CALHM4 channels with two distinct oligomeric states (**Figure 11-C and 12-C**). The smaller channels are composed of ten and the larger of eleven subunits. Both oligomers almost completely dimerize via contacts at the intracellular side. Due to the slightly higher quality of the Ca^{2+}-containing sample, I continue to use this data for further analysis. **Figure 14** shows the final cryoEM maps and corresponding molecular models of decameric and undecameric CALHM4 channels. In each structure, the subunits are arranged around a central axis of symmetry that presumably defines the ion-conduction path (**Figure 14**). The CALHM4 channels form approximately 90 Å high cylindrical proteins that span the lipid bilayer with regions at their respective periphery extending into the aqueous environment on either side of the membrane (**Figure 14**). In the plane of the membrane, the dimensions of decameric and undecameric CALHM4 channels amount to 110 Å and 120 Å respectively (**Figure 14**). Irrespective of their distinct oligomerization, the individual subunits in both assemblies show equivalent conformations. **Figure 15** shows individual CALHM4 proteins constituting a protomer of the channels and mutual interactions between helices and protomers.

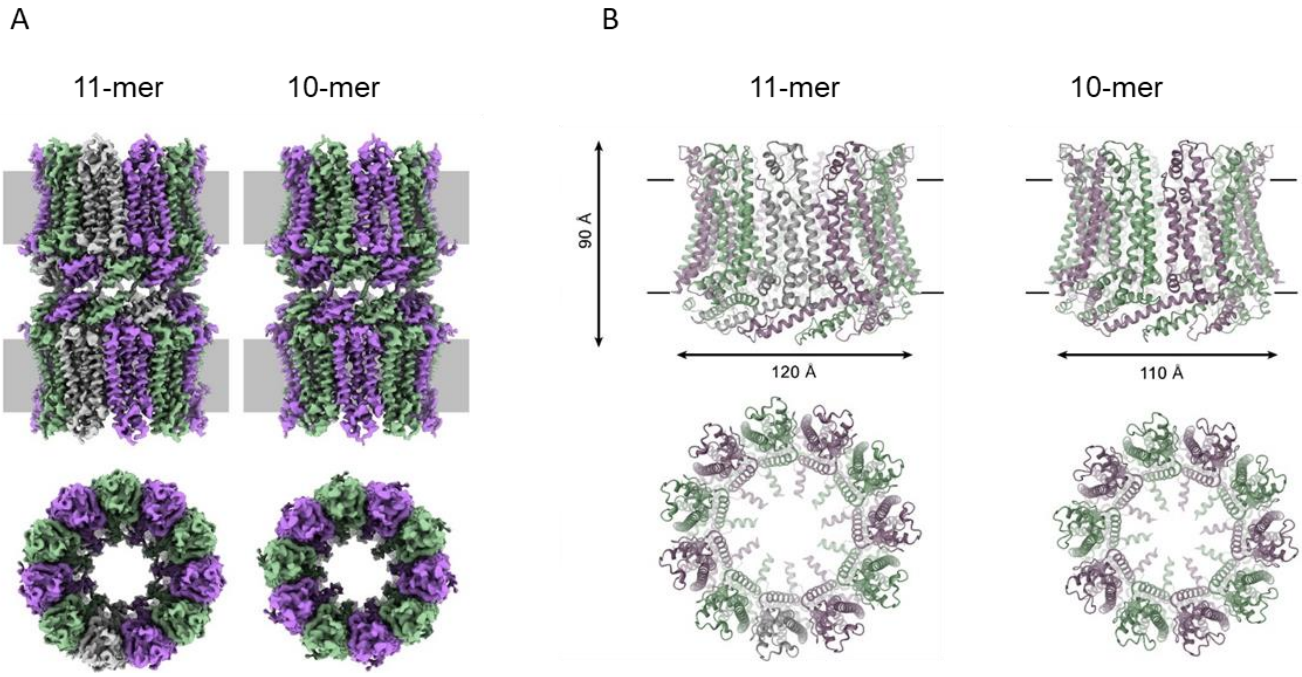

Figure 14. CALHM4 structure. (**A**) Cryo-EM density of undecameric (11-mer) and decameric (10-mer) pairs of CALHM4 channels at 3.8 and 4.1 Å respectively. Data were recorded from a Ca^{2+}-free sample. Subunits are colored in lilac and green, respectively. (**B**) Ribbon representation of, decameric and undecameric CALHM4 channels. Top views are from within the membrane with membrane boundaries indicated, bottom views are from the extracellular side. The approximate dimensions are indicated. Subunits are colored in lilac and green.

CALHM4 subunits contain four transmembrane helices, which run perpendicular to the membrane and, when viewed from the extracellular side, are arranged in an anticlockwise manner (**Figure 15-A and B**). The helices of the CALHM subunit are organized as two layers conferring an overall trapezoid cross-section (**Figure 15-B**). The outer layer of the CALHM subunit is composed of the interacting α-helices TM2-4, which are arranged in one row sharing mutual interactions only with their respective neighbor (**Figure 15-A and B)**. The inner layer consists of TM1, which, on its entire length, exclusively interacts with TM3, the central helix of the outer layer (**Figure 15-A and B)**. Assembled into oligomers, the helices of the outer layer form a ring, which defines the boundaries of the channel (**Figure 15-B)**. In this outer ring, the peripheral helices TM2 and 4 are involved in extended interactions with neighboring subunits resulting in a tightly packed interface (**Figure 15- B)**. Apart from a small fenestration between TM3 and 4 in the center of each subunit, this structural unit shields the interior of the pore from the surrounding membrane (**Figure 15-C**).

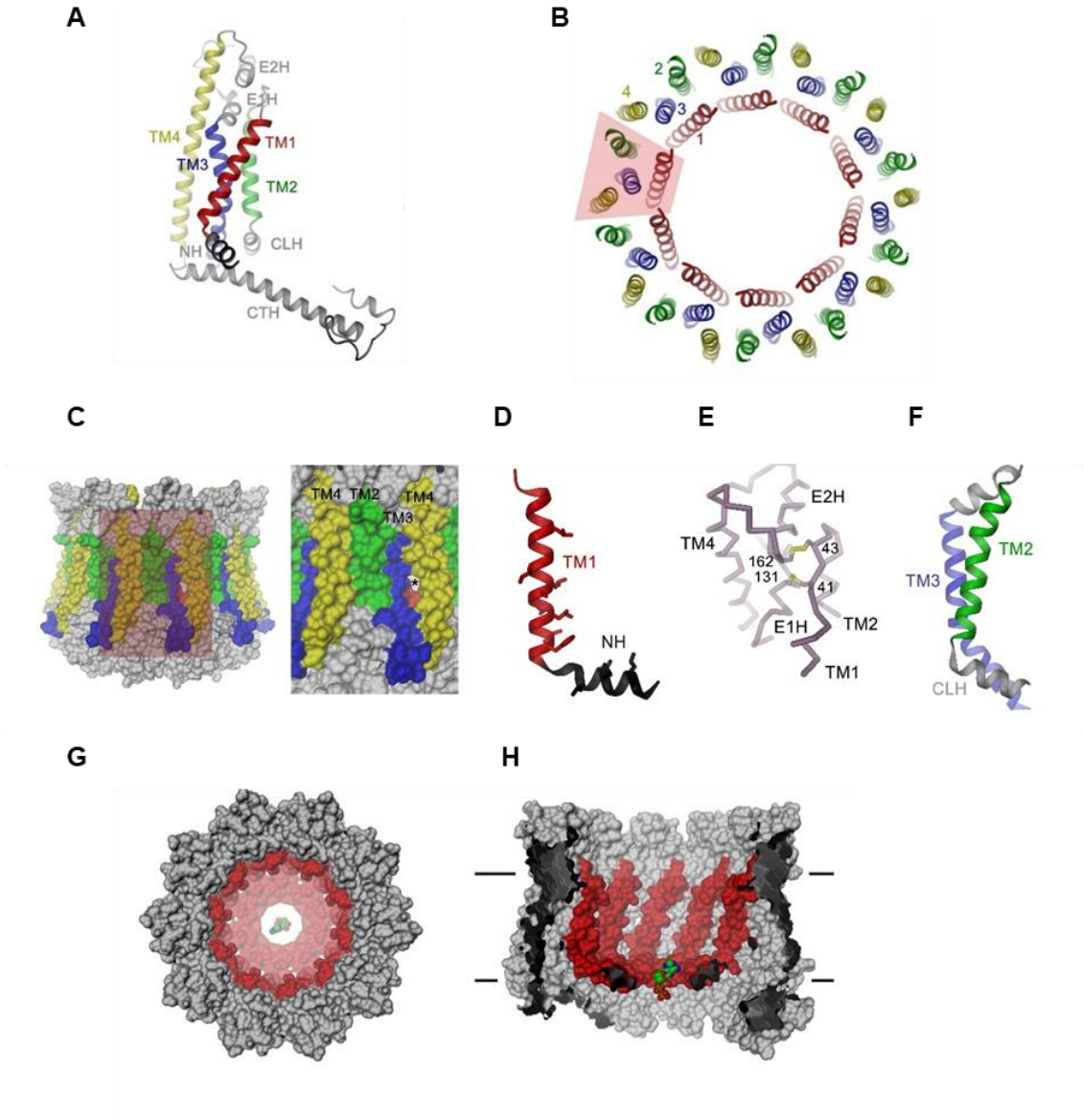

Figure 15. CALHM4 structure features. (**A**) Ribbon representation of the CALHM4 subunit. Secondary structure elements are labeled and transmembrane α-helices are shown in unique colors. (**B**) View of the transmembrane α-helices of the CALHM4 decamer, the color code is as in (**A**), transmembrane segments of one subunit are numbered. The general shape of a single subunit is indicated. (**C**) Molecular surface of the CALHM4 decamer viewed from within the membrane (left) and zoom into the highlighted region showing the interface between two subunits (right). Asterisk indicates the location of a small fenestration on the surface between TM3 and TM4 of the same subunit. (**D**) Ribbon representation of TM1 and the N-terminal α-helix NH, with side chains of hydrophobic residues facing the pore displayed as sticks. (**E**) Cα-trace of the extracellular region of CALHM4 with disulfide bridges shown as sticks and labeled. (**F**) Ribbon representation of TM2, the intracellular α-helix CLH and TM3. (**G**) Surface representation of the CALHM4 decamer. The view is from the outside. ATP is shown as a space-filling model for comparison (**H**), Slice through the CALHM4 pore viewed from within the membrane. TM1 and the N-terminal α-helix NH are colored in red, ATP is shown as a space-filling model for comparison.

In contrast, the respective TM1 helices forming the inner layer are distant from each other and thus not involved in mutual inter-subunit interactions (**Figure 15-B and G**). In the region preceding TM1, the residues of the N-terminus form a helix (NH) that is oriented perpendicular to the first transmembrane segment parallel to the plane of the lipid bilayer (**Figure 15-D**). On the extracellular side, a short loop bridges α-helices TM1 and 2 and an extended region containing two short α-helices (E1H and E2H), connects TM3 with the long TM4, which extends beyond the membrane plane (**Figure 15-A**). The extracellular domain is stabilized by two disulfide bridges connecting both extracellular segments at the C-terminal end of TM1 in the observed conformation (**Figure 15-E**). On the intracellular side, TM2 precedes a short helix (CLH) that projects away from the pore axis with TM3 being bent in the same direction (**Figure 15-F**). Both α-helices are connected by a 12-residue long loop that is probably mobile and thus not defined in the density. Downstream of TM4, we find an extended intracellular region. The first halve of this region consists of a long α-helix (CTH), which is tilted by 70º towards the membrane plane and which tightly interacts with the corresponding parts of neighboring subunits thus forming a 30 Å-high intracellular ring (**Figure 15-A**). Distal to CTH, a 62-residue long extended loop, which includes partly defined in the cryo-EM density interspersed secondary structures, folds back towards the intracellular ring on the outer surface of the channel with its C-terminus extending to the opposed subunit of the juxtaposed CALHM4 channel (**Figure 16**). These contacts form the bulk of the interaction relating CALHM4 channel pairs in an arrangement whose relevance in a cellular context is ambiguous.

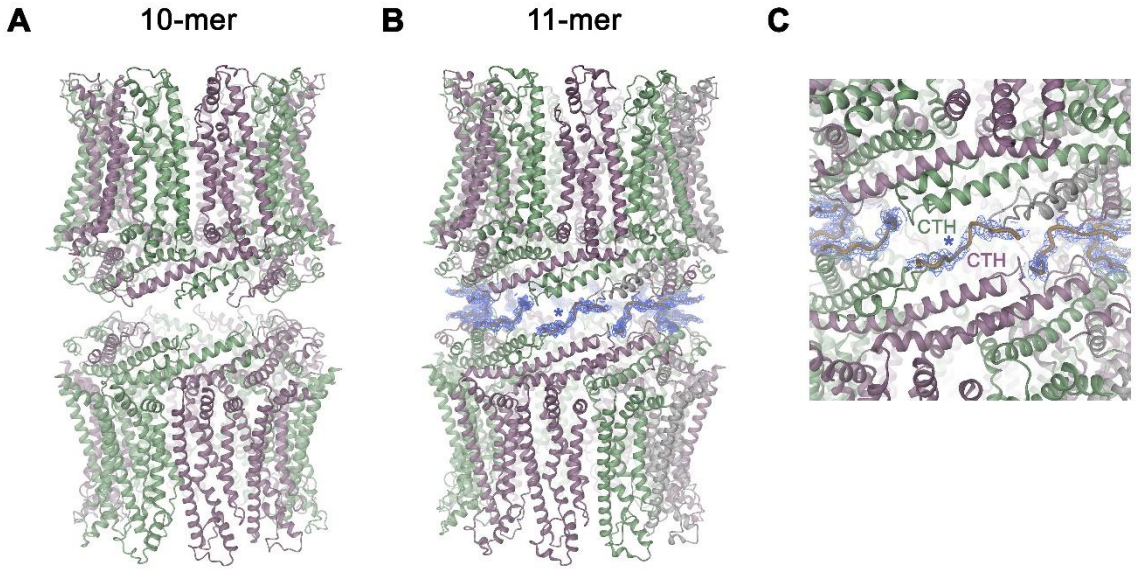

Figure 16. Features of the CALHM4 channel dimers. Ribbon representation of (**A**), decameric and (**B**), undecameric channel pairs as observed in the CALHM4 dataset. In both cases, the proteins interact via their intracellular regions. Residual density at the C-terminus connecting both channels is shown as blue mesh and modeled as a poly-glycine chain. (**C**) Close-up of the interface between channel pairs shown in B.

2.1.6 Cylindrical pore architecture of CALHM4 channels

Decameric and undecameric CALHM4 channels contain wide pores, which are cylindrical throughout except for a constriction at the intracellular membrane boundary. **Figure 17** shows features of the CALHM4 channel pore. The diameter at both entrances of the pore measures about 52 Å and 60 Å for decameric and undecameric assemblies respectively, thus defining the properties of an unusually large channel, which could be permeable to molecular substrates (**Figure 17-A**) . Even at the constriction located at the intracellular membrane leaflet where the respective N-terminal helices NH project towards the pore axis, the decameric channels are about 20 Å and undecameric channels 30 Å wide (**Figure 17-A)**. In both cases the pore would thus be sufficiently large to accommodate an ATP molecule, consistent with the view of CALHM as proteins forming ATP-permeable channels (**Figure 15-G**).

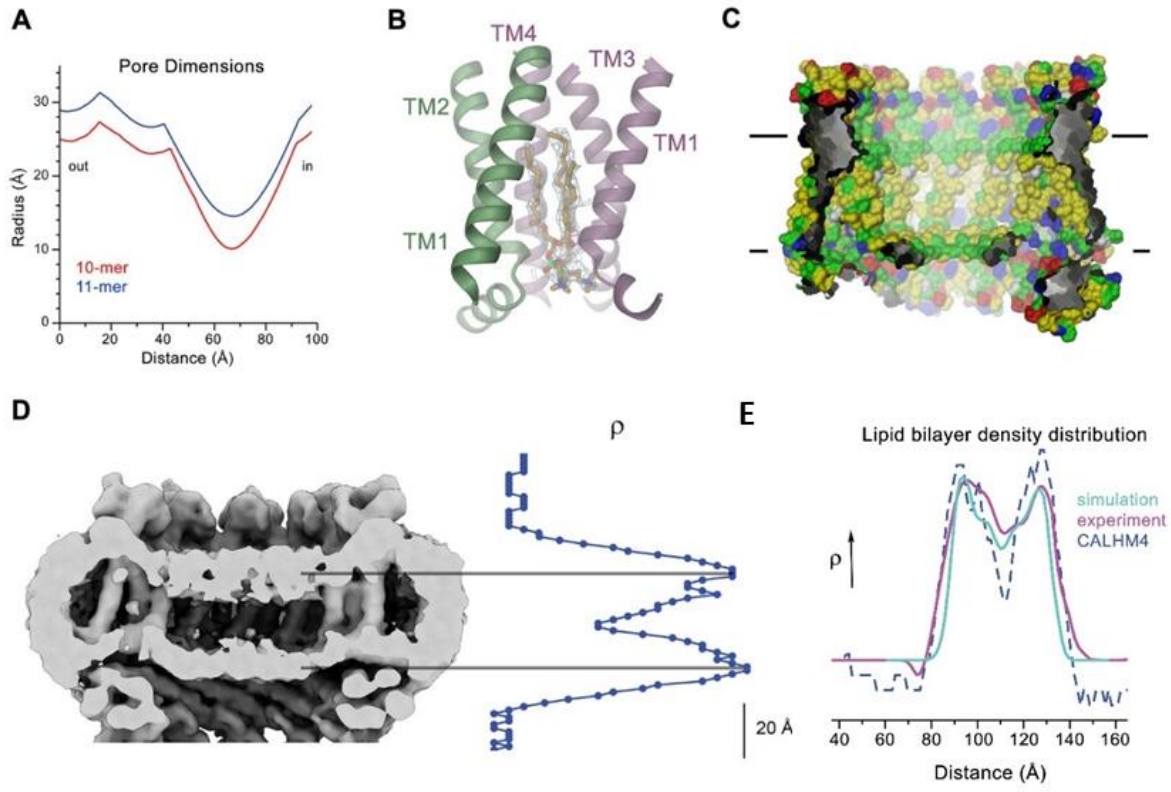

Figure 17. CALHM4 pore properties and lipid interactions. (**A**), Pore radius of the CALHM4 decamer (red) and undecamer (blue) as calculated in HOLE. (**B**) Two phosphatidylcholine molecules modeled into residual cryo-EM density (blue mesh) in a cavity at the interface between neighboring α-helices TM1. Secondary structure elements are indicated. (**C**) Chemical properties of residues lining the pore of the CALHM4 channel. Shown is a slice through the pore viewed from within the membrane. The protein is displayed as molecular surface. Hydrophobic residues are colored in yellow, polar residues in green, acidic residues in red and basic residues in blue. (**D**) Slice through the pore region of the CALHM4 decamer viewed from within the membrane. Shown is non-averaged density in a single copy of the decameric CALHM4 channel pair at low contour to highlight the location of increased density within the pore corresponding to a bilayer of either phospholipids or detergents. A plot of the density along the pore axis showing two maxima that are separated by the expected distance between the headgroup regions of lipid bilayer is shown right. (**E**) Comparison of the observed pore density distribution (dashed blue line, CALHM4) to equivalent distributions obtained from membrane simulations (cyan, simulation) and cryo-EM data of liposomes (magenta, experiment). All distributions display equivalent features.

Within the membrane, the pore diameter of CALHM4 is defined by the ring of non-interacting TM1 helices, which is placed inside an outer ring of the channel formed by helices TM2-4 (**Figure 15 B and G**). This arrangement creates clefts between neighboring helices of the inner ring which are delimited by helices TM2 and 4 at the respective subunit interfaces (**Figure 15-B**). In our sample, this cleft appears to be filled with lipids as indicated by the residual density observed in the cryo-EM maps (**Figure 17-B**). Due to the prevalence of aliphatic residues lining the pore at the assumed location of the membrane core, the pore is highly hydrophobic, whereas the regions extending into the aqueous environment contain polar and charged residues (**Figure 17-C**). Similarly, the side of the helical N-terminus, which faces the membrane at its intracellular boundary, is hydrophobic (**Figure 15-D**). In light of its large cross-section and high hydrophobicity, it is conceivable that the interior of the pore would accommodate lipids, which potentially could form bilayers that would restrict ion permeation. In our data, we find strong evidence for a layered distribution of density inside the pore within the presumed membrane region in non-symmetrized maps and after application of symmetry, which could either reflect the presence of lipids or detergent molecules arranging in a bilayer-like structure facilitated by the confined pore geometry (**Figure 17-D**). The observed density distribution displays features that quantitatively match the corresponding properties of lipid membranes as judged by a comparison to cryo-EM density of liposomes and computer simulations (**Figure 17-E**). We thus analyzed the composition of small molecules that are co-purified with CALHM4. For this purpose we have methanol-extracted hydrophobic compounds existing in the sample of purified CALHM4 proteins. The extractions were further analyzed for their content with liquid chromatography-mass spectrometry (LC-MS). **Figure 18** shows the results of the LC-MS experiment. In the first step of the analysis, we have selected highly abundant compounds that were enriched in the CALHM4 sample versus a blank sample of the buffer alone (**Figure 18-A**). Further, based on retention times and mass to charge ratios of the compounds, their identity has been determined and we were able to detect phospholipids that are commonly found in the membranes of HEK cells (**Figure 18-B and C**).

Collectively, our data is compatible with the presence of a membrane located within the pore region of CALHM4 channels, which could interfere with the diffusion of charged substances. Thus, despite of its large pore diameter, it is at this point unclear whether the CALHM4 structure defines a conductive conformation of CALHM channel or alternatively a conformation that harbors a membrane-like assembly residing inside the pore that would impede ion conduction.

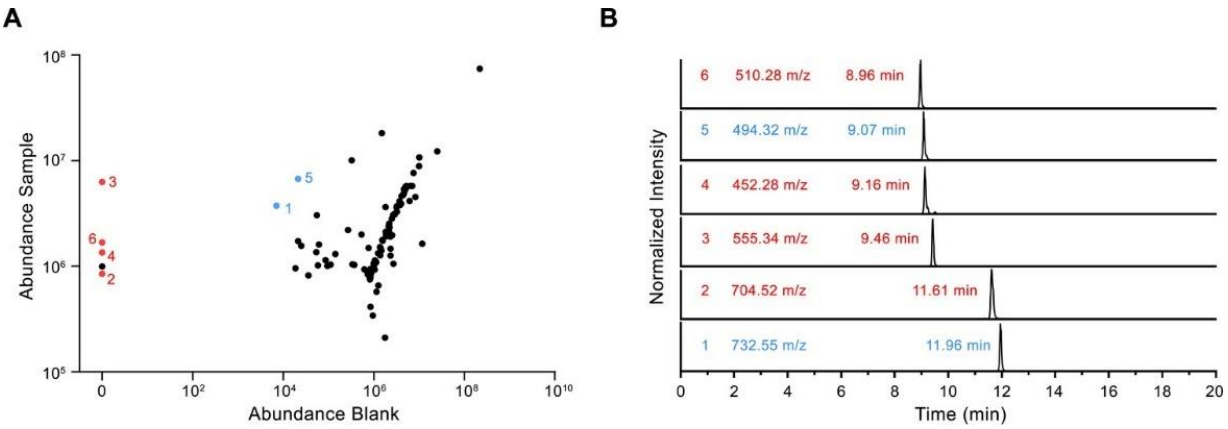

C

Nr.	Retention time (min)	*m/z*	Mass error (ppm)	Lipid category
1	11.96	732.55	-0.31	Glycerophospholipids
2	11.61	704.52	-0.12	Glycerophospholipids
3	9.46	555.34	0.27	Glycerophospholipids
4	9.16	452.28	0.24	Glycerophospholipids
5	9.07	494.32	0.33	Glycerophospholipids
6	8.96	510.28	-0.10	Glycerophospholipids

Figure 18. LC-MS analysis of co-purified lipids. (A) Scatter plot depicting the relative amounts of the 100 most abundant hydrophobic compounds detected in the LC-MS analysis of the CALHM4 sample compared to the blank. Red dots represent compounds that are detected in the CALHM4 sample only and blue dots represent compounds that are highly enriched in the CALHM4 sample compared to the blank (fold change >100). (B) TIC chromatograms of compounds indicated in A, with assigned mass to charge ratio (m/z) and retention time. (C) Table summarizing the properties of compounds isolated from the CALHM4 sample. The chemical identity was identified in a search against the LipidMaps (LM) library with matching tolerances of 1 ppm in mass accuracy and >90% in isotope similarity.

2.1.7 Structure determination of CALHM6 channels

For the structure determination of CALHM6 channels samples were prepared in the presence of Ca^{2+}. **Figure 19** shows details of the processing strategy. The detailed description can be found in the figure legend and in the Methods section. The strategy was similar to the one employed for the CALHM4 datasets and included particle picking, extraction and a subsequent cleaning of particles in several rounds of 2D and 3D classification, further 3D refinement while applying C10 or C11 symmetry and post-processing steps (**Figure 19-A, B and C**). This approach yielded maps at 4.54 Å and 6.23 Å for undecameric and decameric assemblies of CALHM6 respectively (**Figure 19-D**). Unlike CALHM4, the lower resolution of the CALHM6 densities, precludes a detailed interpretation of the structure for all parts of the protein. Still, the high homology between the two paralogs and density attributable to large side chains has constrained the placement of helices and conserved loop regions and thus allows the

credible analysis of major conformational differences. **Figure 20** shows representative cryo-EM densities. Details on model building can be found in the Methods section.

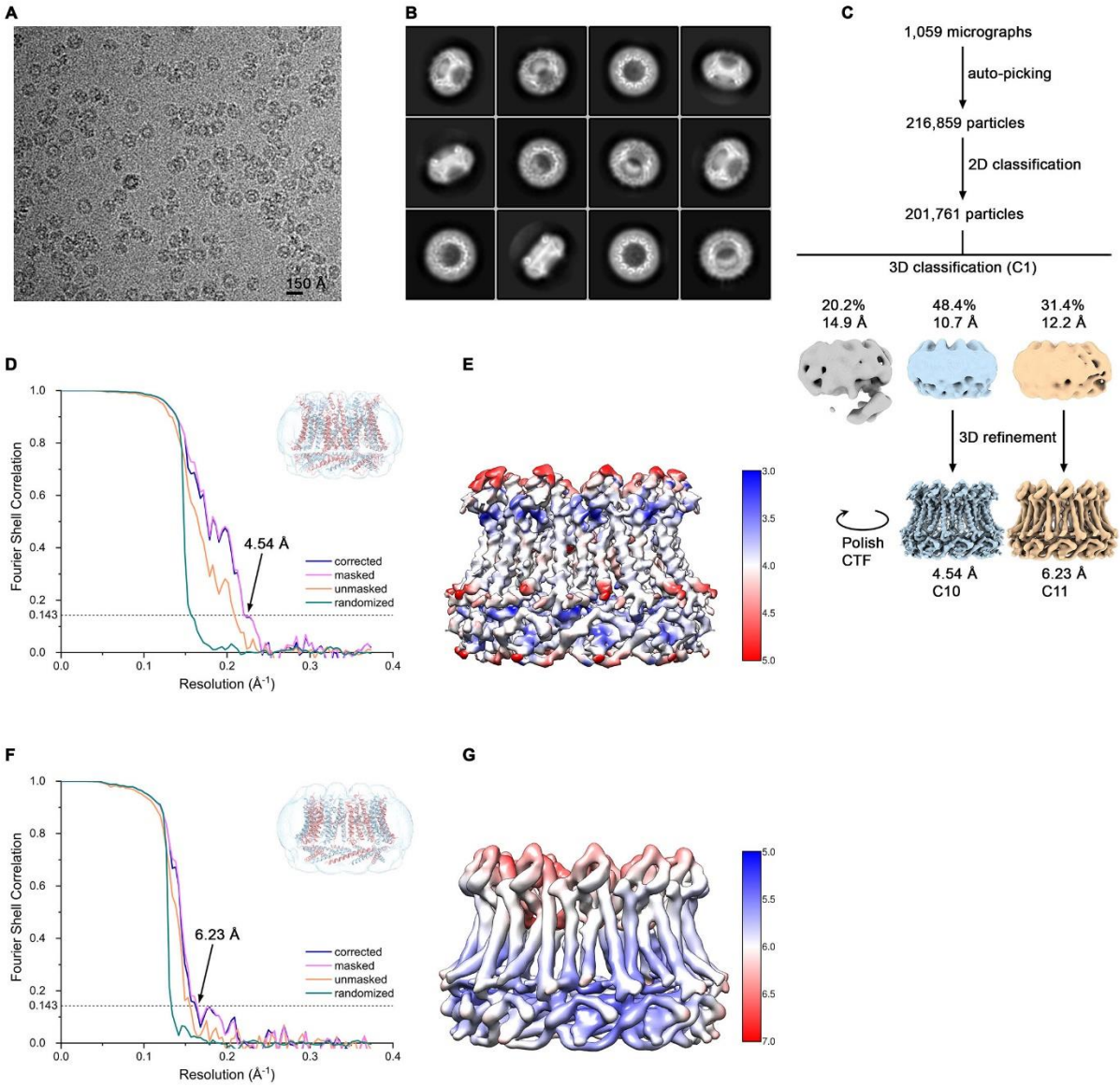

Figure 19. Cryo-EM reconstruction of CALHM6 in presence of Ca^{2+}. (**A**) Representative cryo-EM micrograph acquired with a Tecnai G^2 Polara microscope equipped with a K2 camera. (**B**) 2D class averages of CALHM6 in presence of Ca^{2+}. (**C**) Data processing workflow. Non-symmetrized 3D classification allowed to isolate two populations of particles representing decameric and undecameric assemblies. The particles were further refined with either C10 or C11 symmetry imposed and iterative per-particle CTF refinement and Bayesian polishing. The distribution of all particles (%) and the resolution of each class is indicated. (**D**) FSC plot of the final refined decameric unmasked (orange), masked (pink), phase-randomized (green) and corrected for mask convolution effects (blue) cryo-EM density map of CALHM6. The resolution at which the FSC curve drops below the 0.143 threshold is indicated. The inset shows the atomic model within the mask that was applied for calculations of the resolution estimates. (**E**) Final 3D reconstruction of decameric CALHM6 colored according to local resolution. (**F**) FSC plot of the final refined undecameric unmasked (orange), masked (pink), phase-randomized (green) and corrected for mask convolution effects (blue) cryo-EM density map of CALHM6. The resolution at which the FSC curve drops below the 0.143 threshold is indicated. The inset shows the atomic model within the mask that was applied for calculations of the resolution estimates. (**G**) Final 3D reconstruction of undecameric CALHM6 colored according to local resolution.

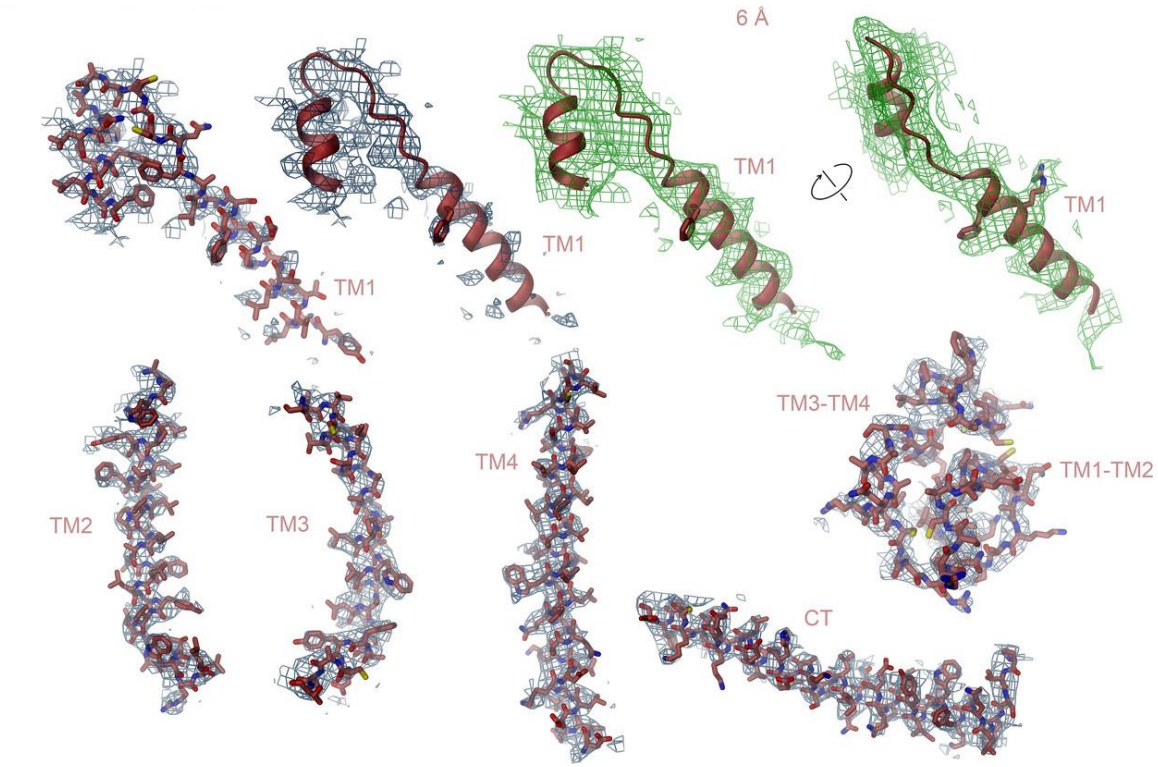

Figure 20. Cryo-EM density of CALHM6. Cryo-EM density at 4.5 Å of selected regions of the decameric CALHM6 structure superimposed on the model. Structural elements are indicated. '6 Å' marks cryo-EM density low-pass filtered to 6 Å superimposed on a ribbon of TM1 and parts of TM2, which displays extended density for the entire TM1 region that is partly not defined in the density at higher resolution due to its intrinsic mobility. Density is shown from two different views with indicated relationship. Large side chains that are recognizable in the low-pass filtered map are displayed as sticks.

2.1.8 Comparison of CALHM4 and CALHM6 structures

Similar to CALHM4, heterogeneous distribution of decameric and undecameric channels of CALHM6, is observed, although in case of CALHM6 decamers amount to 60% of the classified particles (**Figure 19**). **Figure 21** shows the final map and corresponding molecular model of the CALHM6 channels. Unlike in CALHM4, there is no dimerization of CALHM6 channels and the C-terminal region following the cytoplasmic helix CTH instead engages in intramolecular interactions with the outside of the cytoplasmic rim for most of its length (**Figure 21-B**). This observation further supports the notion that the dimerization of CALHM4 might be a consequence of interactions formed between solubilized proteins where the mobile C-terminus could equally well engage in intra- and intermolecular interactions, of which the latter would be multiplied in the highly symmetric arrangement. In CALHM6 we also find a slight expansion of the protein parallel to the membrane and an accompanying moderate contraction in perpendicular direction (**Figure 21-B**). While the general organization of CALHM6 channels closely resembles CALHM4, significant differences are observed in the pore geometries of the two channels. Both assemblies of CALHM6 contain subunits with equivalent conformations, which are better defined in the smaller oligomers. **Figure 22** shows the comparison of CALHM4 and CALHM6 structures.

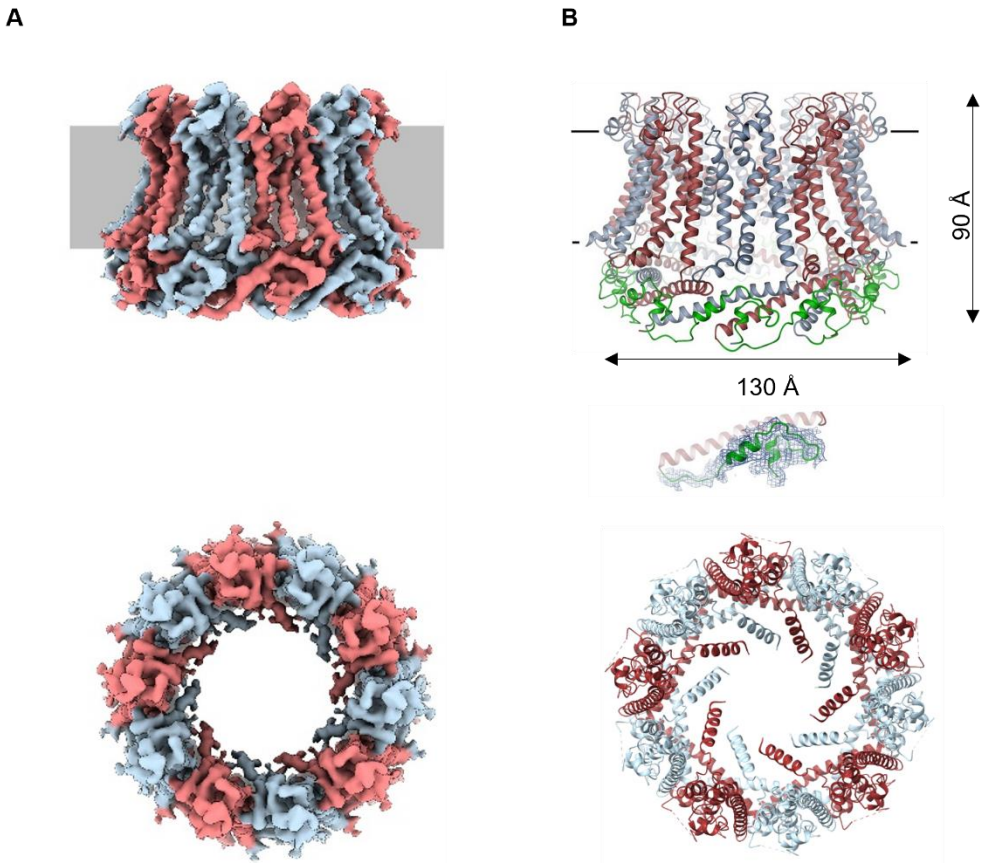

Figure 21. CALHM6 structure. (**A**) Cryo-EM density of decameric (10-mer) CALHM6 channels at 4.54 Å. Subunits are colored in blue and red, respectively viewed from within the membrane (top) and from the extracellular side (bottom). (**B**) Ribbon representation of the decameric CALHM6 structure viewed from within the membrane (top). Subunits are colored in red and light blue. Part of the mobile C-terminus defined in low-pass filtered cryo-EM density that was modeled as Ala and Gly chain is colored in green. Inset (below) shows a close-up of this region with cryo-EM density superimposed. A view of the CALHM structure from the extracellular side is shown on the bottom.

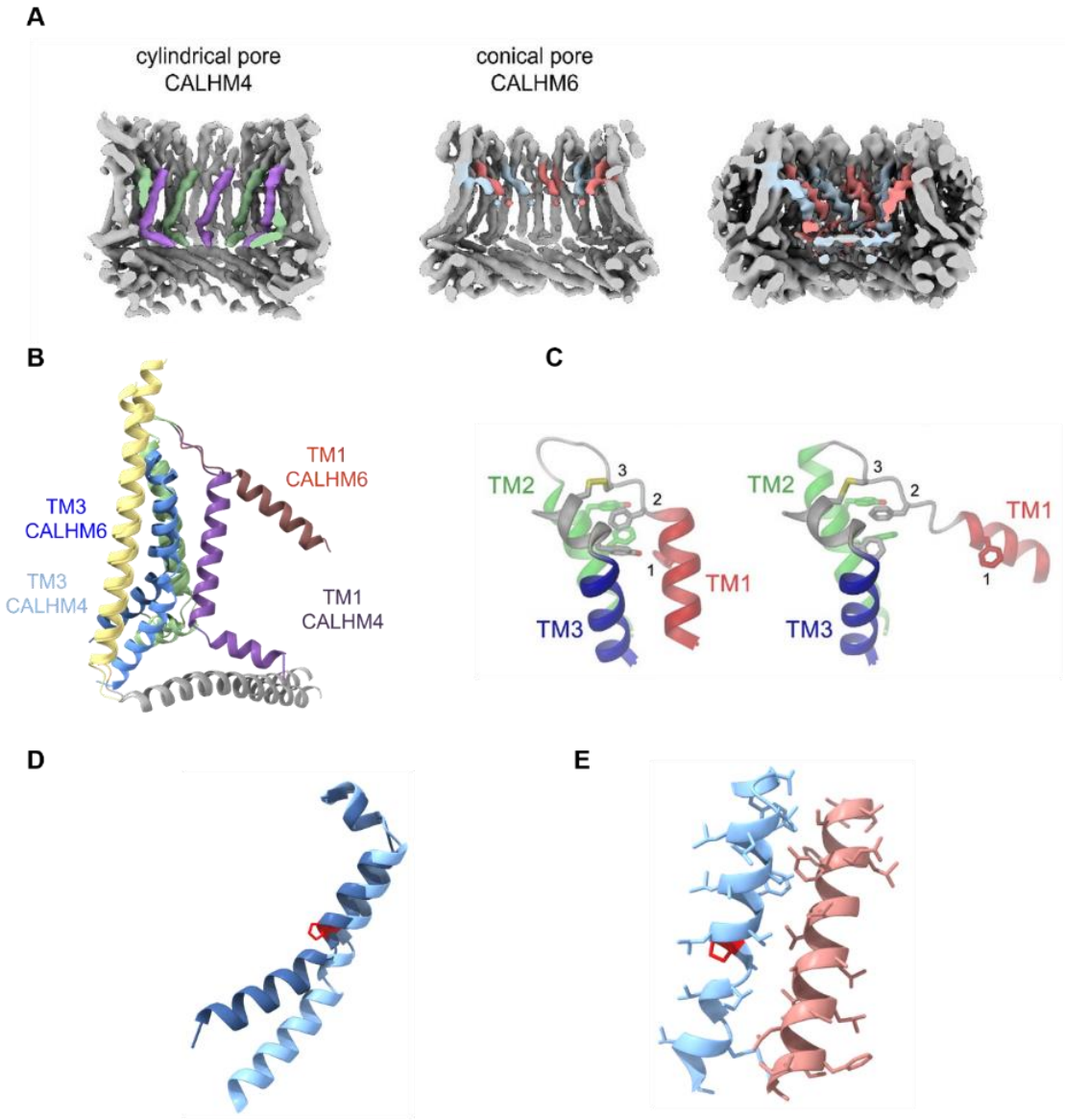

Figure 22. Comparison of CALHM4 and 6 structures. (A) Slices through the CALHM4 (left) and the CALHM6 (right) channels illustrating the distinct features of the cylindrical and conical pore conformations. View of CALHM6 at lower contour (right) shows extended density for the mobile TM1. Maps are low-pass filtered at 6 Å. Density corresponding to TM1 is colored. (**B**) Superposition of single subunits of the CALHM4 and CALHM6 structures illustrating conformational changes. Secondary structure elements exhibiting conformational differences are labeled. (**C**) secondary structure elements on the extracellular side describing differences leading to the cylindrical conformation displayed in CALHM4 and the conical conformation displayed in CALHM6. Residues contributing to a cluster of aromatic residues on TM1-3 and a conserved disulfide bridge are shown as sticks. (**D**) Close-up of the conformational change in TM3 from the cylindrical conformation displayed in CALHM4 to the conical conformation displayed in CALHM6. The conserved proline at the site of conformational changes is colored red and shown as sticks. (**E**) Interaction region of TM1 and TM3 in the CALHM4 structure with the protein shown as Cα trace and side chains of interacting residues as sticks.

The differences in protein conformations of the two homologues, which result in their distinct pore geometries are illustrated. Whereas in CALHM4 we observe wide cylindrical pore, in CALHM6 the pore has a constricted and conical shape (**Figure 22-A**). In a superposition of the subunits, similar conformations are observed for α-helices TM2 and 4 and the C-terminal helix CTH and larger differences in the interacting helices TM1 and 3 (**Figure 22-B and C**). These differences are most pronounced for TM1, which in CALHM6 has detached from TM3 and moved by 60° towards the pore axis around a hinge located upstream of a conserved phenylalanine at the end of TM1 (**Figure 22-B**). In both structures, the conformation of the proximal loop connecting TM1 and 2 is stabilized by two conserved cysteines, which are involved in disulfide bridges with the region connecting TM3 and TM4 (**Figure 22-C**). As a consequence of the disruption of its interaction with TM1, the intracellular halve of TM3 tilts away from the pore axis by 30° around a pivot located close to a conserved proline residue (P115 in CALHM4), which probably destabilizes the helix (**Figure 22-D**). The transition from a conformation observed in CALHM4 to a conformation defined by CALHM6 is accompanied by the dissociation of interactions between TM1 and 3, which are mediated by conserved residues involving a cluster of hydrophobic interactions at the extracellular side and additional interactions on the entire length of both α-helices (**Figure 22-C and E**). The movement of TM1 in the oligomeric channel in its transition between conformations probably requires concerted rearrangements to avoid steric clashes in the crowded environment of the pore. When viewed from the outside this transition thus resembles the closing of an aperture and it converts a cylindrical pore to a funnel which narrows towards the intracellular side while creating a large cavity between TM1 and TM3 that becomes accessible from the cytoplasm (**Figure 14-B and 21-B**). In the CALHM6 cryo-EM density, TM1 is less well defined compared to the rest of the protein reflecting its increased flexibility in the observed structure (**Figure 19 and 21-A**). Since the conformation of NH, which has moved towards the pore axis, is not defined in the density, the size of the CALHM6 channel at its constriction remains ambiguous. It could range from an occluded pore if NH helices make contacts in the center of the channel (modeled as clogged conformation) to a pore with similar diameter as found at the CALHM4 constriction (**Figure 23-A and B**). The latter could be obtained in case the mutual relationship between TM1 and NH remains unchanged compared to the CALHM4 structure (defined as kinked conformation) or if NH straightens in continuation of TM1 (in an extended conformation) (**Figure 23-A and B**).

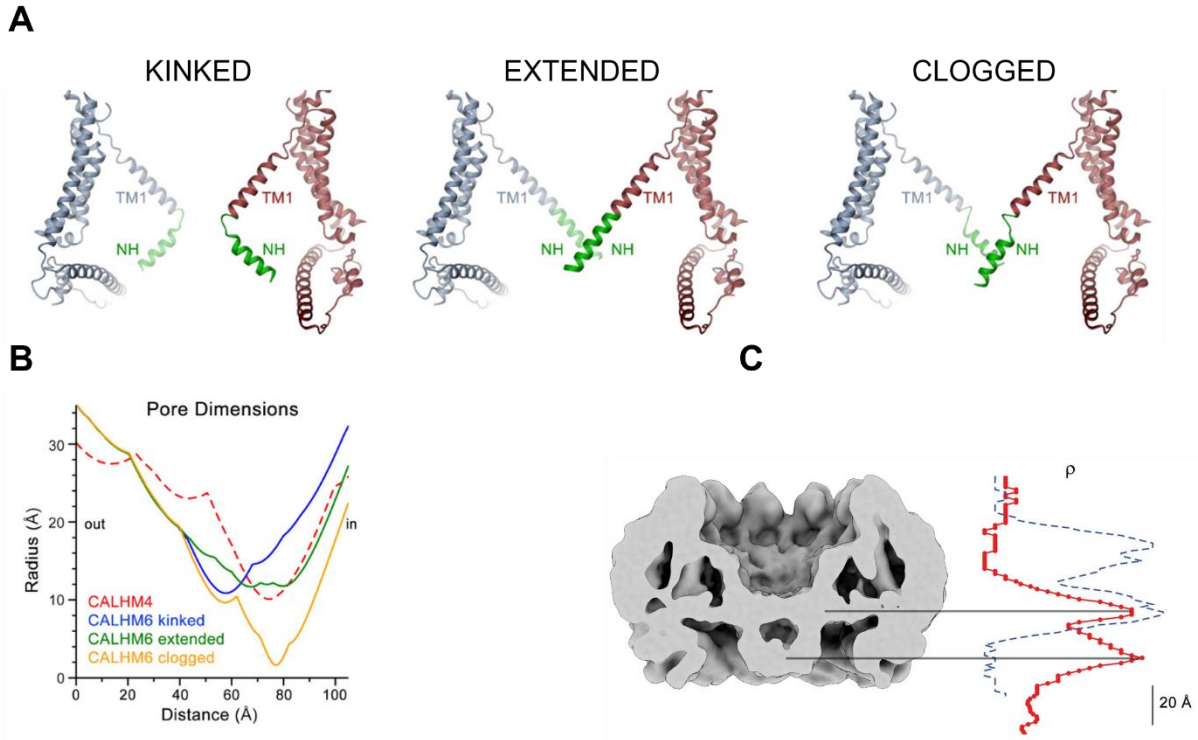

Figure 23. **Features of the CALHM6 structure.** (**A**) Hypothetical pore conformations of the conical conformation displayed in the CALHM6 structure. The disordered N-terminal helix NH (green) was modeled in different conformations. Left, 'kinked' conformation where the mutual relationship between TM1 and NH is as in CALHM4, center left, 'extended' conformation where NH has changed its conformation to extend the TM1 helix. Center right, 'clogged' conformation where the mobile NH helix has moved towards the pore axis. The 10-fold symmetry is maintained in the 'kinked' and 'extended' conformations and broken in the 'clogged' conformation. Opposite subunits of the decameric structures are displayed. (**B**) Pore radii of the different modeled pore conformations of CALHM6 calculated with HOLE compared to the CALHM4 decamer (red dashed) display a similar constricting pore radius as for CALHM4 for 'kinked' and 'extended' conformations and an occluded pore in case of the 'clogged' conformation. (**C**) Slice through the pore region of the CALHM6 decamer viewed from within the membrane. Shown is non-averaged density at low contour to highlight the location of diffuse density within the pore. A plot of the density along the pore axis of CALHM6 is shown in red, the corresponding density in CALHM4 is shown as a dashed blue line for comparison. The two maxima in the CALHM6 density are shifted towards the intracellular side. The density corresponding to the headgroups of the outer leaflet of the bilayer in CALHM4 is absent. Density at the location of the headgroup region at the inner leaflet of the bilayer and further towards the intracellular side could correspond to either lipids or to the poorly ordered N-terminus.

In any case, the large conformational changes would affect the location of lipids within the pore, which in case of an internal bilayer would have to rearrange in response to the severely altered pore geometry. Such rearrangement is reflected in the changed distribution of the residual electron density inside the pore (**Figure 23-C**). Whereas, compared to CALHM4, we find density at the location of the intracellular layer of lipids and further towards the cytoplasm, part of which might be attributable to the mobile N-terminal α-helix NH, the outer layer of density corresponding to the putative extracellular leaflet of a bilayer has disappeared. Thus, despite the pronounced conformational differences to CALHM4 and the fact that the CALHM6 structure appears to contain features of a closed pore, a definitive functional assignment remains also in this case ambiguous.

2.1.9 Summary and conclusions on structural studies of homomeric CALHM channels

The experiments described in this section aimed at obtaining structural information on the CALHM protein family. Screening experiments have shown that human CALHM2, 4, 5 and 6 proteins can be overexpressed and purified as homomeric complexes. Due to their biochemical stability CALHM2, 4 and 6 have been selected for a further biochemical and structural characterization. The structure determination of CALHM2 has failed due to its strong preferred orientation on the grid. Structural analysis of the other two homologues yielded maps at resolutions of 3.7 Å and 4.4 Å for CALHM4 and 6 respectively, which allowed a reliable interpretation of the molecular structures of both proteins. The structures have defined the organization of CALHM proteins as large oligomers, which in case of CALHM4 dimerize via contacts of their intracellular regions. The structures of the two homologues also revealed unique features of CALHM proteins including two distinct conformations of pore-lining N-terminal regions and the first transmembrane helices. Additionally, we observe an extra bilayer-like density in the pore of CALHM4 channels, which may indicate that lipids play a role in their activity regulation. However, due to the lack of functional data the correspondence of these observations with the functional states of both channels remains elusive.

2.2 Functional investigations of homomeric CALHM proteins

Previous studies demonstrated that CALHM1 acts as a voltage gated ion channel that is allosterically modulated by extracellular Ca^{2+} [2]. In contrast, CALHM2 and CALHM3 have been reported to lack such activity[44]. Interestingly, CALHM3, but not CALHM2, has been shown to modulate the activity of CALHM1[44]. At the time of performing the described experiments there were no reports on the activity of CALHM4, CALHM5 and CALHM6. To recapitulate those results and to investigate if the structurally characterized homologues described in this thesis exhibit similar activity as CALHM1, two-electrode voltage-clamp recordings were performed in *Xenopus laevis* oocytes over-expressing CALHM2, 4 and 6. This system has been selected since it proved to be suitable for CALHM1 recordings[2,44,45]. Advantages of the oocyte system include the ease of handling and amplification of the recorded currents as a consequence of the large membrane surface area, which permits the detection of small responses as a result of either low conductance or open probability.

In addition, the study of CALHMs function in vitro, after their reconstitution into proteoliposomes was attempted. Investigating the proteins outside of their cellular environment can be advantageous, as it allows for the exclusion of potential unknown cellular factors that may render the proteins inactive within cells and since it excludes background activities of other proteins present on the cell surface. However, this approach has a disadvantage if unknown cellular factors prove to be necessary for the activation of the reconstituted CALHM channels. As the functional properties of the investigated CALHM homologues were unknown, we employed both approaches to cover these two possibilities.

2.2.1 Two-electrode voltage clamp

Note: Recordings presented in this chapter were performed by Dr. Maria Isabel Bahamonde Santos with the assistance of the author of the thesis

In the two-electrode voltage-clamp method, the membrane potential of oocytes is clamped and the injected currents to compensate for the conduction of open ion channels residing in the plasma membrane of a cell is measured. The extracellular environment can be easily altered by perfusion of the oocytes with various buffers.

Recordings were performed with oocytes that were injected with mRNA encoding human CALHM2, 4 and 6 after 40-60 hours of protein expression. Additionally, oocytes expressing human CALHM1 were prepared as positive control for the comparison of recordings. To assess if expressed homologues localize to the plasma membrane we used surface-biotinylation assay, which confirmed their expression in the surface of the oocytes at the time of the measurements (40-60 hours after injection of mRNA) (**Figure 24**).

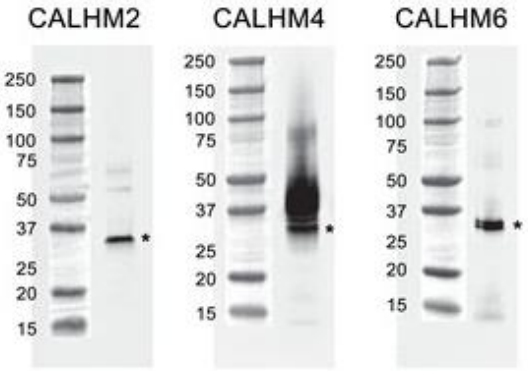

Figure 24. Surface-biotinylation assay of oocytes expressing CALHM2, CALHM4 and CALHM6. Western blot of proteins located in the plasma membrane of *X. laevis* oocytes heterologously expressing the indicated CALHM channels. Protein was isolated after surface-biotinylation by binding to avidin-resin. The proteins are detected with specific antibodies recognizing the respective CALHM paralog. Left, CALHM2, center CALHM4, right CALHM6. The blot demonstrates the targeting of all three paralogs to the plasma membrane. Bands corresponding to the respective CALHM paralogs are indicated by asterisk.

Figure 25 shows the summary and **Figure 26** shows the representative traces of voltage-clamp recordings of CALHM homologues. The recordings were conducted at positive and negative voltage and in the presence and absence of extracellular calcium. Consistent with previous findings, CALHM1 activation was observed upon membrane depolarization and extracellular calcium depletion (**Figure 25 and 26-A and B**). At the positive voltages the current amplitude varied with the concentration of this divalent cation. For extracellular calcium concentrations close to the physiological range (3 mM), small and slow currents were recorded (**Figure 25 and 26-A**). These currents exhibited increased amplitude as the calcium concentration decreased, reaching a maximum at a nominal 0 µM calcium (**Figure 25 amd 26-A**). At the negative voltages, no currents were observed in the presence of calcium, but large currents were observed in its absence (**Figure 25 and 26-A and B**). Notably, when the same conditions were applied to oocytes expressing other CALHM paralogues, no activation was observed (**Figure 25 and 26-D-F**). These currents neither showed pronounced voltage-dependence nor were they altered by

Ca^{2+}-removal in a statistically significant manner and the recorded traces of CALHM2, 4, and 6 displayed no difference compared to a negative control lacking CALHM expression (**Figure 25**). These results thus clearly show that CALHM2, 4 and 6 differ functionally from CALHM1 and their activation mechanism remains unknown.

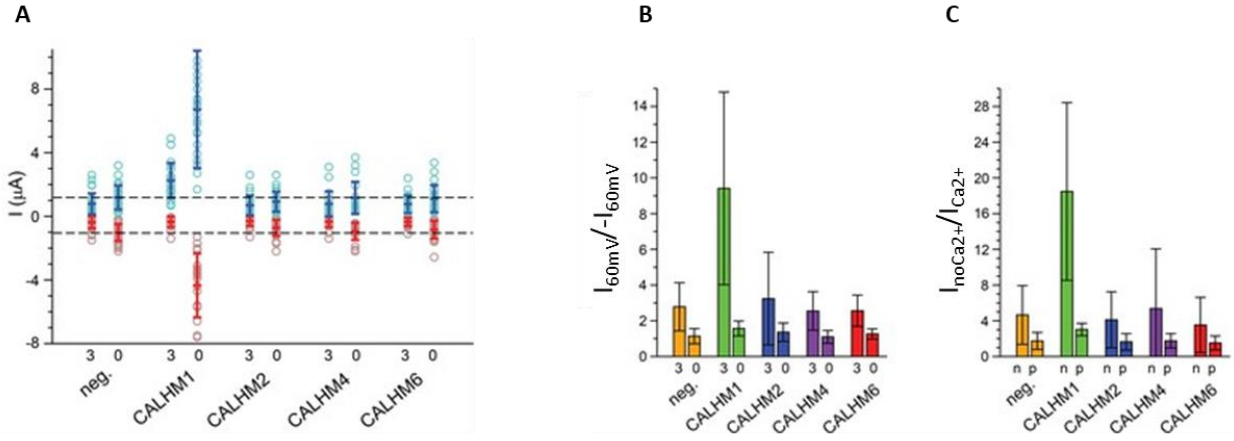

Figure 25. Functional characterization of CALHM channels expressed in *X. laevis* oocytes.
(**A**) Electrophysiological characterization of *X. laevis* oocytes heterologously expressing the paralogs CALHM1, CALHM2, CALHM4 and CALHM6 in comparison to control oocytes (neg.) recorded at extracellular solutions either containing 3 mM Ca^{2+} (3) or 0.5 mM EDTA and 0.5 mM EGTA (Ca^{2+}-free, 0). Data show currents of individual oocytes (circle) recorded by two-electrode voltage-clamp (TEVC) at 60 (light blue) and −60 mV (light red). In each case, currents were tabulated at the end of a 5 s voltage step. Averages are shown as bars in red (−60 mV) and blue (60 mV), respectively. Dashed lines indicate mean current levels of control oocytes (neg.) recorded in Ca^{2+}-free extracellular solutions at 60 and −60 mV. Currents measured for all investigated channels, except CALHM1, are not significantly different from control oocytes (as judged by a Student t-test). (**B**), Rectification of steady-state currents of oocytes displayed in (**A**) expressed as I_{60mV}/I_{-60mV} calculated for individual oocytes at 3 mM Ca^{2+} (3) and in Ca^{2+}-free solutions (0) and averaged. The large value of CALHM1 reflects the activation of the protein at positive voltage in presence of Ca^{2+}. (**C**) Ca^{2+}-dependence of activation. Change of steady-state currents of oocytes displayed in (**A**) after Ca^{2+}-removal expressed as I_{noCa2+}/I_{Ca2+} calculated from individual oocytes at −60 mV (n) and 60 mV (p) and averaged. The large value of CALHM1 at −60 mV reflects the strong activation of currents at negative voltages upon Ca^{2+}-depletion. C, D, The difference between the corresponding values of the CALHM paralogs 2, 4, and 6 and neg. are statistically insignificant (as judged by a Student t-test). B-D, Data show averages of 27 (neg.), 21 (CALHM1), 26 (CALHM2), 19 (CALHM4) and 21 (CALHM6) oocytes respectively. Errors are standard deviations. Figure from [57].

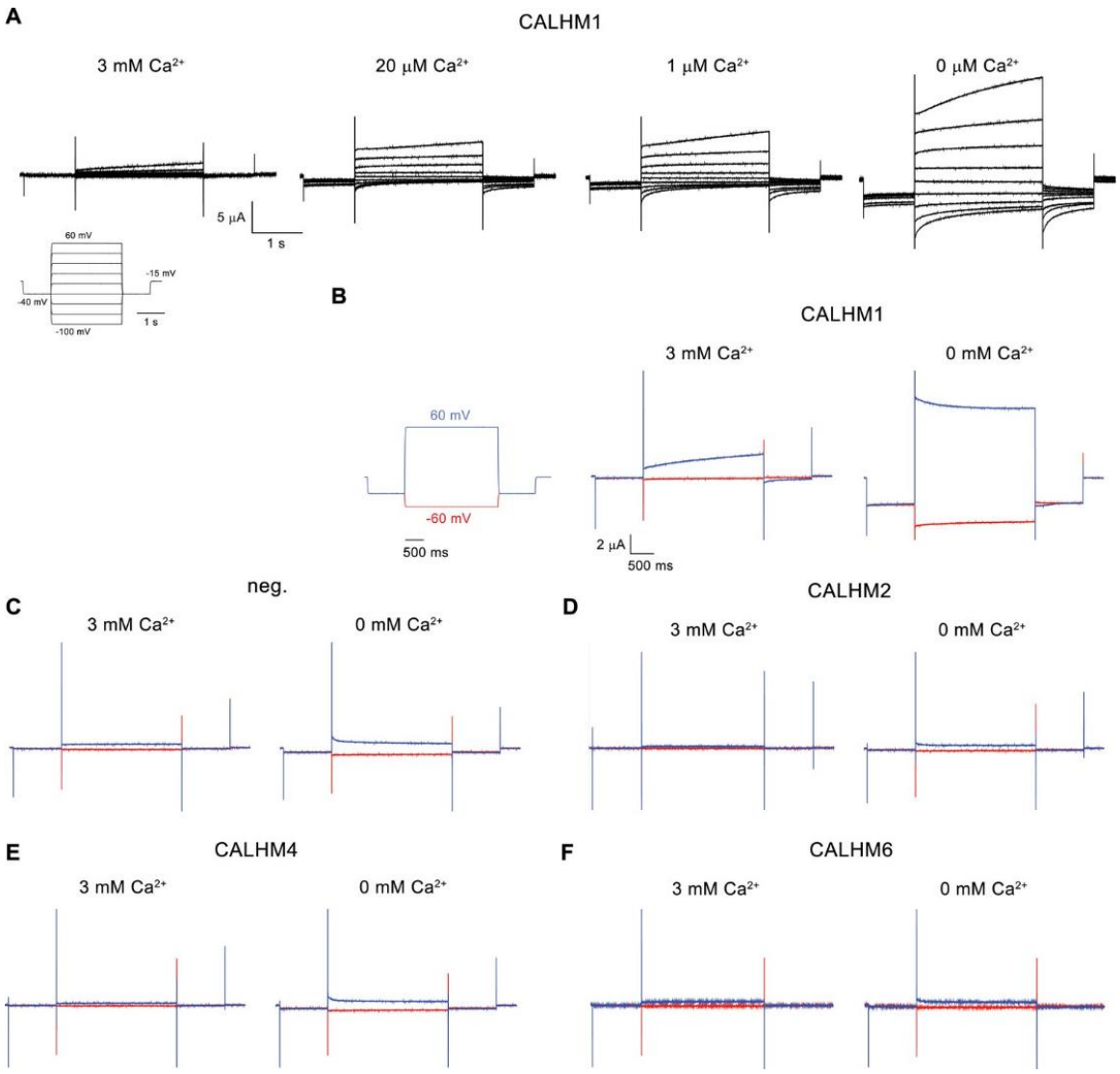

Figure 26. **Two-electrode voltage clamp recordings of CALHM homologues.** (**A**) Representative current traces of CALHM1 recorded at indicated extracellular Ca^{2+} concentrations. The voltage protocol is shown as inset (left). (**B–F**) Representative currents of CALHM paralogs (**B**), CALHM1, (**D**), CALHM2, (**E**), CALHM4 and (**F**), CALHM6 in comparison to (**C**), control oocytes (neg.). The current protocol is shown on the left. Traces including a step to -60 mV are colored in red, traces including a step to 60 mV in blue. A-F, Data were recorded 40–60 hours after injection of mRNA. Figure from [57].

2.2.2 Proteoliposome transport assay

In an attempt to study the function of CALHM homologues in vitro a previously described fluorescence quenching based assay has been chosen[58]. In this assay, the quenching of the fluorophore calcein upon the transport of the divalent cation manganese across the membrane is monitored. The assay is conducted under conditions that establish an inside negative membrane potential. This means that CALHM channels reconstituted in an inside-out orientation would sense depolarizing conditions. Given the large diameter of the CALHM channel pores, I have assumed that active channels should facilitate manganese transport.

2.2.2.1 Reconstitution of the CALHM proteins into the liposomes

To conduct the assay, it was required to reconstitute CALHM proteins into the liposomes. For the three investigated CALHM homologues, various reconstitution conditions have been tested, including the destabilization of preformed liposomes and liposome reconstitution from solubilized lipids. Additionally, different lipid compositions were investigated. The screening of reconstitution conditions is described in more details in the Method section. To monitor the reconstitution of CALHM proteins, their re-extraction from the proteoliposomes followed by an FSEC analysis was conducted. All tested conditions yielded similar results. **Figure 27.** shows representative results of the reconstitution of CALHM2, 4 and 6 into destabilized lipids derived from soy polar extracts. A stably reconstituted protein is expected to elute as peak at a similar volume as the purified protein. Following re-extraction, monodispersed peaks were observed for CALHM2 and CALHM6, indicating their successful reconstitution into the liposomes (**Figure 27**). In contrast, no CALHM4 peak was observed after re-extraction, suggesting that the protein could not be stably reconstituted into the liposomes under the tested conditions (**Figure 27**). This discrepancy is likely due to the dimerization of CALHM4 channels, which presumably hinders their successful reconstitution.

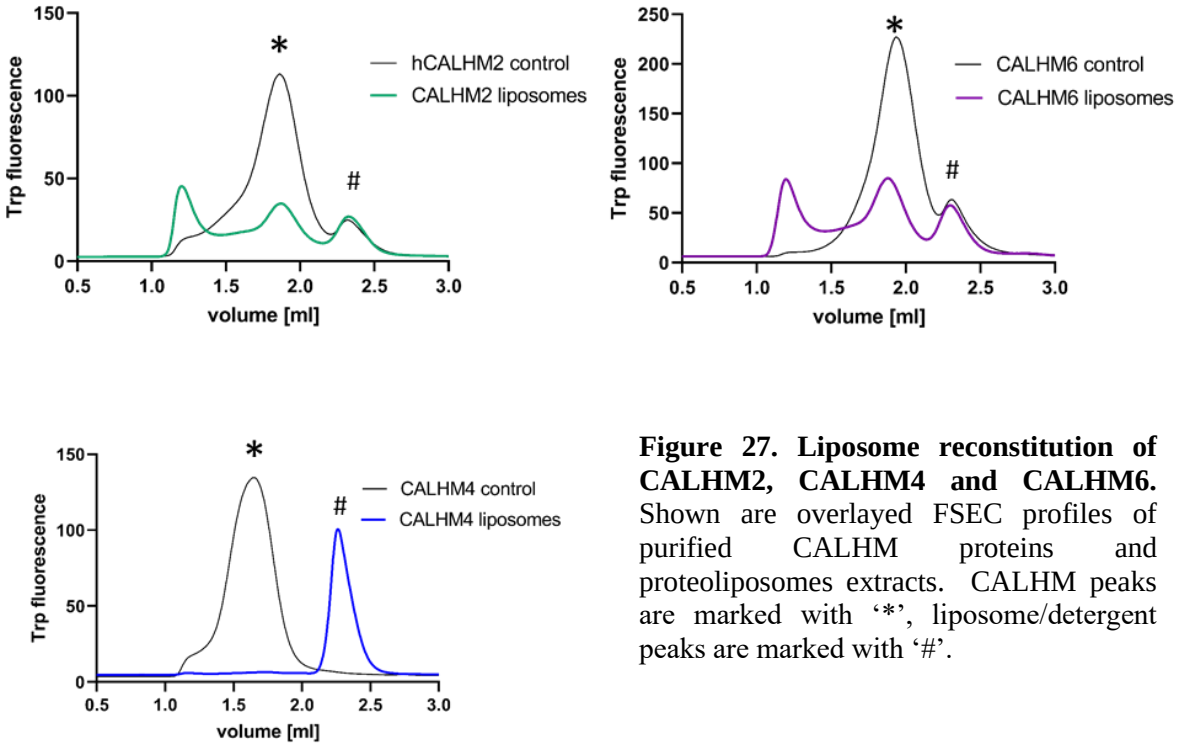

Figure 27. Liposome reconstitution of CALHM2, CALHM4 and CALHM6. Shown are overlayed FSEC profiles of purified CALHM proteins and proteoliposomes extracts. CALHM peaks are marked with '*', liposome/detergent peaks are marked with '#'.

2.2.2.2 Fluorescence quenching-based transport assay

The assay was conducted for CALHM2 and CALHM6, as they were successfully incorporated into the liposomes. CALHM4 was excluded from the assay as it was not observed to reconstitute successfully. Initially, proteoliposomes were mixed with an inside buffer containing a fluorophore and KCl. The mixture was then extruded to facilitate the formation of unilamellar vesicles that contained the trapped fluorophore inside. Following extrusion, the liposomes were washed with a fluorophore-free buffer and diluted into an outside buffer containing NaCl instead of KCl. Valinomycin was added to promote K^+ efflux, creating an inside negative membrane potential that facilitates the transport of cations into the interior of proteoliposomes (assuming that CALHM channels, which would conduct K^+ in an open conformation are initially closed). The substrate manganese was added at different concentrations. The reaction was terminated by the addition of calcimycin, which rendered the liposomes permeable to divalent cations. **Figure 28.** shows the results of the transport assay. In the performed assay, no quenching of the fluorophore was observed in the CALHM2 and CALHM6-containing liposomes, and the resulting traces resembled the negative control consisting of liposomes not containing any protein (**Figure 28**). This results demonstrate the absence of transport through CALHM2 and CALHM6 channels under the tested conditions. It should be noted that the substrate used in this assay is a divalent cation and such (Ca^{2+} and Mg^{2+}) have been shown to have inhibitory effects on CALHM1[2]. Therefore although unlikely, assuming random or inside-out orientation of the channels in the liposomes, it cannot be excluded that manganese inhibited activation of these paralogues in this experiment.

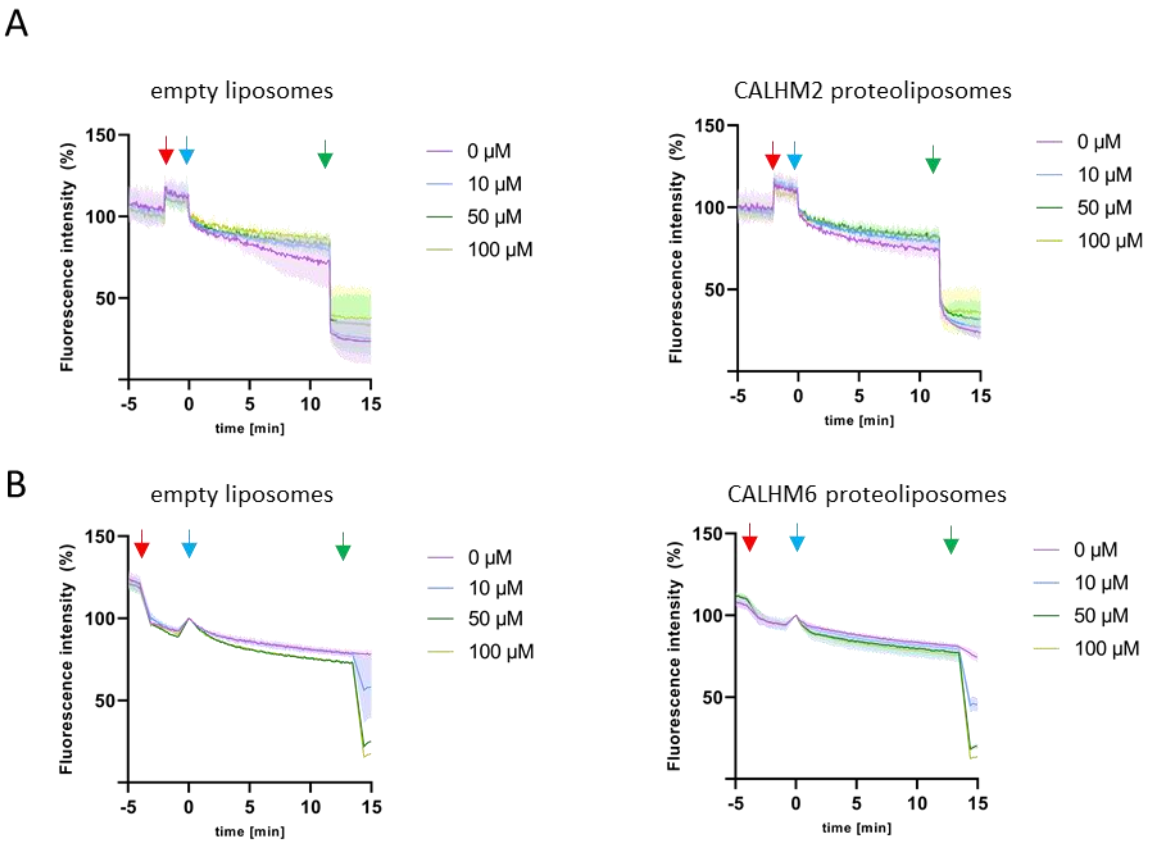

Figure 28. CALHM2 and CALHM6 proteoliposome-based transport assay. Traces of fluorescence quenching-based transport assay of (**A**) CALHM2 and (**B**) CALHM6. Calcein fluorescence is plotted against time. The red arrow indicates the time of the addition of valinomycin, blue of manganese and green of calcimycin. Manganese concentrations are indicated.

2.2.3 Summary and conclusion of functional assays

The functional studies described in this chapter did not show any sign of conduction mediated by the investigated CALHM2, 4 and 6 paralogs in response to stimuli that would activate CALHM1. The conclusions that can be drawn from these results do not claim that these homologues would not constitute ion channels per se, and instead suggest that these proteins would be activated by a mechanism that is distinct from CALHM1. Given the current sparse knowledge on the biology of those proteins, the investigation of their molecular function would require extended screening approaches of various stimuli. As these channels might form heteromers to form functional complexes, the screening should include the pairing of different homologues and described approaches can be used for this purpose.

2.3 Heteromerization of CALHM2 and CALHM4

Many oligomeric membrane proteins are heteromers of homologous subunits with their composition conferring distinct functional properties[12,14]. In the family of CALHM proteins CALHM1 and 3 are known to heteromerize to form ion channels of physiological relevance in taste transduction[44,46]. Whether other members of the family assemble into heteromeric channels to fulfill their functional tasks is still a major unanswered question. Thus, to better understand the role of the investigated CALHM paralogs, we attempted to gain insight into their tissue distribution and, if expressed in the same cell type, to study interactions between co-expressing CALHM members.

2.3.1 Co-expression of CALHM proteins in the human placenta

Note: The qRT-PCR experiments described in this chapter have been performed by Dr. Jonas Zaugg from the group of prof. Christiane Albrecht at the University of Bern.

To date, the data on expression patterns of CALHM proteins is sparse and restricted to generic databases reporting protein expression profiles. Currently, no analysis of CALHM protein levels in specific cell types has been reported and limited data exists on transcripts levels. In our study, we used this limited data to select a tissue to further investigate the expression of CALHM family members under investigation. To this end, we have selected the placenta as a model organ since it was reported that CALHM4 would be highly expressed at a transcript level in this tissue whereas the expression in other organs has not been reported for this homologue[59]. Initially, we experimentally validated the expression CALHM paralogs by quantification of their transcripts by reverse transcription (RT) PCR in healthy human placental tissues obtained from term pregnancies. **Figure 29** shows the results of the RT-PCR of CALHM transcripts in this tissue. The quantification revealed high levels of CALHM2, 4, and 6 and comparably low expression of other paralogs (**Figure 29-A**). Subsequently, we have investigated expression patterns of paralogs in primary trophoblast cells isolated from healthy term placentae and examined changes during the differentiation process of trophoblast precursor cells into mature syncytiotrophoblasts (**Figure 29-B)**. In these experiments, we found enrichment of CALHM2, 4 and 6 during differentiation, which was most pronounced for CALHM4 and which indicates a differentiation-dependent role of these proteins in the human placenta (**Figure 29**). In all cases, the concentrations of the respective CALHM mRNAs are high in comparison to other transport proteins, suggesting their involvement in important placenta-related membrane transport processes (**Figure 29**). Although transcripts levels are supposed to correlate with protein concentrations, they are often not sufficient to predict these levels since certain factors might influence the translation of mRNA into the protein including variable translations rates, delays in protein translation or variabilities in protein half-life[60,61].

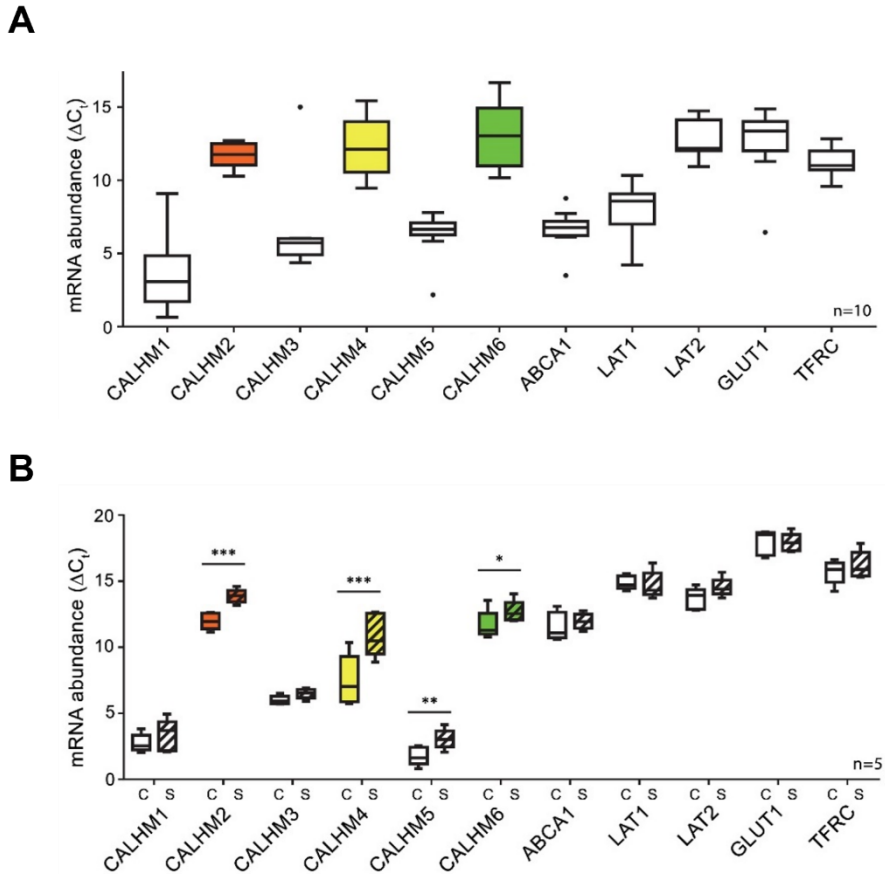

Figure 29. Comparative expression analysis of CALHM genes in the human placenta. mRNA concentrations of different CALMH paralogs and of other transport and receptor proteins in (**A**), human placental tissues (n=10) and (**B**), human trophoblasts isolated from healthy term placentae (n=5) was assessed by quantitative RT PCR and normalized to the reference gene YWHAZ. Abbreviations: ABCA1, ATP-binding cassette transporter A1; CALHM, calcium homeostasis modulator; LAT1 (SLC7A5), L-type amino acid transporter 1; LAT2 (SLC7A8), L-type amino acid transporter 2; GLUT1 (SLC2A1), Glucose transporter 1; TFRC, transferrin receptor complex 1; YWHAZ, Tyrosine 3-monooxygenase/tryptophan 5-monooxygenase activation protein, zeta polypeptide. Figure from [57].

Therefore, in order to investigate the expression of CALHM isoforms at the protein level, immunoprecipitation (IP) experiments from membrane fraction of human placental tissues were performed. The experiments were restricted to CALHM2 and CALHM4 proteins, as lack of suitable anti-CALHM6 antibodies precluded inclusion of this isoform in the study. **Figure 30-A** depicts the simplified scheme of the conducted immunoprecipitation experiment.

A

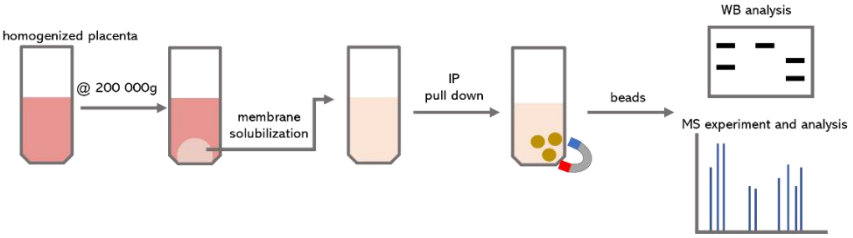

B

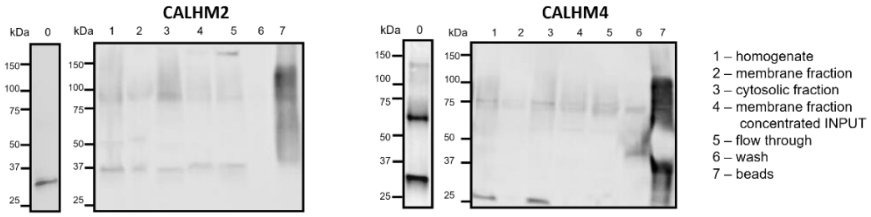

C

#	Accession	Description	Σ Exclusive peptides	Σ Unique peptides	Σ Spectra	% in total Σ spectra
1	P01857	Immunoglobulin heavy constant gamma	7	12	321	1.05
2	P01860	Immunoglobulin heavy constant gamma 3	2	5	186	0.61
3	P01871	Immunoglobulin heavy constant mu	22	33	190	0.62
220	O14880	Microsomal glutathione S-transferase 3	3	4	4	0.01
221	Q5VTL8	Pre-mRNA-splicing factor 38B	4	4	4	0.01
222	Q9HA72	Calcium homeostasis modulator protein 2	4	5	5	0.02
223	P53621	Coatomer subunit alpha	4	4	4	0.01
224	P20742	Pregnancy zone protein	2	2	4	0.01
445	Q9NZM1	Myoferlin	2	2	3	0.01

#	Accession	Description	Σ Exclusive peptides	Σ Unique peptides	Σ Spectra	% in total Σ spectra
1	P55072	Transitional endoplasmic reticulum ATPase	92	184	269	1.70
2	P01871	Immunoglobulin heavy constant mu	39	74	129	0.81
3	Q07157	Tight junction protein	77	112	115	0.72
301	Q8TED0	U3 small nucleolar RNA-associated protein 15 homolog	2	2	2	0.01
302	Q00610	Clathrin heavy chain 1	2	2	2	0.01
303	Q5JW98	Calcium homeostasis modulator protein 4	2	2	2	0.01
304	Q86V81	THO complex subunit 4	2	2	2	0.01
305	Q06830	Peroxiredoxin-1	2	2	2	0.01
355	P67870	Casein kinase II subunit beta	2	2	2	0.01

D

CALHM2
14% coverage
MAALIAENFRFLSLFFKSKDVMIFNGLVALGTVGSQELFSVVAFHCPCSPARNYLYGLAAIGVPALVL
FIIGIILNNHTWNLVAECQHRRTKNCSAAPTFLLLSSILGRAAVAPVTWSVISLLRGEAYVCALSEFV
DPSSLTAREEHFPSAHATEILARFPCKENPDNLSDFREEVSRRLRYESQLFGWLLIGVVAILVFLTKC
LKHYCSPLSYRQEAYWAQYRANEDQLFQRTAEVHSRVLAANNVRRFFGFVALNKDDEELIANFPVEGT
QPRPQWNAITGVYLYRENQGLPLYSRLHKWAQGLAGNGAAPDNVEMALLPS

CALHM4
8% coverage
MCPTLNNIVSSLQRNGIFINSLIAALTIGGQQLFSSSTFSCPCQVGKNFYYGSAFLVIPALILLVAGF
ALRSQMWTITGEYCCSCAPPYRRISPLECKLACLRFFSITGRAVIAPLTWLAVTLLTGTYYECAASEF
ASVDHYPMFDNVSASKREEILAGFPCCRSAPSDVILVRDEIALLHRYQSQMLGWILITLATIAALVSC
CVAKCCSPLTSLQHCYWTSHLQNERELFEQAAEQHSRLLMMHRIKKLFGFIPGSEDVKHIRIPSCQDW
KDISVPTLLCMGDDLQGHYSFLGNRVDEDNEEDRSRGIELKP

Figure 30. Identification of CALHM2 and CALHM4 proteins in human placental tissue. (**A**) Scheme of placental membrane isolation, solubilization and immunoprecipitation on magnetic beads and detection of proteins present in the sample of the membrane fraction. (**B**) Western blot analysis of the samples obtained from immunoprecipitation experiments probed with anti-CALHM2 and anti-CALHM4 antibodies respectively. (**C**) Resulting data of LC-MS/MS analysis for CALHM proteins listed by total spectra count are broken down in the tables for CALHM2 and 4 respectively. The number of unique peptides, their total spectra count and their fraction in the whole sample are indicated. (**D**) CALHM2 and CALHM4 sequences with orange boxes indicating parts covered by the MS experiment.

Briefly, samples of human placentae were homogenized and the cytosolic and membrane fractions was separated (**Figure 30-A**). The membrane fraction was solubilized with detergent buffer, concentrated and incubated with magnetic beads coated with anti-CALHM2 or anti-CALHM4 antibodies (**Figure 30-A**). After several wash steps the beads were collected for the analysis of pulled-down proteins (**Figure 30-A**). All performed steps have been monitored by western blot analysis and the final protein fraction bound to the beads was additionally analyzed by mass spectrometry (**Figure 30-A**). **Figure 30-B-D** depicts the results of the immune-precipitation experiment for CALHM2 and 4 from human placenta. Both CALHM2 and 4 proteins migrate on an SDS-PAGE gel at a molecular mass slightly below 37 kDa, with CALHM4 additionaly displaying a band at around 70 (**Figure 30-B**). Throughout the course of the experiment we observed several bands at around 50 kDa, 100 kDa and above 150 kDa of CALHM2 in Western blots, presumably representing proteins that are non-specifically recognized by the antibodies (**Figure 30-B**). The band at around 37 kDa is also observed, however, it migrates higher in comparison to the control sample of the purified CALHM2 protein (**Figure 30-B**), pointing towards yet another unspecific detection. Consequently, no enrichment of the band at this mass is observed in the bead sample, which would be expected in case of a successful pull down of CALHM2 proteins. In addition, the bead sample shows strong signals ranging from 37 to 150 kDa, originating from anti-CALHM2 antibodies present in the sample, which impede a reliable analysis (**Figure 30-B**). Similar results are observed in the Western blot probed with anti-CALHM4 immunoglobins (**Figure 30-B**). Again, although several bands are present at locations corresponding to a molecular weight of 25 kDa, 60 kDa and 75 kDa, they are not consistent with the masses of the bands observed in the sample of overexpressed and purified CALHM4 and the final bead sample also displays strong signals originating from anti-CALHM4 immunoglobins present in the sample (**Figure 30-B**). Although inconclusive, these results indicate the absence or low abundance of CALHM2 and 4 proteins in placental tissues and thus fail to detect the enrichment of these proteins in pull-down experiments. Due to the described limitations, we aimed to analyze the bead samples by a more sensitive mass spectrometry approach, which additionally has the advantage of a readout that is not being affected by the contamination with anti-CALHM antibodies. For that purpose, the samples bound to the beads were digested with trypsin and analyzed by LC-MS/MS. **Figure 30-C and D** show the results of the LC/MS-MS analysis of the immunoprecipitated proteins. It should be noted that the employed method is not quantitative as the number of peptides does not necessarily correlate with the protein abundance. Thus, although the comparison of peptide counts allows to estimate protein abundance, the conclusions should be taken with caution. More than three hundred proteins have been detected in both samples, the majority of which result from unspecific binding (**Figure 30-C**). Among the detected proteins, only small single-digit number of CALHM2 and 4 peptides were found (**Figure 30-C and D)**. These peptides constitute 0.02% and 0.01% respectively in the total sample peptides count (**Figure 30-C)** and, although striking, such disproportion between unspecific and target antigens is consistent with the observations in Western

blot. Together the results point towards a low abundance of pulled-down CALHM2 and 4. The small number of detected peptides possibly reflects low expression levels or the non-optimal pipeline of the experiment resulting in an inefficient pull down by the antibodies, which might also result in the observed unspecific binding. Still, despite the low number of detected peptides of CALHM2 and CALHM4, the expression of both proteins in placental tissue has been confirmed. In conclusion, the analysis of pulled-down protein using the more sensitive method of mass spectrometry has provided valuable insights into the presence of CALHM2 and CALHM4 in placental tissues. Assuming a co-expression of both proteins in the same cell suggests a possibility of their interaction, which may have significant implications for their functions.

2.3.2 Interactions of CALHM proteins in an over-expression system

As shown in the previous chapter CALHM2, 4 and 6 genes are highly expressed in placental tissues at the mRNA level and the expression of CALHM2 and 4 genes at a protein level could be confirmed by mass spectrometry. Based on the similar expression pattern and the observed heteromerization of CALHM1 and 3, I reasoned that the placental paralogs might interact in a similar manner to form heteromeric ion channels[44]. To determine whether CALHM2, 4 and 6 would heteromerize, I have performed a pull-down assay on heterologously expressed CALHM proteins, since the insufficient amounts of CALHM proteins and the lack of suitable antibodies precluded a biochemical analysis of interactions in native tissues. Therefore, CALHM paralogues have been co-expressed after transfection with a 1:1 plasmid ratio in HEK293T cells, with one of the paralogs carrying C-terminally reporter (Myc and GFP) and affinity tag (SBP) and the other a C-terminal reporter tags only. After lysis of the cells, the CALHM paralog carrying the SBP tag was captured by binding to Strep-Tactin resin and served as a “bait” protein for the CALHM paralog without the affinity tag. The resin was washed several times and proteins pulled-down on the resin eluted. To assess the interactions, the elution samples were analysed with SDS-PAGE. **Figure 31.** shows the results of the pull-down performed on the co-expressed CALHM2, 4 and 6 proteins.

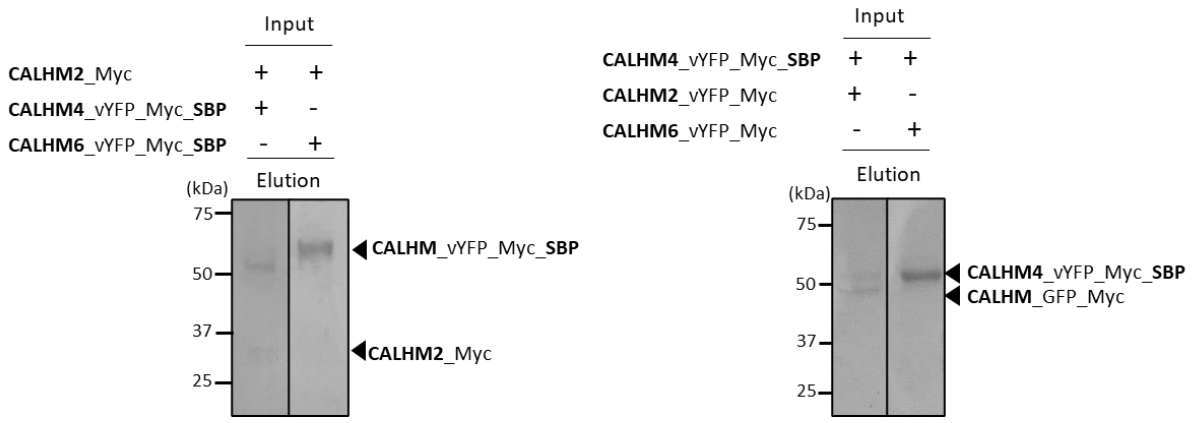

Figure 31. Interactions of CALHM paralogues in an overexpression system. SDS-page analysis of the final elution samples of the pull-down experiment performed on CALHM proteins heterologously co-expressed in HEK293T cells. 'Input' section indicates co-expressed constructs of the CALHM paralogs.

In case of the formation of heteromers, two bands should be observed, one originating from the CALHM used as "bait" and the other from the pulled down homologue. Two bands are observed in samples originating from the co-expression of CALHM2 and CALHM4 but not in co-expressions with CALHM6 (**Figure 31**). Based on these results, I conclude that CALHM2 and CALHM4 interact to form heteromeric channels while CALHM6 does not show sign of interaction with the two other homologues.

To further characterize the interaction between CALHM2 and 4 proteins, I aimed to obtain a sample containing pure CALHM2/4 complexes. For this purpose, I co-expressed CALHM2 tagged with vYFP_Myc_SBP and CALHM4 tagged with Myc_His in HEK293T cells and performed tandem purification to separate the heteromeric complexes from homomeric channels. The proteins were affinity purified on Strep-Tactin resin followed by Ni-NTA resin and a final size exclusion chromatography. The course of the experiment was monitored by Western blot probed with an anti-Myc antibody, which allowed for a semi-quantitative estimation of CALHM2 and 4 protein yields in the samples. **Figure 32** shows the results of the tandem purification of CALHM2 and CALHM4. The analysis of the lysate sample revealed both homologues to be co-expressed at comparable levels (**Figure 32-A**). As expected in the flow-through sample of Strep-Tactin resin, excess of CALHM4 in comparison to CALHM2 is observed with even stronger disproportion in the wash sample and in turn an excess of CALHM2 is observed in the elution from this resin (**Figure 32-A**).

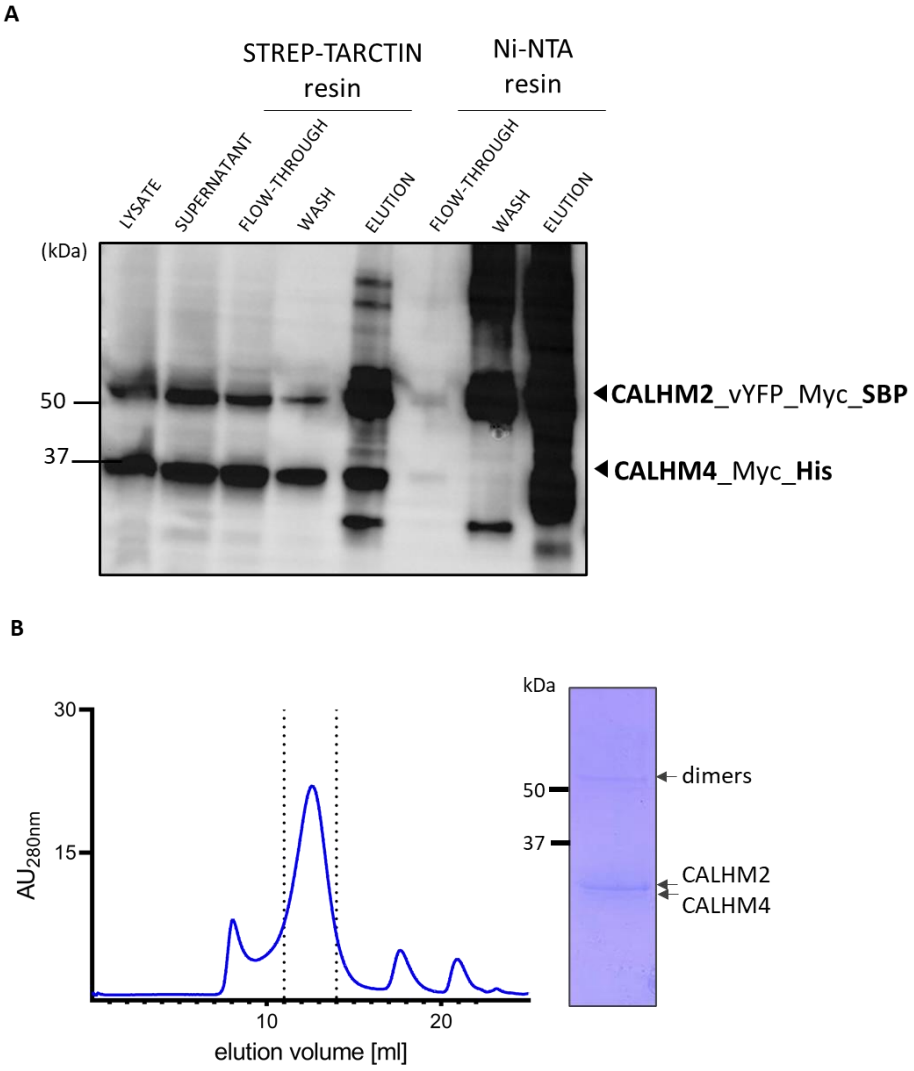

Figure 32. **Tandem purification of CALHM2/4 complex.** (**A**) Western blot analysis of the samples from the tandem affinity purification; **LYSATE** – whole cell extract, **SUPERNATANT** – whole cell extract after clarification with centrifugation, **FLOW-THROUGH** – flow-through after binding to resin, **WASH**- flowthrough after wash steps, **ELUTION** – elution from affinity resin. (**B**) SEC profile of the CALHM2/4 complex after purification with tandem-affinity chromatography. Inset shows the SDS-page analysis of the indicated fractions of the peak.

The opposite ratio is observed in the separation on a nickel binding resin with the excess of CALHM2 found in the wash sample (**Figure 32-A**). The analysis of the final elution sample indicated a presence of both protein, however the estimation of the relative abundance in this sample is precluded due to the overload (**Figure 32-A**). Such prepared sample was subjected to size exclusion chromatography (SEC) (**Figure 32-B**). The SEC profile revealed a monodisperse peak eluting at low column volume indicating large oligomeric state of the purified proteins (**Figure 32-B**). SDS-page gel analysis of peak-corresponding fractions showed the presence of both, CALHM2 and 4 proteins confirming their interaction with a predominance of the CALHM2 paralogue in the complex (**Figure 32-B**). Collectively, these data demonstrate that CALHM2 and 4 proteins interact forming biochemically stable complexes.

2.3.3 Summary and conclusions on the co-expression and purification of CALHM2/4 heteromers

In my study initial pull-down assays of co-expressed paralogs have provided first evidence for the interaction between CALHM2 and CALHM4 proteins. Subsequently, tandem purification was employed to confirm this interaction and provide insight into the relative abundance of respective subunits in complexes. Despite comparable expression levels in total extracts, CALHM2 was enriched in the final sample. A coarse estimation of the purification yields between heteromeric to homomeric complexes, latter of which amount to 6% of the total protein, suggests a strong preference for homomeric assemblies. However, this estimation fails to account for the protein losses in tandem purification and the complexity introduced by co-expressing two proteins, heavily relying on the chance of co-expression in a single cell. The available literature on co-transfection efficiencies is sparse making it challenging to obtain accurate estimations of plasmid uptake by HEK cells, which undoubtedly impacts the relative abundances of expressed homologues. A comparative analysis of cells expressing single constructs versus both could provide the actual relative abundances. This could be achieved as demonstrated by others [62] through techniques such as sorting and fluorescence estimation, wherein two different fluorescent tags are used for co-transfection. Or ideally single plasmid encoding both proteins could be used to overcome this particular limitation listing only one and simple way of more controlled co-transfection. A second and possibly more relevant cause for the predominance of homomers might be the higher affinity of homomeric subunit interactions, which has also been found in heteromers of the LRRC8 family[63,64].

However, furthermore the assembly of heteromeric ion channels remains a largely understudies field with limited understanding of the factors driving their formations. It is possible to consider that the relative abundances of subunits and assembly chaperones contribute to this process which is likely regulated. The overexpressed system used in our study might lack certain components that are essential for the assemblies. Additionally, the actual physiological relative abundances of CALHM2 and CALHM4 proteins are currently unknown. Although our mRNA studies indicate similar abundances supporting a 1:1 ratio in our co-transfection experiments, it is conceivable that altering this ratio could influence the resulting relative and total abundances obtained.

2.3.4 Patch-clamp electrophysiology

Observed *in vitro* interactions between CALHM2 and CALHM4 proteins suggest the potential formation of heteromeric channels, similar to the previously reported CALHM1 and CALHM3[44]. When CALHM1 is paired with CALHM3, it results in an ion channel with accelerated kinetics and higher sensitivity to voltage compared to the homomeric CALHM1[44]. In our studies using *Xenopus laevis* oocytes, CALHM2 and CALHM4 alone did not show any activity. To investigate whether pairing these two homologues could reverse these results, I employed patch-clamp electrophysiology, which was previously reported to study CALHM1 and CALHM1/3 channels activity in mammalian cells[2,44]. This technique allows to directly measure and analyze currents across the cell membrane. The whole-cell configuration, which was used in this study, involves creating a high-resistance seal between the glass pipette electrode and the cell membrane followed by local rupture of the attached membrane. This allows to establish contact between the pipette solution and the cell's cytoplasm while maintaining the cell's internal environment intact. In this configuration the responses to a voltage change can be investigated in a straightforward manner and the extracellular environment can be easily controlled by perfusion with solutions of defined composition.

The recordings were performed in HEK cells that were transfected with either an empty vector (as negative control) or CALHM constructs tagged with vYFP-Myc-SBP at a C-terminus to facilitate the identification of channels with high surface expression of the transfected constructs. I have included CALHM1 and CALHM1/3 in my study as positive control to reproduce the functional behavior of channels that were previously characterized, as well as CALHM2, CALHM4, and the co-transfection of both protein constructs[2,44]. Currents were recorded in a response to voltage step protocol in the absence and presence of extracellular calcium, conditions which readily activate CALHM1 and CALHM1/3 channels[2,44].

Figure 33-A shows example traces of whole-cell patch-clamp recordings from cells expressing different CALHM proteins. Consistent with previous reports on CALHM activity in mammalian cells, expression of CALHM1 evokes small and slowly activating outwardly rectifying currents indicating its activation at positive voltages (**Figure 33-A**)[2,44]. The co-expression of CALHM3 with CALHM1 generates large currents with faster activation kinetics (**Figure 33-A**)[2]. No significant differences were observed between recordings measured in absence of Ca^{2+}, probably due to the limited number of recordings performed (**Figure 33-A and B**). In line with our previous findings from two-electrode voltage clamp recordings, no currents were observed in cells expressing CALHM2 or CALHM4 alone (**Figure 33-A and B**). Similarly, co-expression of both CALHM2 and CALHM4 failed to generate any detectable currents beyond the negative control (**Figure 33-B**). These results indicate that, unlike CALHM1 and CALHM1/3, neither homomeric CALHM2 or CALHM3 nor heteromeric CALHM2/4 channels are activated by membrane depolarization or extracellular calcium depletion. The functional consequences of CALHM2 and CALHM4 interaction remain thus unclear.

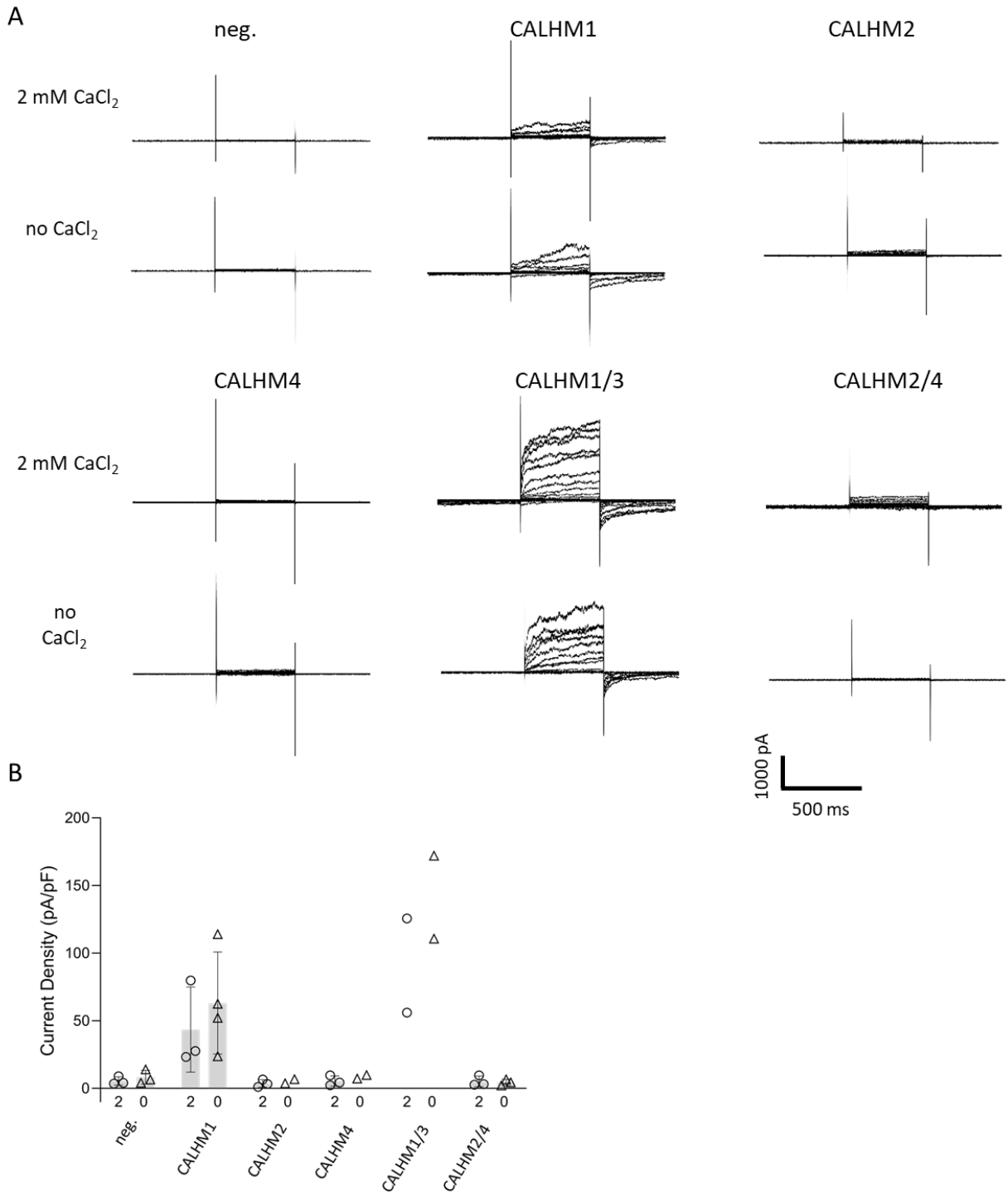

Figure 33. Whole-cell patch-clamp recordings of cells expressing CALHM homologues. (**A**) Example traces recorded from HEK cells expressing either human CALHM1, CALHM2, CALHM4 and cells that co-express CALHM1 and 3, and CALHM2 and 4 are shown. Currents evoked by mock-transfected cells (neg.) are shown for comparison. Currents were evoked by 500 ms voltage pulses from -80 mV to 100 mV in 10 mV increments from a holding potential of -40 mV. (**B**) Summary of current densities recorded as in (**A**). Data show current densities of single cells at 100 mV recorded in 2 mM $CaCl_2$ containing (circles) or $CaCl_2$-free (triangles) extracellular solutions. Mean currents (grey bars) and standard deviations (error bars) are given for replicates with n greater than 2.

2.4 Structural studies of heteromeric CALHM2/4 channels

Because of the compelling evidence for the interaction between CALHM2 and CALHM4 proteins, yet lack of the activity observed, I decided to determine the structure of the complex to get an insight into the nature of their interaction. I expected that the structures would reveal how these two proteins mutually affect each other and potentially reveal features that are integral to their currently unknown functional roles. Oligomeric assemblies of homomeric CALHM channels offer various possibilities in which CALHM2 and 4 proteins could interact with each other. For example, the interaction could occur within a single channel, by dimerization of homomeric channels or it could have the character of an accessory protein not being a part of the channel itself. Moreover, various stoichiometries of the arrangements could be expected, including an interaction-dependent heterogeneity of conformations of subunits of the same kind. The method of choice to determine the structure was cryo-EM, however, such efforts require tools to overcome the similarity of homologues to be able to distinguish them in heteromeric assemblies. I suspected, that the lack of distinct structural features of CALHM2 and 4 paralogues would disturb particle alignment, particularly if heterogeneous assemblies would be present. Such difficulties have been reported by others, during the analysis of structures of heteromeric large-pore ion channels, which impeded the resolution of distinct subunit patterns[28,65,66]. Thus, in an attempt to overcome this issue, I decided to introduce artificial structural features specific for the subunits to aid the unambiguous alignment and thus the subunit identification in the complex.

2.4.1 Binders generation and characterization

Synthetic nanobodies, also known as sybodies, are engineered protein-based binders that specifically bind to their targets[67,68]. They are designed to mimic the natural shape diversity of camelid nanobodies and possess three complementarity determining regions (CDRs), which are variable domains that constitute the epitopes[68]. The variable length and arrangement of CDR3 determines one of the three binding modes: concave, loop, and convex, with each name reflecting the geometry of the binding surface[68]. Three sybody libraries have been constructed by randomizing sequences of CDRs in a controlled manner[68]. This approach aimed to involve sequences that have been previously reported to be beneficial for binding, in particular of membrane proteins, while excluding unfavorable sequences[68]. As a result, the predefined scaffold and the variety of sybodies generate an optimal surface complementarity to the limited hydrophilic epitopes of membrane proteins[68]. In addition to their selective binding properties, sybodies offer several advantages over traditional antibodies[68]. They are smaller in size, have a higher stability and are easier to produce[68]. Thus, to specifically label CALHM2 and CALHM4 proteins within the complex, I decided to select sybodies against each protein.

One of the prerequisites of conducting sybody selection is a biochemically stable sample of pure protein[67,68]. The purification protocols for CALHM2 and 4 have been established as described in the **section 2.1.2**. The other requirement is protein biotinylation as the sybody platform utilizes biotin-streptavidin interactions to selectively immobilize target proteins in the selection and characterization process.

2.4.1.1 Biotinylation

Biotinylation of CALHM2 and CALHM4 has been performed with a derivative of a biotin reagent that targets primary amines such as the side-chain of lysines or the amino-termini of polypeptides. The procedure is straightforward and involves incubation of the reagent with the protein. The degree of the biotinylation can be easily controlled by adjusting protein concentration and incubation time. For sybody selection, attention should be paid not to over-biotinylate a protein as this could reduce available epitope surface[67]. Conversely, under-biotinylation should also be avoided as it could result in a loss of binders[67]. In case of CALHM proteins, their high oligomeric state has been utilized, to biotinylate only a fraction (one tenth) of proteins. This ensured efficient immobilization of the channels while retaining unbiotinylated lysins in some of the protomers. Thus, short incubations have been performed for CALHM2 and 4 and the biotinylation was assessed with the SDS-PAGE analysis. **Figure 34** shows an SDS-page analysis of biotinylated CALHM2 and CALHM4. Since biotin-streptavidin binding is resistant to SDS denaturation, upon complex formation a band corresponding to the streptavidin-CALHM complex can be observed (**Figure 34**). A diffuse band at higher oligomeric state is observed in the sample of the mixture of streptavidin and CALHM, when compared to the samples of streptavidin or CALHM only, while the intensity in the CALHM bands is reduced (**Figure 34**). This confirms the successful biotinylation of CALHM2 and CALHM4, which were both further used for selecting anti-CALHM sybodies.

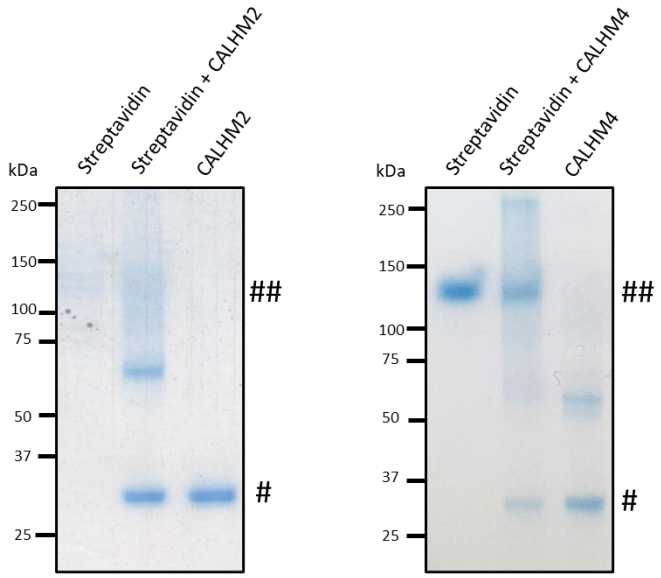

Figure 34. Biotinylation of CALHM2 and CALHM4. SDS-page analysis of samples of streptavidin, a mixture of streptavidin and biotinylated CALHM2 or CALHM4 and biotinylated CALHM2 or CALHM4 only. '##' indicates the region of streptavidin-CALHM complex migration, '#' indicates CALHM proteins only.

2.4.1.2 Selection of synthetic nanobodies

To select sybodies targeting CALHM2 and CALHM4 I employed a standardized protocol[67]. In this procedure I used mRNA libraries of concave, loop and convex sybodies kindly provided by prof. Markus Seeger from the Institute of Medical Microbiology, UZH. The sybody platform is an in vitro system constructed as a selection cascade, which involves multiple steps that enrich a pool of binders that exhibit binding affinity towards the target proteins[67,68]. The process began with one round of ribosome display, where sybodies were displayed on ribosomes against CALHM proteins. Subsequently, two rounds of phage display were conducted, utilizing the enriched ribosome-displayed sybodies. Following the phage display rounds, potential binding candidates were identified using an enzyme-linked immunosorbent assay (ELISA). In ELISA screening, the signal strength relates to the amount of a sybody present in the sample. To identify binders, the ratio of the signal against CALHM to the signal against the negative control was evaluated, and sybodies were classified as positive hits if the ratio exceeded a factor of 1.5 as recommended in the protocol[67]. **Figure 35** shows the results of ELISA assays for sybodies against target CALHM2 and CALHM4.

A

a

	1	2	3	4	5	6	7	8	9	10	11	12
A	26.52471	6.858745	40.72591	4.812357	43.79466	41.98771	26.52471	6.858745	40.72591	4.812357	43.79466	41.98771
B	13.1082	30.4405	12.83544	26.43602	30.53987	43.6375	13.1082	30.4405	12.83544	26.43602	30.53987	43.6375
C	1.288355	22.98662	38.94673	46.55699	29.70732	42.5672	1.288355	22.98662	38.94673	46.55699	29.70732	42.5672
D	17.00114	53.11416	34.21792	13.28571	23.24741	11.3257	17.00114	53.11416	34.21792	13.28571	23.24741	11.3257
E	28.45478	43.85117	28.45647	35.27069	10.7748	63.35941	28.45478	43.85117	28.45647	35.27069	10.7748	63.35941
F	0.606186	34.12623	1.142373	38.36082	42.89678	52.65479	0.606186	34.12623	1.142373	38.36082	42.89678	52.65479
G	4.57933	28.202	31.64678	53.52294	1.458239	7.157407	4.57933	28.202	31.64678	53.52294	1.458239	7.157407
H	2.125874	42.2521	63.05761	20.34868	19.73276	12.22449	2.125874	42.2521	63.05761	20.34868	19.73276	12.22449

b

	1	2	3	4	5	6	7	8	9	10	11	12
A	3.299197	2.994881	3.063745	1.75641	5.16451	10.65143	3.299197	2.994881	3.063745	1.75641	5.16451	10.65143
B	1.294766	3.080718	1.922401	1.985141	11.24288	2.235555	1.294766	3.080718	1.922401	1.985141	11.24288	2.235555
C	49.50313	1.533758	1.758416	2.494078	2.690526	5.477832	49.50313	1.533758	1.758416	2.494078	2.690526	5.477832
D	16.83201	2.220199	1.769841	1.359511	3.017751	1.777778	16.83201	2.220199	1.769841	1.359511	3.017751	1.777778
E	41.6976	4.716346	1.602015	1.38326	2.410714	2.620047	41.6976	4.716346	1.602015	1.38326	2.410714	2.620047
F	1.288732	2.302548	16.1051	1.367925	1.114641	1.56513	1.288732	2.302548	16.1051	1.367925	1.114641	1.56513
G	2.944762	1.507223	1.843014	1.541586	1.170159	2.581633	2.944762	1.507223	1.843014	1.541586	1.170159	2.581633
H	36.95019	29.62396	1.317716	1.711155	2.86148	9.331877	36.95019	29.62396	1.317716	1.711155	2.86148	9.331877

c

	1	2	3	4	5	6	7	8	9	10	11	12
A	26.19905	24.14307	1.907725	19.37743	22.05812	42.29939	26.19905	24.14307	1.907725	19.37743	22.05812	42.29939
B	1.647687	30.60472	2.175299	42.19483	1.955253	31.89921	1.647687	30.60472	2.175299	42.19483	1.955253	31.89921
C	62.74088	36.82677	52.62879	45.37374	62.76009	50.19965	62.74088	36.82677	52.62879	45.37374	62.76009	50.19965
D	41.63899	12.40778	7.634329	1.606667	27.7479	41.51899	41.63899	12.40778	7.634329	1.606667	27.7479	41.51899
E	44.51235	9.069307	21.72583	14.64516	2.282378	31.55399	44.51235	9.069307	21.72583	14.64516	2.282378	31.55399
F	3.176471	19.72359	20.81957	3.351119	3.880455	44.09797	3.176471	19.72359	20.81957	3.351119	3.880455	44.09797
G	2.29495	5.624413	16.9257	21.16842	9.937388	53.64273	2.29495	5.624413	16.9257	21.16842	9.937388	53.64273
H	24.10729	23.26737	4.393442	29.80825	18.02303	31.66936	24.10729	23.26737	4.393442	29.80825	18.02303	31.66936

B

a

	1	2	3	4	5	6	7	8	9	10	11	12
A	8.078788	8.417294	9.196347	7.726316	10.33745	8.801724	30.20179	11.78099	7.223684	8.792531	6.670694	18.72088
B	0.010582	0.005051	0.010499	0.008798	0.032934	0.012	0.034483	0.107042	34.79915	0.044304	0.084746	0.054902
C	13.01549	5.328652	8.796364	13.8435	9.04955	6.815574	6.635179	8.94012	8.551282	7.739682	9.915094	5.584071
D	7.645162	91.28405	43.41892	59.77358	8.310219	13.25424	10.11983	8.033223	11.84539	81.56225	17.86245	5.376842
E	8.716101	7.5	36.36564	10.11345	6.040892	46.38514	6.682142	10.74317	12.59259	8.185022	6.574913	6.461806
F	9.210001	9.822299	36.72152	8.41453	53.63889	10.36321	14.78899	33.9619	53.87313	8.884956	8.22449	5.394231
G	15.98322	9.291139	18.2186	52.00373	11.25248	20.05682	13.31884	10.84324	10.09045	23.85027	14.81985	6.931464
H	26.48948	23.10648	9.190082	11.41177	10.05556	11.74157	13.49419	9.764706	4.56168	3.99793	10.5266	6.60596

b

	1	2	3	4	5	6	7	8	9	10	11	12
A	4.484979	2.106329	1.902632	2.481771	1.672289	2.48184	1.817102	2.624691	1.899767	1.78271	2.167043	2.271357
B	1.052991	4.599182	2.473347	2.237089	1.973094	1.729592	1.454546	1.44358	2.705128	1.56982	1.762014	2.870588
C	3.186666	1.732843	3.048649	2.169451	1.680693	1.942786	2.181586	1.735135	2.251152	2.56658	1.614796	1.856269
D	1.529284	3.155702	3.019139	0.994071	2.820093	2.01269	1.206651	2.055	1.174825	1.442661	2.002674	1.908127
E	3.803704	2.217262	3.040541	1.521008	3.508772	1.811494	2.447293	1.732442	1.745614	1.75841	1.653543	2.774603
F	1.762376	1.489744	1.588083	1.441253	2.722864	2.201511	1.302439	1.885204	1.008753	1.816038	1.891667	1.858065
G	1.778723	1.303951	1.390879	1.294617	1.56231	1.732143	1.59292	1.407166	1.336182	1.756598	1.377193	1.380645
H	1.344311	1.142145	1.197778	1.727749	1.590909	1.165025	1.254279	1.425	1.010482	1.334096	1.245333	1.458599

c

	1	2	3	4	5	6	7	8	9	10	11	12
A	7.295858	69.81188	29.54655	8.414635	42.63208	9.526923	16.05208	4.041152	9.264705	2.778791	37.76412	16.84594
B	23.25721	47.84404	12.28772	24.0133	14.83804	12.29954	6.183381	7.724638	18.77083	75.58537	28.87547	20.68077
C	10.04622	6.810026	12.84161	6.559681	41.64592	91.44776	7.513208	52.78601	9.891697	50.84541	111.5234	5.622282
D	5.357477	5.414815	5.588921	4.447964	5.571429	7.359195	8.801653	7.290229	4.791262	5.778393	5.171717	4.571739
E	9.105634	6.714286	9.864978	9.048544	2.85967	70.11258	14.80952	11.73529	16.85379	7.086519	8.433884	37.01107
F	11.44582	58.04084	19.59049	4.308	5.26151	6.755618	4.595186	23.06415	36.15862	13.36449	9.995727	6.273118
G	6.578534	6.459183	6.480287	6.765171	5.817536	6.98481	19.31456	46.19415	5.489071	47.61446	6.907651	51.95725
H	6.305804	3.916667	4.498141	37.15208	7.056847	4.560396	5.493151	5.88978	4.551948	62.9536	21.38655	4.789963

Figure 35. **Screening of sybodies targeting CALHMs in an ELISA assay.** Data are presented as ratios of signals against (**A**) CALHM2 or (**B**) CALHM4 to the signals against the negative control, TM287/288 for (**a**) convex (**b**) loop and (**c**) concave sybody libraries. Entries are colored on a gradient scale, ranging from blue for the lowest values to red for the highest values. H12 is a positive control of protein TM287/288 and its specific sybody.

The data shows generally higher signal values for CALHM compared to the negative control for the majority of selected sybodies in all three libraries, indicating positive hits. To obtain their genetic sequences, thirty hits from the ELISA were randomly selected from each library and subjected to sequencing. As recommended in the protocol[67], we did not exclude low ratio sybodies, as the signal does not necessarily correlate with binding affinity. After eliminating flawed and redundant sequences, **Figure 36** displays the alignment of the variable regions of the 96 sequenced sybodies for each paralog. The sybodies originating from libraries convex, loop, and concave were annotated with 'R', 'B', and 'G', respectively, for sybodies targeting CALHM2. For sybodies targeting CALHM4, they were annotated with 'r', 'b', and 'g'. The second part of the name corresponds to the row and column in the ELISA screening tests (**Figure 35**).

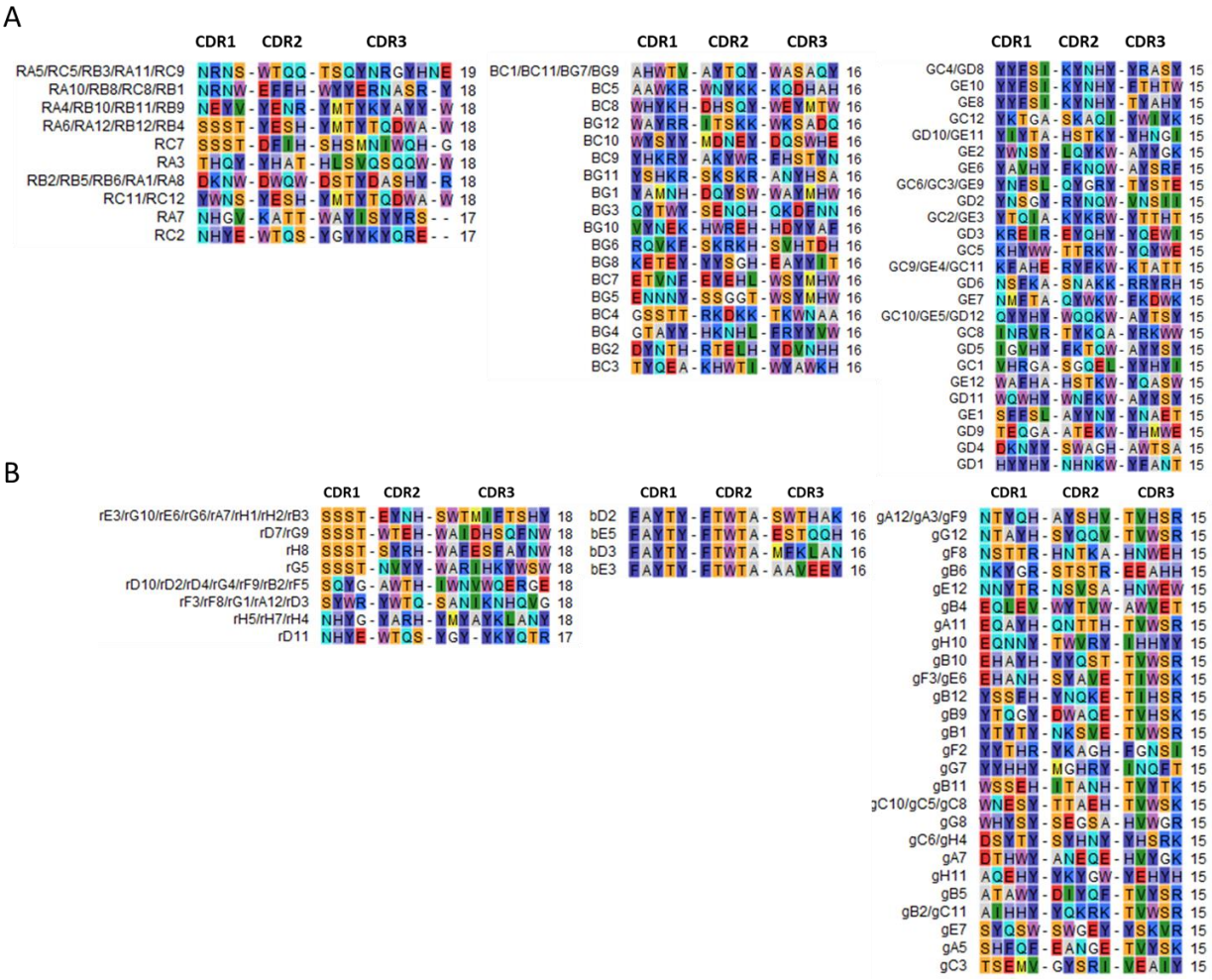

Figure 36. **Sequence alignment of ELISA hits.** Shown are the aligned three complementary determining regions (CDR) of convex, loop and concave libraries for sybodies targeting (**A**) CALHM2 and (**B**) CALHM4.

2.4.1.3 Purification of ELISA hits

Note: purification and binding tests of sybodies targeting CALHM4 have been performed by Martina Peter as part of her master project carried out under the supervision of the author of the thesis.

To ensure their suitability for downstream applications, the biochemical properties of the identified binders were assessed. To this end, sybodies have been expressed in small scale in bacterial cultures and subsequently purified by affinity chromatography followed by size exclusion chromatography. Desirable features include high purification yield and lack of aggregation or oligomerization. **Figure 37** and **37** display size exclusion profiles of fifteen evaluated sybodies for CALHM2 and 4, respectively. For both homologues more than half of the tested sybodies exhibited a high yield and demonstrated monomeric elution on the column, making them suitable for downstream application, thus they were subjected to further characterization (**Figure 37 and 38**). Other sybodies were excluded due to their low expression levels or strong interaction with the column.

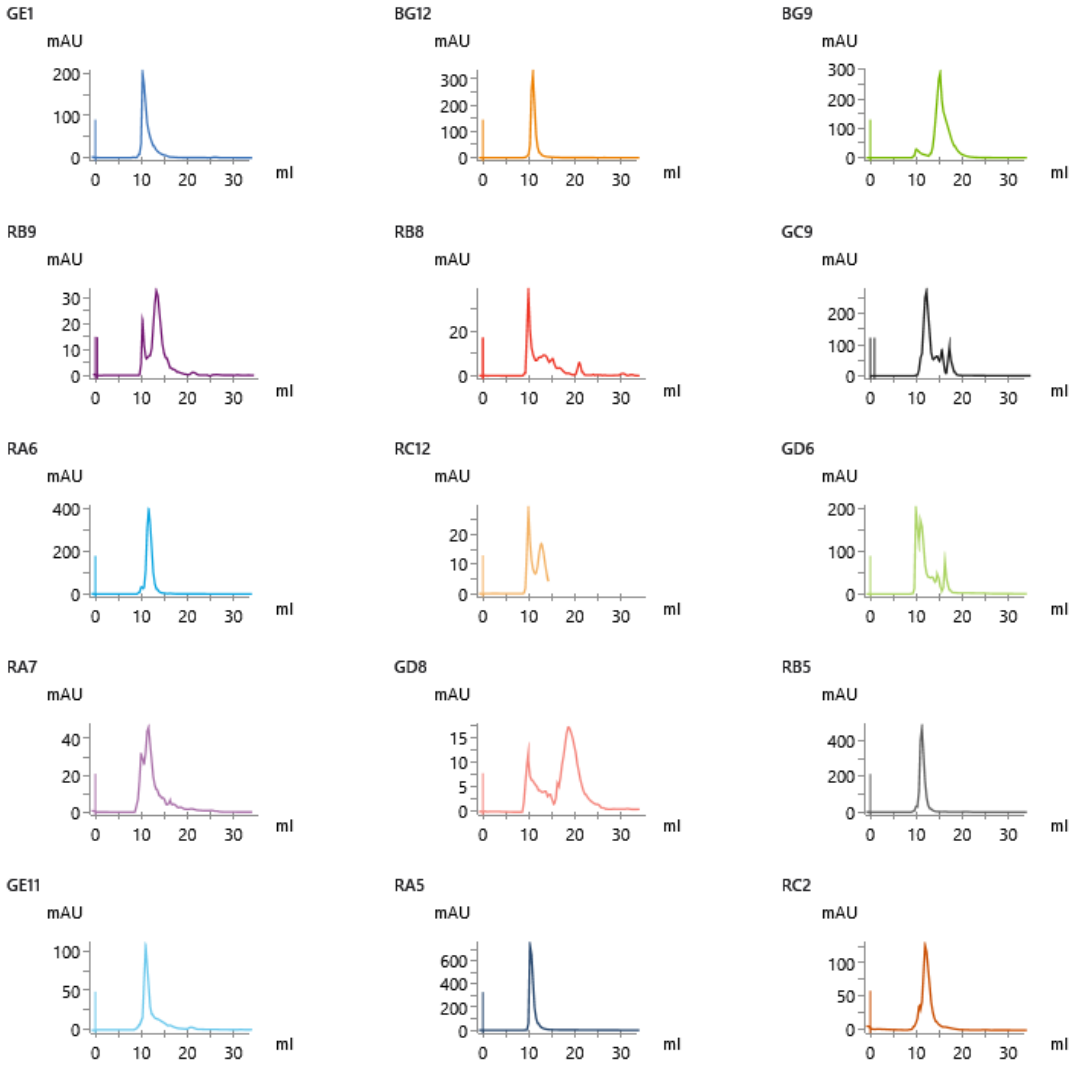

Figure 37. **Purification tests of sybodies targeting CALHM2.** Size exclusion profiles of sybodies targeting CALHM2 purified on an SRT-10C SEC 100 column are shown. The void volume of the column is at 9 ml. Monomeric sybodies elute between 10.5 ml and 12 ml. Sybodies eluting later than 12.5 ml display strong hydrophobic interaction with the column.

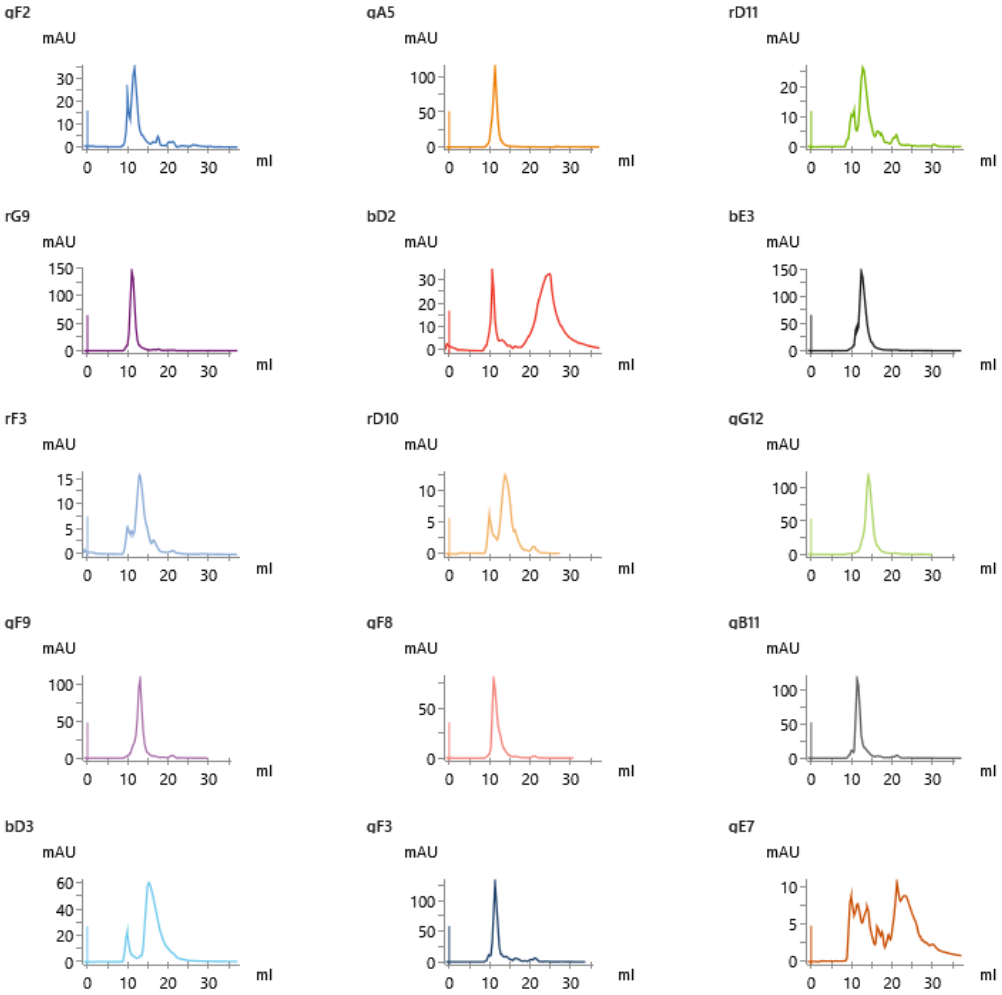

Figure 38. **Purification tests of sybodies targeting CALHM4.** Size exclusion profiles of sybodies targeting CALHM2 purified on an SRT-10C SEC 100 column are shown. The void volume of the column is at 9 ml. Monomeric sybodies elute between 10.5 ml and 12 ml. Sybodies eluting later than 12.5 ml display strong hydrophobic interaction with the column.

2.4.1.4 SEC binding assay

In the final step, sybodies were tested with respect to their binding properties to the target protein through binding assays. One commonly used method to evaluate protein interaction is size exclusion chromatography. In this assay, a mixture of target protein and a binder are loaded on a size-exclusion column alongside the target protein alone. Since the elution volume is determined by the hydrodynamic radius of the protein or protein complex, the interaction of two proteins results in a shift towards lower elution volumes compared to un-complexed protein, although this shift could be small for large membrane protein complexes. To performed this assay mixtures of CALHM proteins and sybodies were prepared at the final CALHM concentration of 25 µM and twice molar excess of sybodies. **Figure 39 and 40** shows the results of the binding assay for the target CALHM2 and CALHM4 protein with the selected sybodies.

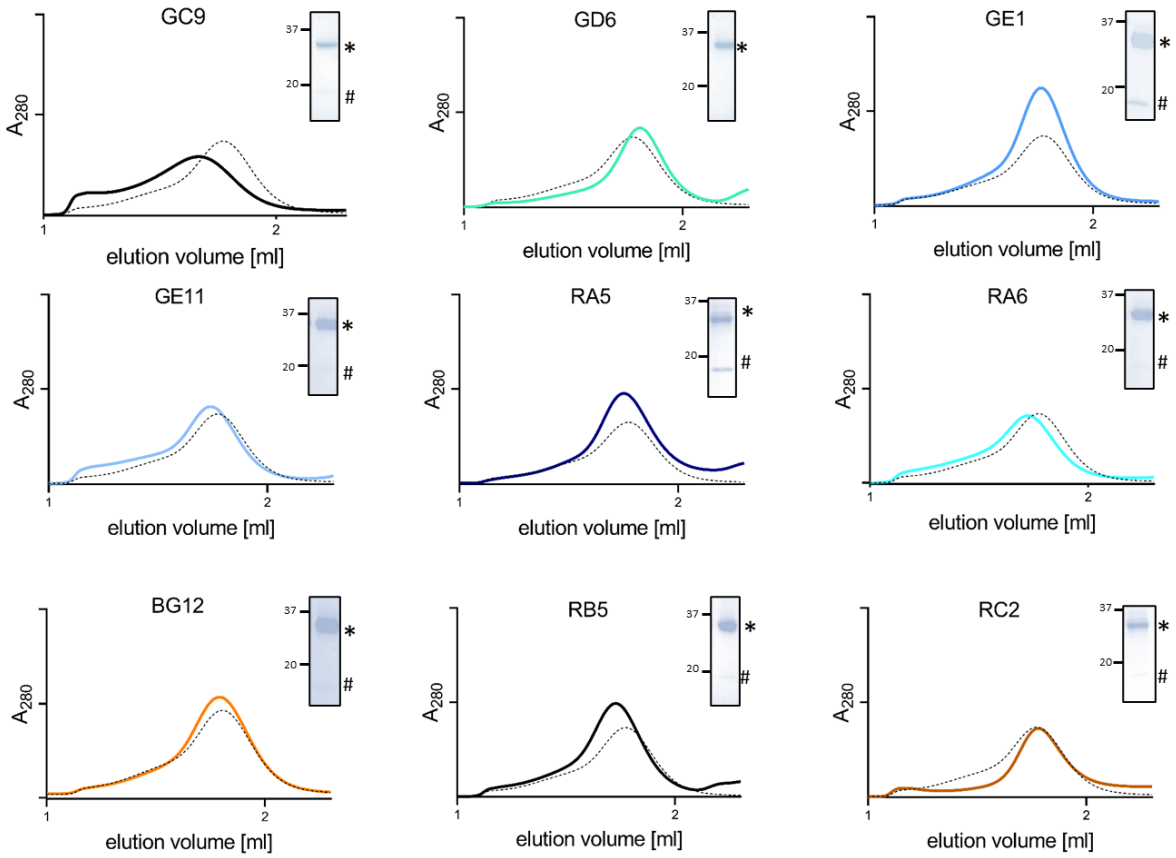

Figure 39. **SEC binding assay of sybodies targeting CALHM2.** Overlayed Superose S6 SEC profiles show comparison of elution volumes of samples of CALHM2 (dashed line) and mixtures of CALHM and sybody (continuous line). Insets show SDS-page gel analysis of peak fractions containing CALHM2 (*) and co-eluted sybody (#).

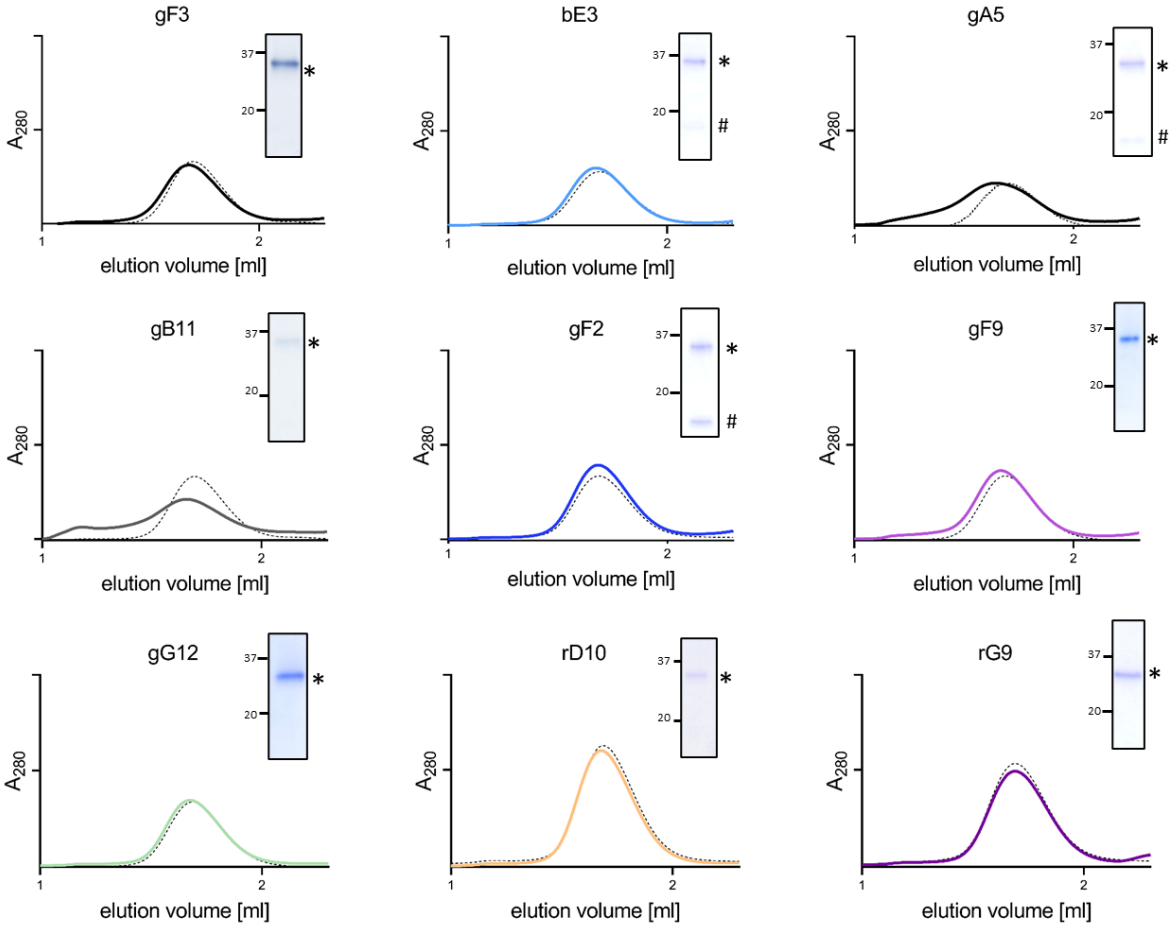

Figure 40. **SEC binding assay of sybodies targeting CALHM4.** Overlayed Superose S6 SEC profiles show comparison of elution volumes of samples of CALHM2 (dashed line) and mixtures of CALHM and sybody (continuous line). Insets show SDS-page gel analysis of peak fractions containing CALHM4 (*) and co-eluted sybody (#).

For CALHM2, small shifts towards the lower elution volume are observed for several sybodies combined with an increase in the absorbance, which indicates complex formation (**Figure 39**). The fractions of the peak corresponding to the putative complex were additionally analysed by SDS-PAGE. In eight samples, this analysis revealed a co-eluted sybody, thus confirming complex formation (**Figure 39**). Due to their large number, I did not include all promising sybodies in the subsequent experiments and instead selected sybody RA5 as the most promising candidate, due to its high expression yield and monodisperse peak of the formed complex and the high amount of the sybody detected on the SDS PAGE gel (**Figure 39**).

Surprisingly, we obtained different results for sybodies selected against CALHM4. A broadening of the peak, rather than its shift to lower volumes was observed for two sybodies, gB11 and gA5 (**Figure 40**). Additionally, when analysed by SDS-PAGE, either no or only faint band of coeluted sybody was observed (**Figure 40**). A strong sybody band observed for gF2, was not accommodated by a shift in elution volume or an increase in the absorption (**Figure 40**). Although the lack of increase in absorbance

is puzzling, the unaltered elution volume might be a consequence of the size of the complex and the limited resolution of the column (**Figure 40**). CALHM4 forms large complexes eluting close to the void volume, where the resolution of the column is probably not good enough to observe the shift upon binding of the small sybodies (**Figure 40**). Additionally, there might be technical artifacts that result in slight shifts in the chromatograms that do not originate from changes in molecular masses. In case of CALHM4, SEC profiles thus proved not to be sensitive enough to draw conclusions concerning complex formation.

2.4.1.5 Pull-down binding assays

Because of the limitations encountered in the SEC binding tests, I decided to complement the evaluation of sybody binding by pulldown assays. To this end, sybodies and CALHM4 were co-expressed in HEK293T cells. Upon lysing the cells, the affinity tagged sybody was immobilized on a resin and served as a "bait" for untagged CALHM4 protein. The course of the assay was monitored by SDS-PAGE in-gel fluorescence as both proteins were fluorescently labelled. The assay was performed with sybodies rD10 and rD11 as they gave high ELISA signals (above 15) but their evaluation in the SEC binding assay was restricted by their low expression yields.

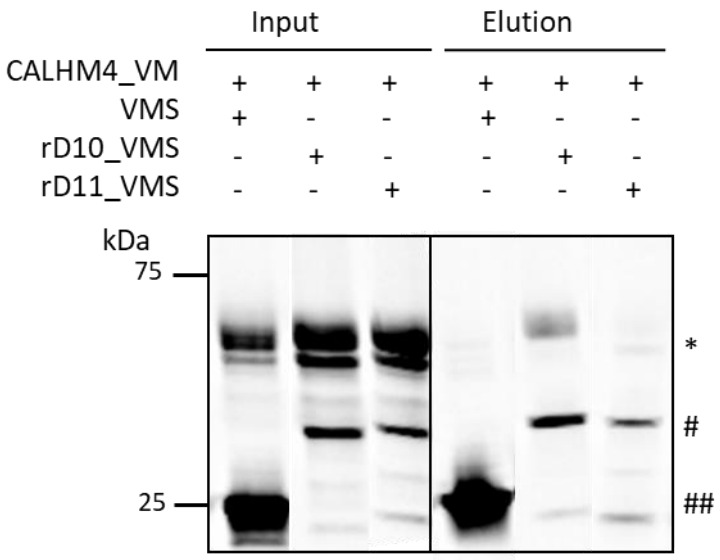

Figure 41. **Pull-down binding assay of sybodies targeting CALHM4.** SDS-PAGE in-gel fluorescence analysis of sybody-CALHM4 interactions. Input: whole cell lysates of cells co-transfected with fusion to fluorescent proteins. Elution: elution from affinity chromatography. * indicates CALHM4, # sybody, ## tag only.

The results of the pulldown binding assays are shown in **Figure 41**. The presence of CALHM4 and sybodies bands in the cell extracts confirms their successful co-expression (**Figure 41**). To examine complex formation, the eluted samples from affinity purification were analysed. For the negative control and rD11, a weakening of the CALHM4-band from the supernatant to the eluates is observed (**Figure 41**). In case of rD10, an enrichment of CALHM4 band is observed in the elution sample compared to the negative control, suggesting that CALHM4 was co-eluted with rD10 due to complex formation (**Figure 41**). These indicates that rD10 binds CALHM4. Although simple and generally promising, it is difficult to make final conclusions concerning binding properties with this pulldown method. The sybodies are co-expressed together with CALHM4 in the HEK293T cells. Whereas CALHM4 expresses

to comparably high levels in the cells, we have no control over amounts of expressed and well-folded sybodies and those amounts differ between sybodies. Such differences might significantly affect the efficiency of binding the pull down of the target protein. Sybodies identified as non-binders when employing this method could thus possibly still bind CALHM4 when investigated under different conditions.

2.4.1.6 Summary of sybody selections

Several binders were successfully generated for both homologues using the sybody technology. The highest number of binders was selected from the concave library, which could be attributed to its complementarity to the target. In the SEC binding tests, more sybodies were identified for CALHM2 than for CALHM4. This discrepancy is intriguing, yet difficult to explain. Although stability assays were not conducted at this stage, a preliminary analysis using size exclusion chromatography after a 2-hour incubation at -4 ^{o}C did not reveal significant differences in the stability of the two proteins (data not shown). In fact, CALHM2 exhibited a small amount of aggregation, whereas CALHM4 did not show any significant stability issues. Hence, the difference cannot be explained by the lower stability of CALHM4 target. In this case a plausible explanation of the difference might either be related to the oligomeric state of the samples affecting the exposure of possible epitopes, since CALHM4 forms channel dimers, handling of the sample during the selection or low affinity of the anti-CALHM4 sybodies. Additionally it should be noted that SEC binding assays may not be an optimal method for the investigation of sybody binding, as evidenced by at least one sybody yielding a false negative result in this screen. Therefore, caution should be exerted when making conclusion based on the results of this assays, as they might reflect errors in the sample preparation rather than real differences (e.g. different intensities of CALHM4 are observed on the gel insets corresponding to the CALHM4 input where equivalent amounts of protein were assumed to be loaded (**Figure 40**). Utilization of higher excess of sybodies in the mixture sample could aid identification of the complex assuming that the observed results are a consequence of low affinities. Thus, the number of the identified sybodies is by no means final and further screening would likely reveal more binders. For the purpose of this study, we chose RA5 targeting CALHM2, and rD10 and gF2 targeting CALHM4 for the further structural characterization. **Figure 42** shows the sequences of the sybodies selected for further characterization.

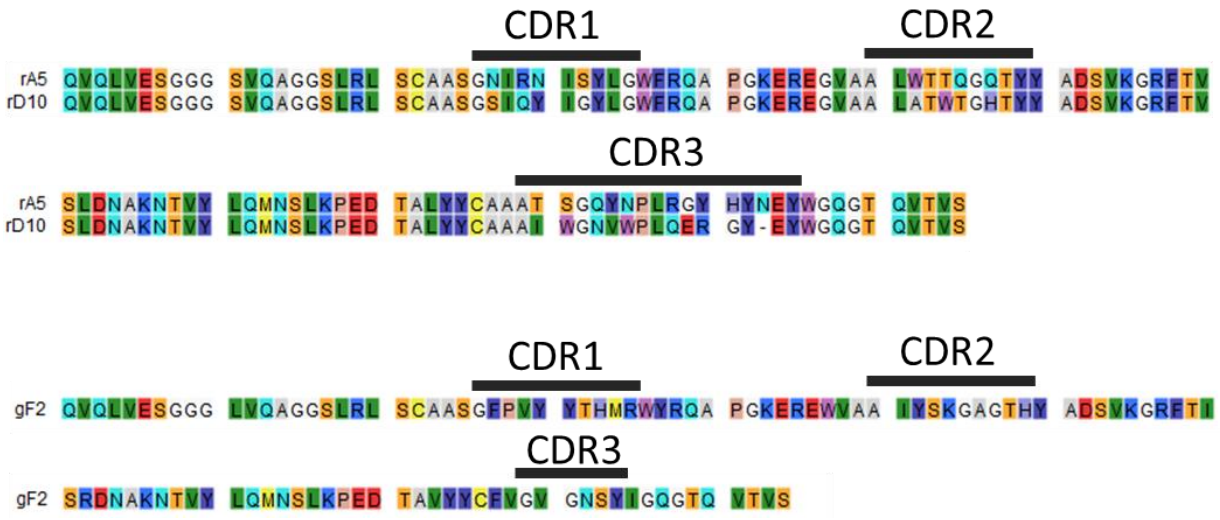

Figure 42. **Sequence alignment of sybodies targeting CALHM2 and CALHM4.** The regions of three complementary determining regions (CDR) are indicated.

2.4.2 Structure determination of CALHM-sybody complexes

Binder selection resulted in the identification of several sybodies targeting CALHM2 and CALHM4. Based on their promising biochemical and binding properties, we have selected one sybody targeting CALHM2 and two sybodies targeting CALHM4 for structural studies. Prior to the structural characterization of heteromeric CALHM2/4 complexes I decided to elucidate the binding sites of the sybodies in complexes with their targets. For the purpose of resolving CALHM subunit patterns in heteromeric complexes, the epitope is ideally located within single CALHM subunit independent from adjacent homologues. Since CALHM proteins form large complexes and proved to be suitable targets for cryoEM, the specific labeling of individual subunits was my attempted goal for the characterization of CALHM heteromers.

2.4.2.1 Structure determination of CALHM2 in complex with sybody RA5

In our attempt to the determine the apo structure of CALHM2 described in chapter 2.1.3, the channels displayed preferred orientation which prevented the reconstruction of a 3D density at high resolution. However, the presence of binders often changes the behavior of a sample on the grid and the identification of sybody RA5 thus offered a new approach for the structure determination of CALHM2. Therefore, the sample was prepared as described previously and prior to vitrification mixed with a 1.5 molar excess of RA5 to reach a final concentration of the complex of 45 µM. A large dataset of 8500 images was collected on a Titan Krios equipped with an energy filter and a K3 camera. **Figure 43** shows details of the processing strategy. In brief, around one million particles were picked and subjected to two rounds of 2D classification (**Figure 43- A-C**). Particles showing features of CALHM channels were sorted by ab-initio reconstruction, which revealed undecameric and decameric assemblies (**Figure 43C**).

Subsequently, the particles of the predominant undecameric assembly were classified and refined by heterogenous refinement (**Figure 43-C**).

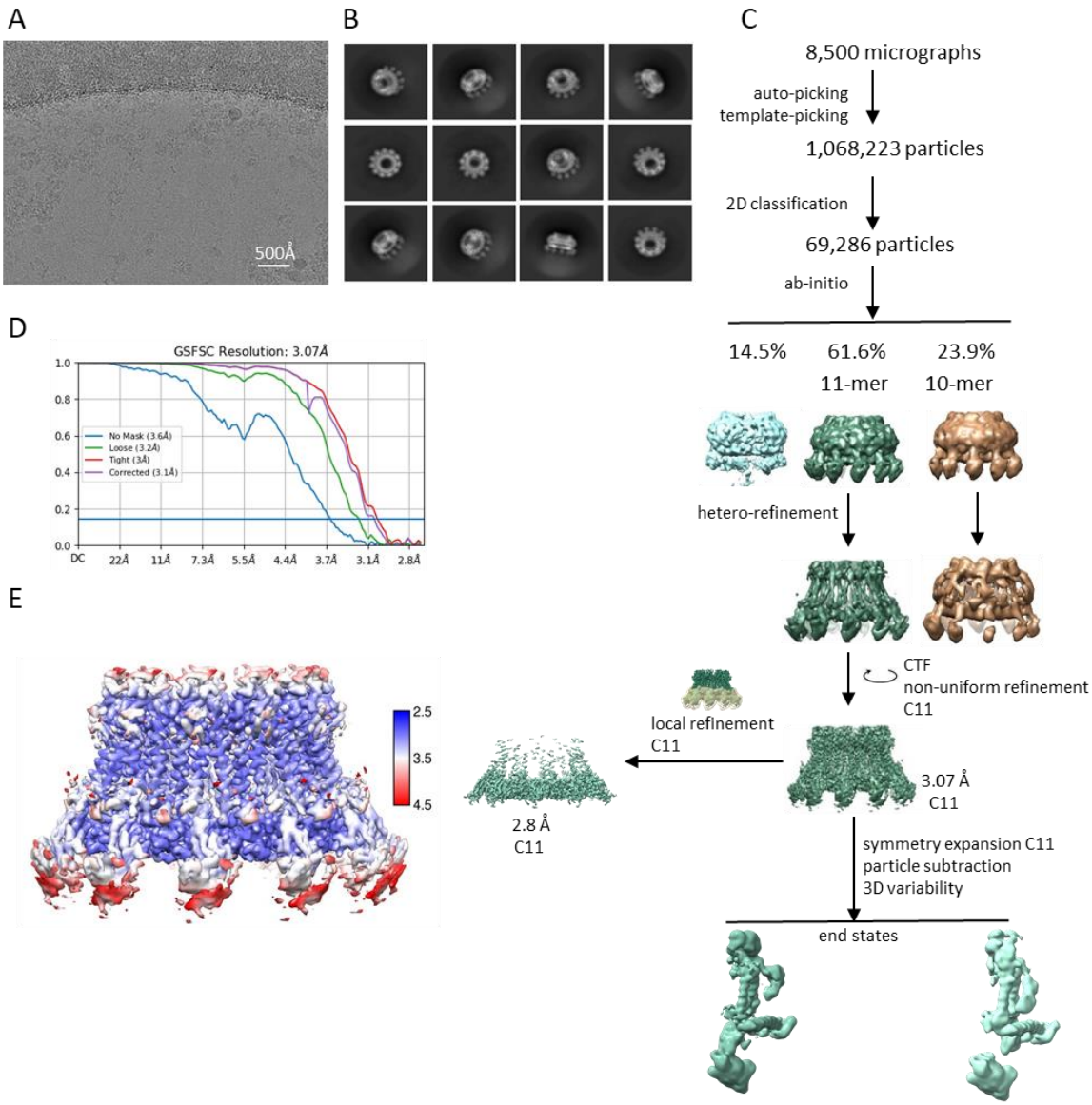

Figure 43. Cryo-EM reconstruction of CALHM2 in complex with sybody RA5. (**A**) Representative cryo-EM micrograph acquired with a Titan Krios microscope equipped with an energy filter and a K3 camera. (**B**) 2D class averages of CALHM2 in complex with the sybody (**C**) Ab-initio reconstruction allowed to isolate two populations representing decameric and undecameric assemblies. The particles were further sorted by heterogenous refinement and undecameric assemblies were refined with several rounds of iterative non-uniform and CTF refinement. The distribution of particles (%) of each class is indicated. To address the flexibility of the pore lining region, an approach that combined symmetry expansion and signal subtraction was employed, in which all of the subunits were subtracted and subjected to the 3D variability analysis with resolution filtered to 9 Å. (**D**) FSC plot of the final refined undecameric structure unmasked (blue), loose (green) and tight (red) masked, and corrected for mask convolution effects (purple) cryo-EM density map of CALHM2-RA5 complex. The resolution at which the FSC curve drops below the 0.143 threshold is indicated. (**E**) Final 3D reconstruction of CALHM2-sybody complex colored according to local resolution.

The subset of high-quality particles was then refined with several rounds of non-uniform and CTF refinement and C11 symmetry was imposed in the final refinement step (**Figure 43-C**). This approach yielded a map at a global resolution of 3.07Å for undecameric CALHM2 (**Figure 43-D and E**). Additionaly, to improve the resolution of the sybody binding region, local refinement with a tight mask around the intracellular region was performed, which improved the resolution of this region to 2.8Å (**Figure 43-C**). The obtained map permitted the interpretation of the bulk of the structure by an atomic model. **Figure 44** shows representative sections of the cryo-EM density superimposed on the model. The densities of NTH and TM1 are poorly resolved, therefore we did not model these regions (**Figure 44**). To further analyze the underlying reason for this poorly resolved regions, we have applied a combination of symmetry expansion, particle subtraction and 3D variability analysis, which revealed a conformational heterogeneity in the sample with two distinct end states that are discussed in more detail further in this chapter (**Figure 43-C**).

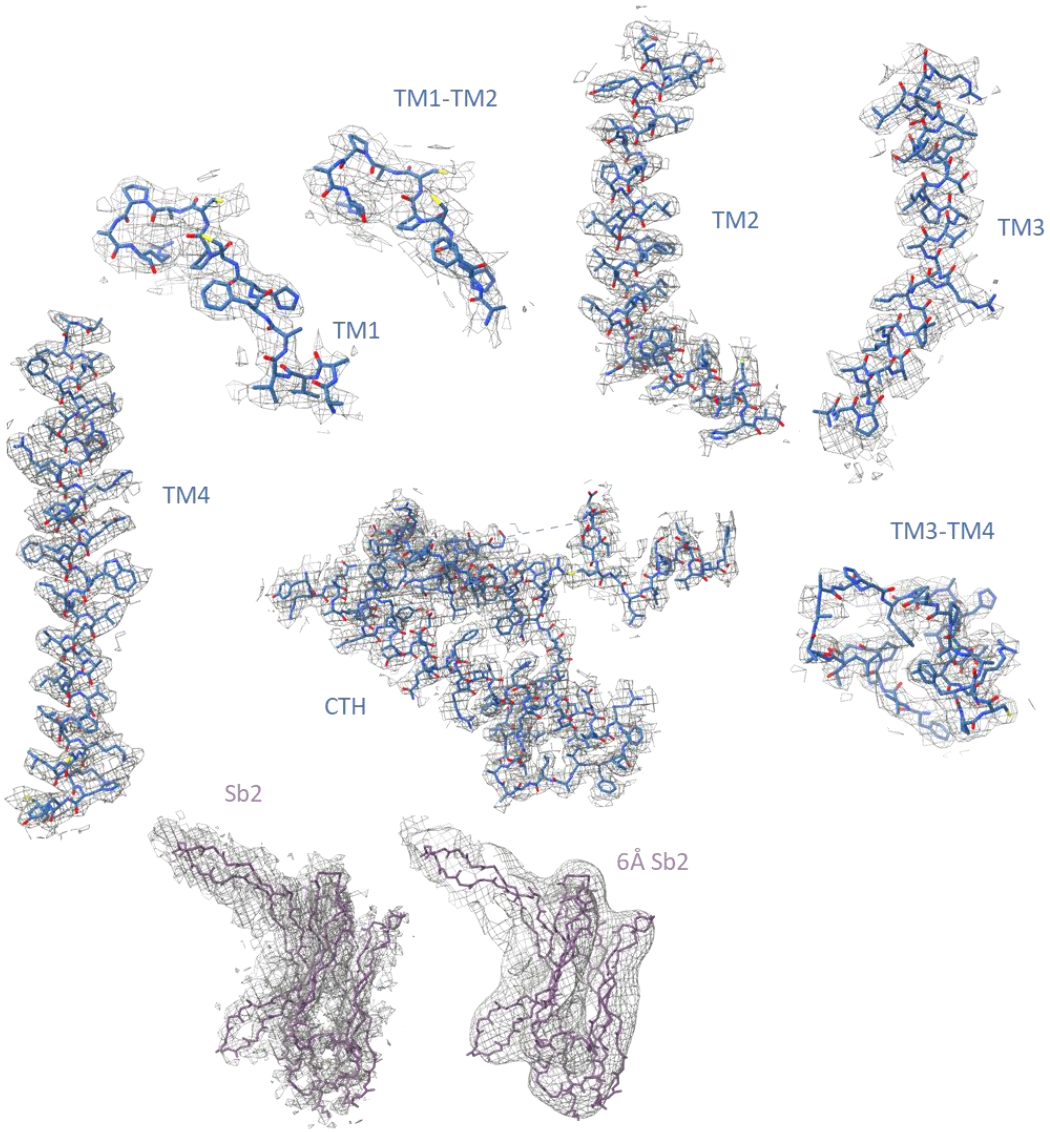

Figure 44. Cryo-EM density of CALHM2. Cryo-EM density at 3.07 Å of selected regions of the undecameric CALHM2 structure superimposed on the model. Structural elements are indicated.

2.4.2.2 General architecture of CALHM2 channels

Similarly to CALHM4 and 6 samples, in the CALHM2 dataset we observe decameric and undecameric assemblies of CALHM2 channels (**Figure 43-C**). As the case for CALHM6 and in contrast to CALHM4, the distribution is not uniform with undecameric assemblies constituting the majority of the channels and no dimerization of the channels is observed (**Figure 43-C**). A high-resolution reconstruction was obtained for larger assemblies only, thus the structure of CALHM2 discussed in this chapter is based on the model of undecamers. **Figure 45** shows the final cryoEM map and corresponding molecular model of undecameric CALHM2 channels.

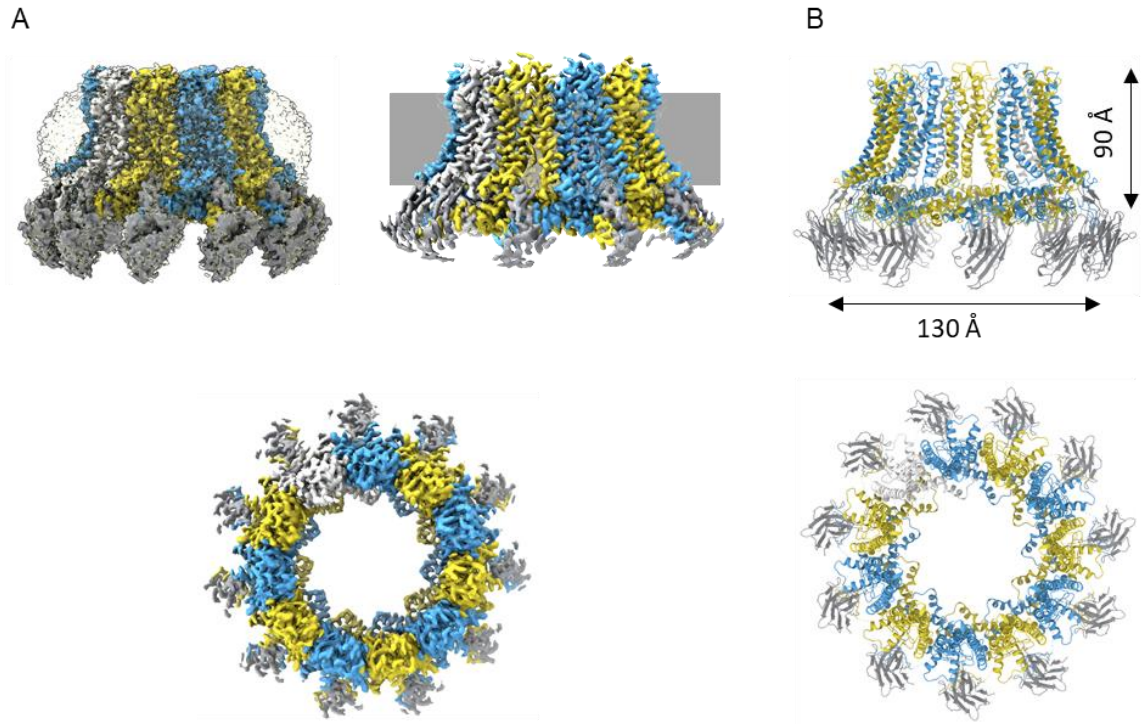

Figure 45. CALHM2 structure. The views are from within the membrane (top) and from the extracellular side (bottom). CALHM2 subunits are colored in blue and yellow, respectively and the sybody is colored in grey. (**A**) Cryo-EM density of undecameric CALHM2 channels at 3.07Å. (**B**) Ribbon representation of the undecameric CALHM2 structure.

The structure of CALHM2 channels is similar to that of CALHM4 and 6, where the subunits arrange around an axis of symmetry, which defines the large central pore (**Figure 45**). Consistently, CALHM2 subunits adopt a similar architecture as the two other homologues. **Figure 46** shows a structure of CALHM2 subunit and its comparison to CALHM4 and 6. Subunits of the three homologues are composed of four transmembrane helices and a long cytoplasmic C-terminal helix (CTH) followed by loops and short helices (**Figure 46-A**). On the extracellular side, two disulfide bonds between extracellular regions connecting TM1 with TM2 and TM3 with TM4 are conserved among the three CALHM homologs (**Figure 45-C**). The contacts between subunits proceed through hydrophobic

interactions between TM2 and TM4 of adjacent subunits and the stacking of the CTHs (**Figure 46-B**). In the cytoplasmic region, the three CALHM homologs adopt similar architectures, however, an additional helix is present in CALHM2 (**Figure 46-A)**. The defined cytoplasmic region of CALHM2 consists of the long α-helix (CTH) followed by an extended region, which folds towards the pore and turns back towards the outer ring forming an extra short α-helix and two additional conserved short α-helices (**Figure 46-A**). Following this region and after a short sequence stretch that is not defined in the density, there is another loop that is unique to the CALHM2 structure. This loop interacts with hydrophobic and polar surfaces of the C-terminal and intracellular loops of the adjacent subunit (in counterclockwise orientation when viewed from the intracellular side) directly beneath the transmembrane domain (**Figure 46-B**).

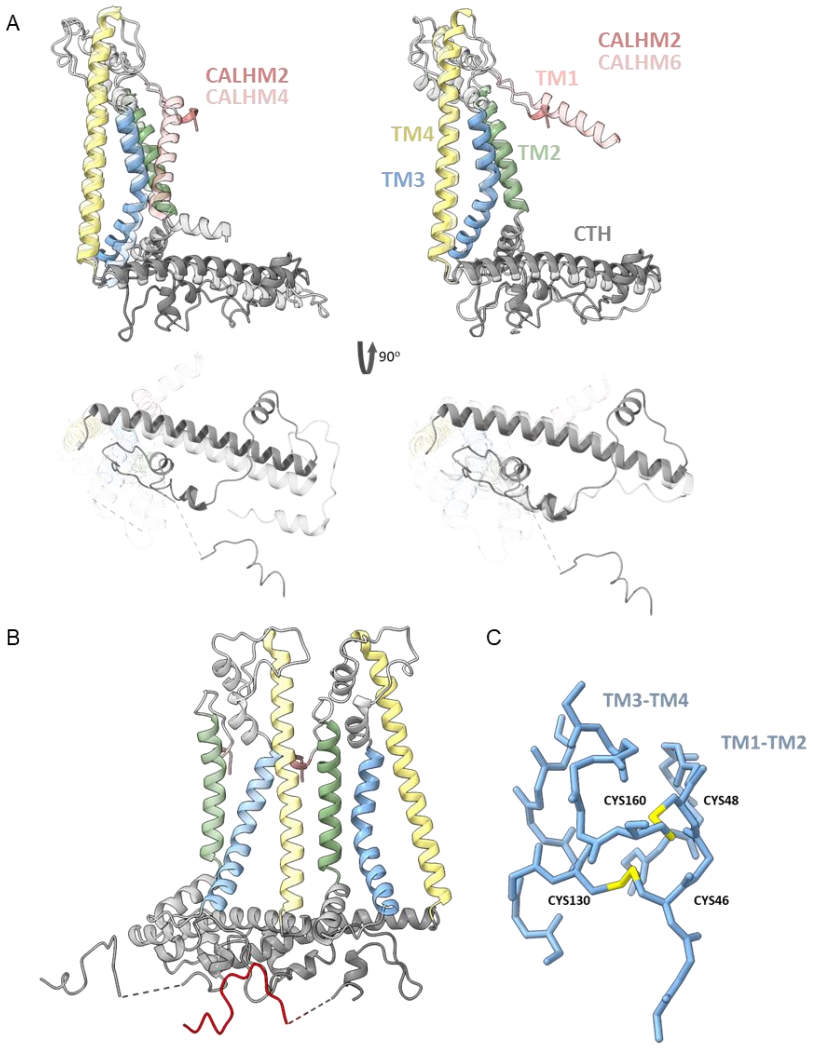

Figure 46. CALHM2 subunit. (**A**) Superimposition of the CALHM2 subunit with subunits of CALHM4 (left) and CALHM6 (right). The views are from within the pore (upper panel) and cytoplasm (bottom panel). Secondary structures are color coded as indicated in the figure. Structures of CALHM4 and 6 are shown transparent. (**B**) Two subunits of CALHM2 viewed from the membrane. The C-terminal loop of the right subunit is colored in red. (**C**) Conserved disulfide bonds connecting two extracellular loops.

2.4.2.3 Pore geometry of CALHM2 channels

The densities of pore-lining α-helices NT and TM1 are not resolved in the reconstruction of CALHM2, indicating an enhanced flexibility of these regions (**Figure 44)**. Thus, I refrained from modeling both elements. Though the absent densities prohibits the unambiguous analysis of the pore-lining regions, I have attempted to describe its properties to some extent. **Figure 47** shows features of the CALHM2 channels pore and pore lining TM1.

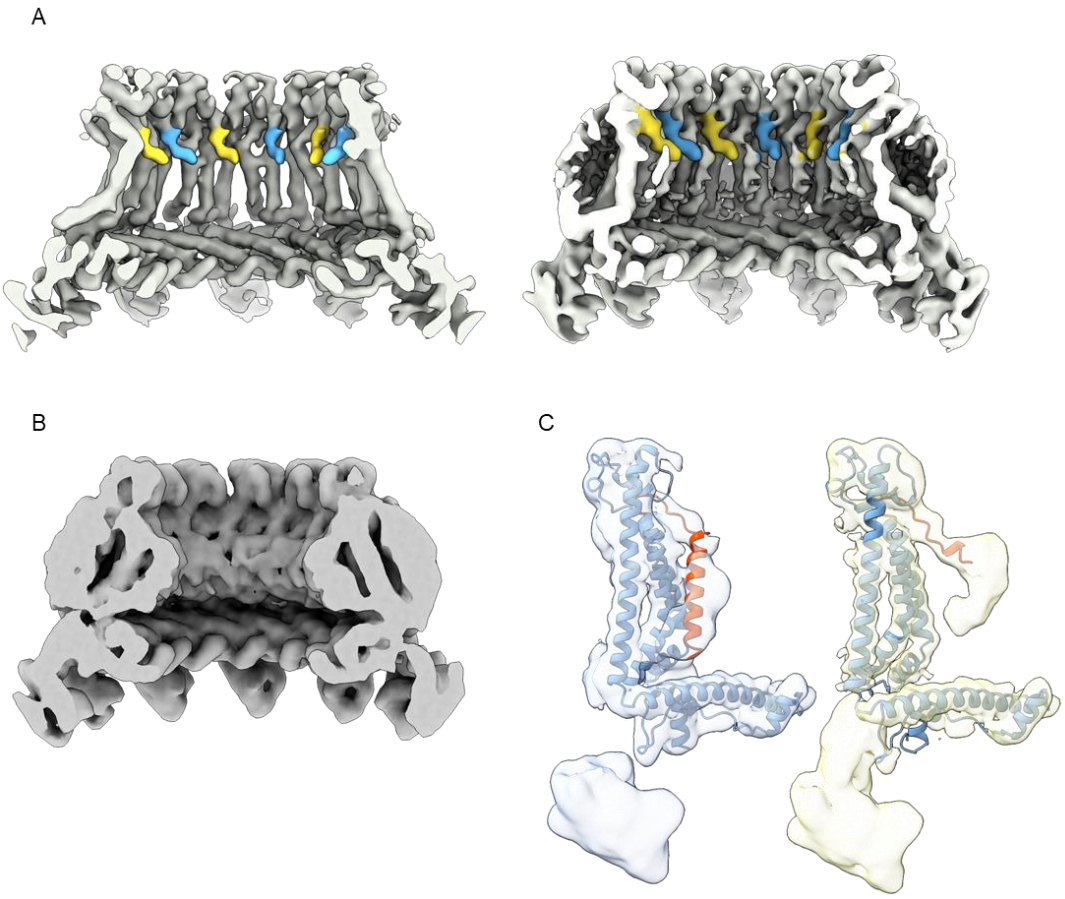

Figure 47. CALHM2 pore geometry. (**A**) Slices through the CALHM2 (left) channels viewed from within the membrane illustrating the density of pore lining TM1. View of CALHM2 at lower contour (right) shows extra density for this mobile element. Maps are low-pass filtered at 6 Å. Density corresponding to TM1 is colored. (**B**) Slice through the pore region of CALHM2. Shown is non-averaged density at low contour to highlight nonresolvable densities. (**C**) Superposition of single CALHM2 subunits in the densities illustrating conformational heterogeneity of TM1.

The observed density at the very end of TM1 aligns well with the lifted conformation of TM1 of CALHM6 (**Figure 46-A**), however the analysis of the map at the higher contour revealed the extra density in the region of TM1 (**Figure 47-A**). This density runs parallel to the TM bundle and is nearly perpendicular to the density projecting towards the pore (**Figure 47-A**). Whether this branching originates from two independent conformations of TM1 is unclear, however, it indicates the conformational heterogeneity of subunits. In an attempt to address this ambiguity, I employed symmetry expansion followed by signal subtraction and 3D variability analysis of individual CALHM2 subunits (**Figure 43-C)**. This approach separated two discrete end states, one with TM1 density projecting towards the pore and the other with more prominent extra density projecting parallel to the transmembrane domain, indicating that they represent two different conformations (**Figure 47-C**). Upon superimposing a CALHM2 subunit on both reconstructions, the former accommodates well the lifted end of TM1, which later surprisingly bends in opposite direction away from the pore (**Figure 47-C**). When superimposing a CALHM2 subunit onto the other reconstruction, the down conformation, resembles the orientation of TM1 observed in CALHM4 (**Figure 47-C**). However, the 3D classification of individual subunits failed to separate the two conformations (data not shown), which suggests that both states might either represent partialy resolved distinct regions of the same conformation or that we observe a range of conformations, which cannot easily be separated. E.g. the length of the not resolved TM1 and NTH allows to speculate that from the down conformation of TM1, the NTH could fold upwards along the pore, forming a flexible loop that reaches towards the extracellular region of TM1. Additionally, the analysis has been performed on a single subunit isolated from the adjacent protomers, however, another possibility that the extra densities originate from the neighbouring subunit cannot be excluded. Therefore caution should be exerted when interpreting these results. Nonetheless, the heterogeneity and flexibility are likely contributing factors to the inability to clearly resolve these regions and it is probable that the branched densities inside the pore represent intermediate states between the lifted and down conformation of TM1.

2.4.2.4 Binding of the sybody RA5 to CALHM2

In the map of the CALHM2/RA5 complex pronounced density is visible, which originates from the sybody RA5 binding to CALHM2 channels. **Figure 48** shows details of the binding of RA5 to CALHM2. The binding of sybodies to all eleven subunits is observed involving interactions with the cytoplasmic region of each subunit (**Figure 45-A,B and 48**).

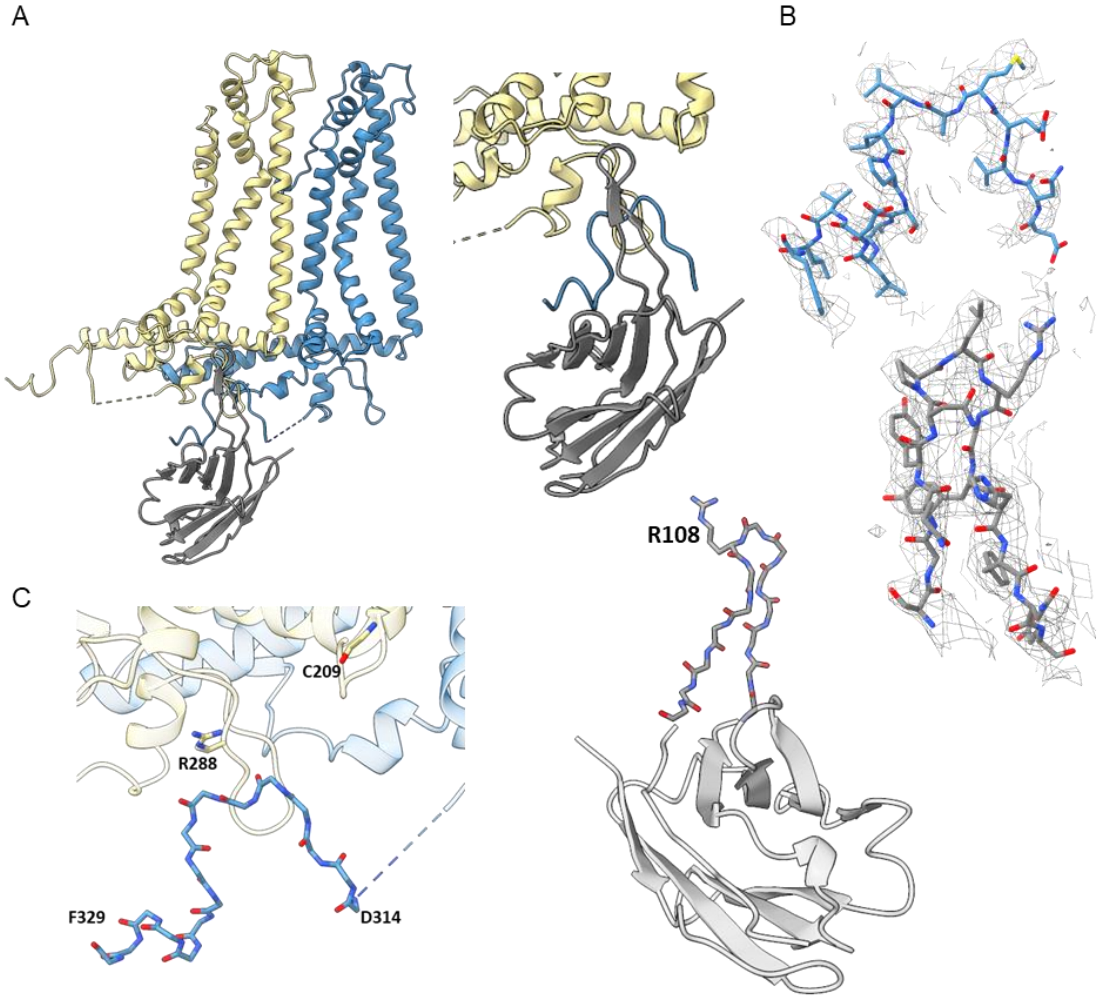

Figure 48. Details of RA5 sybody binding to CALHM2. (**A**) Ribbon representation of two CALHM2 subunits (yellow and blue) with one sybody (grey) bound shown. On the right close-up on the binding site, which involves both subunits is shown. (**B**) Cryo-EM densities of the CALHM2 epitope (blue) and RA5 paratope (grey). (**C**) View on the interaction interface. The interacting sites are shown as Cα trace with the sidechains of interacting residues displayed as sticks.

The high quality of the map allowed for a detailed interpretation of this interaction (**Figure 48-B**). The binding is mediated by the C-terminal loop of one subunit, which interacts with the cytoplasmic region of the adjacent subunit beneath the bundle of helices of the cytoplasmic part of CALHM2 (**Figure 48-A**) . The primary interaction between the sybody and the C-terminal loop of CALHM2 involves the backbone of the loop and the elongated CDR3 of the sybody (**Figure 48-A and C**). This extended interaction is further stabilized by ARG288 of the adjacent CALHM2 subunit, which is coordinated by carbonyl groups on CDR3 (**Figure 48-C**). Conversely, ARG108 of CDR3 is in turn coordinated by carbonyl groups of the CALHM2 cytoplasmic region (**Figure 48- C**). Interestingly, this epitope is poorly conserved and it concerns a region that was not well defined in CALHM4 and 6 structures, suggesting that the sybody binding is selective and stabilizes this flexible loop at the cytoplasmic rim of CALHM2.

2.4.2.5 Structure determination of CALHM4 in complex with sybodies

Note: The structure determination of CALHM4-sybody complexes has been performed by Martina Peter during her Master project carried out under the supervision of the author of the thesis

For the structure determination of CALHM4 in complex with sybodies, the sample was prepared in GDN. The sample at a concentration of 50 µM was then mixed with either of two sybodies gF2 or rD10 at a 1.5 molar excess and plunge frozen in a mixture of liquid propane and ethane. Datasets of 3,696 and 1,666 images were collected with the cryo-electron microscope for complexes with sybodies gF2 and rD10, respectively. **Figure 49 and 50** show details of the processing strategy. More explicit details of cryoEM data processing can be found in the Method section. In brief, picked particles were subjected to 2D classification followed by initial model generation with the imposition of C10 symmetry. In the cryoEM data processing, it is strongly discouraged to apply symmetry at early stages of the data analysis[69]. However, both datasets suffered from severe preferred orientation of the complexes with a predominance of side views, which was partially mitigated by the early imposition of symmetry (**Figure 49 and 50**). Thus we proceeded with 3D classification and refinement while imposing symmetry (**Figure 49 and 50**). The applied point groups were optimized to enhance the sybody densities (**Figure 49 and 50**). As a result, only dimers of decamers have been reconstructed, in contrast to the apo structure of CALHM4 where both undecameric and decameric channels have been observed at about equal ratios. This discrepancy likely does not reflect an absence of the larger assemblies in the sample, as such assemblies are observed in the 2D class averages (**Figure 50-B**). Instead, it is probably a result of the early imposition of C10 symmetry, which might have artificially masked sample heterogeneity. Additionally, the CALHM4-rD10 complex structure exhibits both the compression of the hemichannel and the absence of sybodies visualized at this channel when using a high contour (**Figure 50-E**). I ascribe this to the poor quality of the dataset and the applied symmetry. Despite these issues, this approach yielded maps at a global resolution of 3.7 Å and 4 Å for complexes of CALHM4-gF2 and CALHM4-rD10 respectively (**Figure 49-E and 50-E**). In both maps, the CALHM4 density is of high resolution

allowing the placement of the previously obtained model of CALHM4 (**Figure 49-E and 50-E**). In contrast, the respective densities of the sybodies are of lower resolution (**Figure 49-E and 50-E**), which could be a result of different reasons including the partial occupancy of binding sites, the intrinsic mobility of bound sybodies or the applied processing strategy. Although the fragmented density did not allow to build detailed atomic models of the sybodies, I was able to fit models of the their constant region to define their plausible orientation in the structure.

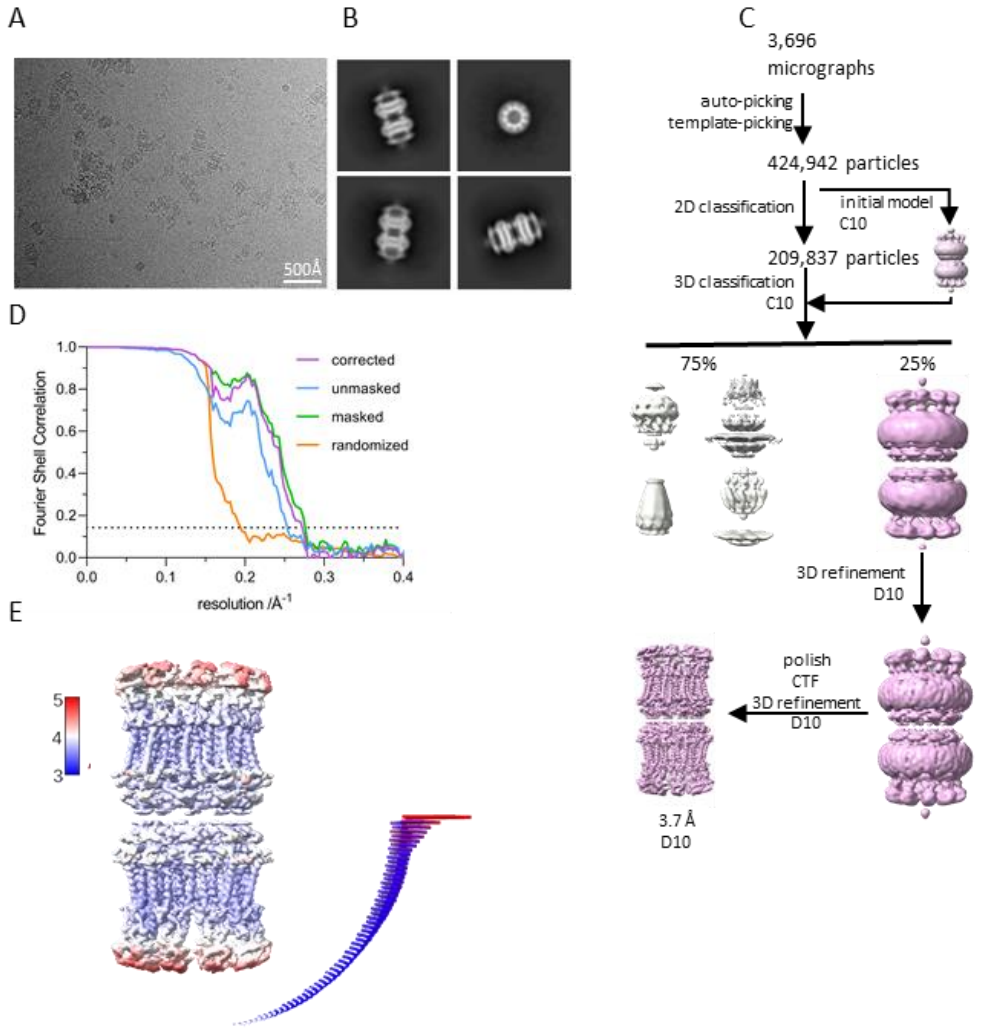

Figure 49. Cryo-EM reconstruction of CALHM4 in complex with sybody gF2. (**A**) Representative cryo-EM micrograph acquired with a Titan Krios microscope equipped with a K3 camera. (**B**) 2D class averages of the CALHM4-gF2 complex. (**C**) 3D classification allowed to isolate CALHM4-gF2 particles. The particles were further refined with iterative polishing, and 3D and CTF refinements. (**D**) FSC plot of the final refined undecameric unmasked (blue), masked (green), randomized (orange) and corrected for mask convolution effects (purple) cryo-EM density map of the CALHM4-gF2 complex. The resolution at which the FSC curve drops below the 0.143 threshold is indicated. (**E**) Final 3D reconstruction of CALHM4-gF2 complex colored according to local resolution.

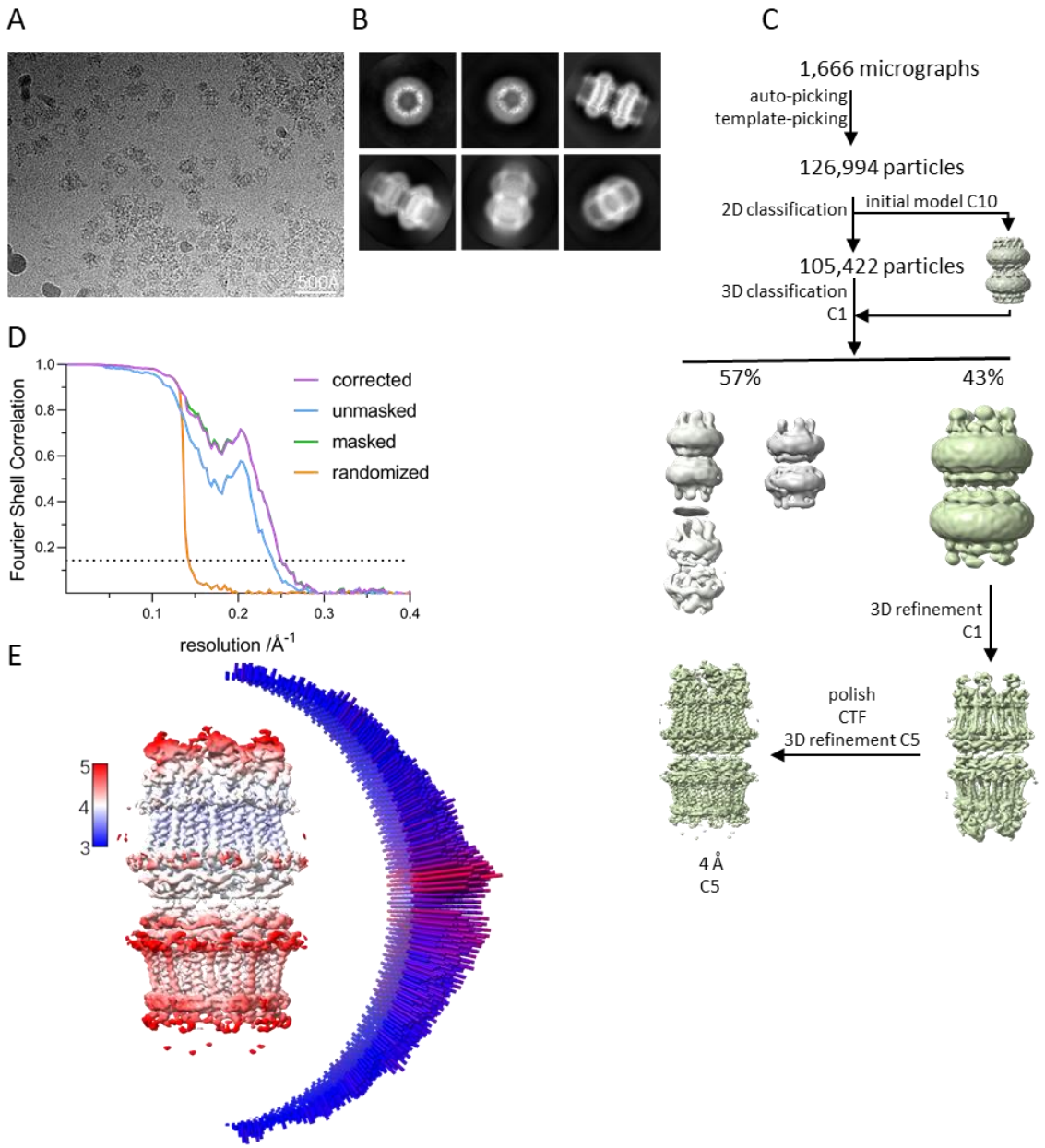

Figure 50. Cryo-EM reconstruction of CALHM4 in complex with sybody rD10. (**A**) Representative cryo-EM micrograph acquired with a Titan Krios microscope equipped with a K3 camera. (**B**) 2D class averages of a CALHM4-rD10 complex. (**C**) 3D classification allowed the isolation of high quality CALHM4-rD10 particles. The particles were aligned and their orientation was further refined by iterative polishing, and 3D and CTF refinements. (**D**) FSC plot of the final refined undecameric unmasked (blue), masked (green), randomized (orange) and corrected for mask convolution effects (purple) cryo-EM density map of the CALHM4-gF2 complex. The resolution at which the FSC curve drops below the 0.143 threshold is indicated. (**E**) Final 3D reconstruction of CALHM4-rD10 complex colored according to local resolution.

2.4.2.6 Binding of sybodies gF2 and rD10 to CALHM4

Figure 51-A and B show the final cryoEM maps of the CALHM4-gF2 and CALHM4-rD10 complexes. The maps revealed the presence of ten gF2 and five rD10 sybodies situated in the extracellular region of the channel (**Figure 51-A and B**). The structure and conformation of CALHM4 in both complexes is identical to the apo structure of this channel. Based on the fits of homology models, the CDR loops of both sybodies bind the extracellular region of CALHM4, in a slightly different manners (**Figure 51-C and D**). In case of gF2, all three CDR loops target the region connecting TM3 and TM4 of CALHM4 (**Figure 51-C**), therefore the epitope of gF2 is confined to a single CALHM4 subunit (**Figure 51-A and C**). In case of rD10, the epitope on CALHM4 includes the TM3-TM4 connecting region, which is targeted by CDR2 and CDR1 (**Figure 51-D**). In addition the interface between the subunits is targeted by CDR1 and CDR3. Such binding of rD10 has a remarkable consequence of preventing the binding of a second sybody to the adjacent subunit (**Figure 51-D**). Therefore, only five rD10 sybodies bind ten CALHM4 subunits in an alternating manner (**Figure 51-B**). Although the described binding mode is approximate, it is supported by a sequence analysis of the epitopes and paratopes within these models. The extracellular region of CALHM4 is enriched in polar residues. Similarly variable regions of CDR1 and CDR2 of both sybodies targeting this region predominantly consist of polar residues (**Figure 36-B**). In contrast, CDR3 of rD10 is composed of predominantly hydrophobic (**Figure 42**) residues and it extends towards the interface of subunits, which contains polar and hydrophobic residues, potentially engaging in interactions with corresponding residues on CDR3.

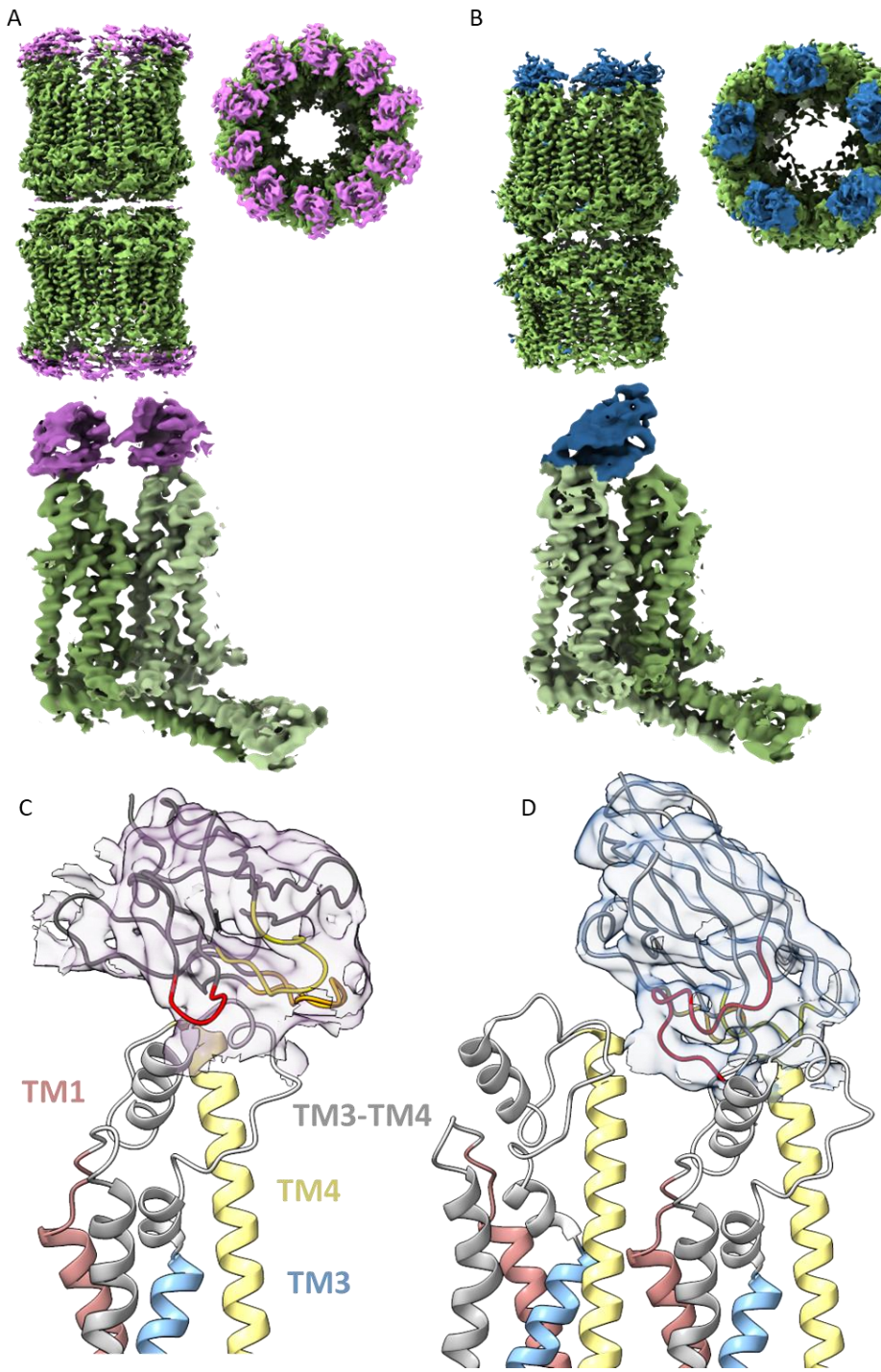

Figure 51. Details of rD10 and gF2 sybodies binding to CALHM4. Final cryoEM map of (**A**) CALHM4-gF2 and (B) CALHM4-rD10 complexes. The views are from within the membrane (left) the extracellular side (right) and on two neighboring subunits from with the pore (bottom). (**B**) Fitting of the homology model of (**C**) a concave sybody into the density corresponding to the gF2 sybody and of (**D**) a convex sybody into the density of rD10 sybody. The densities are blurred with a *b*-factor of 100. The regions of CDR1, 2 and 3 are colored yellow, orange and red respectively. The secondary structures of CALHM4 are labelled and color coded.

2.4.2.7 Selectivity determination by surface plasmon resonance

Note: The SPR measurements were performed by Marton Liziczai and Martina Peter

In order to selectively label individual CALHM homologues with sybodies, it was essential that they specifically bind their intended target and do not exhibit cross-reactivity. To assess whether the selected sybodies meet this criterion, surface plasmon resonance (SPR) measurements were performed. **Figure 52** shows the results of the SPR measurement for sybodies RA5 (targeting CALHM2) and gF2 (targeting CALHM4) against both CALHMs. While the suboptimal quality of the sample prevented a quantitative determination of the affinity for sybody RA5 (**Figure 52-A**), the obtained results did confirm the binding of both sybodies to their targets and, importantly, no cross-reactivity to the second CALHM paralog was observed for any of the two sybodies distinguishing them as subunit selective binders (**Figure 52**).

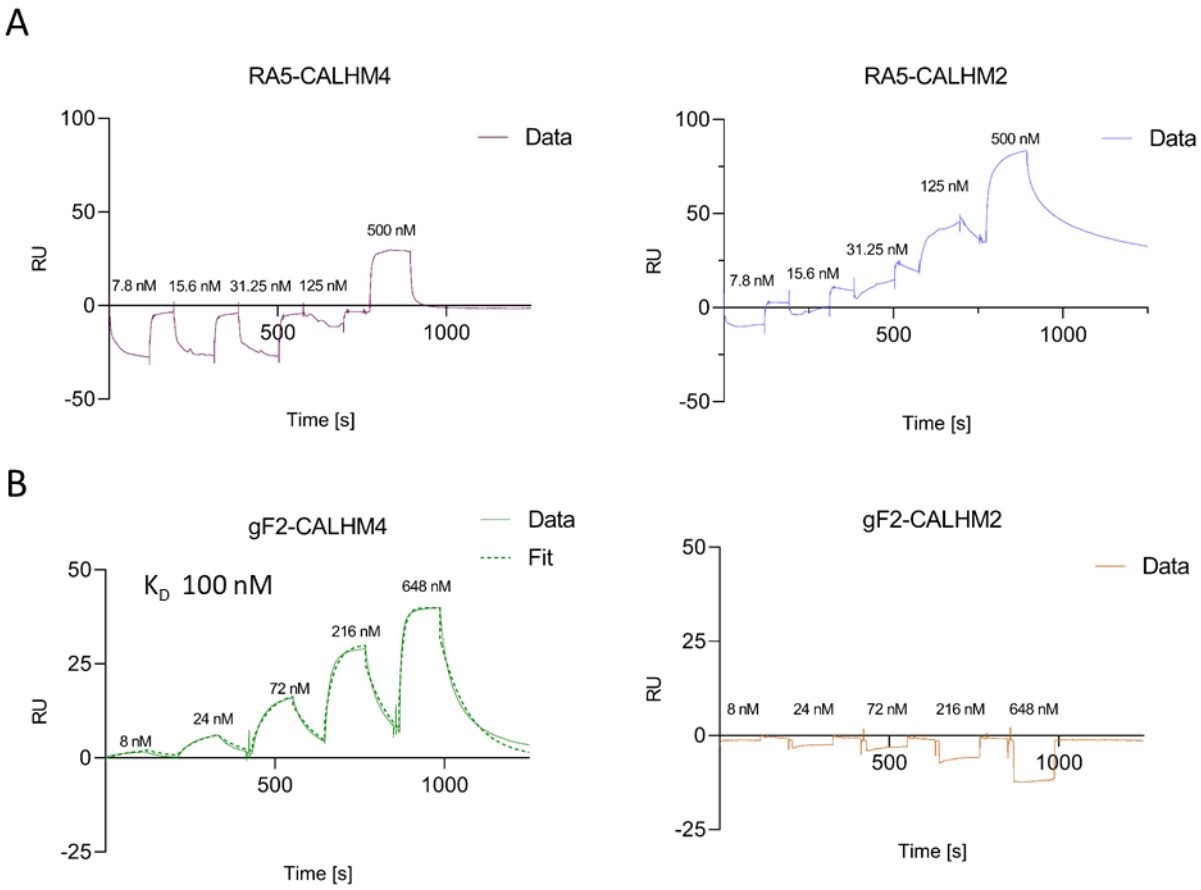

Figure 52. SPR measurement of the interaction of sybodies gF2 and rD10 with CALHM2 and CALHM4. (A) Sensograms of sybody RA5 against CALHM2 (left) and CALHM4 (right). (B) Sensograms of sybody gF2 against CALHM4 (left) and CALHM2 (right). Solid lines show the measured response curve, dotted lines the fits to a 1:1 binding model. The injected concentrations are indicated. The determined affinity of sybody gF2 is indicated.

2.4.2.8 Summary and conclusion on homomeric CALHM-sybody complex structures

Three sybodies have been structurally characterized in complex with their CALHM targets, RA5 targeting CALHM2, and rD10 and gF2 targeting CALHM4. The structure determination of the CALHM2-RA5 complex provided novel insight into the structural properties of CALHM2, which were not obtained in my previous studies on the apo CALHM2 due to a preferred orientation of the protein on the grids. Consequently, it is safe to assume that the binding of the sybodies reverses the preferred partition of the cytoplasmic region of CALHM2 to the air water interface[70] resulting in a desirable random orientation of particles. The structure of CALHM2 is generally similar to that of the two other CALHM homologues CALHM4 and CALHM6 but, in contrast to CALHM4, the conformations of the pore lining TM1 and NT are not well defined due to their large flexibility. The RA5 targets cytoplasmic region of CALHM2 and the epitope is constituted by two subunits. In contrast to RA5 targeting intracellular region of CALHM2, sybodies rD10 and gF2 target the extracellular region of CALHM4. While the epitope of gF2 is confined to a single CALHM4 subunit, the epitope of rD10 is located at the extracellular interface of adjacent subunits. Importantly, the binders are strongly selective towards their respective targets and do not exhibit cross-reactivity between the two homologues.

For the purpose of resolving the detailed subunit distribution in heteromeric CALHM2/4 complexes, it is essential that the sybody epitope is confined to a single subunit and thus not affected by the pairing of homologues subunits. Among the tested sybodies, only gF2 meets this criterion. Therefore, gF2 has been selected as binder assisting the structure determination of CALHM2/4 complexes. Additionaly, we decided to determine the structure in a presence of both gF2 and RA5 sybodies, leveraging their opposite localizations and facilitating the characterization of the potential heterogeneity of assemblies.

2.4.3 Structure determination of heteromeric CALHM2/4 channels

For the structure determination of CALHM2/4 complexes, the sample has been purified using tandem affinity chromatography followed by size-exclusion chromatography in GDN. Two samples were prepared at a final concentration of approximately 45 µM of CALHM proteins. One sample was supplemented with a 1.5 molar excess of gF2, while the second sample contained both, a 1.5 molar excess of gF2 and a 2.5 molar excess of RA5. Large dataset were collected for both samples and a similar data processing strategy was employed. **Figures 53** and **54** show the details of the processing. First, particles were picked and subjected to 2D classification, which yielded single oligomeric channels and dimers of channels resembling those of homomeric CALHM4 (**Figure 53-B and 54-B**). In the 2D classes, densities of sybodies were apparent, which varied in number between classes, indicating a heterogeneity of assemblies (**Figure 53-B and 54-B**). 3D classification further confirmed the heterogeneity of the sample and revealed three features: the presence or absence of dimerization of channels, varying oligomeric states of channels ranging from decamers to undecamers and different subunit stoichiometries that could not be unambiguously defined at this stage (**Figure 53-B and 54-B**). Attempts to refine the individual assemblies did not yield high resolution reconstructions, likely for two

main reasons. Firstly, the high number of different assemblies resulted in a low number of particles per assembly, which hampered the refinement. Secondly, the heterogeneity within the classes was not completely removed, which is evident in the different level of sybody densities within an oligomer (**Figure 53-B and 54-B**), indicating that particles with subunits that do not bind the sybody contribute to the reconstruction. Thus, the variation of the contour of the map does in many classes cause the emergence or disappearance of additional sybody densities, further supporting that channels of different stoichiometry contribute to the class. Additionally, some of the reconstructions display ambiguous densities of CALHM subunits that prevented the determination of the exact oligomeric states of these channels (**Figure 53-B and 54-B**). Due to the described issues, a different approach has been taken to obtain a high-resolution structure. In the first step to reduce the heterogeneity, particles of dimers of channels have been excluded at the level of 2D classification and only particles featuring single channels were subjected to an ab initio reconstruction (**Figure 53-B and 54-B**). It is important to note that this approach excluded only particles of dimers in the side view orientation. A similar approach was not applied to sorting of the top views, except one class in CALHM2/4-gF2-RA5 dataset (**Figure 54-B**) which clearly exhibited predominant occupation of the channels by CALHM4, which we suspected to promote dimerization. After ab-initio reconstruction, to further sort out spurious particles, the remaining particles were subjected to heterogenous refinement which separated undecameric and dodecameric assemblies with similar distributions in both datasets (**Figure 53-B and 54-B**). The set of predominant undecameric particles was further improved using hetero- and non-uniform refinement (**Figure 53-B and 54-B**). This approach resulted in reconstructions at a global resolution of 3.9 Å for CALHM2/4 complexes with gF2 only, and 3.26 Å for complexes containing both gF2 and RA5 (**Figure 53-C and 54-C**). Those reconstructions partially resolved the subunit pattern in the channels, although some positions exhibited lower local resolution (**Figure 53-D and 54-D**). Specifically, two subunits showed lower resolution, likely due to a mixed occupancy of those positions by either of the two homologues (**Figure 53-D and 54-D**). Further classification of those particles did not yield a better resolution nor did it provide new information. Despite the compromised resolution, it was possible to unambiguously assign the subunits in ten out of eleven positions (**Figure 55**). Where possible, respective subunit structures obtained from homomers were fitted into the densities, except for positions showing novel conformations, which were built de novo. The detailed description of model building can be found in the Method section. Although the employed processing strategy did not allow to fully resolve discrete states of the channels, it reveals predominant assemblies and their structural characteristics. Therefore, I proceed to describe the diversity of assemblies based on the results of 3D classification and the detailed features of CALHM2/4 channels based on the obtained high-resolution structures.

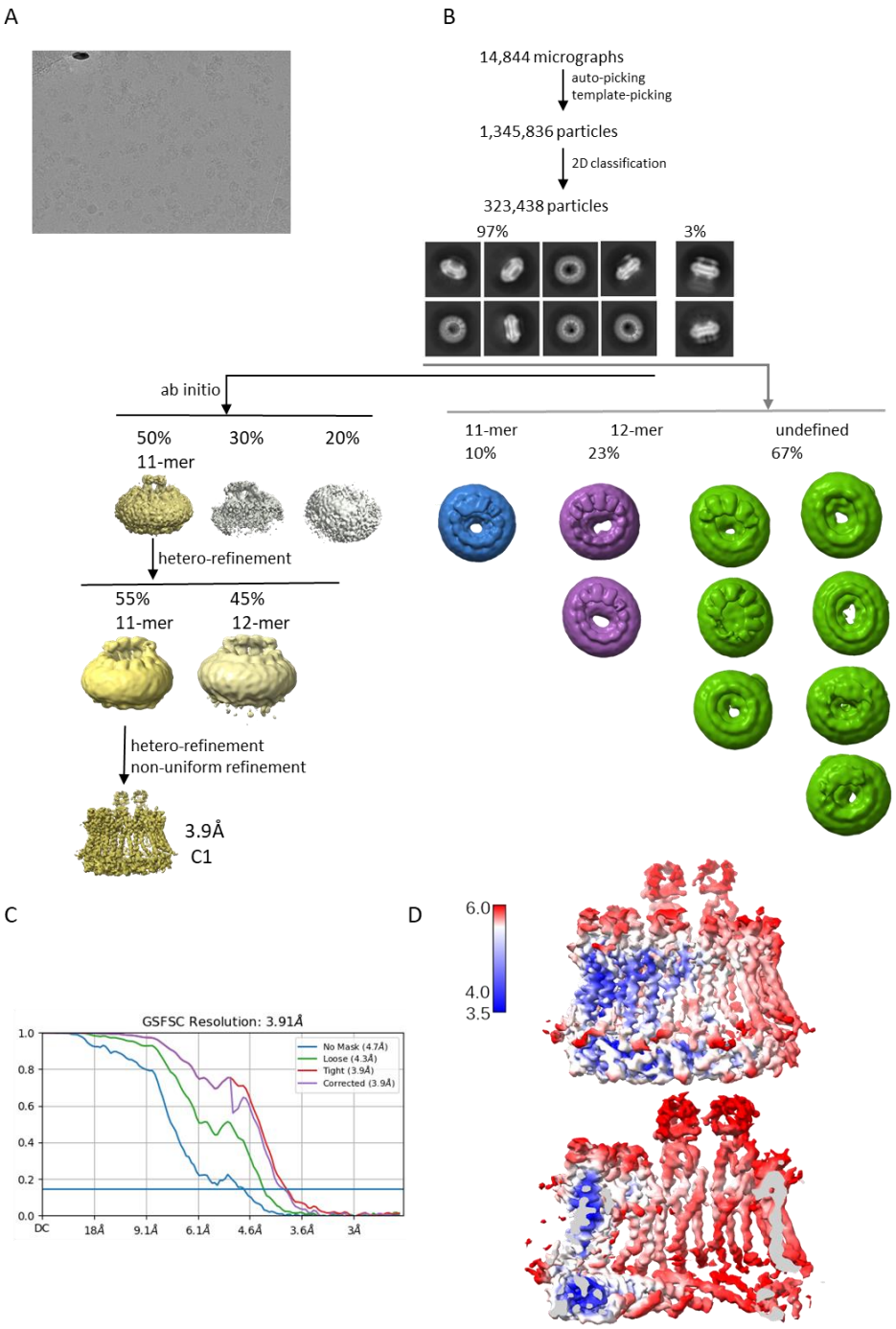

Figure 53. Cryo-EM reconstruction of CALHM2/4 in complex with sybody gF2. (**A**) Representative cryo-EM micrograph acquired with a Titan Krios microscope equipped with a K3 camera. (**B**) 2D class averages allowed for the initial separation of populations of single channels and their dimers. 3D classification on all high quality particles allowed to partially further separate different assemblies. Ab initio reconstructions on particles featuring single channels resulted in low resolution maps of undecameric assemblies. Further steps of heterogenous refinement have separated undecamers and dodecamers. The smaller channels were refined to high resolution via several cycles of hetero- and non-uniform refinement. (**C**) FSC plot of the final refined unmasked (blue), masked (green), randomized (orange) and corrected for mask convolution effects (purple) cryo-EM density maps of an undecameric CALHM4-gF2 complex. (**D**) Final 3D reconstruction of a CALHM2/4-gF2 complex colored according to local resolution.

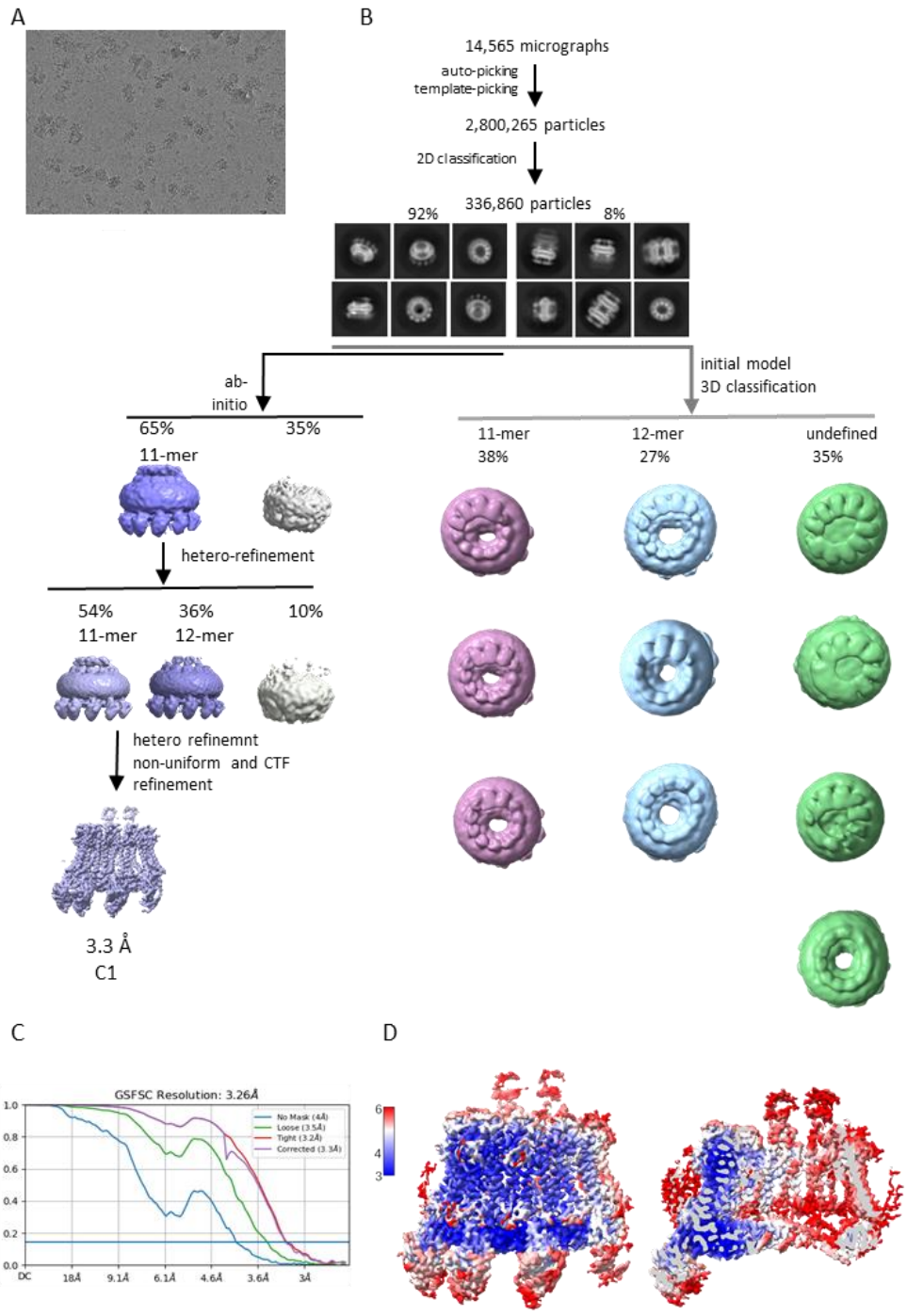

Figure 54. Cryo-EM reconstruction of CALHM2/4 in complex with sybodies gF2 and RA5. (**A**) Representative cryo-EM micrograph acquired with a Titan Krios microscope equipped with a K3 camera. (**B**) 2D class averages revealed populations of single channels and dimers of channels. 3D classification of all the particles allowed for a partial separation of different assemblies. Ab-initio reconstructions on particles featuring single channels yielded undecameric assemblies. The subsequent heterogenous refinement separated undecameric and dodecameric channels. The undecameric assemblies were further improved to high resolution with hetero, non-uniform and Ctf refinement. (**C**) FSC plots of the final refined unmasked (blue), masked (green), randomized (orange) and corrected for mask convolution effects (purple) cryo-EM density maps of an undecameric CALHM2/4-gF2-RA5 complex. (**D**) Final 3D reconstruction of the CALHM2/4-gF2-RA5 complex colored according to local resolution.

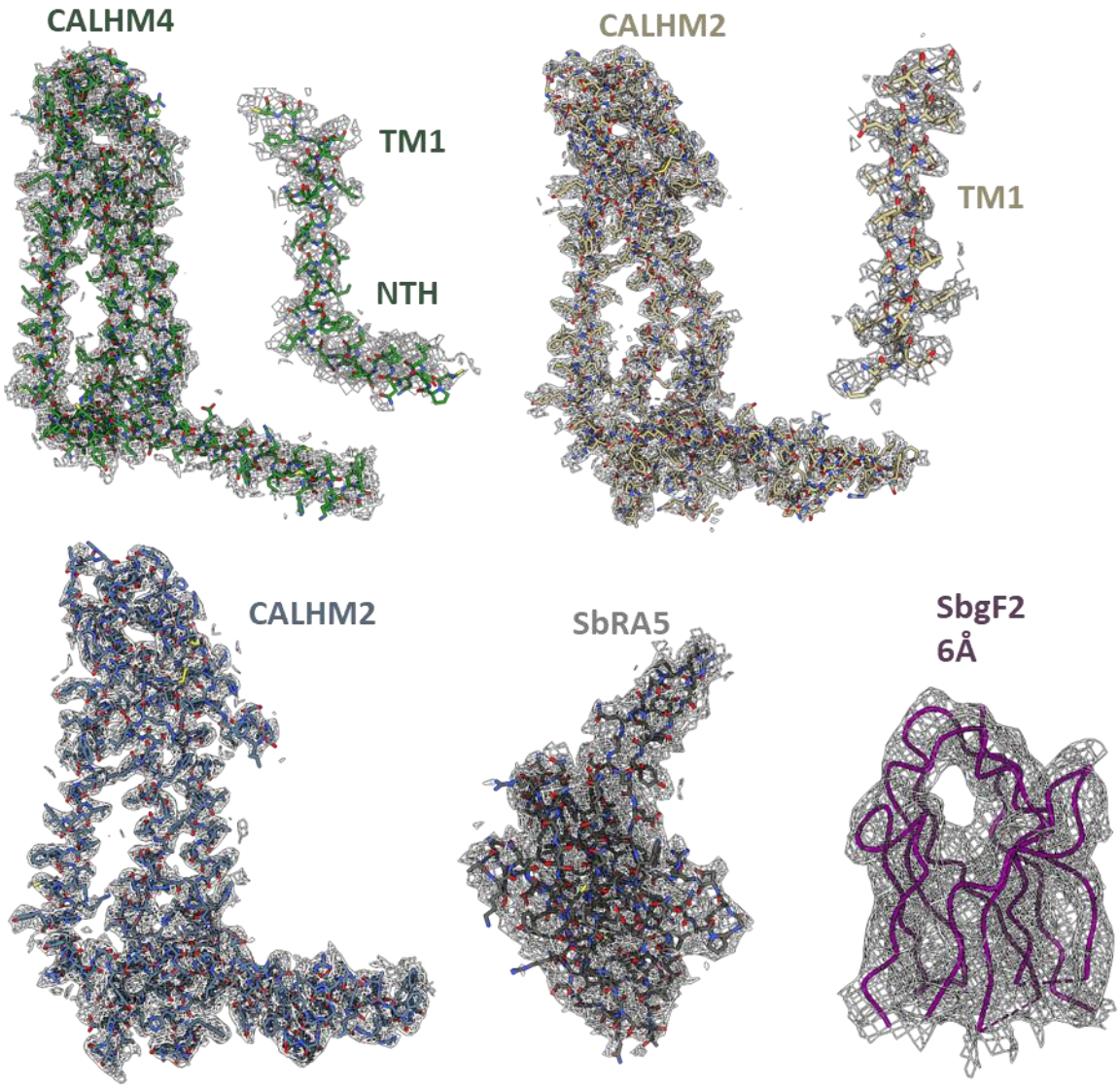

Figure 55. Cryo-EM density of CALHM2/4. Cryo-EM density of selected regions of the undecameric CALHM2/4 structure superimposed on the model. Proteins and structural elements are indicated.

2.4.4 Features of heteromeric CALHM2/4 assemblies

The two paralogs CALHM2 and CALHM4 form heteromeric assemblies with diverse oligomeric organizations and subunit stoichiometries (**Figure 53 and 54**). In both datasets obtained in this study, decameric, undecameric and dodecameric assemblies were observed although with uneven distribution (**Figure 53 and 54**). In the complexes with one sybody targeting CALHM4, the predominant assemblies are undefined, contrasting the distribution in the complex with two sybodies, each targeting one of the two paralogs, were undecamers and dodecamers constitute the predominant assemblies (**Figure 53 and 54**). It is apparent that the accuracy in the determination of the distribution in the CALHM2/4 complex with gF2 is severely compromised by heterogeneous assemblies, which likely contain a mixture of particles of the three different oligomeric states which were difficult to separate. However, a similar distribution is expected in both datasets. Since the heterogeneity is better resolved in the complex containing two sybodies (**Figure 53-B and 54-B**), I will continue to describe the general properties of CALHM2/4 channel assemblies based on the data obtained for CALHM2/4_gF2_RA5 complexes. These assemblies can be divided into two main groups, one predominantly composed of CALHM4 subunits containing a smaller fraction of the total particles and the other being predominantly composed of CALHM2 subunits, which constitute the majority of particles. **Figure 56** illustrates the representative assemblies of CALHM2/4 channels.

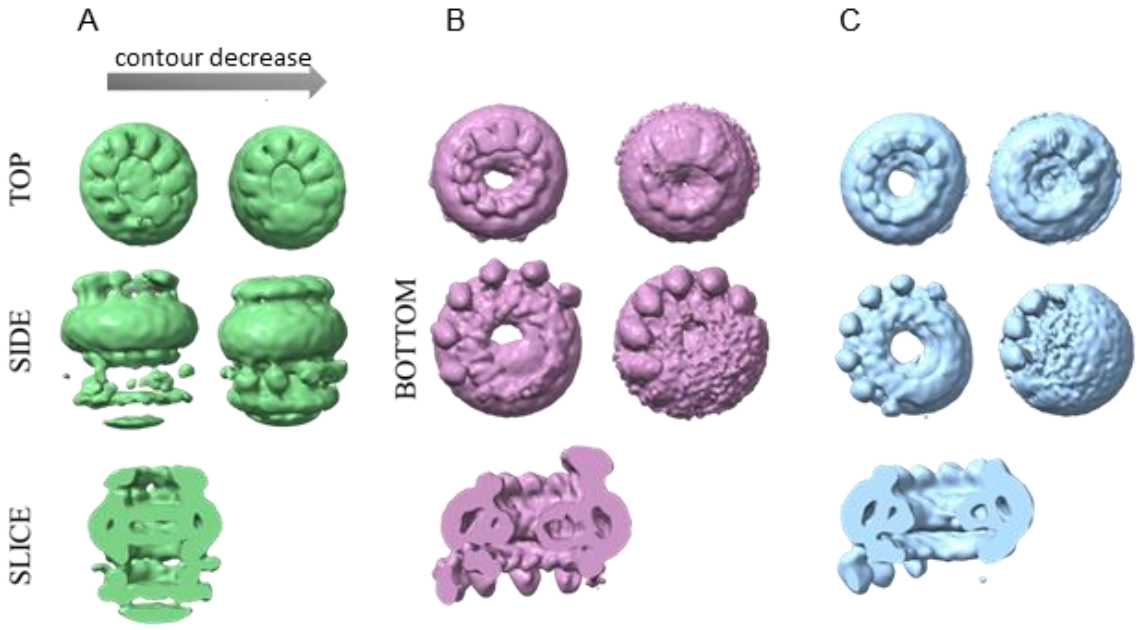

Figure 56. Representative assemblies of CALHM2/4 channels in complex with gF2 and RA5 sybodies. Reconstructions of 3D classes of (**A**) Oligomers dominated by CALHM4, (**B**) undecameric assemblies dominated by CALHM2 and (**C**) dodecameric channels dominated by CALHM2. Shown are reconstructions at two contour levels to illustrate the heterogeneity of sybody positions. The arrow indicates the decrease of the contour of the maps. The directions of the views are indicated.

The predominance of distinct homologues in assemblies has consequences on the oligomeric states and the dimerization of the observed particles (**Figure 54-B and 56**). The CALHM4-dominated channels are not well resolved, including the density of the bound sybodies (**Figure 54-B and 56-A**). Nonetheless, the number of the extracellular sybody densities indicate predominantly decameric assemblies of those channels, which dimerize at their intracellular parts (**Figure 54-B and 56-A**). Although the low quality of these reconstruction prevents the accurate assignment of subunits, the presence of CALHM2 in those assemblies is indicated by the unequal strength of the densities of gF2 sybodies (**Figure 54-B and 56-A**). Additionally, sybody-like density at the interface of the dimer, corresponding to the intracellular region of the channels, which are targeted by anti-CALHM2 sybodies, is clearly visible in the 2D class averages (**Figure 54-B and 56-A**), which indicates the presence of CALHM2 subunits in these particles. Moreover, when analyzing CALHM4-dominant channels reconstructions at the low contour, fragmented density at the intracellular side of the channel emerges (**Figure 56-A**). This density likely originates from the dimeric assemblies of the same channels that are clearly defined in 2D classes (**Figure 54-B**). The low quality of the densities of the interacting channel is presumably the result of a compromised dimerization due to the presence of CALHM2 subunits. The CALHM2 dominated assemblies are considerably better resolved, which allows for a more detailed analysis (**Figure 54-B and 56-B and C**). Two oligomeric assemblies belonging to this group either form undecamers or dodecamers (**Figure 54-B and 56-B and C**). Similar to CALHM4-dominated reconstructions, a variable strength of the sybody density is observed, where the apparent number of CALHM4 subunits ranges between two to five. Notably, while assemblies not exhibiting any strong gF2 density are also observed (**Figure 54-B and 56- C**), residual density at the extracellular site observed at low contour together with similar weak density of RA5 in the same position (**Figure 56-C**) indicates a partial occupancy of either homologue which could not be efficiently separated and thus leads to a larger heterogeneity. The best resolved classes constitute undecamers with either two or three CALHM4 subunits, which indicates that such assemblies would be thermodynamically most stable and thus dominate the distribution. Despite the differences in oligomeric states and relative abundances of subunits there is a common feature in that subunits of the same kind are found to cluster (**Figure 53, 55 and 56**). Additionally, it was found that the nature of the subunit and its position in the channel correlates with distinct pore conformations (**Figure 56**).

2.4.5 Features of a CALHM2/4 consensus structure

To describe detailed features of heteromeric CALHM channels, I have attempted to obtain a high resolution consensus structures of both datasets (containing either one or two different sybodies) (**Figure 53 and 54**). Despite resulting from the averaging of slightly different stoichiometries (i.e. from channels containing either 2 or 3 CALHM4 subunits), these consensus structures provide detailed insight into the conformational properties of the complex. Both consensus structures are very similar and the structure described here is generally based on the CALHM2/4-gF2-RA5 complex unless stated otherwise. **Figure 57** shows the final cryoEM map and the corresponding model of a heteromeric CALHM2/4 channel containing the two different sybodies. The overall architecture of the channel resembles that of homomeric CALHM2 channels and consists of eleven CALHM protomers (**Figure 57)**. Within this assembly, strong density of two extracellular gF2 sybodies label a pair of CALHM4 subunits, whereas equally strong density of six intracellular RA5 sybodies indicate the arc-like arrangement of six CALHM2 subunits (**Figure 57-A)**. Three positions surrounding a pair of CALHM4 subunits, one in the anticlockwise direction and two in the clockwise direction (when viewed from the extracellular side) lack sybody densities (**Figure 57-A)**. Although the sybody is absent in the anticlockwise position, the resolution in this region allows for the clear identification of CALHM2 (**Figure 55)**. In contrast, the subunit located counter-clockwise to CALHM4 cannot be clearly defined and likely results from the averaging of partially occupied CALHM2 and 4 subunits, which would average out the sybody density **(Figure 54-D and 57-A)**. Hence no sybody density is visible in this position (**Figure 57-A**). The subsequent subunit following this position contains CALHM2 and the absence of its respective sybody is probably due to the heterogeneity its neighbour which would contributes part of the epitope (**Figure 57-A**).

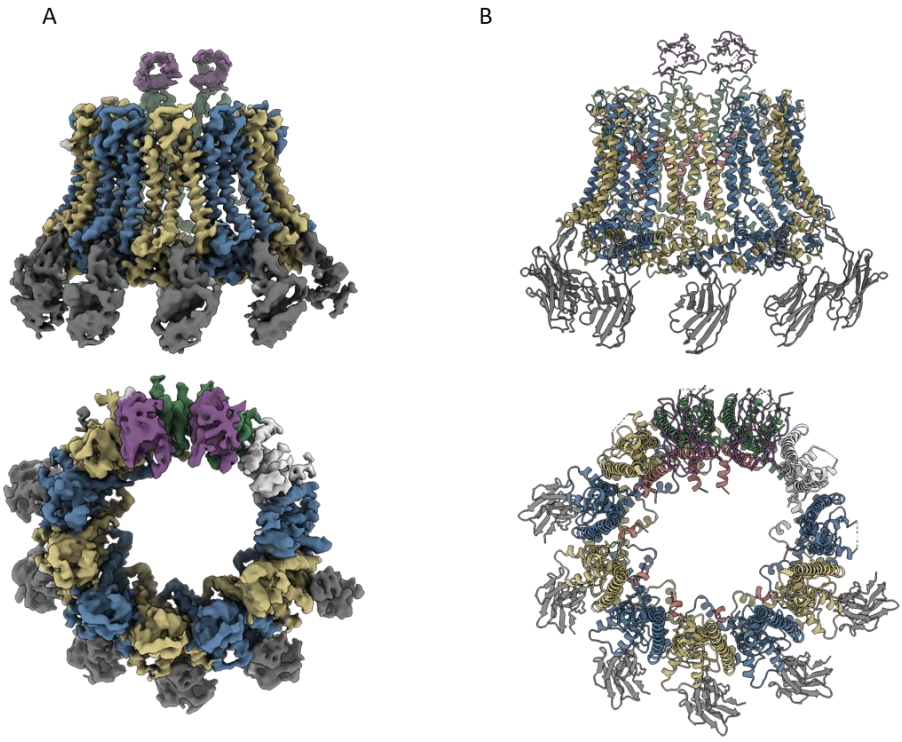

Figure 57. CALHM2/4 structure in complex with sybodies gF2 and RA5. (**A**) Cryo-EM density of undecameric CALHM2/4 channels in complex with both sybodies at a global resolution 3.34 Å. (**B**) Ribbon representation of the undecameric CALHM2/4 in complex with bound sybodies. The views are from the membrane (top) and from extracellular site (bottom). CALHM2 subunits are colored in blue and yellow, CALHM4 subunits in green and one unassigned subunit in white. gF2 sybodies are colored purple and RA5 sybodies in grey.

Three pairs of subunits with unique interfaces can be distinguished in the heteromeric CALHM2/4 channel relating either the same or two different subunits which are depicted in **Figure 58**. The interface between both homomeric and heteromeric pairs of CALHM proteins involves contacts between TM2, TM4, and CTH of interacting subunits (**Figure 58**). However, in all cases, the conformation of the pore lining regions vary depending on the type of subunit and its location in the channel, which results in four unique interfaces (**Figure 58**). TM1 helices in the pair of CALHM4 subunits (positions A and B) adopt a downward conformation parallel to the pore axis as found in the homomeric CALHM4 structure (**Figure 58 and 59-B**). In contrast, the conformation adopted by the TM1 of CALHM2 subunits varies depending on their environment in the channel.

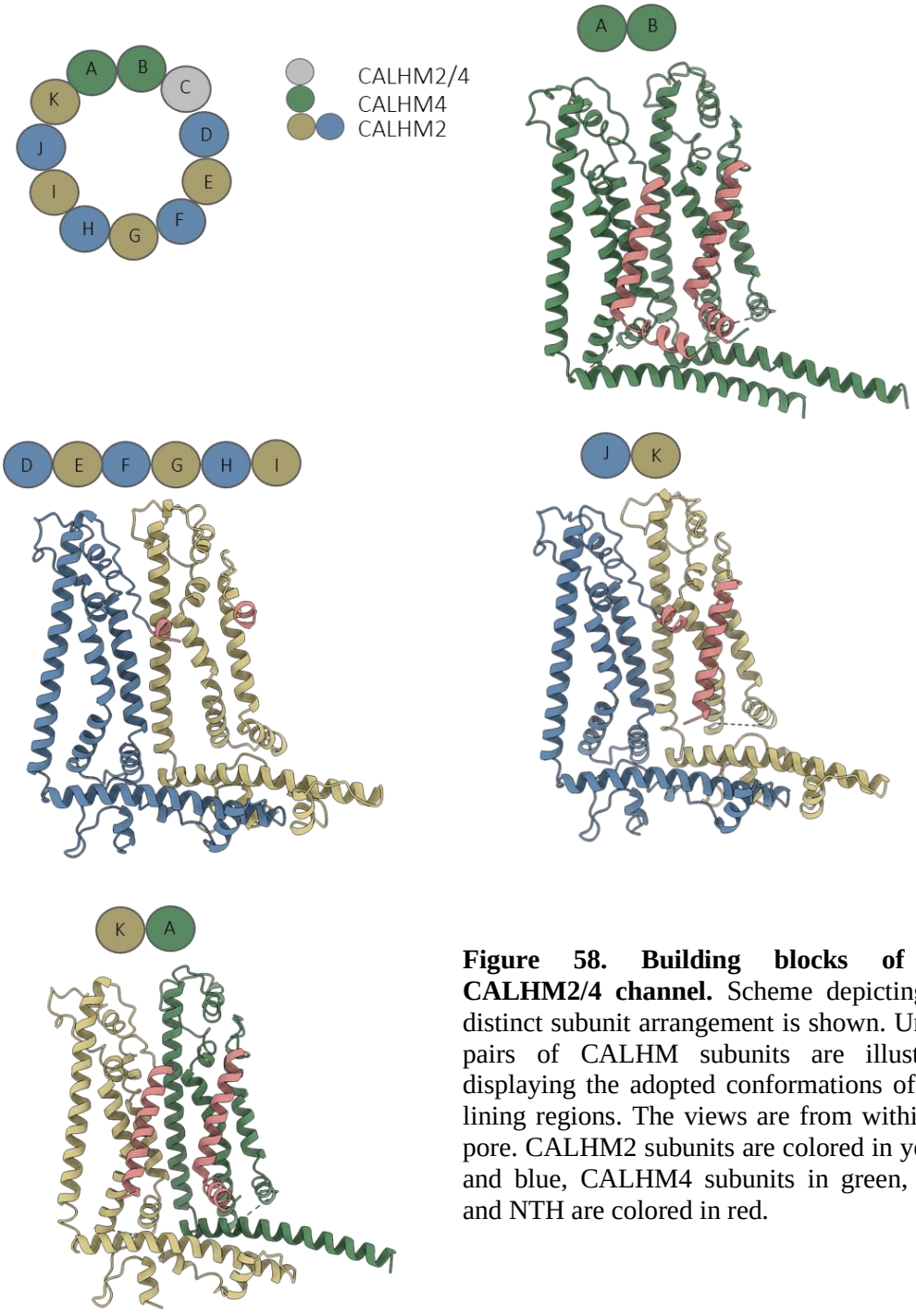

Figure 58. Building blocks of the CALHM2/4 channel. Scheme depicting the distinct subunit arrangement is shown. Unique pairs of CALHM subunits are illustrated displaying the adopted conformations of pore lining regions. The views are from within the pore. CALHM2 subunits are colored in yellow and blue, CALHM4 subunits in green, TM1 and NTH are colored in red.

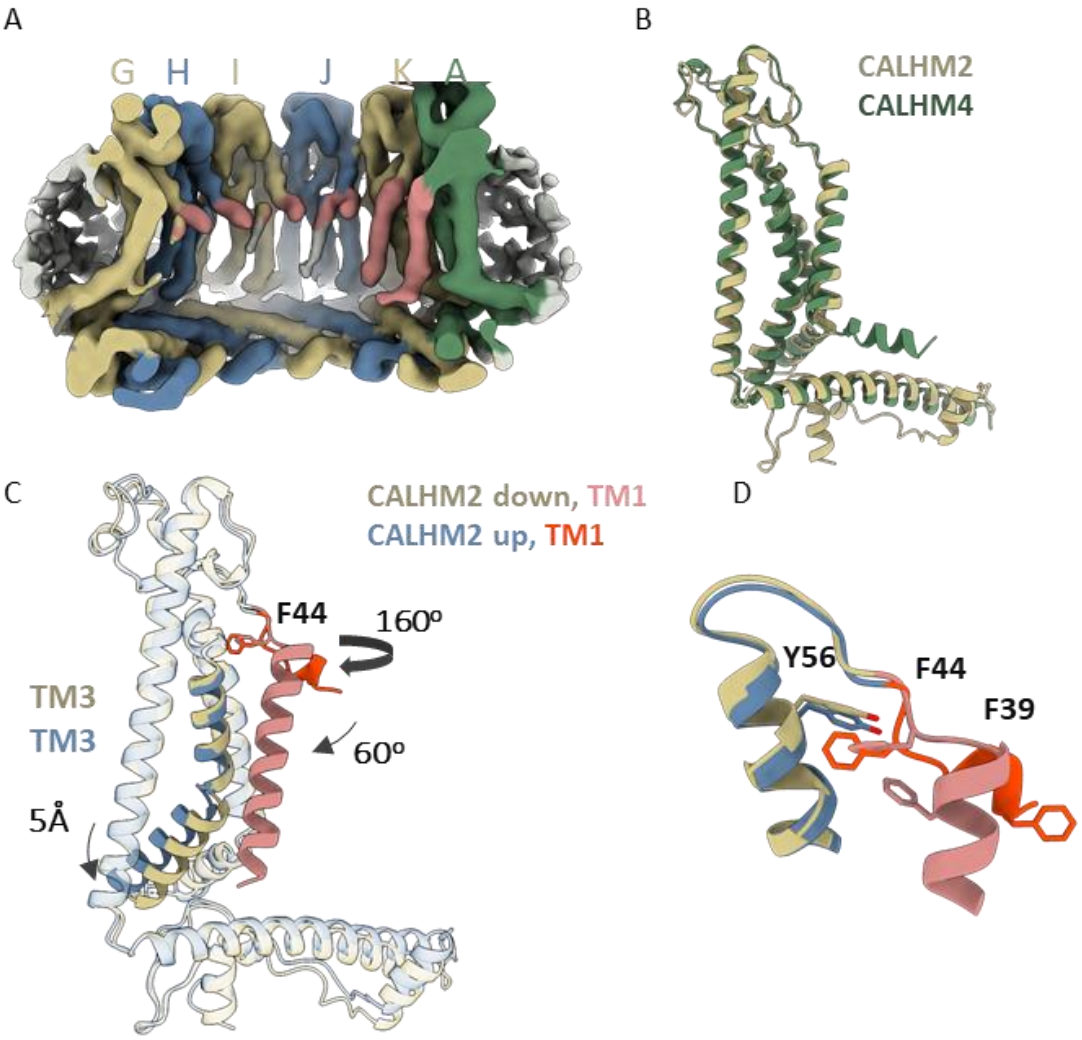

Figure 59. Subunits of the CALHM2/4 channel. (**A**) Slice through the channel illustrating the heterogeneity of TM1 conformations in CALHM2 subunits. (**B**) Superposition of CALHM2 and 4 subunits in downward conformations. (**C**) Superposition of CALHM2 subunits in lifted and downward conformations. The conformational rearrangements are indicated. Phenylalanine 44 is shown as sticks. (**D**) The close-up on the CALHM2 extracellular region involved in the conformational change. Residues contributing to the cluster of aromatic residues are shown as sticks.

Seven adjoining CALHM2 subunits distal from CALHM4 (positions D-J) exhibit predominantly lifted conformations as evidenced by the protrusion at the end of TM1 (**Figure 48 and 59-A**). The same conformation was previously observed in homomeric CALHM2 channels. In both cases, the NT and TM1 regions display large flexibility and a 'branching' of the density close to the end of TM1 indicates heterogeneity of upward and downward conformations of this mobile unit (**Figure 59-A**). Interestingly, there is an apparent gradient in the extent of the extra 'downward' density, which steadily increases in CALHM2 positions that are closer to CALHM4 subunits (**Figure 55 and 59-A**). This observation is more pronounced in the structure of the complex containing only the anti-CALHM4 gF2 sybody. Evidently, the CALHM2 subunit next to CALHM4 fully adopts a downward conformation (position K) (**Figure 58 and 59-A**). This conformation of CALHM2 resembles that of CALHM4, though in this case, the NTH region is not resolved indicating its higher flexibility (**Figure 59-B**). Despite the difference in the flexibility of NTH, the two subunits superimpose with a RMSD of 0.933Å (for 123 pruned residues) (**Figure 49-B**). Compared to CALHM2 in the upward conformation, TM1 undergoes a rotation around the hinge close to phenylalanine 44 and descends towards the bundle of helices where it loosely interacts with TM3 and extracellular region of TM2 (**Figure 59-C**). Similar to CALHM4, the interaction in the extracellular region involves a cluster of aromatic residues, which is disrupted in the lifted conformation as previously observed in the CALHM6 structure (**Figure 59-D**). Additionally, there is a change in the position of TM3, which moves towards the channel axis, accompanying the downward relocation of TM1 (**Figure 59-C**). This conformational change may explain the weaker density observed for the sybody in this position (**Figure 57-A**) as the descents of TM3 might lead to a steric clash with the epitope of the sybody, thereby potentially reducing its binding affinity (**Figure 60**). Consequently, there are two unique interfaces formed, one relating CALHM2 subunits in the up- and downward conformations (positions J and K) and a heteromeric interface between CALHM2 and CALHM4 both in downward conformations (positions K and A) (**Figure 59**).

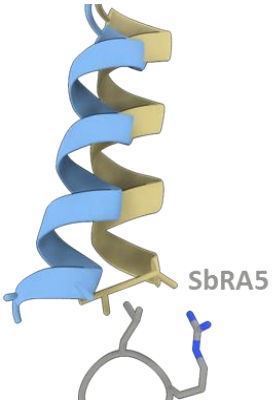

Figure 60.
Superposition of the TM3 helices of CALHM2 undergoing conformational change. Shown in grey is a part of the sybody RA5 paratope. Colour coding like in Figure 59.

2.4.6 Pore geometry of heteromeric CALHM2/4 channels

The different conformations of the pore residing N-terminal and TM1 regions adopted in heteromeric CALHM2/4 channels lead to unique features in its pore region. **Figure 61** shows properties of this pore ,which is asymmetric due to the downward conformations of CALHM4 and the adjoining CALHM2 subunit, and the remaining CALHM2 subunits residing in a predominant upward conformation (**Figure 59 and 61**). As observed in homomeric structures of CALHM4, the pore lining residues of CALHM4 and CALHM2 in a downward conformation share a generally hydrophobic character (**Figure 61-B**).

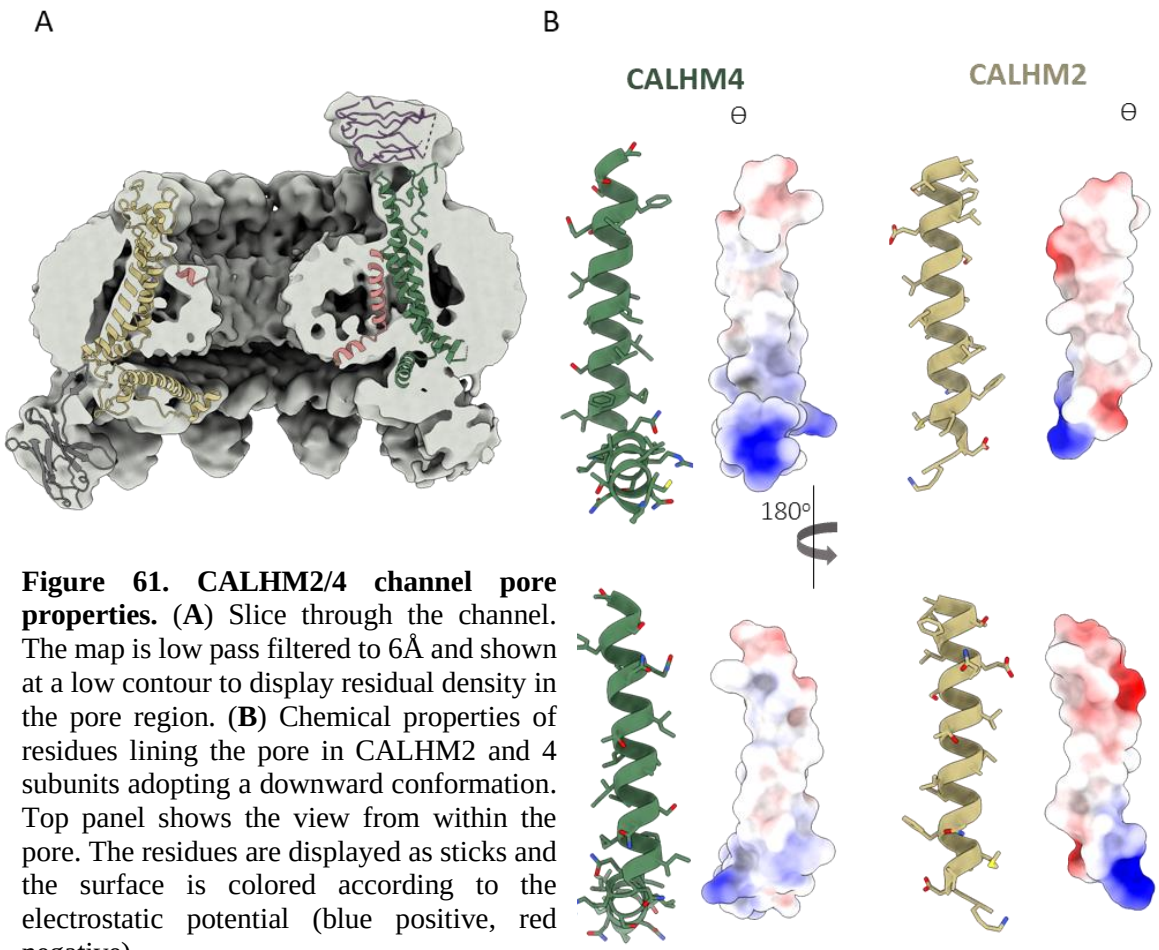

Figure 61. CALHM2/4 channel pore properties. (**A**) Slice through the channel. The map is low pass filtered to 6Å and shown at a low contour to display residual density in the pore region. (**B**) Chemical properties of residues lining the pore in CALHM2 and 4 subunits adopting a downward conformation. Top panel shows the view from within the pore. The residues are displayed as sticks and the surface is colored according to the electrostatic potential (blue positive, red negative).

Although the character of the pore-facing residues of the flexible NT and TM1 of other CALHM2 subunits in an upward position cannot be determined with certainty, distinct features in the pore reveal remarkable properties that are related to the different conformational state of subunits. Extra density found in the half of the pore lined by the down-facing helices (**Figure 61-A**). This density has a convex shape with its interior facing TM1(**Figure 61-A**). Based on its shape and low signal I attribute this density to a micellar structure, presumably formed by detergents used for protein purification or by co-purified lipids. In the channels of homomeric CALHM4, the extra density resembles a lipid bilayer with similar spacing of high-density region as expected for the headgroup regions. In the heteromeric structure, this arrangement is disrupted (**Figure 61-A**), which is likely a consequence of the introduction of CALHM2 subunits residing in a predominant upward conformation. As micelles inherently have an amphipathic character, it is plausible that the hydrophobic part of the detergent or lipids would face the hydrophobic region of TM1 of CALHM4 and CALHM2 in down conformations, whereas the hydrophilic part interacts with polar residues exposed to the pore centre harbouring the mobile N-terminal region of CALHM2 in upward conformations. Such change in the chemical character of the CALHM2 residues facing the pore would be facilitated by the rotation of the TM1 region accompanying the conformational change (**Figure 59-C and 61-B**).

2.4.7 Summary and conclusion on the structures of heteromeric CALHM2/4 channels

In conclusion, my studies revealed that CALHM2 and 4 are capable of assembling into heteromeric channels with different stoichiometries, in which subunits of the same paralog were found to cluster. The structural features of the observed channel assemblies is dictated by the predominant subunit, resulting in channels bearing the general features of the corresponding homomeric assemblies. The better separation of heterogeneous channels during classification was achieved for the complex containing both sybodies. This suggests that the presence of the anti-CALHM2 sybody facilitated the alignment, possibly due to the introduction of additional features and the generally stronger density, compared to gF2 sybody. The highest resolution was obtained for a mixture of undecameric assemblies being an average of 9:2 and 8:3 stoichiometries, which suggests that these assemblies are predominant in the sample. However, the assessment of their distribution by 3D classification might not be accurate as particular assemblies might be less suited for reconstruction. As an example, the complex of CALHM4-gF2 exhibited preferred orientation, which hampered its 3D reconstruction. It is thus expected that in heteromeric assemblies with predominant CALHM4 fraction this would also be the case, which would hinder the high resolution reconstruction of those channels compared to the well behaving particles of other assemblies.

Compared to homomeric channels, the CALHM2/4 complex shows pronounced differences in the pore geometry due to distinct conformations adopted by its subunits. The proximity of CALHM4 subunits favorizes a downward conformation of adjacent CALHM2 subunits, in contrast to the majority of CALHM2 subunits, which adopt an upward conformation with a flexible NT and TM1 region, which was also observed in homomeric channel complexes. The identification of the downward conformation of CALHM2 supports the notion that pore lining regions of CALHM2 proteins can change their conformation, allowing for a coexistence of different TM1 conformations in a channel without causing steric clashes between adjacent subunits. Notably, whereas the sybody RA5 targeting CALHM2 appears to prefer its upward conformation, the observed variability of conformations in the homomeric channels indicates that it is not sufficient to fully stabilize CALHM2 in this conformation. Interestingly, while CALHM4 subunits affect the conformation of CALHM2, the reverse seems not to be the case since in the structures I did not see any sign of mobility of the pore lining region of CALHM4 subunits.

The break of the symmetry of the CALHM2 assembly in heteromeric channels provided insight into the mechanism how this movement might be coordinated. Different conformations adopted by the CALHM2 subunits indicate that they may function independently without causing steric clashed of adjoining subunits adopting different conformations. Such work mode would allow a large flexibility of pore dimensions to accommodate a transport of molecules of various sizes.

3. Discussion

3.1 Overview of the results

Based on their predicted topology containing four membrane-spanning helices, CALHM proteins were assigned to belong to the superfamily of large-pore channels, which also includes gap junction-forming connexins and innexins, as well as distantly related pannexins and LRRC8 proteins[71]. While these other families have been extensively studied on a functional and structural level, CALHM proteins constitute the most novel and least described branch of large-pore channels[20,22,23]. At the start of this project, the functional knowledge was limited to a single member of the family, CALHM1, which was reported to form ion channels with unique properties activated by membrane depolarization and extracellular calcium depletion and which was later found to heteromerize with its paralog CALHM3, which on its own does not form functional channels[1,44]. However, there were no structures of CALHM proteins available that would illustrate the structural basis of the mechanism underlying their activation. Therefore, the goal of this project was to gain functional and structural insight into this family, with a focus on the uncharacterized members of the human CALHM family.

The first part of this thesis describes efforts to biochemically and structurally characterize the members of the CALHM family. As a result, three CALHM family members, CALHM2, 4, and 6, have been found to be biochemically stable and promising candidates for structural characterization. The structural characterization was performed using cryoEM. While this approach did not yield the structure of CALHM2, high-resolution structures of human CALHM4 and CALHM6 were obtained, revealing remarkable and unexpected properties of these proteins. CALHM4 and CALHM6 assemble to form channel-like structures, which was expected based on previous observation showing that the homologous CALHM1 forms ion channels with a predicted hexameric assembly. However, the two homologues characterized here form significantly larger assemblies, with channels forming either decamers or undecamers. Moreover, CALHM4 dimerizes through their intracellular region, resulting in the formation of a junction-like arrangement similar to a gap junction, yet with interactions on the opposite sites of the pores. In both homologues and in all observed oligomeric states, the assemblies result in exceptionally large central pores with dimensions displaying unusually large diameters compared to other large-pore channels. As predicted, protomers of both CALHM4 and CALHM6 consist of four transmembrane α-helices, with cytoplasmic N and C termini. Remarkably, while three helices appear to form a stable core, the first membrane-spanning α-helix TM1, lining the pore lumen shows drastic differences in conformation between the two homologues. As a result of this difference, the pore of the two channels show distinct geometries and overall dimensions. The pore of CALHM4 channels is wide and cylindrically-shaped, whereas in CALHM6 channels, the pore size narrows from the extracellular towards the intracellular side, resulting in the shape of an inverted cone. Remarkably, non-proteinaceous extra density is observed in the wide pore of CALHM4, resembling a lipid bilayer. This suggests that lipids may play a role in the regulation of CALHM4 channel gating. To gain insight

into the functional properties of these proteins, electrophysiological and liposome-based *in vitro* studies were employed, using conditions, which lead to the activation of the functionally characterized homologue CALHM1. However, these functional studies showed that CALHM2, 4, and 6 are not activated by the same stimuli as their homologue, and their activation mechanism remains unknown.

In the second part of this thesis, attempts to gain insight into the expression patterns of the three homologues are described in the expectation that such information would hint towards the functional role of these proteins. As a result, we found that, on an mRNA level, CALHM2, 4, and 6 are highly expressed in the placenta. Furthermore, an attempt was made to examine the expression of CALHM2 and 6 homologues at the protein level in this tissue. However, this proved challenging, and only a small amount of CALHM2 and 4 was found in the placenta, in contrast to the high mRNA levels. Unfortunately, this limitation did not allow for the study of the proteins in their native context. Due to these limitations, potential interactions of these homologues were investigated by overexpression, where I have found that CALHM2 and 4 interact to form heteromeric channels.

This finding led to the studies described in the last part of this thesis, which focused on the characterization of the heteromeric CALHM2/4 complex. Although functional data, similar to homomeric CALHM channels and in contrast to the altered phenotype of CALHM1/3 heteromers, showed no activity of these subunit pairs, the structural characterization of the heteromeric complexes was pursued. To overcome the challenge of such characterization, resulting from the overall similarity of the involved family members, sybodies specific to each homologue were generated to facilitate their distinction. Prior to the structure determination of heteromeric channel complexes, the homomeric CALHM paralogs in complex with their respective sybodies were structurally characterized. The resulting data permitted the identification of the binding sites, and yielded a structure of CALHM2, which, in the apo-state was precluded by the preferential orientation of these channels. This structure revealed that CALHM2 forms large channels similar to the two other homologues. However, the pore-lining helix showed significant mobility, contrasting with observations in CALHM4 and resembling features of CALHM6.

The structure of CALHM2/4 complexes revealed channels consisting of CALHM2 and 4 proteins that resemble homomeric channels in their general architecture. In these channels, subunits of the same homologue cluster to forming channels of different oligomeric states, ranging from decamers to dodecamers, with various subunit stoichiometries. A high-resolution structure was obtained for undecameric channels composed of eight CALHM2 and two CALHM4 subunits, with one subunit remaining unidentified. Strikingly, the pore of heteromeric channels exhibits significant differences compared to homomeric channels. It is intrinsically asymmetric due to the distribution of different subunits and their distinct conformational preference. Interestingly, similar to the CALHM4 structure, extra density is observed in the pore, which could be attributed to either detergent or copurified lipids, further support the notion that lipids may play an important role in CALHM channel gating.

This study, unfortunately, did not provide insight into the functional properties of the investigated CALHM proteins. Instead, it provides a detailed structural analysis of uncharacterized members of the family. Clearly, due to limited functional data, a definitive link between structure and function cannot be established. Following, I will proceed to discuss the obtained structures, focusing on similarities and differences between CALHM family members and other structures of the large pore-channels from different families. The implications of the observed CALHM assemblies will be discussed, as well as structural features that are potentially integral to their function, considering results of existing functional data.

3.2 Do CALHM2, CALHM4 and CALHM6 form ion channels?

This study has focused on three poorly characterized homologues of the human CALHM family: CALHM2, CALHM4, and CALHM6. At the start of this project, only CALHM1 had been shown to form an active ion channel. In my functional studies employing electrophysiological recordings and *in vitro* liposome-based assays, no activity was observed for the three homologues upon extracellular calcium depletion and membrane depolarization, two stimuli reported to activate CALHM1[2]. While no functional studies were previously reported for CALHM4 and CALHM6, our results on CALHM2 are consistent with the study by Ma et al., which showed no activity for murine CALHM2 in *Xenopus laevis* oocytes and by Syrjanen et al. who reported no activity for human CALHM2 in HEK cells[44,72]. However, contrasting results were obtained by Choi et al., who reported macroscopic currents of human CALHM2 recorded in HEK cells activated upon depletion of extracellular calcium, whose open probability, in contrast to CALHM1, does not show obvious voltage dependence[73]. Moreover, the studies by Choi et al. showed inhibition of CALHM2 currents in the presence of ruthenium red, an inhibitor of CALHM1, which is wakened after the mutation of a residue assigned to bind the inhibitor[45,73]. These discrepancies in the results are currently puzzling and difficult to explain.

One possible reason why the channel-forming proteins did not yield currents, could be related to the sub-cellular localization of the proteins which might not be expressed on the plasma membrane. However, in our studies, and the study by Ma et al., the localization to the plasma membrane was confirmed in oocytes[44]. Moreover, the *in vitro* liposome system, which ensures the access of the protein to the outside solution, did not show activity of CALHM2 in my experiments neither. Therefore, discrepancies originating from differences in localization in the different studies can be excluded. Another possibility could be related to differences in the expression hosts, however, three studies including ours and the study by Choi et al., which reported CALHM2 activity, performed the recordings in HEK cells, therefore such reason can also be excluded[72,73]. Similarly, the differences in the expression constructs likely did not contribute to the discrepancy as the two studies and ours were performed in HEK cells expressing CALHM2 constructs that were C-terminally tagged with either SBP or GFP[72,73].

Inconsistent data also exist for CALHM6. Recently, Danielli et al. reported that CALHM6 forms a constitutively active ion channel in immune cells[74]. In their study the electrophysiological recordings in

mammalian cells did not show CALHM6 conductance, which the authors ascribe to a lack of plasma membrane localization. In contrast, the authors observed activity of CALHM6 in *Xenopus laevis* oocytes where they claimed that the constitutive activity of CALHM6 would be toxic for the oocytes[74]. Consequently, the authors expressed murine CALHM6 at a very low levels, which enabled them to obtain recordings with small outwardly-rectifying currents that were inhibited by Gd^{3+} [74]. This reported behavior contrasts our results, which neither showed activity in *X. laevis* oocytes, despite the surface expression, nor for reconstituted protein in liposomes. However, it should be noted that the reported conduction of CALHM6 was obtained for the murine homologue, whereas our studies have investigated the human protein[74]. It thus cannot be excluded that the two orthologs exhibit different activities. Moreover, the constructs used in our studies contained additional amino acids at both termini as a result of the cloning technique employed[75]. Although unlikely, the possibility that their presence would interfere with activation cannot be excluded neither.

In summary, a consensus in the field regarding the activity of recently characterized CALHM family members has yet to be reached. Ultimately, it will be necessary to repeat the functional characterization while keeping careful attention to the expression and recording conditions and with precautions taken to ensure the lack of endogenous conductance. The observed differences in the functional properties of different CALHM paralogs, underline the notion of a diverse group of membrane channels with complex function and activation properties. A careful analysis of existing structures, including a systematic comparison of similarities and differences within the family, may thus prove to be useful in making progress towards the understanding of the family.

3.3 Unique architecture of the CALHM channels

As predicted, CALHM proteins consist of four transmembrane helices and intracellular N- and C-termini, a topology that is similar to other large-pore channels[35]. However, a comparison of the CALHM protomer with those of connexins, innexins, pannexins, and LRRC8 shows notable differences in size, shape, and organization (**Figure 62**)[26-29,66,76-79]. What makes CALHM proteins unique among those families is the arrangement of the four transmembrane helices (**Figure 62-A**). When viewed from the extracellular side, the TM1, TM2, TM3, and TM4 helices are arranged anticlockwise in CALHM proteins, with TM2, TM3, and TM4 approximately lined up in a row (**Figure 62-A**). By contrast, the arrangements of the four helices in the other families are all clockwise, with helices TM1-4 forming a compact helix bundle (**Figure 62-A**)[26,28,29,33,66,76,78]. This translates to a difference in the position of the pore-facing α-helix TM1, which in CALHM channels either loosely interacts with TM3, or which is detached from the core defined by TM2-4 in an alternative conformation observed in certain homologues (**Figure 62-B**). Instead, in connexins, innexins, pannexins, and LRRC8, TM1 is an integral part of the helix bundle and forms extensive interactions with TM2, TM4, and TM1 of neighboring subunits (**Figure 62-B**). In addition, proteins from all families contain a short N-terminal helix (NTH) prior to TM1, which has been shown to be highly mobile and proposed to play a role in channel gating (**Figure**

62-B)[43]. In all families, the protomers are arranged to form large channels, but the regions involved in subunit interactions varies significantly between CALHM and the other families (**Figure 62 and 63**). In CALHM channels, the contact between subunits proceeds through interactions between TM2, TM4, and the CTH of the neighboring subunits (**Figure 62-A**). In contrast, in other families of large-pore channels, interactions between the transmembrane regions are loose, contacts in the cytoplasmic region scarce, and interactions largely proceed through the extracellular regions (**Figure 62-A and 63**)[26-29,33,66,76,77,80]. This is also reflected in the different shapes of the channels, with connexins, innexins, pannexins, and LRRC8 channels having a conical shape narrowing towards the extracellular side, which has been shown in many cases to determine the selectivity of the channel and modulate gating (**Figure 63**)[20,28,30,66,81,82]. On the other hand, in the conformation observed in CALHM4, the channel has a more cylindrical shape, and the extracellular region does not form a constriction but rather a wide entrance to the channel (**Figure 63**).

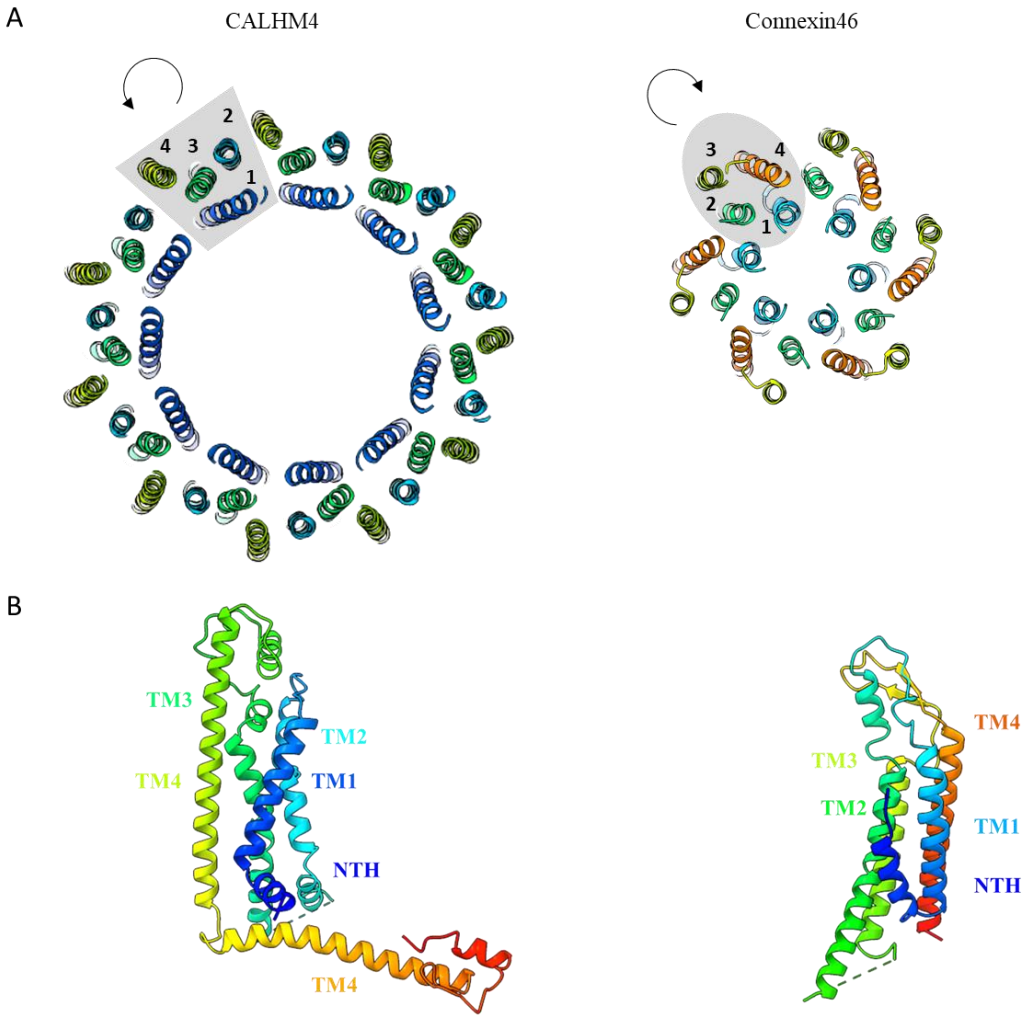

Figure 62. Comparison of CALHM4 with connexin-46. (**A**) View of the transmembrane α-helices of the CALHM4 undecamer and connexin-46 (6MHQ) from the extracellular side. The general shape of a single subunit is indicated. (**B**) Ribbon representation of the CALHM4 and connexin-46 subunit. Secondary structure elements are labelled and α-helices are shown in unique colors.

3.4 Assembly patterns

Currently, 25 structures of CALHM proteins have been reported, including structures of CALHM1, CALHM2, CALHM4, CALHM5, CALHM6, CLHM1, as well as chimeras of CALHM1 and 2, all forming large channel assemblies[72,73,83-87]. Perhaps the most surprising structural feature of the CALHM family members is that their oligomeric organizations varies between homologues and within a single species, ranging from heptamers to tridecamers[72,73,83-87]. This variability in oligomeric states is in contrast to other large-pore channel families, where the channels predominantly assemble with a single defined number of subunits[27-30,33,66,76-78]. Although it is worth noting that recent studies on LRRC8 proteins revealed variability of oligomeric states within the family, with LRRC8C homologues assembling as heptamers in contrast to LRRC8A and D assembling as hexamers[63]. However, the strong variability within a single member remains unique to the CALHM family. Interestingly, Ren et al. proposed that subunit exchange might be a part of CALHM channel gating[86]. The authors observed heptamers and octamers of *danio rerio* CALHM1 channels and noted that in the smaller channels, TM1 and the NTH region move down towards the cytoplasmic site to avoid steric clash with neighboring helices[86]. This suggests that the oligomeric rearrangement and accompanying conformational changes, which result in a much smaller pore diameter, may regulate channel's activity. In other CALHM members, such rearrangement does not cause a conformational change or significant pore constriction, therefore it seems unlikely that subunit exchange would be a part of channel gating in homomeric CALHM2, CALHM4, and CALHM6. Moreover, whether CALHM channels exhibit a similar variability in their oligomeric states in cells is unknown. It is possible that the observed diversity of assemblies are artifacts of the overexpression system, in which subunits are abundant, and in the comparably small energetic penalty for the recruitment of additional subunits in large assemblies, where the incorporation of another subunit does not result in significant rearrangements of subunit interfaces. It is plausible that in cells, the abundance of available subunits would be much lower, thereby favoring smaller assemblies, or that yet unknown chaperones regulate the biogenesis of those channels and govern their oligomeric states.

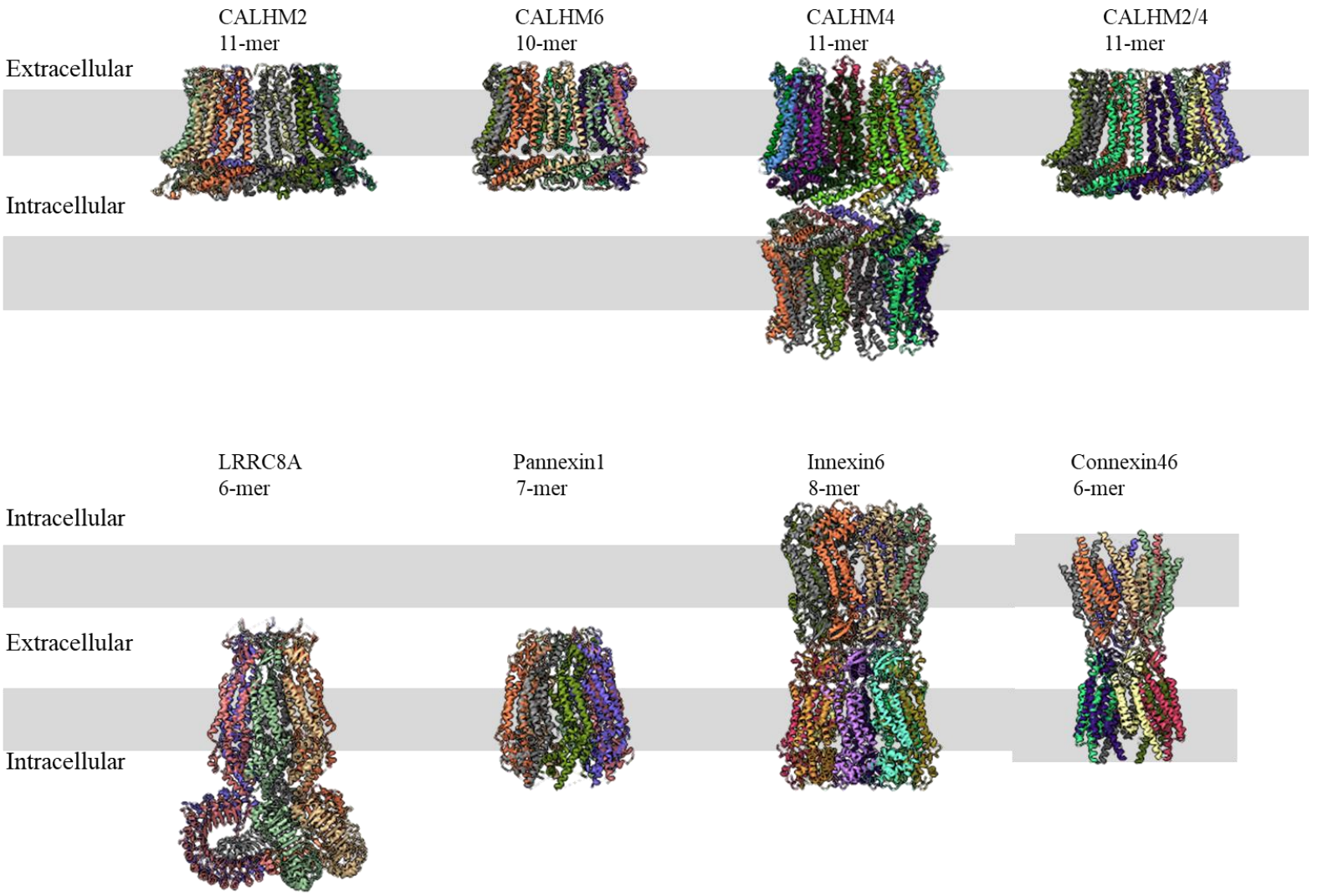

Figure 63. Overall structure comparison of large-pore channels. The view is parallel to the membrane. LRRC8A (PDB: 6G9O), Pannexin1 (PDB: 6WBF), Innexin6 (PDB: 5H1R), connexin46 (PDB: 6MHQ).

Studies by Syrjanen et al. and Demura and colleagues have investigated the regions in CALHM structures that drive the observed oligomerization of CALHM channels[72,83]. Structural comparisons revealed that the TM4-CTH linker adopts different conformations between certain homologues, which affect the orientations of the C-terminal domain (CTD) and hence determine the oligomeric state (**Figure 64-A**). Further analysis identified a conserved proline in the linker that appears to play a role in defining the angle between TM4 and CTH and thus the oligomeric state[71,72,83]. Interestingly, CALHM2, CALHM4, and CALHM6 channels, which all assemble into decamers and undecamers, contain this critical proline in the same position in the linker, supporting this observation (**Figure 64-B**). It was also noted that the proline is in the same position in CALHM1 and CALHM3, which both form heteromers, suggesting that the shared conformation in this region, defining their presumed oligomeric state, might be an important determinant of the interaction between homologous CALHM proteins[72] (**Figure 64-B**). However, our study has shown that while CALHM2 and CALHM4 interact, both paralogs do not interact with CALHM6, indicating that other factors beyond the shared oligomeric state are necessary for the interaction between CALHM proteins. Although there is currently no evidence for the existence of heteromeric CALHM2/4 channels in a cellular environment, it is worth noting that the structures obtained in this study may share features with heteromeric CALHM1/3 channels. Studies of concatemers of CALHM1 and CALHM3 proteins indicated that only in constructs permitting the clustering of the same subunits, the recorded current resembled those generated by co-expression of single CALHM1 and CALHM3 subunits, suggesting that also in heteromeric CALHM1/3 channels, subunits of the same homologue cluster, indicating a higher affinity of homomeric compared to heteromeric interactions[44]. A similar clustered arrangement has also been reported in LRRC8A/C heteromeric channels, suggesting that this might be a general feature of heteromeric large-pore channels[63,64].

Interestingly, the C-terminal region was, besides contributing to the stability of CALHM channels, also proposed to be involved in CALHM1 channel gating in one study[86]. The authors observed ordered and disordered states of this region and proposed that the conformation of the C-terminus, together with oligomeric rearrangements, regulate channel permeation, resembling a mechanism described for pannexins, which become ATP-permeable upon cleavage of the C-terminus[29,86]. This is yet another observation that distinguishes CALHM1 from other members of the CALHM family, in which changes in the arrangement of the C-terminus were not observed. Therefore, it is unlikely that such mechanism would apply to the other CALHM channels.

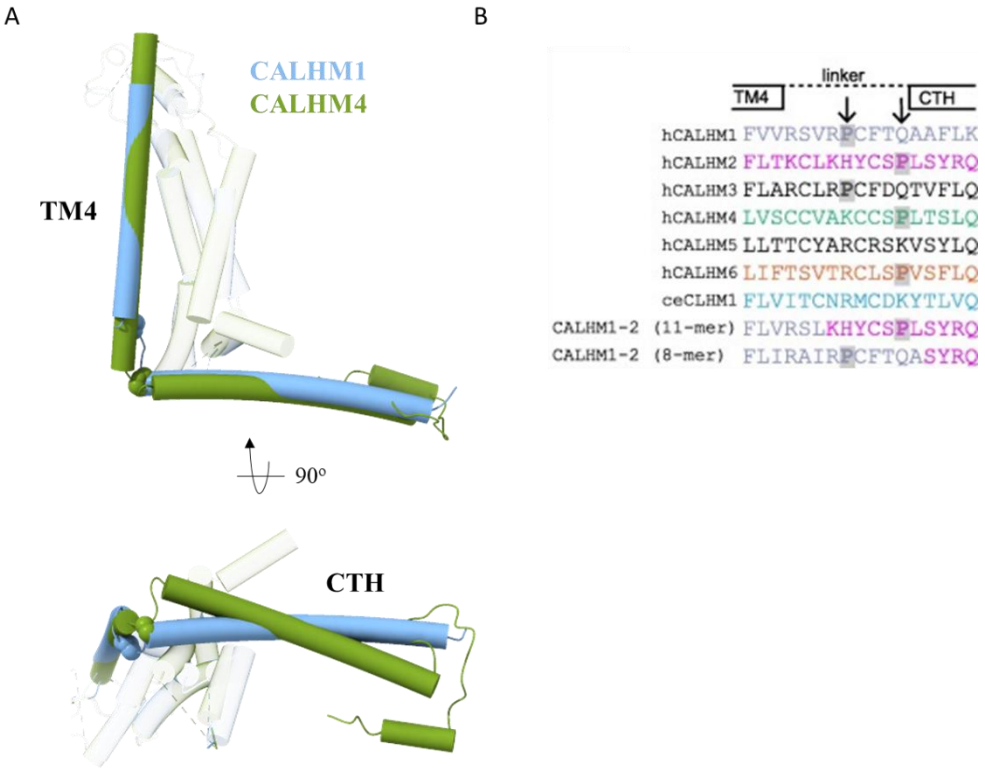

Figure 64. CTH orientation in CALHM proteins (**A**) Superposition of human CALHM4 and chicken CALHM1 (6VAM) showing differences in the CTH orientation. Prolines in the linker regions are shown as spheres. (**B**) Sequence alignment of the TM4-CTH linker region. Figure B is from[71].

Junction assemblies

Another surprising feature of CALHM channels is the observation of junction-like assemblies of two different types. Head-to-head gap junction-like assemblies were reported for CALHM2 channels by Syrjanen et al. and Choi et al. [72,73,84]. This observation could suggest that CALHM2 forms intercellular gap junctions between two adjacent cells, similar to connexins and innexins. We observed CALHM4 channels to dock in a tail-to-tail manner, and such assemblies were also reported for CLHM1[87]. These junction-like assemblies could in principle indicate the existence of a novel different type of intracellular gap junction between the plasma membrane and certain organelles. However, currently, there are no functional studies indicating a role of CALHM channels in intra- and intercellular communication, so the physiological relevance of the observed assemblies remains questionable. It thus should be emphasized that that the observed junction assemblies could be artifacts of *in vitro* purification, where docking sites of two channels can access each other, and where comparably weak interactions between single subunits are amplified throughout large numbers of protomers, whereas in a membrane, such contacts would be prevented or confined to neighboring subunits.

3.5 Calcium binding site and voltage sensor

CALHM1 has been shown to be activated by the depletion of extracellular calcium[2]. However, the binding site for calcium and the conformational changes associated with calcium binding have not been revealed in any existing structure of CALHM1. Similarly, in our CALHM4 structure, no differences were observed between structures obtained in the presence and absence of calcium. This observation is also consistent with studies in connexins, which are also activated by the depletion of extracellular calcium and where structures in the presence and absence of calcium did not show significant conformational differences[82]. Instead, a change in the electrostatic potential in the extracellular region of the channel has been proposed in response to Ca^{2+}-binding, suggesting the formation of an electrostatic barrier for ion flow. A similar mechanism as proposed for connexins could be plausible for hepta- or octameric CALHM1 due to the comparatively narrow constriction formed by the extracellular region. However, for the CALHM proteins that form larger channels, this mechanism appears unlikely. Furthermore, the extracellular region of CALHM1 is more negatively charged than that of CALHM4 and CALHM6 (**Figure 65**). Such analysis for CALHM2 is precluded due to the low resolution of the CALHM2 extracellular regions, which is unfortunate as this homologue has been reported to be regulated by extracellular calcium. Nevertheless, these observations suggest that the regulation of CALHM4 and CALHM6 might be distinct from CALHM1, at least regarding their regulation by calcium.

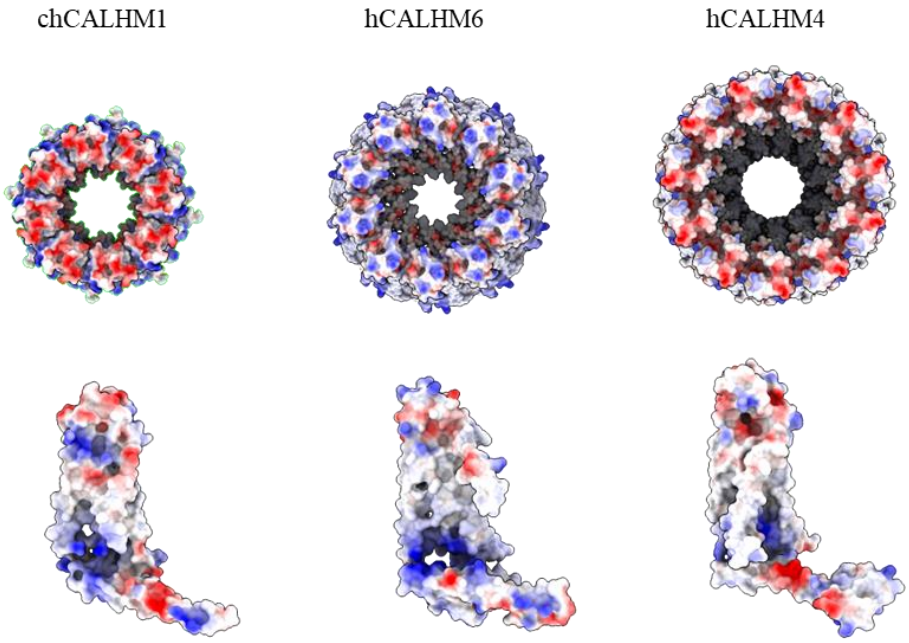

Figure 65. Chemical properties of the extracellular regions of the CALHM channels. Shown is the comparison of chicken CALHM1 (6VAM), human CALHM4 and human CALHM6. The surface is colored according to the electrostatic potential (blue positive, red negative).

Besides the depletion of extracellular Ca^{2+}, CALHM1 has also been shown to be activated by membrane depolarization, indicating its intrinsic sensitivity to voltage[2]. The canonical voltage sensor in ion channels typically consists of an arrangement of several arginines localized in the membrane region[88]. However, no such motif is found in any of the CALHM members. This lack of a canonical voltage sensor is similar to other large-pore channels that are regulated by voltage[27,29,30]. Therefore, it is likely that CALHM channels, particularly those that are sensitive to voltage changes, sense the transmembrane electric field through still unidentified residues that may be distributed within the subunits and influence the global structure of the channels or alternatively by interacting ions such as Ca^{2+}.

3.6 CALHM channel pore and hypothetical gating mechanisms

Typical ion channels consist of a pore that is sterically constricted when closed, and which permits the flow of ions when open. As defined in their structure, CALHM channels contain large pores that are placed along their axis of symmetry. The exact channel diameters vary due to the different oligomeric states and conformational differences in the pore-lining regions. The smallest reported pore size of 10 Å is found in the structure of the heptameric *D. rerio* CALHM1, which although too small for hydrated ATP to pass is permeable to small ions[86,89]. The flexibility of the pore lining regions in CALHM2 and CALHM6 structures impedes the accurate estimation of their exact pore sizes. However, based on the modeled regions and depending on the conformation of undefined parts, the resulting pore diameters could be large enough to allow the permeation of ATP. CALHM4, on the other hand, has a well-resolved pore region, with pore sizes of 20 Å and 30 Å for decameric and undecameric channels, respectively. None of the reported structures so far exhibited a fully constricted pore that would prevent ion flow[71,83-85,87,90]. Strikingly, the wide pores are in contrast to our functional data, which did not show activity of the three studied CALHM homologues. In other large-pore channel families, electrostatic or steric constrictions in the extracellular and cytoplasmic regions were proposed to play a role in the regulation of their permeation properties[26-29,66,76,82]. However, CALHM channels lack such features, and the large size of CALHM channels would likely render any electrostatic barrier ineffective, except for CALHM1, which forms smaller channels. This raises the question of how the large CALHM channels remain inactive in the membrane. Although the limited and conflicting functional data make it difficult to establish a definitive link between functional states and observed structures, these structures still provide insight into mechanisms of how these channels might be gated.

The pore of CALHM channels is lined by the helix TM1 and the preceding N-terminus. Different conformations of TM1 have been observed, greatly impacting the pore size and geometry (**Figure 66**). In the "down" conformation, TM1 adopts a vertical position with respect to the membrane, resulting in a wide cylindrical pore. In the "up" conformation, in contrast, TM1 is lifted towards the pore axis, presumably constricting its size and creating a conically shaped permeation path (**Figure 66**). Currently, structures of CALHM1, CALHM4, and CALHM5 exhibit a ‘down’ conformation of TM1, while CALHM6 structures display the ‘up’ conformation (**Figure 66**). CALHM2 structures show both

conformations demonstrating that they likely present distinct states of the same channel (**Figure 66**).[72,80,83,84,86,87,91]. Syrjanen et al. and Choi et al. initially reported the down conformation in their CALHM2 structures (**Figure 66**).[72,73]. Similarly, we observed the 'down' conformation of CALHM2 neighboring CALHM4 in the heteromeric CALHM2/4 channels and the 'up' conformation in both, heteromeric CALHM2/4 complexes and the homomeric CALHM2-RA5 structure. (**Figure 66**). It should be noted that the displayed models of CALHM2 represent interpretations of a presumable conformation of TM1 since all of these structures display a large flexibility in this region, indicating a large heterogeneity of conformations (**Figure 67-A**). Currently, the best-resolved 'down' conformation of a CALHM2 subunit is found in the CALHM2/4 complex, which, in contrast to other structures, allowed the modeling of side chains in this region. Interestingly, Choi et al. obtained the structure of CALHM2 in the 'up' conformation in the presence of the inhibitor ruthenium red (RuR) (**Figure 66**) and thus proposed a gating mechanism for CALHM channels, in which the down conformations represent a wide-open pore (**Figure 66 and 67**) and the up conformation, stabilized by the blocker, represents a closed pore with the flexible N-terminal helix constricting its size (**Figure 66 and 67**) [73].

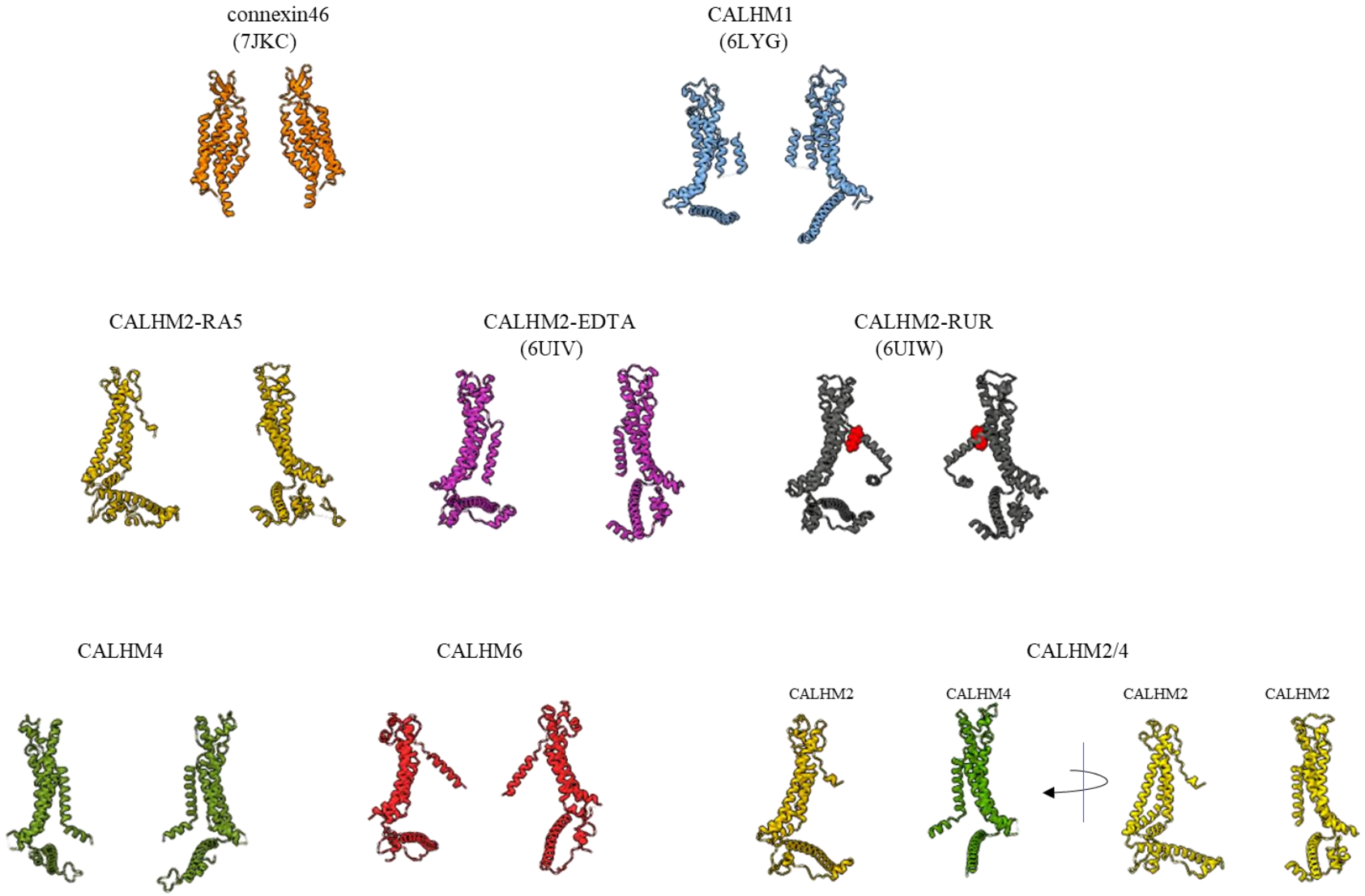

Figure 66. Comparison of pore conformations of the CALHM channels. Ribbon representation of facing protomers in CALHM channels illustrating different conformations of TM1 and NTH and resulting pore geometries. PDB codes are indicated.

It should be noted that the same density assigned by the authors to the inhibitor, is also present in our structure of homomeric CALHM2-RA5, and, as noted in a review by Syrjanen et al., is also present in the structure of the same group obtained in the absence of the blocker (**Figure 67**)[71]. This density aligns with the residual density in our CALHM2-RA5 structure, indicating that it might originate from a smaller population of subunits residing in a 'down' conformation of TM1 rather than from RuR (**Figure 67-B**). Choi et al. also performed functional studies with a mutant of a residue assigned to bind the inhibitor, E37R, and reported insensitivity of this mutant to the blocker (**Figure 67-B and C**)[73]. In the 'down' conformation of CALHM2 in CALHM2/4 channels, E37 appears to interact with an arginine on TM3 (**Figure 67-D**). It is thus conceivable that the introduction of a positive charge in this position destabilizes the 'down' conformation of CALHM2, potentially increasing its open probability in the presence of an appropriate stimulus.

Despite remaining ambiguities, the relationship between observed pore conformations and their corresponding functional states, as proposed by Choi et al., appears evident (**Figure 68**)[73]. However, there are still puzzling questions which prevent a definitive assignment. The lack of conductance observed in functional recordings, despite the large diameter of the CALHM4 pore, remains puzzling. Additionally, none of the reported structures of CALHM1, CALHM4, and CALHM5 exhibit the 'up' conformation, regardless of the absence of calcium or the presence of the RuR blocker[72,84,86,87,90,91]. Recent functional studies on CALHM6 also contradict the proposed model by reporting its constitutive activity[74].

In that respect, the presence of lipids within the pore of large CALHM channels is noteworthy as it offers a potential alternative mechanism for regulation. The hydrophobic nature of TM1 residues in the 'down' conformations of CALHM2, CALHM4, and CALHM5 indicates a possible interaction with lipids[91]. In our structure of CALHM4, we find residual cryo-EM density within the hydrophobic interior of CALHM4, which either originates from detergents or co-purified lipids that assemble as bilayers in the constrained environment of the pore. Similar extra densities in the pore were observed by other groups in CALHM2 and CALHM5 in down conformations[72,85]. This distribution of density changes markedly in the conical structure of CALHM6 and hints towards a potential role of lipids in shaping the activation and permeation properties of CALHM channels (**Figure 68**). Thus, two alternative scenarios could be envisioned, which might underlie regulation in CALHM channels, where the gate in the closed state could either be formed by part of the protein or by lipids (**Figure 68**). The regulation of activity of large pore channels by pore-residing lipids has also been recently proposed for connexins, innexins, pannexins, and LRRC8 channels, which would indicate that such a regulatory mechanism extends beyond the CALHM family[64,77,81,92].

However, it should be noted that the presence of detergents or lipids in the pore may be an artifact introduced by either overexpression or during cryo-EM sample preparation. Moreover, such a mechanism does not appear to be in agreement with the structures of CALHM1. The TM1 of CALHM1 is composed mainly of hydrophilic residues, and MD simulations reported by Syrjanen et al. showed

that, in contrast to CALHM2, it cannot accommodate an ordered lipid bilayer inside its pore[72], presumably due to its smaller pore area which might destabilize such lipid arrangement. Moreover, a unique feature of the N-terminal region (NH) was observed in the majority of CALHM1 structures, where this region interacts with the pore-facing residues of TM1, partially burying its hydrophobic residues (**Figure 66**)[83,86,87,90]. Such arrangement is in contrast to location of the NH of CALHM4 and CALHM5 (**Figure 66**), which in both cases is placed horizontally at the inner membrane leaflet with the N-terminus directed towards the pore axis.

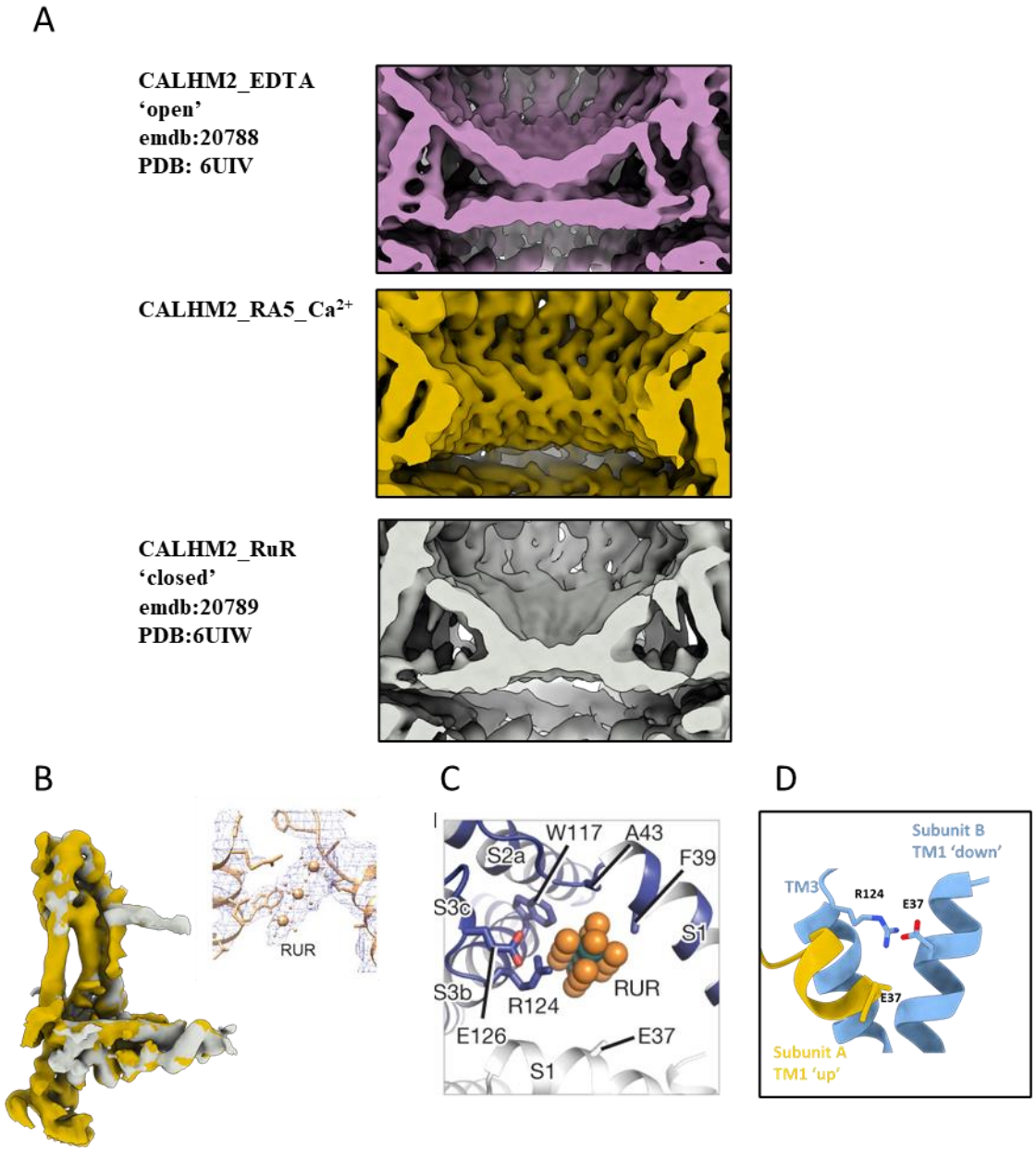

Figure 67. Pore characteristics of CALHM2 channels in different conformations (A) Comparison of pore densities of CALHM2 channels determined in the absence of calcium (top) (emdb:20788)[73], presence (middle) and presence of the blocker RuR (bottom) (emdb:20789)[73]. The maps are low-pass filtered to 6 Å. **(B)** Superposition of the maps of the single subunit of CALHM2 with the sybody and CALHM2 in the presence of RuR. Insets is from [73] and indicates putative RuR density. **(C)** is from [73] and shows the RUR-binding site, (D) shows the same site in the 'down' conformation of CALHM in a structure of CALHM2/4.

And is in agreement with other large-pore channels, in which such an arrangement of TM1 and NTH is observed but not the swing motion of TM1[26-29,66,76,79,81,92]. Both models are at this stage hypothetical, and it is possible that smaller CALHM1 channels have a gating mechanism that is distinct from larger CALHM channels.

Despite these uncertainties, our heteromeric CALHM2/4 structures may provide interesting insight into how the movements of pore lining regions may be coordinated. Previously, Choi et al. have speculated that TM1 and the N-terminus of CALHM subunits may move individually rather than in a concerted manner[73]. The different conformations adopted by CALHM2 subunits found in our heteromeric structure shows that subunits may change their conformation autonomously, without causing steric clashes with their neighbors, supporting this initial proposal. This independent working mode would allow for a flexible adjustment of the pore dimensions to accommodate molecules of various sizes but it is not clear whether such a heterogeneity of conformations would also be found in an activated channel.

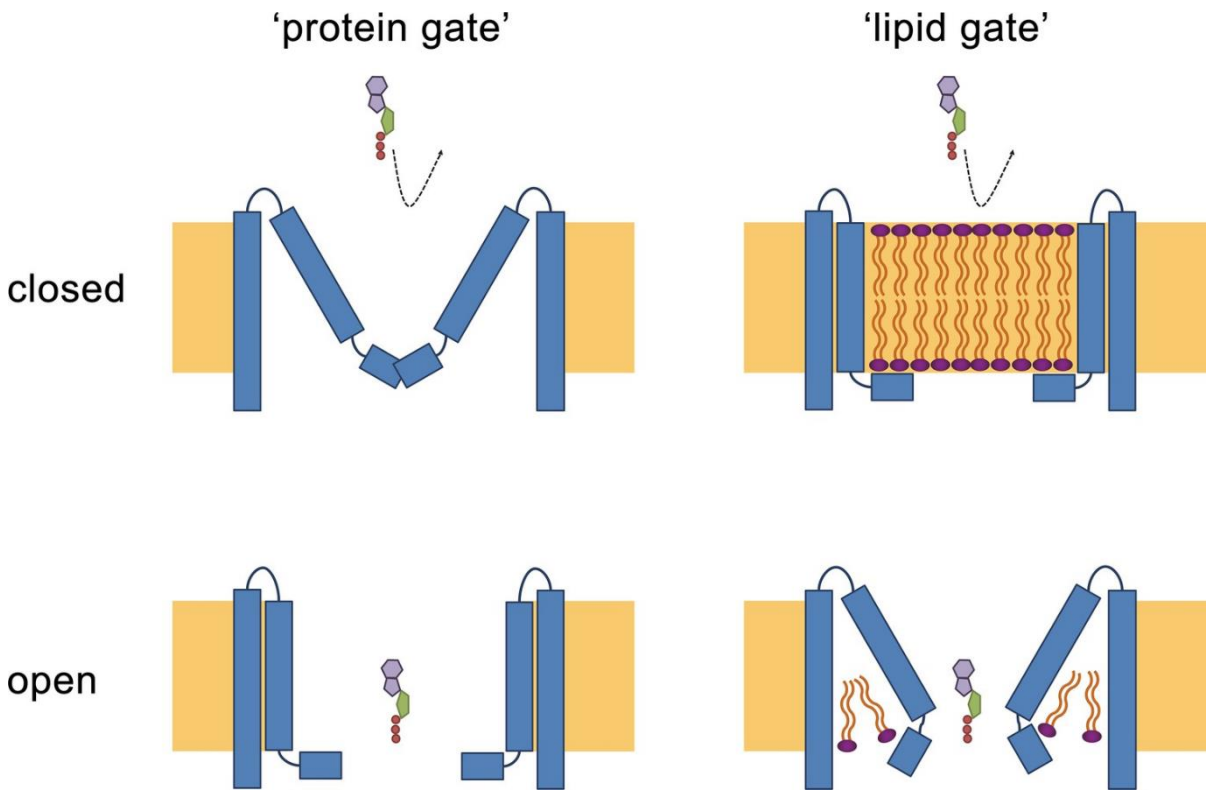

Figure 68. Hypothetical gating mechanisms. Schematic illustration of hypothetical gating mechanisms of large CALHM channels. Left, 'protein gate'. The gate impeding ion conduction of large CALHM channels (i.e. CALHM2, 4, 6) in the closed state is formed by the N-terminus of the protein, which closes the pore as observed in the modeled 'clogged' conformation of CALHM6 (top). In this case the conical conformation of CALHM6 would display a closed pore and the cylindrical conformation (bottom) an open pore. Right, 'lipid gate'. The gate impeding ion conduction of large

CALHM channels in the closed state is formed by lipids assembling as a bilayer within the protein, which impedes ion conduction. Since bilayer formation is facilitated in the cylindrical conformation of CALHM4, this structure represents a closed pore (top) whereas the structure of the bilayer would be disturbed in the conical conformation of CALHM6 (bottom). Since both the 'kinked' and 'extended' pore conformations of CALHM6 show a large opening, these conformations could represent open pores. Figure from [57]

To summarize, the gating of large CALHM channels likely involves the mobility of TM1 and the N-terminus, with different conformations affecting the diameter and permeability of the channel. The presence of lipids in the pore may influence permeation and ensure tight closure of the pores of large CALHM channels. This supports the idea that large-pore channels are not simply free diffusion pores but rather employ complex regulatory mechanisms, which likely differ between distinct members of the family.

In light of the functional data, it should also be considered that some CALHM homologues do not function as channels on their own but instead form heteromeric complexes with other homologues. The predominant localization of CALHM4 to the plasma membrane observed upon overexpression, could suggest a role in channel trafficking, while CALHM2, with its high flexibility in dependence of its neighboring subunits, may act as a regulatory protein. Further studies are needed to investigate the interaction patterns within the CALHM family.

3.7 Outlook

This thesis provides a detailed analysis of the CALHM family of channels, focusing on their structural characterization. By combining the findings from various research groups, which became available since then, valuable insights into the mechanistic properties of CALHM channels have been obtained. However, despite this significant progress, several key questions about CALHMs remain unanswered.

One of the primary questions is to whether CALHM2, CALHM4, CALHM5, and CALHM6 indeed function as ion channels. If they do, it is crucial to determine the specific stimuli that activate them. Conversely, if they do not function as ion channels, their role in cellular processes needs to be elucidated. These essential pieces of information are necessary to establish a clear connection between the observed structures and the functional states of CALHM channels. To address this question, extensive electrophysiological studies, in combination with *in vitro* liposome-based assays, could be employed. These techniques would allow for a detailed investigation of the ion channel properties of CALHM2, CALHM4, CALHM5, and CALHM6 and their response to various stimuli. Additionally, further studies should explore the interactions between family members and with accessory proteins and their specific roles within CALHM channels found in a cellular environment. Complementary approaches, such as electrophysiology and pull-down assays from native tissue samples could provide valuable insights in this regard.

Along the same line, structural studies of CALHM channels derived from native tissues would contribute to a better understanding of their organization and functional properties in a physiological context. Emerging techniques like the imaging of membrane proteins in native vesicles or liposomes hold promise for shedding light on the role of lipids in the regulation of CALHM channels.

In summary, this thesis presents a detailed structural characterization of CALHM channels and thus contributes to our understanding of these proteins. Nevertheless, further research is needed to fully grasp the mechanisms underlying CALHM channel function. By employing structural and functional studies on overexpressed and endogenous proteins, we should gain deeper insight into the activation stimuli, interactions, and regulation of CALHM channels, ultimately enhancing our knowledge of these proteins and clarifying their role in their cellular environment.

4. Methods

4.1 Cell cultures

4.1.1 Adherent HEK cell cultures

Adherent HEK293T cells were obtained from ATCC. Cells were cultured in DMEM (Dulbecco's modified Eagles medium) supplemented with 10% FBS and 100 U/ml penicillin/streptomycin in humidified incubator under a 5% CO_2 at 37 °C.

4.1.2 Suspension HEK cell cultures

HEK293S GnTI$^-$ cells were obtained from ATCC. Cells were adapted to suspension culture and grown in HyCell HyClone TransFx-H media supplemented with 2% fetal bovine serum (FBS), 4 mM L-glutamine, 1.5% poloxamer 188 and penicillin/streptomycin. Cells were grown in TPP Tubespin 600 bioreactors in a humidified incubator under a 5% CO_2 atmosphere at 37 °C, while shaking at 185 rpm (50 mm orbital radius). Cells were diluted to a density of $0.5 \cdot 10^6$ cells/ml once they reached approximately $3\text{-}5 \cdot 10^6$ cells/ml.

4.2 Cloning and construct preparation

cDNAs of human CALHM proteins were obtained from GenScript as synthetic constructs where SapI restriction sites were removed. For expression in *X. laevis* oocytes, cDNAs of CALHM1, CALHM2, CALHM4 and CALHM6 were cloned into a pTLNX vector. For expression in mammalian cells, cDNAs of all human CALHM homologs were cloned into a modified pcDNA 3.1 vector. The pcDNA 3.1 vector was modified to be compatible with the FX cloning technique[75] and was designed to encode a C-terminal 3C protease cleavage site followed by vYFP, Myc and streptavidin binding peptide (SBP) or Myc and a hexahistidine tag or GFP and Myc.

The sybody sequences were cloned into the FX-compatible pSb_init vector, which contains a chloramphenicol-resistance gene and an arabinose-inducible promotor[67]. The pSb_init vector contains an N-terminal pelB leader sequence and a C-terminal hexahistidine tag. To obtain tag-free sybodies, sequences were cloned into pBXNPHM3 vector.

4.3 Protein expression

4.3.1 Expression in adherent culture of HEK 293 cells

Adherent HEK293T cells were transiently transfected using polyethyleneimine (PEI) transfection reagents. One day before transfection, cells were seeded at a density of $3.5 \cdot 10^6$ cells/well in 10 cm dishes. The transfection mixture contained branched or linear PEI and DNA. For transfection in a 10 cm dish, 12 µg of DNA and 48 µg of PEI were used. For the co-expression of different CALHM proteins, a total of 12 µg of DNA containing an equivalent molar ratio of construct DNA was used. The mixture was incubated for 15 minutes at room temperature and then added dropwise to the cells. The expression was carried out for 36 hours. After this period, the cells were pelleted by centrifugation at 500 g for 5 minutes, washed with ice-cold PBS buffer, flash frozen and stored at -80 ºC for further use.

4.3.2 Expression in HEK 293 suspension cell culture

HEK293S GnT- cells adapted to suspension culture were transiently transfected. One day before transfection, the cells were diluted to a density of $0.5 \cdot 10^6$ cells/ml. Cells were transiently transfected with a mixture of DNA and PEI. For 300 ml of cell culture, 0.5 mg of DNA and 1.2 mg of PEI MAX were suspended in 20 ml of DMEM medium. After incubation for 5 minutes, the DNA solutions were mixed with the PEI solutions and incubated for 15 minutes. To increase transfection efficiency, the mixture was supplemented with 4 mM valproic acid. The transfection mixtures were then added to cell cultures and expression was carried out for 36 hours. After this period, the cells were pelleted by centrifugation at 500 rcf for 15 min, washed with PBS buffer and stored at -20 °C for further use.

4.3.3 Expression in bacterial cultures

DNA constructs of sybodies were transformed into *E. coli* MC1061 by a heat shock procedure and grown in Terrific Broth medium supplemented with 25 µg/ml chloramphenicol at 37 °C at 100 rpm. Cultures were scaled to 50 ml for purification assays and to a liter scale for downstream applications. Bacteria were first grown at 37 °C for 2 hours. The temperature was then lowered to 22 °C and when the cultures reached an OD_{600} of 0.5, L-arabinose was added to a final concentration of 0.02%. After 16-18 hours of expression, bacteria were harvested by centrifugation at 8,000 rcf for 20 min and pellets were either used immediately or stored at -80 °C until further use.

4.4 Protein isolation

4.4.1 Extraction tests

Cells were thawed on ice and lysed with lysis buffer (25 mM HEPES, 150 mM NaCl, 0.5 mM $CaCl_2$, 2 mM $MgCl_2$, 2% glyco-diosgenin (GDN), protease inhibitors, RNase, DNase, pH 7.6). The cells were

incubated in lysis buffer for one hour and the extract was clarified by centrifugation at 16,000 g for 10 min. The obtained supernatants were filtered through 0.22 µm centrifugal filters and injected onto a Superose 6 5/150 column pre-equilibrated with elution buffer (10 mM HEPES, 150 mM NaCl, 50 µM GDN pH 7.6) and eluted in the same buffer. Proteins were identified by monitoring the fluorescence emitted by the attached Venus YFP. All steps were performed at 4 °C.

4.4.2 Purification from HEK cells

Cells were thawed on ice and lysed with lysis buffer (25 mM HEPES, 150 mM NaCl, 1% lauryl maltose-neopentyl glycol (LMNG), 0.5 mM $CaCl_2$, 2 mM $MgCl_2$, protease inhibitors, RNase, DNase, pH 7.6). The resuspended cells were incubated at 4 ºC for 1 hour under gentle agitation. For CALHM4 purification in Ca^{2+}-free conditions, Ca^{2+} was replaced by 5 mM EGTA after extraction. Lysates were clarified by centrifugation at 15,000 rcf for 15 minutes to remove debris. Supernatants filtered through a 0.5 µm filter were applied to Strep-Tactin Superflow affinity resin and incubated with the slurry for 2.5 hours under gentle agitation. For the tandem affinity purification, the supernatants were applied to Ni-NTA affinity resin prior to this step. In both affinity chromatography steps, unbound proteins were removed by washing of the resin with wash buffer ((10 mM HEPES, 150 mM NaCl, 50 µM GDN, 2 mM $CaCl_2$/2 mM EGTA, pH 7.6), and bound proteins were eluted with elution buffer (resin containing 10 mM HEPES, 150 mM NaCl, 50 µM GDN, 2 mM CaCl2 and 300 mM imidazole, pH 7.6 for elution from Ni-NTA resin and 10 mM HEPES, 150 mM NaCl, 50 µM GDN, 2 mM CaCl2 and 10 mM d-desthiobiotin, pH 7.6 for elution from Strep-Tactin resin). For cleavage of fusion tags, eluates were incubated with a 1:1 molar ratio of 3C protease for 30 min. Samples were then concentrated using Amicon Ultra 15 mL centrifugal filters (100 kDa cut-off, Ultracel), filtered through 0.22 µm filters and subjected to size exclusion chromatography on a Superose 6 10/300 GL column equilibrated with SEC buffer (10 mM HEPES, 150 mM NaCl, 50 µM GDN, 2 mM CaCl2/2 mM EGTA, pH 7.6). Peak fractions were pooled and concentrated on 100 kDa MWCO centrifugal filters. All steps were performed at 4 °C.

4.4.3 Purification from bacterial cultures

Bacterial pellets from 50 mL cultures were suspended in 5 ml periplasmic extraction buffer (20% sucrose (w/v), 50 mM Tris-HCl pH 8.0, 0.5 mM EDTA, 0.5 µg/ml lysozyme) and lysed for 30 min with agitation. TBS (20 mM Tris-HCl, 150 mM NaCl, pH 7.4) supplemented with 1 mM $MgCl_2$ was then added to the lysate and the cell debris was pelleted at 4000 rcf for 20 min. The supernatant was supplemented with imidazole to a final concentration of 15 mM. 500 µl Ni-NTA resin was added to the supernatant and incubated for 1 hour. The resin was then retained in a gravity column and washed with TBS supplemented with 30 mM imidazole. Sybodies were eluted with TBS supplemented with 300 mM imidazole. Eluates were filtered through a 0.22 µm centrifugal filter and subjected to size exclusion chromatography on a Sepax SRT-10C SEC100 column equilibrated in TBS.

Bacterial pellets from liter-scale cultures were resuspended in TBS supplemented with 0.1 mg/ml lysozyme at a 1:30 w/v ratio. Bacteria were lysed by three freeze-thaw cycles followed by sonication. The lysates were centrifuged at 8,000 rcf for 30 min at 4 ºC. The supernatants were collected and mixed with Ni-NTA resin and incubated for 0.5 hours. The resin was then retained in gravity columns, washed with TBS and the sybodies were eluted with TBS supplemented with 300 mM imidazole. To obtain tag-free sybodies, the eluates were incubated overnight with 3C protease while dialyzing with a MWCO of 5 kDa. The eluates were then concentrated and filtered through a 0.22 µm centrifugal filter and subjected to size exclusion on a Sepax SRT-10C SEC100 column equilibrated in TBS. Fractions of the monomeric sybody peaks were collected and stored at -80 ºC for further use.

4.5 LC-MS analysis of co-purified lipids

LC-MS analysis was carried out in collaboration with Dr. Sebastian Streb and Dr. Endre Laczko from the Functional Genomics Center Zurich. A detailed description of this analysis can be found in the manuscript resulting from this work [57].

4.6 Protein reconstitution into liposomes

Soybean polar lipid extracts supplemented with 20% or 25% (mol/mol) cholesterol or brain polar lipid extracts were solubilized in chloroform. The chloroform was evaporated under a nitrogen stream, and the lipids were washed with diethyl ether and dried by desiccation overnight. The dried lipids were then resuspended in a solution containing 100 mM KCl and 20 mM HEPES at pH 7.5 (inside buffer) to a concentration of 20 mg/ml. A fraction of liposomes was solubilized by adding 35 mM CHAPS. The liposomes were aliquoted, flash frozen in liquid nitrogen, and stored at -80 °C.

On the day of reconstitution, the liposomes were diluted to a concentration of 4 mg/ml with inside buffer. Liposomes were subjected to three freeze-thaw cycles, followed by extrusion through a 400 nm polycarbonate filter (Avestin, LiposoFast-Basic), and destabilized by stepwise addition of Triton X-100. The extent of destabilization was monitored by measuring the absorbance at 540 nm using a spectrophotometer. To the prepared solubilized and destabilized liposomes, solutions of pure proteins were added at protein-to-lipid ratios of 1:50, 1:75, or 1:100 (wt/wt). To prepare empty liposomes, an equivalent volume of SEC buffer was added. The mixtures were incubated at room temperature for 15 minutes under gentle agitation. After the incubation period, biobeads SM-2 (Biorad) were added to the mixtures at a ratio of 10 mg per 1 mg of lipids and incubated for 0.5 hours. The addition of biobeads was repeated three times after 1 hour, 2 hours, and before an overnight incubation, all at 4 °C and with gentle agitation. The next day, biobeads were separated from the sample by filtration on a gravity column at room temperature. The flow-through was collected, and the empty liposomes and proteoliposomes were harvested by ultracentrifugation at 170,000 rcf for 0.5 hours. Proteolipsomes were resuspended in

a solution containing 100 mM KCl and 20 mM HEPES at pH 7.5, to a concentration of 40 mg/ml, and stored at -80 °C. To assess the efficiency of reconstitution, proteins were re-extracted from the liposomes with a buffer containing 1% of LMNG or 2% of GDN, filtered through a 0.22 µm filter and loaded onto a Superose 6 Increase 5/150 column equilibrated in SEC buffer. The protein signal was monitored using tryptophane fluorescence. SEC profiles of extracted proteins were compared with profiles of pure untreated proteins at equivalent amount as used for reconstitution. The screening of reconstitution conditions is shown in **Figure 69**.

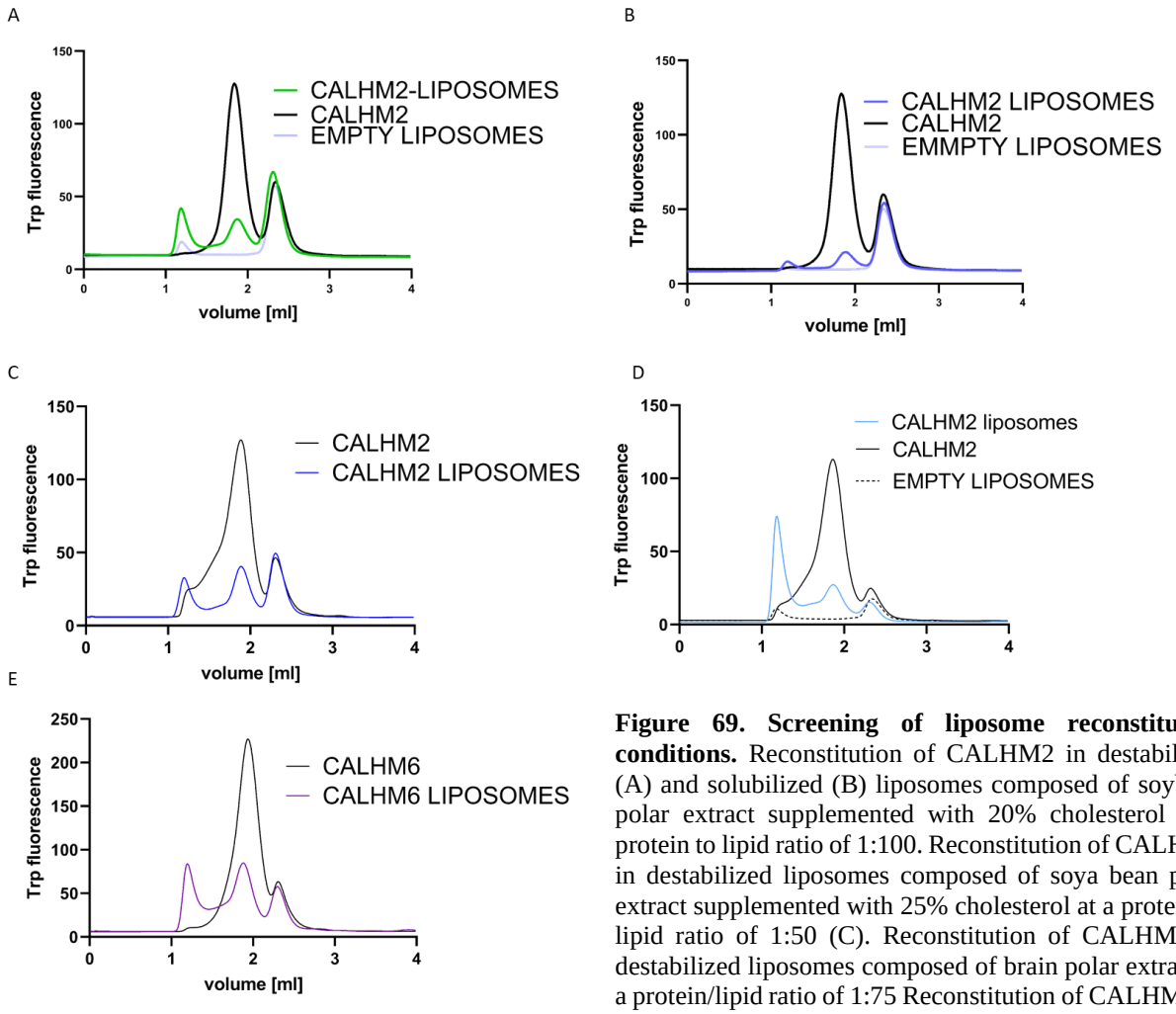

Figure 69. Screening of liposome reconstitution conditions. Reconstitution of CALHM2 in destabilized (A) and solubilized (B) liposomes composed of soybean polar extract supplemented with 20% cholesterol at a protein to lipid ratio of 1:100. Reconstitution of CALHM2 in destabilized liposomes composed of soya bean polar extract supplemented with 25% cholesterol at a protein to lipid ratio of 1:50 (C). Reconstitution of CALHM2 in destabilized liposomes composed of brain polar extract at a protein/lipid ratio of 1:75 Reconstitution of CALHM6 in destabilized liposomes composed of soya bean polar extract supplemented with 25% cholesterol at a protein to lipid ratio of 1:50 (E).

4.7 Fluorescence quenching-based proteoliposome assay

On the day of the assay, empty liposomes and proteoliposomes were resuspended in a buffer containing 20 mM HEPES, 100 mM KCl, and 250 µM calcein at pH 7.5, at a ratio of 1:400 (wt/v). The liposomes were then subjected to three freeze-thaw cycles. Next, the liposomes were extruded through a 400 nm polycarbonate filter (Avestin, LiposoFast-Basic), harvested by ultracentrifugation at 170,000 rcf for 20 minutes, washed twice with calcein-free buffer, and resuspended in this buffer to a concentration of 40 mg/ml. Subsequently, the liposome solution was diluted 100-fold in a buffer containing 20 mM HEPES and 100 mM NaCl at pH 7.5. Batches of 100 µl of the prepared liposome suspensions were aliquoted into a 96-well plate, and fluorescence was measured every 4 seconds using a Tecan Infinite M1000 fluorometer. To generate membrane potential, valinomycin was added to a final concentration of 100 nM. After 30 cycles of equilibration, manganese was added at different concentrations. The reaction was then terminated by adding calcimycin to a final concentration of 100 nM.

4.8 Two-electrode voltage clamp recordings

This part of the project was mostly performed by Dr. Maria Isabel Bahamonde Santos with assistance from the thesis author. A detailed description on the two-electrode voltage clamp recordings and cell surface biotinylation can be found in the manuscript resulting from this work [57].

4.9 Immunoprecipitation from placental tissue

Samples of human placentae (provided by Prof. Christiane Albrecht from the Institute of Biochemistry and Molecular Medicine at the University of Bern) were pre-homogenized in PBS buffer supplemented with protease inhibitors and stored at -80°C until further use. On the day of the experiment, tissues were homogenized using a rotor-stator homogenizer and sonicated for 20 minutes at 100 W in a 5-second on/3-second off cycle. To remove debris, suspensions were centrifuged at 10,000 rcf for 30 minutes at 4 °C. To isolate the membrane fraction, the supernatant was collected and centrifuged at 200,000 rcf for 1 hour at 4 °C. The membrane fractions were resuspended in a buffer containing 25 mM HEPES, 150 mM NaCl, 1% LMNG and protease inhibitors, pH 7.5. The suspension was incubated on a rotating wheel at 4 °C for 3 hours and centrifuged at 200,000 rcf at 4 °C. The supernatants were incubated overnight with magnetic beads coated with antibodies directed against either human CALHM2 or CALHM4 proteins. The next day, the beads were extensively washed with PBS buffer supplemented with 1% GDN. The progress of the experiment was monitored by Western blotting, with samples from each step probed with the appropriate antibodies. In addition, the fraction of proteins pulled down on the beads was trypsinized and peptides were extracted from the beads with a 0.1% TFA/50% acetonitrile solution. The supernatants were analyzed by LC-MS/MS at the Functional Genomic Center Zurich.

4.10 Protein biotinylation

CALHM proteins were chemically biotinylated using amine-reactive EZ-Link™ NHS-PEG4-Biotin (ThermoFisher Scientific). Proteins were diluted to a concentration of 1 mg/ml in their SEC buffers and the coupling agent was added in 8-fold molar excess. Samples were incubated for 1 hour on ice and the reaction was quenched by the addition of 5 mM Tris-HCl, pH 8.0. Excess biotin was separated from the biotinylated protein on a PD-10 desalting column. The eluted proteins were concentrated, mixed with glycerol to a final concentration of 10%, aliquoted, flash frozen in liquid N_2 and stored at -80 °C. The success of biotinylation was assessed by SDS-PAGE analysis comparing samples of CALHM proteins alone and streptavidin alone with samples of the mixture of both.

4.11 Sybody selection and ELISA screening

Sybody selection was performed as previously described[67]. Three synthetic ribosome-display libraries, named concave (G), loop (B), and convex (R) libraries, and the plasmids, were kindly provided by Prof. Markus Seeger from the Institute of Medical Microbiology, UZH. Sybodies were selected against chemically biotinylated CALHM proteins. In brief, one round of ribosome display was performed, and the output RNA was reverse transcribed and cloned into a phage-display compatible vector. The obtained plasmids were transformed into *E. coli* SS320 cells to produce phages using a helper phage M13KO7. The produced phages were then used in subsequent two rounds of phage display. Phagemids were isolated from the output phages of the second round, and the encoded sybody sequences were subcloned into the pSB_init expression vector. The resulting plasmids were transformed into *E. coli* MC1061 and the bacteria were plated on agar plates to isolate single clones. The single clones were expressed on a small scale and used for binding screening tests using an ELISA assay. Positive clones identified were sequenced.

4.12 Binding tests

4.12.1 SEC binding assay

Pure CALHM proteins were mixed with pure sybodies in a ratio of 1:2 to a final concentration of 25 µM CALHM proteins. Prior to mixing, sybodies were supplemented with GDN to a final concentration of 50 µM. Samples of CALHM proteins alone and protein mixtures were applied to a Superose 6 5/150 Increase column equilibrated with SEC buffer. Protein signal was monitored by absorbance at 280 nm. Peak fractions corresponding to CALHM proteins were collected, concentrated using Amicon Ultra 0.5 mL centrifugal filters (10 kDa cut-off, Ultracel) and analyzed by SDS-PAGE.

4.12.2 Pulldown binding assays

Adherent HEK293T cells were transiently transfected with mixtures of two vectors in a 1:1 ratio. For pulldowns of CALHM4 with sybodies a mixture of vectors encoding CALHM4-vYFP fusion protein and sybody-vYFP_Myc_Strep fusion protein were used. For pull-downs between CALHM homologues cells were transfected with mixtures of vectors encoding CALHM-Myc and CALHM_vYFP_Myc_SBP or CALHM_vYFP_Myc and CALHM_vYFP_Myc_SBP. All steps of the pulldown binding assay were performed at 4 °C. Cells were lysed in lysis buffer (25 mM HEPES, 150 mM NaCl, 1% lauryl maltose-neopentyl glycol (LMNG), protease inhibitors, RNase, DNase, 0.5 mM $CaCl_2$, 2 mM $MgCl_2$, pH 7.6) for 1 hour and the lysates were cleared by centrifugation at 16,000 rcf for 10 min. The supernatants were filtered through a 0.22 µm filter and mixed with 50 µl Strep-Tactin resin equilibrated in wash buffer (10 mM HEPES, 150 mM NaCl, 50 µM GDN, 2 mM $CaCl_2$, pH 7.6). Supernatant and resin were incubated for 2 hours with gentle agitation. The resin was then retained on a gravity column, washed with wash buffer and bound proteins eluted with elution buffer (wash buffer supplemented with 10 mM d-desthiobiotin, pH 7.6). The course of the assay was monitored by SDS-PAGE analysis. In-gel fluorescence was imaged using a Viber Fusion FX7 imager, excitation wavelength 480 nm and emission wavelength 535 nm.

4.12.3 SPR measurements

SPR measurements were performed at the Functional Genomic Centre Zurich using a Biacore T200 instrument (GE Healthcare). The CALHM proteins, chemically biotinylated, were immobilized on a streptavidin-coated sensor chip (XanTec), resulting in a maximum response value of approximately 600 response units (RU). Measurements were performed at a temperature of 10 °C and a flow rate of 30 µl/min. The buffer used during the experiments consisted of 10 mM HEPES at pH 7.6, 150 mM NaCl, 2 mM $CaCl_2$ and 50 µM GDN for $CALHM_2$ or 0.01% LMNG for CALHM4. Flow cell 1 was left empty to act as a reference cell for the measurements. Prior to measurements, the system was equilibrated with the appropriate buffer for 2 hours. The sybodies RA5 and gF2 were injected in a single cycle kinetic measurement at concentrations of 7.8, 15.6, 31.25, 125 and 500 nM for sybody RA5 and 8, 24, 72, 216 and 648 nM for sybody gF2. The data obtained were analyzed using BIAevaluation software (GE Healthcare) and fitted to a single-site binding model where the quality of the data allowed such fits.

4.13 Negative staining EM

Copper grids with a continuous carbon film were glow discharged for 30 s using low pressure air plasma. Purified protein solutions were diluted to a concentration of 0.03 mg/ml and 2 µl samples were applied to the grids for 1 min. Excess solutions were removed from the edge with a piece of filter paper and 2 µL of 1% uranyl acetate was applied for 1 min. Excess stain was removed with filter paper and the grids were allowed to dry. The samples were imaged using a Tecnai G2 Spirit electron microscope.

4.14 Cryo-EM sample preparation and data collection

Samples of pure proteins and protein mixtures were applied to glow-discharged holey carbon grids (Quantifoil R1.2/1.3 or R0.6/1 Au 200 mesh). Excess liquid was removed in a controlled environment (4 °C and 100% relative humidity) by blotting grids for 2–6 s. Grids were subsequently flash frozen in a liquid propane-ethane mix using a Vitrobot Mark IV (Thermo Fisher Scientific) and stored in liquid nitrogen. Details on sample preparation are found in **Table 1.**

Samples of homomeric CALHM proteins were imaged in a 300 kV Tecnai G^2 Polara (FEI) with a 100 μm objective aperture and data were collected using a post-column quantum energy filter (Gatan) with a 20 eV slit and a K2 Summit direct detector (Gatan) operating in counting mode. Dose-fractionated micrographs were recorded in an automated manner using SerialEM[93] with a defocus range of –0.8 to –3.0 μm. Datasets were recorded at a nominal magnification of 37,313 corresponding to a pixel size of 1.34 Å/pixel.

Samples of CALHM proteins in complex with sybodies were imaged in a 300 kV Titan Krios G3i with a 100 μm objective aperture and data were collected using a post-column BioQuantum energy filter with a 20 eV slit and a K3 direct electron detector operating in a super-resolution counted mode. Dose-fractionated micrographs were recorded with a defocus range of -1 μm to -2.4 μm in an automated mode using EPU 2.9. Datasets were recorded at a nominal magnification of 130,000 corresponding to a pixel size of 0.651 Å per pixel (0.3255 Å per pixel in super-resolution mode). More details regarding data collection are found in **Table 1.**

Sample	CALHM concentration [μM]	Sybody excess	Microscope	pixel size [Å]	Electron exposure [e–/Å^2]	Electron exposure/frame [e$^-$/Å^2/frame]	Total exposure time [s]	number of collected micrographs
CALHM2	40	-	FEI Tecnai G^2 Polara	1.34	55	1.4	12	2 116
CALHM4 in 2 mM Ca^{2+}	83	-	FEI Tecnai G^2 Polara	1.34	40	1.3	12	1 693
CALHM4 in 5 mM EDTA	97	-	FEI Tecnai G^2 Polara	1.34	32	1	12	1 077
CALHM6	40	-	FEI Tecnai G^2 Polara	1.34	40	1.3	12	1 704
CALHM2 with RA5	20	1.5	FEI Titan Krios	0.3255	72	2	1	9 232
CALHM4 with gF2	47	1.5	FEI Titan Krios	0.3255	70	1.9	1	3 696
CALHM4 with rD10	43	1.5	FEI Titan Krios	0.3255	70	1.9	1	1 669
CALHM2/4 with gF2	~38	1.5	FEI Titan Krios	0.3255	60	1.3	1.26	18 906
CALHM2/4 with gF2 and RA5	~45	1.5 and 2.5	FEI Titan Krios	0.3255	60	1.3	1.26	18 958

Table 1. Details on cryo-EM sample preparation and data collection.

4.15 Cryo-EM image processing

Micrographs from all datasets were pre-processed in a similar manner. Micrographs of datasets of samples of CALHM2 with sybody RA5 and CALHM2/4 with sybodies gF2 only and both sybodies gF2 and RA5 were additionally binned prior to processing resulting in a pixel size of 0.651Å.

CALHM

For datasets of CALHM proteins not containing sybodies, the raw movies were used for correction of the beam-induced movement using a dose-weighting scheme in RELION's own implementation of the MotionCor2 algorithm available in version 3.0[94]. The CTF parameters were estimated on summed movie frames using CTFFIND4.1[95]. Low-quality micrographs showing a significant drift, ice contamination or poor CTF estimates were discarded.

CALHM2

Visual inspection of micrographs in the CALHM2 dataset during pre-processing hinted at a preferential orientation of particles. 2D class averages generated from the particles picked with the Laplacian-of-Gaussian method showed primarily views from the extracellular side with a small percentage of side or tilted views, similar to those found in CALHM4 datasets (showing dihedrally-related dimers) and the CALHM6 dataset (showing monomers). In order to recover projections at orientations other than from the extracellular side, representative 2D class averages of CALHM4 and 6 were combined and used as 2D templates for auto-picking. The pool of 417,612 particles was subjected to two rounds of 2D classification, after which the dataset was reduced to 71,555 particles. 2D class averages showed that the majority of the remaining particles comprised a view from the extracellular side with only a small fraction representing other orientations. As a consequence of this preferential orientation, projections from other angles were underpopulated and did not show high-resolution features. In order to separate monomeric and dimeric populations, non-symmetrized 3D classification was performed using low-pass filtered reconstructions of CALHM4 and CALHM6. However, both monomeric and dimeric 3D reconstructions of CALHM2 suffered from missing views and therefore did not converge to a reliable model during 3D auto-refinement. Additional 2D classification on particles classified either as CALHM2 monomers or dimers showed a significant amount of remaining heterogeneity in form of undecameric and dodecameric assemblies, which together with the preferential orientation impeded a high-resolution reconstruction from this dataset.

Ca^{2+}-CALHM4

The dataset of CALHM4 in presence of calcium was processed with the RELION version 3.0[69]. Particles of CALHM4 were initially picked using the Laplacian-of-Gaussian method and subjected to 2D classification. 2D class averages showing protein features were subsequently used as templates for more accurate auto-picking as well as input for generating an initial 3D model. 422,281 particles were extracted with a box size of 234 pixels, down-scaled three times and subjected to 2D classification. Having discarded particles not containing protein or particles of poor quality, the dataset was reduced

to 201,782 particles. Two rounds of non-symmetrized 3D classification using the 60 Å low-pass filtered initial 3D model as a reference allowed to isolate two populations of homogenous particles representing dihedrally-related decameric and undecameric assemblies. These two subsets were refined separately with either D10 or D11 symmetry imposed followed by unbinning to an original pixel size and iterative rounds of 3D refinement, per-particle CTF correction and Bayesian polishing[95,96]. Extra 3D classification without angular alignment showed increased flexibility within the dimerization interface of interacting intracellular regions in the decameric assembly while no such flexibility was observed for the undecameric population. In order to improve the resolution of the reconstructions, localized reconstruction was performed. For this purpose, the signal corresponding to the detergent belt and to one dihedrally-related monomer was subtracted from each particle followed by auto-refinement of merged in silico modified particles in the presence of a soft mask around the protein density with either C10 or C11 symmetry imposed. The final map of the decameric and undecameric assembly was improved to 4.07 Å and 3.92 Å, respectively. The maps were sharpened using isotropic b-factors of –200 Å^2 and –177 Å^2, respectively.

Ca^{2+}-free CALHM4

The dataset of CALHM4 in an absence of calcium was processed in RELION version 3.0. Particles of CALHM4 were initially picked using the Laplacian-of-Gaussian method and subjected to 2D classification. 2D class averages showing protein features were subsequently used as templates for more accurate auto-picking as well as input for generating an initial 3D model. 576,841 particles were extracted and cleaned by 2D classification. The pool, reduced to 97,978 particles, was subjected to non-symmetrized 3D classification that also yielded two populations of dihedrally-related decameric and undecameric assemblies. The final map of the decameric assembly at 4.07 Å and of the undecameric assembly at 3.69 Å was sharpened using isotropic b-factors of –169 Å^2 and –126 Å^2, respectively.

CALHM6

The dataset of CALHM6 was processed in RELION version 3.0[69]. Particles of CALHM6 were initially picked using the Laplacian-of-Gaussian method and subjected to 2D classification. 2D class averages showing protein features were subsequently used as templates for more accurate auto-picking and as input for generating an initial 3D model. 216,859 particles were extracted with a box size of 200 pixels and reduced to 201,761 particles after 2D classification. Non-symmetrized 3D classification also revealed decameric and undecameric populations, although no dihedrally-symmetrized dimers, as in case of CALHM4 in the presence and absence of Ca^{2+}, were observed. The final auto-refined map of the decameric assembly at 4.39 Å and of the undecameric assembly at 6.23 Å was sharpened using isotropic b-factors of –259 Å^2 and –435 Å^2, respectively.

In all cases, resolution was estimated in the presence of a soft solvent mask and based on the gold standard Fourier Shell Correlation (FSC) 0.143 criterion[97-99]. High-resolution noise substitution was applied to correct FSC curves for the effect of soft masking in real space[97]. The local resolution was estimated using RELION.

CALHM in complexes with sybodies

For datasets of CALHM proteins in complex with sybodies, the raw movies were used to correct for beam-induced motion using patch motion correction in cryoSPARC v.3.2.0 and v.4.0.3, followed by patch CTF estimation[100], unless stated otherwise. Poor quality images with significant drift, ice contamination or poor CTF estimates were discarded.

CALHM2 in complex with sybody RA5

In CALHM2 dataset in complex with the sybody RA5, particles were initially picked with the blob picker and subjected to 2D classification to generate 2D average templates for more accurate template-based particle picking. Particles were selected and extracted with a box size of 512 pixels, downscaled twice. Particles were then subjected to four rounds of 2D classification to remove false positives and low-quality particles. This procedure resulted in 62,286 particles that were subjected to an *ab initio* reconstruction with three classes. The classes obtained included decameric, undecameric and ambiguous assemblies of CALHM2. Particles belonging to classes showing an undecameric assembly were further sorted by a round of heterogeneous refinement using three *ab initio* reconstructions as references. The same procedure was used for particles belonging to classes showing a decameric assembly, which yielded a low-quality reconstruction. Therefore, further processing was restricted to the more promising undecameric assemblies. The quality of the reconstruction was further improved by CTF global and local refinements and non-uniform refinement with C11 symmetry imposition, yielding a map at 3.07 Å. The local resolution was estimated with cryoSPARC. To improve the resolution of the CALHM-sybody interface region, a local refinement with C11 symmetry imposed was performed in the presence of a tight mask restricted to the region surrounding the sybody binding site, yielding a reconstruction of this region at a global resolution of 2.8 Å. To assess the structural heterogeneity of the first transmembrane helix, the particles yielding a final map were subjected to a procedure combining symmetry expansion and signal subtraction. All subunits were subtracted and subjected to 3D variability analysis with the resolution of the map low-pass filtered to 9Å. Two different final states were generated, likely representing two different conformations of the first transmembrane helix.

CALHM4 in complex with sybody gF2 and rD10

The cryo-EM datasets were processed in RELION-3.1[69]. Particles were first selected by Laplacian-of-Gaussian based auto-picking and subjected to a first round of 2D classification to generate 2D average templates. In the case of CALHM4-gF2, four 2D classes with protein-like features were used as references for a second template-based picking, resulting in 424,942 particles. The particles were extracted with a box size of 720 pixels and downscaled four times. A second 2D classification was performed and the particles from the five best classes were used for the initial 3D model generation, imposing C10 symmetry. The extracted particles from the second 2D classification round were subjected to a round of 3D classification using the initial model as a reference map, which was low pass filtered to 60 Å with C10 symmetry imposed. The best 3D class was selected, reducing the number of particles to 52,248. The particles were un-binned to their original pixel size and subjected to 3D refinement with

C10 symmetry imposed. Additionally CTF and aberration refinement and Bayesian polishing was applied[95,96]. The map was sharpened with an isotropic b-factor of -153 Å2, resulting in a global resolution of 3.7 Å. The CALHM4-rD10 dataset was processed in a similar manner. Template-based auto-picking using the best 2D classes as a reference resulted in 133,236 particles picked. In addition, 10 157 particles were manually picked, to enrich the scarce tilted views, and subjected to 2D classification. 2D classes with protein-like features generated with the manually picked particles were used for template-based auto-picking, resulting in 126,994 picked particles. Particles were extracted with a box size of 500 pixels and downscaled twice and used for initial 3D model generation (with C10 symmetry) and subjected to 3D classification. The best 3D class was further refined with 3D (with C5 symmetry) and CTF refinements and Bayesian polished. This approach yielded a map at a global resolution of 4 Å.

CALHM2/4 heteromers in complex with sybodies

Particles from CALHM2/4 datasets either containing sybody gF2 targeting CALHM4 only or additionally sybody RA5 targeting CALHM2 were initially picked with the blob picker and subjected to 2D classification to generate 2D templates for more accurate template-based particle picking. Particles were selected and extracted with a box size of 512 pixels, downscaled twice. Particles were then subjected to multiple rounds of 2D classification to remove false positives and poor-quality particles. This process resulted in 415,074 particles of CALHM2/4 in complex with gF2 and 336,860 particles of CALHM2/4 in complex with gF2 and RA5.

Visual inspection of the 2D classes indicated the presence of different assemblies in the datasets. To separate these assemblies, particles were exported to RELION (version 4.0)[101] and used to generate initial models. Further particles were subjected to several rounds of 3D classification, using the initial models as references. In the first two rounds of classification, low quality particles were excluded and only particles belonging to the high-quality classes were subjected to a final class 3D classification grouping them in 10 distinct classes.

In order to obtain high resolution reconstructions of complexes, particles belonging to the 2D classes showing channel dimers were excluded and only particles belonging to the high quality 2D classes with single channels were used to generate *ab initio* reconstructions. This yielded decoy reconstructions and undecameric reconstructions. Particles of undecameric reconstructions were used as input for heterogeneous refinements with three references: a decoy reconstruction and twice the same undecameric reconstruction. This resulted in reconstructions of undecameric and dodecameric assemblies. The heterogeneous refinement was repeated four times, each time using as input particles belonging to the undecameric assembly from the previous refinement and as references undecameric and dodecameric reconstructions. Resulted undecameric reconstructions were further improved with non-uniform refinement. Additionally, a CTF refinement was performed on the dataset with both sybodies RA5 and gF2. These approaches yielded maps with global resolutions of 3.9Å and 3.3Å for

the CALHM2/4-gF2 and CALHM2/4-gF2-RA5 complexes, respectively. The local resolution of the maps was estimated within cryoSPARC.

4.16 Model building and Refinement

The models were built in Coot [102]. CALHM4 model was built de novo into the cryo-EM density of the dimer of undecameric channels at 3.82 Å obtained from the CALHM4 dataset in the absence of calcium. The slightly better resolved cryo-EM density of the unpaired undecameric channel at 3.69 Å obtained by local reconstruction and a map blurred in Coot with a *b*-factor of 50 aided map interpretation. CALHM6 was built using the CALHM4 structure as reference with the aid of modified cryo-EM maps of CALHM6 which were either low-pass filtered to 6 Å, blurred in Coot with a *b*-factor of 200 or sharpened in Coot with a *b*-factor of −50. The cryo-EM density of CALHM4 was of sufficiently high resolution to unambiguously assign residues 4–83 and 94–280. The cryo-EM density of CALHM6 allowed us to assign residues 20–82 and 94–282. CALHM2 model was built using the published structure as a reference (PDB:6UIW) [73] into the cryo-EM density at 3.07 Å of undecameric channels obtained from the CALHM2-RA5 dataset. The cryo-EM density of CALHM2-RA5 allowed us to assign residues 38-88, 106-138, 156-162, 177-235, 237-307, 314-328. Sybody RA5 was initially modelled based on a high resolution structure of the sybody (PDB 1ZVH) with CDRs which interact with CALHM2 being rebuilt into the cryo-EM density. The model of the heteromeric CALHM2/4 in complex with sybodies gF2 and RA5 was built by placing nine CALHM2 subunits and two CALHM4 subunits into the cryo-EM density obtained from the CALHM2/4-gF2-RA5 dataset at 3.3 Å using the structure of the homomeric CALHM2-RA5 and homomeric CALHM4. The 19-46 region of CALHM2 in the downward conformation was built de novo. The atomic models were improved iteratively by cycles of real-space refinement in PHENIX [103]with secondary structure and 22-fold (for CALHM4), 10-fold (for CALHM6) and 11-fold (for CALHM2-RA5) NCS constraints applied followed by manual corrections in Coot. Validation of the models was performed in PHENIX. Surfaces were calculated with MSMS[104]. Figures containing molecular structures and densities were prepared with DINO (http://www.dino3d.org), PyMOL[105] and ChimeraX[106].

Appendix A: Sequence alignment of the human CALHM paralogs

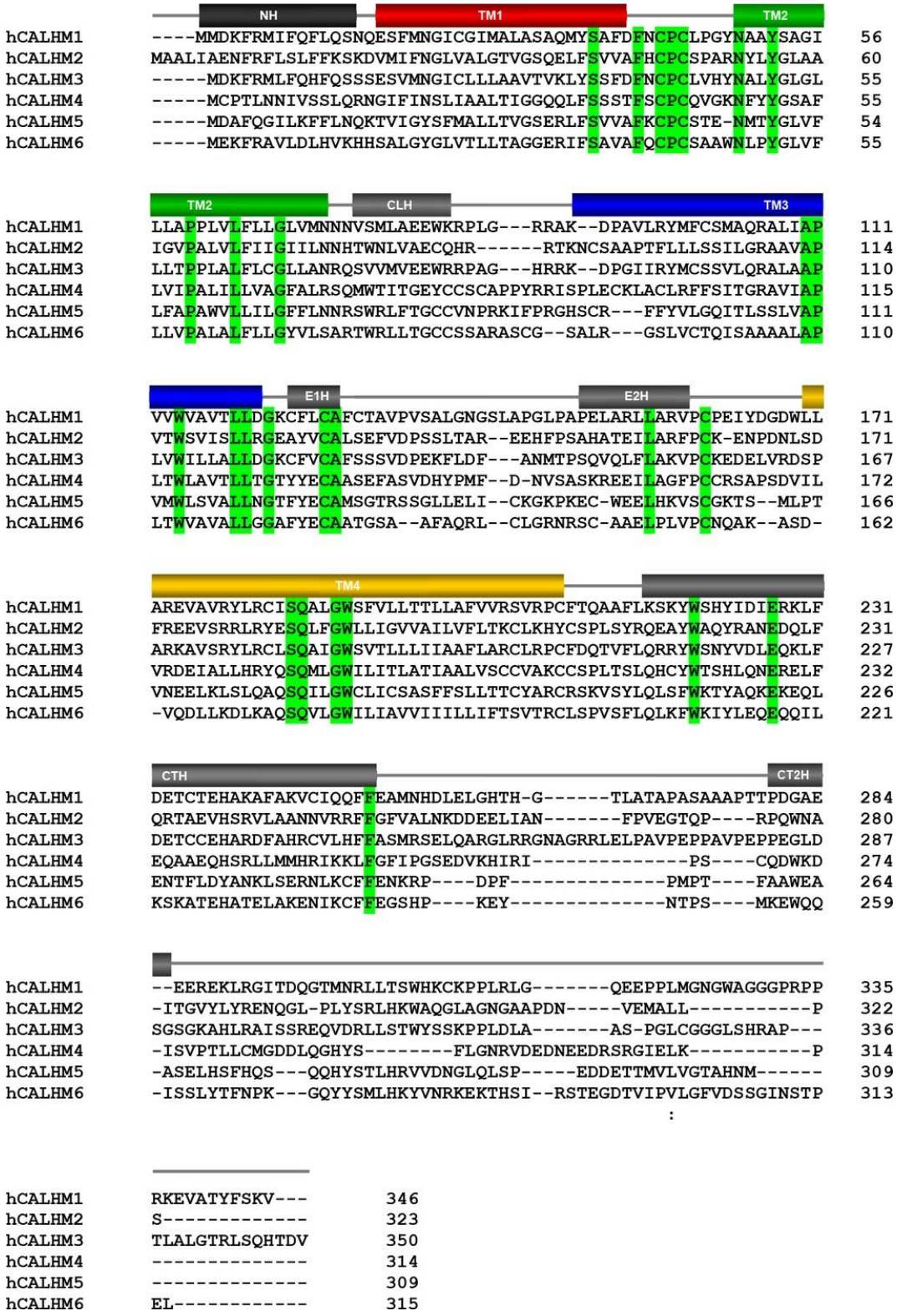

Figure from [57].

Appendix B

eLife

RESEARCH ARTICLE

Cryo-EM structures and functional properties of CALHM channels of the human placenta

Katarzyna Drożdżyk[1†], Marta Sawicka[1†*], Maria-Isabel Bahamonde-Santos[1], Zaugg Jonas[2], Dawid Deneka[1], Christiane Albrecht[2], Raimund Dutzler[1*]

[1]Department of Biochemistry, University of Zurich, Zurich, Switzerland; [2]Institute of Biochemistry and Molecular Medicine, University of Bern, Bern, Switzerland

Abstract The transport of substances across the placenta is essential for the development of the fetus. Here, we were interested in the role of channels of the calcium homeostasis modulator (CALHM) family in the human placenta. By transcript analysis, we found the paralogs CALHM2, 4, and 6 to be highly expressed in this organ and upregulated during trophoblast differentiation. Based on electrophysiology, we observed that activation of these paralogs differs from the voltage- and calcium-gated channel CALHM1. Cryo-EM structures of CALHM4 display decameric and undecameric assemblies with large cylindrical pore, while in CALHM6 a conformational change has converted the pore shape into a conus that narrows at the intracellular side, thus describing distinct functional states of the channel. The pore geometry alters the distribution of lipids, which occupy the cylindrical pore of CALHM4 in a bilayer-like arrangement whereas they have redistributed in the conical pore of CALHM6 with potential functional consequences.

*For correspondence: m.sawicka@bioc.uzh.ch (MS); dutzler@bioc.uzh.ch (RD)

†These authors contributed equally to this work

Competing interests: The authors declare that no competing interests exist.

Funding: See page 23

Received: 07 February 2020
Accepted: 05 May 2020
Published: 06 May 2020

Reviewing editor: Kenton J Swartz, National Institute of Neurological Disorders and Stroke, National Institutes of Health, United States

Introduction

The placenta, a complex organ that develops during pregnancy, serves as a hub for the exchange of nutrients and waste products between the mother and the fetus. The flow of substances across the placenta is controlled by two distinct cell-layers, namely fetal capillary endothelial cells and syncytiotrophoblasts (STB). While endothelial cells lining the fetal vessels allow to a certain extent diffusion of (small) molecules through paracellular pathways (***Edwards et al., 1993***; ***Lewis et al., 2013***), the STB layer constitutes a tight diffusion barrier. STB are polarized multinucleated cells presenting their apical side towards the maternal blood and their basal side towards the fetal capillaries. Hence, the targeted expression of receptors, channels or transport proteins of the STB determines the directionality of transport across the placenta, which is essential for the adequate development of the fetus (***Lager and Powell, 2012***). Among the transport proteins in the placenta, the role of the calcium homeostasis modulator (CALHM) family is currently unknown. In humans, the CALHM family encompasses six paralogs, some of which function as non-selective channels that are permeable to large substances such as ATP (***Ma et al., 2016***). CALHM1, the currently best characterized paralog, forms ion channels that are activated by depolarization and a decrease in the extracellular Ca^{2+}-concentration (***Ma et al., 2012***; ***Taruno et al., 2013b***) with mutations being associated with an increased risk for late-onset Alzheimer's disease (***Dreses-Werringloer et al., 2008***). Although functional on its own (***Ma et al., 2012***), in a physiological context CALHM1 probably forms heteromers with the subunit CALHM3 (***Ma et al., 2018b***). These heteromeric channels play an important role as secondary receptors for sweet, bitter and umami taste reception in type II taste bud cells by catalyzing the non-vesicular release of ATP (***Ma et al., 2018b***; ***Taruno et al., 2013a***; ***Taruno et al., 2013b***). A second paralog with an assigned physiological role is CALHM2, which is ubiquitously expressed and was proposed to mediate ATP release in astrocytes (***Ma et al., 2018a***). The role of other

paralogs has thus far remained elusive. Insight into the structural properties of the family was recently provided from studies on CALHM1 and 2 by cryo-electron microscopy (**Choi et al., 2019**; **Demura et al., 2020**; **Syrjanen et al., 2020**). CALHM2 was found to assemble into undecameric channels, which in certain cases dimerize via contacts on the extracellular side in an assembly that resembles gap-junctions. Based on this architecture, a potential role of CALHM2 as intercellular channels was proposed. Although predicted to be related to connexins and volume-regulated anion channels (VRACs) of the LRRC8 family (**Siebert et al., 2013**), the four membrane-spanning helices of the CALHM subunit exhibit a distinct arrangement, which refutes a common structural ancestry between these protein families (**Choi et al., 2019**). In contrast to CALHM2 channels, the structure of CALHM1 shows a smaller octameric organization (**Demura et al., 2020**; **Syrjanen et al., 2020**), thus suggesting that the functional properties of activation and conduction might not be conserved within the family.

In the present study we were investigating the structural and functional properties of CALHM channels in the context of the placenta. We identified the three paralogs, CALHM2, 4 and 6, to be highly expressed in this organ. A systematic comparative functional characterization by electrophysiology did not reveal pronounced activity of either of these paralogs under conditions where CALHM1 channels are open, thus suggesting that the former might be regulated by different and currently unknown mechanisms. The structural characterization of the three paralogs reveals insight into their organization and into potential gating transitions which, although related to previously described properties of CALHM2, show distinct features with respect to subunit organization, conformational changes and the distribution of lipids residing inside the wide pore of CALHM channels.

Results

Expression of CALHM channels in the human placenta

To investigate the role of CALHM channels in the placenta, we have characterized the expression of family members in healthy human placental tissues obtained from term pregnancies. Quantification of transcripts by reverse transcription (RT) PCR revealed high levels of CALHM2, 4, and 6, but comparably low expression of other paralogs (**Figure 1A**). We also analyzed the expression patterns of CALHM paralogs in primary trophoblast cells isolated from healthy term placentae and examined

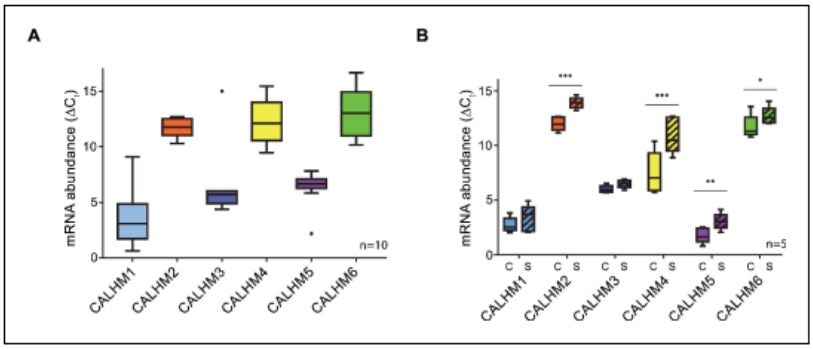

Figure 1. Expression analysis of CALHM genes in the human placenta. mRNA abundances of different CALMH paralogs in (A), human placental tissues (n = 10) and (B), human trophoblasts isolated from healthy term placentae (n = 5) was assessed by quantitative RT PCR and normalized to the reference gene YWHAZ. The relative amounts of the different CALHM genes are shown as ΔC$_t$ values (ΔC$_t$ = C$_t$ value of YWHAZ – C$_t$ value of CALHM gene). Comparative transcript data are presented as mRNA abundance (ΔCt = Ct$_{reference\ gene}$ – Ct$_{target\ gene}$) between undifferentiated cytotrophoblasts (C) and differentiated syncytiotrophoblast (S) cells. Data analysis and statistical evaluations were performed using paired 2-way ANOVA with Sidak's multiple comparisons test; *p<0.05; **p<0.01; ***p<0.001.

The online version of this article includes the following figure supplement(s) for figure 1:

Figure supplement 1. Comparative mRNA expression data for other physiologically relevant transporters/receptors in the human placenta.

changes during the differentiation process of trophoblast precursor cells into mature STB. We found marked upregulation of CALHM2, 4 and 6 during differentiation, which was most pronounced for CALHM4 (**Figure 1B**) and which might indicate a differentiation-dependent role of these proteins in the human placenta. In all cases, the concentrations of the respective CALHM mRNAs are high in comparison to other transport proteins (**Figure 1—figure supplement 1**) suggesting their involvement in important placenta-related membrane transport processes.

Functional characterization of CALHM paralogs

Due to the abundance of CALHM2, 4, and 6 in the placenta, we have focused our subsequent investigations on these three paralogs. Apart from CALHM2, which was described to form ATP-conducting channels in astrocytes (**Ma et al., 2018a**), they have so far not been characterized. For a functional comparison of channels composed of the three placental subunits with the well-studied protein CALHM1, we have expressed the homomeric proteins in *X. laevis* oocytes and recorded currents by two-electrode voltage-clamp electrophysiology. This method has previously allowed a detailed characterization of CALHM1, which is activated by depolarization and the removal of Ca^{2+} from the extracellular side (**Ma et al., 2012**). To detect proteins in the plasma membrane, we have used a surface-biotinylation approach and found all placental paralogs to be expressed and targeted at high levels to the surface of oocytes at the time of the measurement (*i.e.* 40–60 hr after injection of mRNA) (**Figure 2A**). Assuming that CALHM proteins form channels of large conductance, we thus can directly compare the average magnitude of recorded currents between populations of oocytes expressing the respective constructs and relate their activation properties in response to voltage change and the depletion of extracellular Ca^{2+} to the well-characterized CALHM1. In our studies, we were able to reproduce the functional hallmarks of CALHM1, which are manifested in the absence of currents at negative voltage and slowly activating currents at positive voltage at millimolar concentrations of extracellular Ca^{2+} and a strong increase of currents upon Ca^{2+} removal in the entire voltage range (**Figure 2**, **Figure 2—figure supplement 1A and B**). In contrast to CALHM1, the current response of homomeric CALHM2, 4, and 6 channels was generally small and within the range of endogenous currents of *X. laevis* oocytes not expressing any of the proteins (**Figure 2A**, **Figure 2—figure supplement 1C-F**). These currents neither showed pronounced voltage-dependence nor were they altered by Ca^{2+}-removal in a statistically significant manner (**Figure 2B–D**). We thus conclude that the CALHM channels expressed in the placenta are not regulated in a similar manner as CALHM1-subunit containing channels and that their activation instead proceeds by distinct, currently unknown mechanisms.

Biochemical characterization and structure determination of CALHM2, 4, and 6

For a biochemical and structural characterization of placental CALHM channels, we have expressed constructs coding for human CALHM2, 4 and 6 in HEK293 cells. In contrast to the poor yields obtained for human CALHM1, all three placental paralogs expressed high levels of protein. The elution properties of fusions to green fluorescent protein (GFP) extracted in the detergent glycol-diosgenin (GDN) and analyzed by fluorescent size-exclusion chromatography (FSEC) (**Kawate and Gouaux, 2006**) indicate assemblies of high molecular weight (**Figure 3—figure supplement 1A**). We next proceeded with a scale-up of homomeric CALHM2, 4 and 6 channels in HEK293 cells and purified each protein in the detergent GDN. Consistent with FSEC studies, all purified constructs eluted as large oligomers during gel-filtration chromatography, although at different volumes. The highest elution volume was observed for CALHM6, a similar but slightly lower volume for CALHM2 and the smallest volume for CALHM4, thus hinting towards distinct oligomeric organizations of the three proteins with CALHM4 forming larger complexes than CALHM6 (**Figure 3—figure supplement 1B**). The peak fractions were concentrated, vitrified on cryo-EM grids and used for data collection by cryo-electron microscopy (**Figure 3—figure supplements 2–6**, **Tables 1–2**). As expected from the size-exclusion profiles, all paralogs form large and heterogenic multimeric assemblies containing between 10 and 12 subunits. Whereas in the CALHM6 sample a vast majority of these oligomeric channels do not interact (**Figure 3B**, **Figure 3—figure supplement 4**), we have found almost complete dimerization for CALHM4 (**Figure 3A**, **Figure 3—figure supplements 2–3**) and a significant fraction of particles to dimerize in case of CALHM2 (**Figure 3C**, **Figure 3—figure supplement**

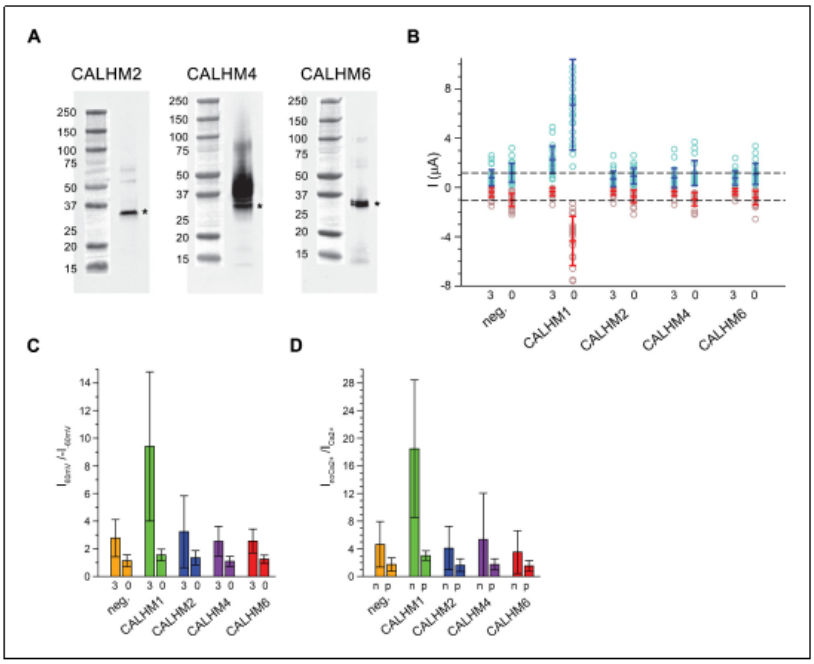

Figure 2. Functional characterization of CALHM channels expressed in *X. laevis* oocytes. (A) Western blot of proteins located in the plasma membrane of *X. laevis* oocytes heterologously expressing the indicated CALHM channels. Protein was isolated after surface-biotinylation by binding to avidin-resin. The proteins are detected with specific antibodies recognizing the respective CALHM paralog. Left, CALHM2, center CALHM4, right CALHM6. The blot demonstrates the targeting of all three paralogs to the plasma membrane. Bands corresponding to the respective CALHM paralogs are indicated by asterisk. (B) Electrophysiological characterization of *X. laevis* oocytes heterologously expressing the paralogs CALHM1, CALHM2, CALHM4 and CALHM6 in comparison to control oocytes (neg.) recorded at extracellular solutions either containing 3 mM Ca^{2+} (3) or 0.5 mM EDTA and 0.5 mM EGTA (Ca^{2+}-free, 0). Data show currents of individual oocytes (circle) recorded by two-electrode voltage-clamp (TEVC) at 60 (light blue) and −60 mV (light red). In each case, currents were tabulated at the end of a 5 s voltage step. Averages are shown as bars in red (−60 mV) and blue (60 mV), respectively. Dashed lines indicate mean current levels of control oocytes (neg.) recorded in Ca^{2+}-free extracellular solutions at 60 and −60 mV. Currents measured for all investigated channels, except CALHM1, are not significantly different from control oocytes (as judged by a Student t-test). (C), Rectification of steady-state currents of oocytes displayed in (B) expressed as I_{60mV}/I_{-60mV} calculated for individual oocytes at 3 mM Ca^{2+} (3) and in Ca^{2+}-free solutions (0) and averaged. The large value of CALHM1 reflects the activation of the protein at positive voltage in presence of Ca^{2+}. (D) Ca^{2+}-dependence of activation. Change of steady-state currents of oocytes displayed in (B) after Ca^{2+}-removal expressed as I_{noCa2+}/I_{Ca2+} calculated from individual oocytes at −60 mV (n) and 60 mV (p) and averaged. The large value of CALHM1 at −60 mV reflects the strong activation of currents at negative voltages upon Ca^{2+}-depletion. C, D, The difference between the corresponding values of the CALHM paralogs 2, 4, and 6 and neg. are statistically insignificant (as judged by a Student t-test). B-D, Data show averages of 27 (neg.), 21 (CALHM1), 26 (CALHM2), 19 (CALHM4) and 21 (CALHM6) oocytes respectively. Errors are standard deviations.
The online version of this article includes the following figure supplement(s) for figure 2:

Figure supplement 1. Electrophysiology traces.

Table 1. Cryo-EM data collection, refinement and validation statistics of CALHM4.

	Dataset 1				Dataset 2		
	CALHM4_Ca^{2+}				CALHM4_Ca^{2+}_free		
	10-mer		11-mer		10-mer	11-mer	
Data collection and processing							
Microscope	FEI Tecnai G^2 Polara				FEI Tecnai G^2 Polara		
Camera	Gatan K2 Summit + GIF				Gatan K2 Summit + GIF		
Magnification	37,313				37,313		
Voltage (kV)	300				300		
Electron exposure (e–/Å^2)	40				32		
Defocus range (μm)	-0.8 to -3.0				-0.8 to -3.0		
Pixel size (Å)	1.34				1.34		
Initial particle images (no.)	422,281				576,841		
Final particle images (no.)	35,229	70,458[♦]	27,094	54,188[♦]	21,264	25,703	51,406[♦]
Reconstruction strategy[2T]	Std	Loc	Std	Loc	Std	Std	Loc
Symmetry imposed	D10	C10	D11	C11	D10	D11	C11
Global map resolution (Å) FSC threshold 0.143	4.24	4.07	4.02	3.92	4.07	3.82	3.69
Map resolution range (Å)	4.0-5.1	3.8-5.0	3.8-5.0	3.8-5.0	3.8-5.0	3.6-4.4	3.5-4.3
Map sharpening *B* factor (Å^2)	-200	-200	-185	-177	-169	-145	-126
EMDB identifier	10920	10920[♦T]	10921	10921[♦T]	10917	10919	10919[♦T]
Refinement		N/A		N/A			N/A
Model resolution (Å) FSC threshold 0.5	4.2		4.0		4.0	3.7	
Model composition Non-hydrogen atoms Protein residues	 41,620 5,340		 45,782 5,874		 41,620 5,340	 45,782 5,874	
B factors (Å^2) Protein	62		61		34	51	
R.m.s. deviations Bond lengths (Å) Bond angles (°)	 0.005 0.694		 0.005 0.672		 0.003 0.550	 0.005 0.754	
Validation MolProbity score Clash score Poor rotamers (%)	 1.53 10.19 0		 1.57 6.50 0		 1.48 7.59 0	 1.73 9.79 0	
Ramachandran plot Favored (%) Allowed (%) Disallowed (%)	 98.10 1.90 0		 96.66 3.34 0		 97.72 2.28 0	 96.65 3.35 0	
PDB identifier	6YTO		6YTQ		6YTK	6YTL	

[♦]Subparticles from localized reconstruction.

[2T]Std – standard reconstruction; Loc – localized reconstruction.

[3T]Higher-resolution map from localized reconstruction submitted as an additional map under the same entry as the main map.

6). Unlike to previous reports of CALHM2 structures, where interactions between channels were mediated by extracellular loops (***Choi et al., 2019***; ***Syrjanen et al., 2020***), the pairing in the CALHM4 sample proceeds via contacts at the intracellular side (***Figure 3A***). We also observed two distinct protein conformations in our data with CALHM4 and CALHM6 channels forming cylindrical and conical pores, respectively (***Figure 3D***). Although 2D class averages of CALHM2 appear of high quality, 3D classification of this dataset did not yield high-resolution structures. We believe that the strong preferential orientation of CALHM2 particles resulting in a predominance of views along the

Table 2. Cryo-EM data collection, refinement and validation statistics of CALHM6 and CALHM2.

	Dataset 3 CALHM6_Ca^{2+}		Dataset 4 CALHM2_Ca^{2+}
	10-mer	11-mer	
Data collection and processing			
Microscope	FEI Tecnai G^2 Polara		FEI Tecnai G^2 Polara
Camera	Gatan K2 Summit + GIF		Gatan K2 Summit + GIF
Magnification	37,313		37,313
Voltage (kV)	300		300
Electron exposure (e–/Å^2)	40		55
Defocus range (μm)	-0.8 to -3.0		-0.8 to -3.0
Pixel size (Å)	1.34		1.34
Initial particle images (no.)	216,859		417,612
Final particle images (no.)	98,104	63,310	N/A
Reconstruction strategy[a]	Std	Std	Std
Symmetry imposed	C10	C11	C1
Global map resolution (Å) FSC threshold 0.143	4.39	6.23	N/A
Map resolution range (Å)	4.3-5.1	5.0-7.0	N/A
Map sharpening *B* factor (Å^2)	-259	-435	N/A
EMDB identifier	10924	10925	N/A
Refinement			N/A
Model resolution (Å) FSC threshold 0.5	4.4	6.6	
Model composition			
Non-hydrogen atoms	19,560	21,516	
Protein residues	2,520	2,772	
B factors (Å^2)			
Protein	85	86	
R.m.s. deviations			
Bond lengths (Å)	0.004	0.004	
Bond angles (°)	0.773	0.822	
Validation			
MolProbity score	2.14	2.15	
Clash score	16.18	17.75	
Poor rotamers (%)	0	0	
Ramachandran plot			
Favored (%)	93.55	93.95	
Allowed (%)	6.05	5.65	
Disallowed (%)	0.40	0.40	
PDB identifier	6YTV	6YTX	

[a]Std – standard reconstruction; Loc – localized reconstruction.

pore axis combined with sample heterogeneity has limited our data processing workflow to 2D classification (***Figure 3—figure supplement 6***). In general, we found an oligomeric distribution of CALHM2 channels that corresponds to previously determined structure with a majority of channels being organized as undecamers and a smaller population showing dodecameric assemblies (***Figure 3C***, ***Figure 3—figure supplement 6***). Due to the higher quality of the CALHM4 and 6 samples, we continued to use structures derived from these proteins for a detailed characterization of both pore conformations.

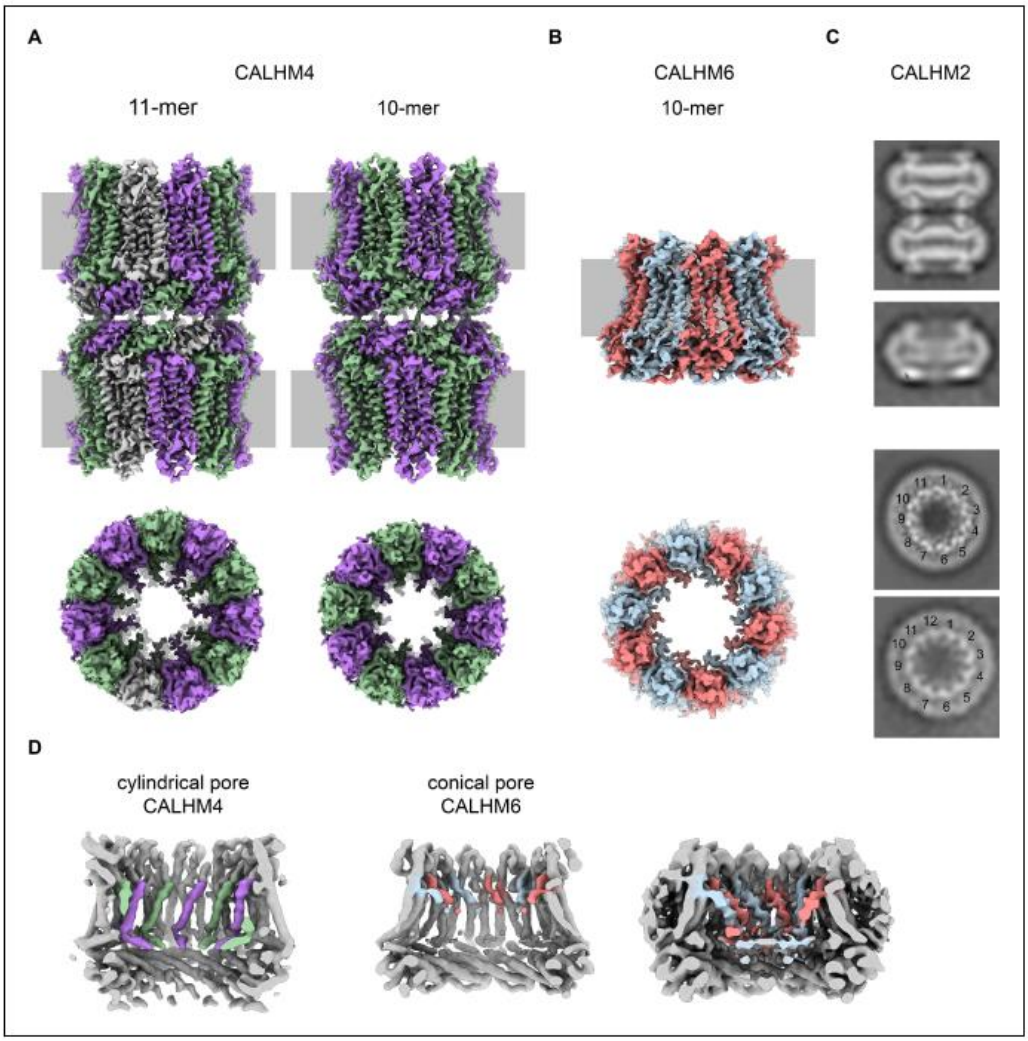

Figure 3. Cryo-EM analysis. (A) Cryo-EM density of undecameric (11-mer) and decameric (10-mer) pairs of CALHM4 channels at 3.8 and 4.1 Å respectively. Data were recorded from a Ca^{2+}-free sample. Subunits are colored in lilac and green, respectively. (B) Cryo-EM density of decameric CALHM6 channels at 4.4 Å. Subunits are colored in red and light-blue, respectively. A, B, Views are from within the membrane with membrane indicated as grey rectangle (top) and from the outside (bottom). (C) Selected 2D classes of the CALHM2 data showing interacting channel pairs and single channels viewed from within the membrane (top) and views of undecameric and dodecameric channels with subunits numbered (bottom). (D) Slices through the CALHM4 (left) and the CALHM6 (right) channels illustrating the distinct features of the cylindrical and conical pore conformations. View of CALHM6 at lower contour (right) shows extended density for the mobile TM1. Maps are low-pass filtered at 6 Å. Colored features refer to density corresponding to TM1 and NH.

The online version of this article includes the following figure supplement(s) for figure 3:

Figure supplement 1. Biochemical characterization.

Figure supplement 2. Cryo-EM reconstruction of CALHM4 in presence of Ca^{2+}.

Figure 3 continued on next page

Figure 3 continued

Figure supplement 3. Cryo-EM reconstruction of CALHM4 in absence of Ca^{2+}.
Figure supplement 4. Cryo-EM reconstruction of CALHM6 in presence of Ca^{2+}.
Figure supplement 5. Cryo-EM density of CALHM4 and CALHM6.
Figure supplement 6. Cryo-EM reconstruction of CALHM2 in presence of Ca^{2+}.

Cylindrical pore conformation of the CALHM4 structure

For the determination of the CALHM4 structure, we have recorded cryo-EM data in the presence and absence of Ca^{2+} and observed similar structural properties in both samples, which are not affected by divalent cations (***Figure 3—figure supplements 2*** and ***3***). In each case, we found a heterogeneous, about equal distribution of particles with two distinct oligomeric states. The smaller particles are composed of decameric and the larger of undecameric assemblies, both of which we refer to as CALHM4 channels (***Figure 4***). Due to the slightly higher quality of the Ca^{2+}-free sample, we continued to use this data for our further analysis unless specifically indicated. The cryo-EM density of the decamers extends to a resolution of 4.1 Å and undecamers to 3.7 Å, which in both cases permitted the unambiguous interpretation by an atomic model (***Figure 3—figure supplements 2***, ***3*** and ***5A***, ***Video 1***, ***Table 1***). In each structure, the subunits are arranged around a central axis of symmetry that defines the ion-conduction path. As described before, both assemblies contain pairs of CALHM4 channels of the same size related by two-fold symmetry that interact via their cytoplasmic parts (***Figure 4—figure supplement 1A–C***). The CALHM4 channels form approximately 90 Å high cylindrical proteins that span the lipid bilayer with regions at their respective periphery

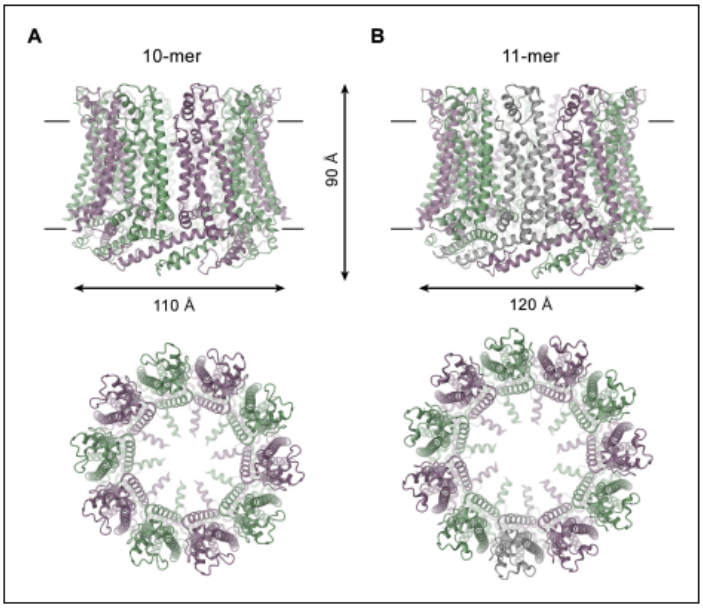

Figure 4. CALHM4 structure. Ribbon representation of (A), decameric and (B), undecameric CALHM4 channels. Top views are from within the membrane with membrane boundaries indicated, bottom views are from the extracellular side. The approximate dimensions are indicated. Subunits are colored in lilac and green.
The online version of this article includes the following figure supplement(s) for figure 4:

Figure supplement 1. Features of the CALHM4 structure.

Video 1. Cryo-EM density map of a single subunit of CALHM4 obtained in absence of Ca^{2+}. Shown is the cryo-EM map of the protein in detergent with the atomic model superimposed.
https://elifesciences.org/articles/55853#video1

extending into the aqueous environment on either side of the membrane (***Figure 4***). In the plane of the membrane, the dimensions of decameric and undecameric CALHM4 channels amount to 110 Å and 120 Å respectively (***Figure 4***, ***Figure 4—figure supplement 1D–E***). Irrespective of their distinct oligomerization, the individual subunits in both assemblies show equivalent conformations, which resemble the recently described structures of CALHM1 and 2 (***Choi et al., 2019***; ***Demura et al., 2020***; ***Syrjanen et al., 2020***) and thus define an organization that is likely general for the CALHM family (***Figure 5A***, ***Figure 5—figure supplement 1***). Although the members of this family were predicted to share their architecture with connexins and related innexin and LRRC8 channels (***Siebert et al., 2013***), this turns out not to be

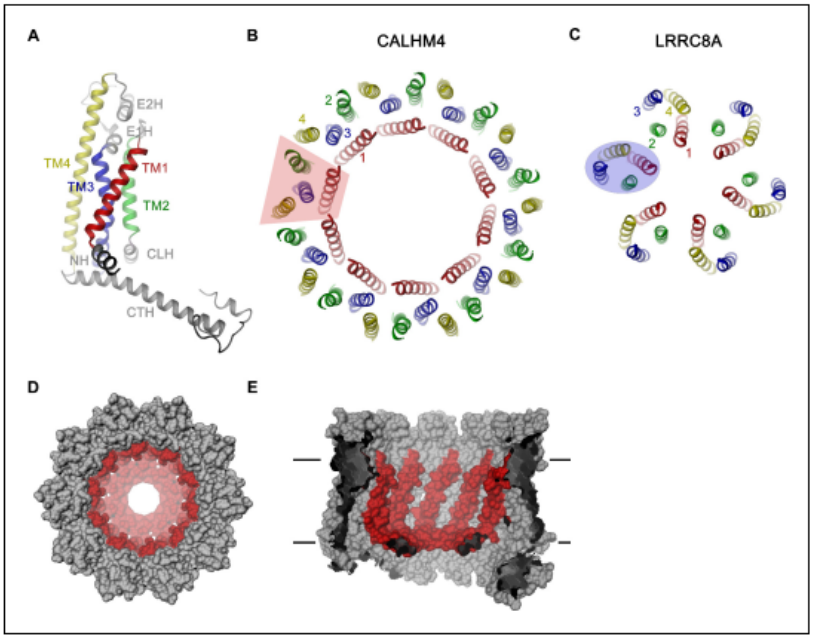

Figure 5. CALHM4 subunit and oligomeric arrangement. (A) Ribbon representation of the CALHM4 subunit. Secondary structure elements are labeled and transmembrane α-helices are shown in unique colors. View of the transmembrane α-helices of (B), the CALHM4 decamer and (C), the volume regulated anion channel LRRC8A from the extracellular side. B-C, color code is as in A, transmembrane segments of one subunit are numbered. The general shape of a single subunit is indicated (B, trapezoid, C, oval). (D) Surface representation of the CALHM4 decamer. The view is from the outside. (E) Slice through the CALHM4 pore viewed from within the membrane. D, E, TM1 and the N-terminal α-helix NH are colored in red.
The online version of this article includes the following figure supplement(s) for figure 5:

Figure supplement 1. Sequence and topology.
Figure supplement 2. Features of the CALHM4 structure.

the case. Whereas subunits in all families contain four transmembrane helices, which run perpendicular to the membrane, the mutual arrangement of these α-helices differs between CALHM channels and their connexin-like counterparts. When viewed from the extracellular side, the transmembrane helices in connexin, innexin and VRAC channels (**Deneka et al., 2018**; **Kasuya et al., 2018**; **Kefauver et al., 2018**; **Maeda et al., 2009**; **Oshima et al., 2016**) are arranged in a clockwise manner, whereas the arrangement in CALHM channels is anticlockwise (**Figure 5B,C**). Moreover, in connexins and related channels, the four helices form a tightly interacting left-handed bundle with a common core, resulting in a structure with an oval cross-section (**Figure 5C**). Conversely, the helices of the CALHM subunit are organized as two layers conferring an overall trapezoid cross-section (**Figure 5B**). Finally, whereas connexins and LRRC8 channels form hexamers, and innexins form octamers, an oligomeric arrangement that has also been observed for CALHM1, the larger CALHM4 channels contain either 10 or 11 subunits (**Figure 4A,B**). The outer layer of the CALHM subunit is composed of the interacting α-helices TM2-4, which are arranged in one row sharing mutual interactions only with their respective neighbor. The inner layer consists of TM1, which on its entire length exclusively interacts with TM3, the central helix of the outer layer (**Figure 5A,B**). When assembled into oligomers, the helices of the outer layer form a ring, which defines the boundaries of the channel (**Figure 5B**). In this outer ring, the peripheral helices TM2 and 4 are involved in extended interactions with neighboring subunits resulting in a tightly packed interface. Apart from a small fenestration between TM3 and 4 in the center of each subunit, this structural unit shields the interior of the pore from the surrounding membrane (**Figure 5—figure supplement 2A**). In contrast, the respective TM1 helices forming the inner layer are distant from each other and thus not involved in mutual inter-subunit interactions (**Figure 5D,E**). In the region preceding TM1, the residues of the N-terminus form a helix (NH) that is oriented perpendicular to the first transmembrane segment parallel to the plane of the lipid bilayer (**Figure 4**, **Figure 5D**, **Figure 3—figure supplement 5A** and **Figure 5—figure supplement 2B**). Among the family members of known structures, the conformations of NH and TM1 are best defined in CALHM4 (**Figure 3—figure supplement 5A**), whereas weaker density of these fragments in the equivalent state of CALHM1 and 2 points towards a higher mobility of this region in latter proteins (**Choi et al., 2019**; **Syrjanen et al., 2020**). On the extracellular side, a short loop bridges α-helices TM1 and 2 and an extended region containing two short α-helices (E1H and E2H), connects TM3 with the long TM4, which extends beyond the membrane plane (**Figure 5A**). Both segments of the extracellular domain are stabilized by two conserved disulfide bridges (**Figure 5—figure supplement 2C**). On the intracellular side, TM2 precedes a short helix (CLH) that projects away from the pore axis with TM3 being bent in the same direction (**Figure 5—figure supplement 2D**). Both α-helices are connected by a 12-residue long loop that is probably mobile and thus not defined in the density. Downstream of TM4, we find an extended intracellular region. The first halve of this region consists of a long α-helix (CTH), which is tilted by 70˚ towards the membrane plane. By mutual interaction with neighboring subunits, the CTH-helices form a 30 Å-high intracellular ring that extends from the membrane into the cytoplasm (**Figures 4** and **5A**, **Figure 4—figure supplement 1C**). Distal to CTH, a weakly defined 62-residue long extended loop, which contains interspersed secondary structure elements, folds back towards the intracellular ring and extends to the juxtaposed CALHM4 channel (**Figure 4—figure supplement 1B,C**). In this way the C-terminal loops mediate the bulk of the interaction relating CALHM4 channel pairs in an arrangement whose relevance in a cellular context is still ambiguous.

Pore architecture

Decameric and undecameric CALHM4 channels contain wide pores, which are cylindrical throughout except for a constriction at the intracellular membrane boundary. The diameter at both entrances of the pore measures about 52 Å and 60 Å for decameric and undecameric assemblies respectively, thus defining the properties of an unusually large channel, which could be permeable to molecular substrates (**Figure 6A**, **Figure 4—figure supplement 1D,E**). Even at the constriction located at the intracellular membrane leaflet where the respective N-terminal helices NH project towards the pore axis, the decameric channels are about 20 Å and undecameric channels 30 Å wide (**Figure 6A**). In both cases the pore would thus be sufficiently large to accommodate an ATP molecule, consistent with the notion of CALHM proteins forming ATP-permeable channels (**Figure 4—figure supplement 1D,E**). Remarkably, this large pore size is in sharp contrast to our functional characterization by electrophysiology where we did not observe appreciable currents for CALHM4 (**Figure 2A**, **Figure 2—**

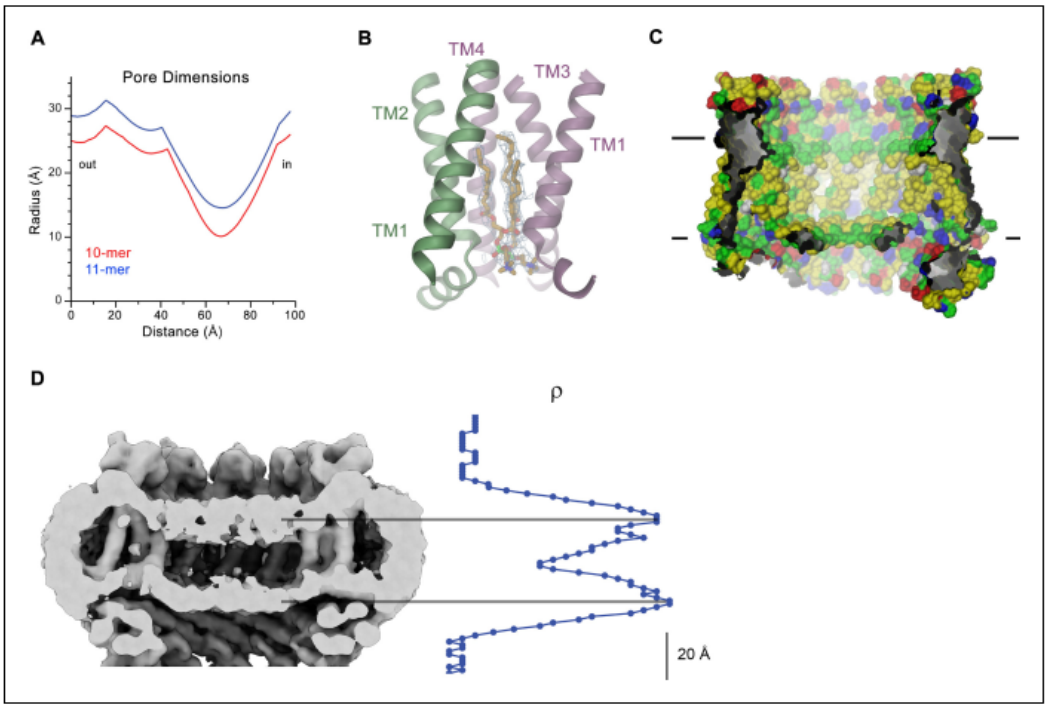

Figure 6. CALHM4 pore properties and lipid interactions. (A), Pore radius of the CALHM4 decamer (red) and undecamer (blue) as calculated in HOLE (*Smart et al., 1996*). (B) Two phosphatidylcholine molecules modeled into residual cryo-EM density (blue mesh) in a cavity at the interface between neighboring α-helices TM1. Secondary structure elements are indicated. (C) Chemical properties of residues lining the pore of the CALHM4 channel. Shown is a slice through the pore viewed from within the membrane. The protein is displayed as molecular surface. Hydrophobic residues are colored in yellow, polar residues in green, acidic residues in red and basic residues in blue. (D) Slice through the pore region of the CALHM4 undecamer viewed from within the membrane. Shown is non-averaged density in a single copy of the undecameric CALHM4 channel pair at low contour to highlight the location of increased density within the pore corresponding to a bilayer of either phospholipids or detergents. A plot of the density along the pore axis showing two maxima that are separated by the expected distance between the headgroup regions of a lipid bilayer is shown right. B, D, Displayed cryo-EM density refers to data from the undecameric channel in presence of Ca^{2+}.
The online version of this article includes the following figure supplement(s) for figure 6:

Figure supplement 1. Lipid interactions in the pore of CALHM4.
Figure supplement 2. LC-MS analysis of co-purified lipids.

figure supplement 1E), which suggests that either the absence of activating or presence of inhibiting components might impede ion conduction.

Within the membrane, the pore diameter of CALHM4 is confined by the ring of non-interacting TM1 helices, which is placed inside an outer ring of the channel formed by helices TM2-4 (*Figure 5B,D*). This arrangement creates clefts between neighboring helices of the inner ring which are delimited by helices TM2 and 4 at the respective subunit interfaces (*Figure 5B,E*). In our sample, this cleft appears to be filled with lipids as indicated by the residual density observed in the cryo-EM maps (*Figure 6B*, *Figure 6—figure supplement 1A,B*). Due to the prevalence of aliphatic residues lining the pore at the assumed location of the membrane core, the pore is highly hydrophobic, whereas the regions extending into the aqueous environment contain polar and charged residues (*Figure 6C*). Similarly, the side of the helical N-terminus, which faces the membrane at its intracellular boundary, is hydrophobic (*Figure 5—figure supplement 2B*). In light of its large cross-section

and high hydrophobicity, it is conceivable that the interior of the pore would accommodate lipids, which potentially could form bilayers that would restrict ion permeation as recently suggested for CALHM2 based on molecular dynamics simulations (*Syrjanen et al., 2020*). In our data, we find strong evidence for a layered distribution of density inside the pore within the presumed membrane region in non-symmetrized maps and after application of symmetry. This density is observed with similar properties in decameric and undecameric proteins in both datasets of CALHM4 obtained in either absence or presence of Ca^{2+} (*Figure 6D*, *Figure 6—figure supplement 1C*). Its distribution displays features that quantitatively match the corresponding properties of lipid membranes obtained from a comparison to cryo-EM density of liposomes and computer simulations (*Figure 6—figure supplement 1D,E*) and could thus either reflect the presence of lipids or detergent molecules arranging in a bilayer-like structure facilitated by the confined pore geometry. We thus analyzed the composition of small molecules that are co-purified with CALHM4 by mass spectrometry and were able to detect phospholipids that are commonly found in the membranes of HEK cells (*Figure 6—figure supplement 2*). Collectively, our data are compatible with the presence of a lipid bilayer located within the pore region of CALHM4 channels, which could interfere with the diffusion of charged substances. Thus, despite of its large pore diameter, it is at this point unclear whether the CALHM4 structure defines a conductive conformation of CALHM channel or alternatively a conformation that harbors a membrane-like assembly residing inside the pore that would impede ion conduction.

Conical pore conformation of the CALHM6 structure

As in case of CALHM4, data of CALHM6 shows a heterogeneous distribution of decameric and undecameric channels, but in this case with a prevalence of the former amounting to 60% of the classified particles (*Figure 3—figure supplement 4*). Both assemblies of CALHM6 contain subunits with equivalent conformations, which are better defined in the smaller oligomers (*Figure 3B*, *Figure 3—figure supplement 4*). We have thus chosen the decameric CALHM6 structure for a description of the conical pore of a CALHM channel (*Figures 3D* and *7A–C*). Unlike CALHM4, the lower resolution of the CALHM6 density of 4.4 Å, precludes a detailed interpretation of the structure for all parts of the protein. Still, the high homology between the two paralogs and density attributable to large side chains constrains the placement of helices and conserved loop regions and thus allows the credible analysis of major conformational differences (*Figure 3—figure supplement 5B*, *Video 2*, *Table 2*). Unlike CALHM4, there is no dimerization of CALHM6 channels and the C-terminal region following the cytoplasmic helix CTH instead appears to engage in intramolecular interactions with the outside of the cytoplasmic rim for most of its length (*Figure 7A*). This observation further supports the notion that the dimerization of CALHM4 might be a consequence of interactions formed between solubilized proteins where the mobile C-terminus could equally well engage in intra- and intermolecular interactions, of which the latter would be multiplied in the highly symmetric arrangement. Although the general organization of the CALHM6 channel closely resembles CALHM4, it shows a distinctly different state of the pore (*Figure 3D*). Upon comparison of decameric channels of both paralogs, in CALHM6 we find a slight expansion of the protein parallel to the membrane and an accompanying moderate contraction in perpendicular direction (*Figure 7—figure supplement 1A*, *Video 3*). In a superposition of the subunits, similar conformations are observed for α-helices TM2 and 4 and the C-terminal helix CTH and larger differences in the interacting helices TM1 and 3 (*Figure 7D*, *Figure 7—figure supplement 1B,C*). These differences are most pronounced for TM1, which in CALHM6 has detached from TM3 and moved by 60˚ towards the pore axis around a hinge located upstream of a conserved phenylalanine at the end of TM1 (*Figure 7B–E*). In both structures, the conformation of the proximal loop connecting TM1 and 2 is stabilized by two conserved cysteines, which are involved in disulfide bridges with the region connecting TM3 and TM4 (*Figure 7F–G*, *Figure 5—figure supplement 2C*, *Video 4*). As a consequence of the disruption of its interaction with TM1, the intracellular halve of TM3 tilts away from the pore axis by 30˚ around a pivot located close to a conserved proline residue (P115 in CALHM4), which probably destabilizes the helix (*Figure 7—figure supplement 1B,D*). The transition from a conformation observed in CALHM4 to a conformation defined by CALHM6 is accompanied by the dissociation of interactions between TM1 and 3, which are mediated by conserved residues involving a cluster of hydrophobic interactions at the extracellular side and additional interactions on the entire length of both α-helices (*Figure 7F–G*, *Figure 7—figure supplement 1C,D*, *Video 4*). The iris-like movement of TM1 in the

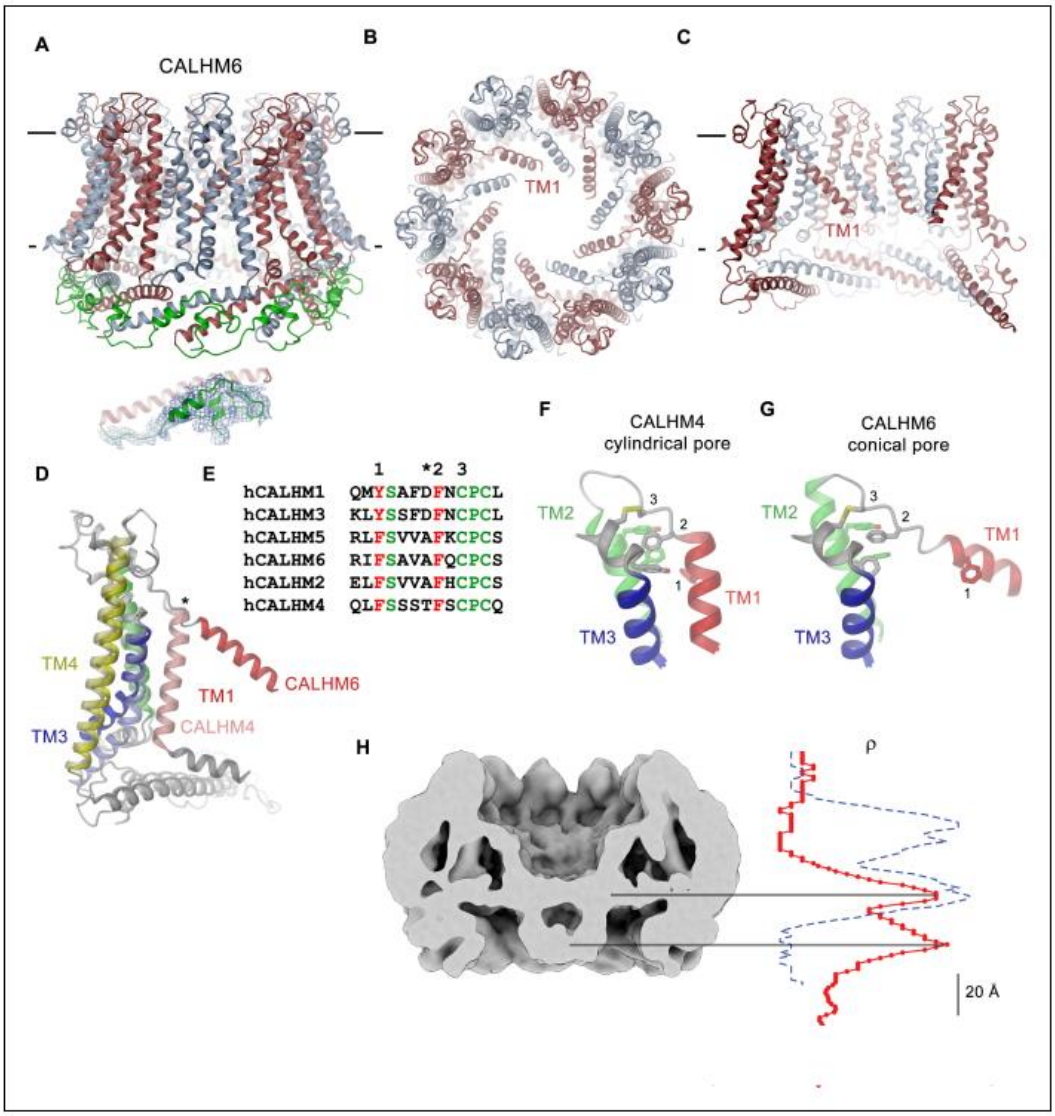

Figure 7. CALHM6 structure. (A) Ribbon representation of the decameric CALHM6 structure viewed from within the membrane. Subunits are colored in red and light blue. The C-terminus following CTH is colored in green. Inset (below) shows a close-up of this region with cryo-EM density superimposed. (B) View of the CALHM structure from the extracellular side. (C) Slice through the pore of the CALHM6 structure. B, C, TM1, which has moved towards the pore axis is labeled. A, C, the membrane boundary is indicated. (D) Superposition of single subunits of the CALHM4 and CALHM6 structures illustrating conformational changes. Coloring is as in *Figure 5A* with CALHM4 shown in brighter shades of the same color. Secondary structure elements are labeled and the hinge for the movement of TM1 is indicated by an asterisk. (E) Sequence alignment of the end of TM1 and the following loop of CALHM paralogs. Selected conserved residues are colored in green and red. Numbering corresponds to residues indicated in panels F and G. Asterisk marks the hinge region displayed in D. Close-up of the extracellular region involved in conformational changes in (F), the cylindrical

Figure 7 continued on next page

Figure 7 continued

conformation displayed in CALHM4 and (G), the conical conformation displayed in CALHM6. Residues contributing to a cluster of aromatic residues on TM1-3 and a conserved disulfide bridge are shown as sticks. Selected positions highlighted in E are labeled. F, G, Coloring is as in ***Figure 5A***. (H) Slice through the pore region of the CALHM6 decamer viewed from within the membrane. Shown is non-averaged density at low contour to highlight the location of diffuse density within the pore. A plot of the density along the pore axis of CALHM6 is shown in red, the corresponding density in CALHM4 is shown as a dashed blue line for comparison. The two maxima in the CALHM6 density are shifted towards the intracellular side. The density corresponding to the headgroups of the outer leaflet of the bilayer in CALHM4 is absent. Density at the location of the headgroup region at the inner leaflet of the bilayer and further towards the intracellular side could correspond to either lipids or to the poorly ordered N-terminus.
The online version of this article includes the following figure supplement(s) for figure 7:

Figure supplement 1. Features of the CALHM6 structure.

oligomeric channel in its transition between conformations probably requires concerted rearrangements to avoid steric clashes in the crowded environment of the pore. When viewed from the outside this transition thus resembles the closing of an aperture and it converts a cylindrical pore to a funnel which narrows towards the intracellular side while creating a large cavity between TM1 and TM3 that becomes accessible from the cytoplasm (***Figure 7C***, ***Video 3***). In the cryo-EM density, TM1 is less well defined compared to the rest of the protein reflecting its increased flexibility in the observed structure (***Figure 3—figure supplement 5B***). Since the conformation of NH, which has moved towards the pore axis, is not defined in the density, the size of the CALHM6 channel at its constriction remains ambiguous. It could range from an occluded pore if NH helices make contacts in the center of the channel (modeled as clogged conformation) to a pore with similar diameter as found at the CALHM4 constriction. The latter could be obtained in case the mutual relationship between TM1 and NH remains unchanged compared to the CALHM4 structure (defined as kinked conformation) or if NH straightens in continuation of TM1 (in an extended conformation) (***Figure 7—figure supplement 1E***). In any case, the large conformational changes would affect the location of lipids within the pore, which in case of an internal bilayer would have to rearrange in response to the severely altered pore geometry. Such rearrangement is reflected in the changed distribution of the residual electron density inside the pore (***Figure 7H***). Whereas, compared to CALHM4, we find density at the location of the intracellular layer of lipids and further towards the cytoplasm, part of which might be attributable to the mobile N-terminal α-helix NH, the outer layer of density corresponding to the putative extracellular leaflet of a bilayer has disappeared. A comparable distribution of pore density is found in the structure of CALHM2 in complex with ruthenium red, which resides in a similar conical pore conformation (***Choi et al., 2019***). Thus, despite the pronounced conformational differences to CALHM4 and the fact that the CALHM6 structure appears to contain features of a closed pore, a definitive functional assignment remains also in this case ambiguous.

Discussion

In the presented study, we have addressed the structural and functional properties of CALHM channels in the human placenta. To identify relevant CALHM paralogs in this organ, we have quantified their expression in samples of the whole placenta and in isolated trophoblast cells and found CALHM2, 4 and 6 to be abundant on a transcript level (***Figure 1***). Their high expression compared to other membrane proteins (***Figure 1—figure supplement 1***) suggests an important functional relevance of these membrane channels in mediating transport processes during the development of the fetus, although their detailed role still awaits to be explored.

The structural characterization of the three placental paralogs by cryo-electron microscopy has provided insight into fundamental features

Video 2. Cryo-EM density map of a single subunit of CALHM6. Shown is the cryo-EM map of the protein in detergent with the atomic model superimposed.
https://elifesciences.org/articles/55853#video2

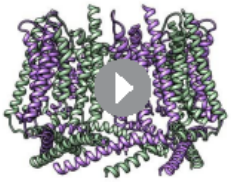

Video 3. Morph between the cylindrical pore conformation of CALHM4 and the conical pore conformation displayed in the 'extended' model of CALHM6. In the latter the N-terminal α-helix NH is modeled in continuation of TM1 resulting in a constricting pore diameter similar to CALHM4.
https://elifesciences.org/articles/55853#video3

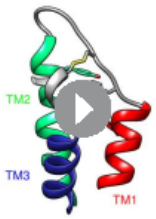

Video 4. Morph of the extracellular region of a single CALHM subunit involved in conformational changes between the cylindrical conformation displayed in CALHM4 and the conical conformation displayed in CALHM6. Residues contributing to a cluster of aromatic residues on TM1-2 and a conserved disulfide bridge are shown as sticks. Coloring is as in ***Figure 5A***.
https://elifesciences.org/articles/55853#video4

of the family which largely conform with properties that have recently been described for CALHM1 and 2 (***Choi et al., 2019***; ***Demura et al., 2020***; ***Syrjanen et al., 2020***) but which also show substantial differences. Similar to previous studies, our structures have defined the architecture of the CALHM subunit which, although containing the same number of membrane-spanning helices as VRACs and gap-junctions forming connexins, innexins and pannexins, is distinct from these proteins (***Figure 5B,C***). The CALHM subunits thus constitute unique modular building blocks that assemble with different stoichiometries into large membrane channels. In contrast to previously described CALHM structures, where the oligomeric state of individual channels was described as uniform, our data show heterogeneous populations with CALHM4 and CALHM6 assembling as decameric and undecameric channels with similar abundance and CALHM2 as predominantly undecameric proteins with a smaller population of dodecamers (***Figure 3***, ***Figure 3—figure supplements 2–4*** and ***6***). The diverse oligomerization of different paralogs is generally consistent with the assemblies observed for the previously described CALHM1 and CALHM2 structures, which were reported to form octamers and undecamers, respectively (***Choi et al., 2019***; ***Demura et al., 2020***; ***Syrjanen et al., 2020***), and it underlines the ability of CALHM proteins to constitute membrane channels of different sizes. Although the physiological role of these different oligomeric states is currently unclear, the observed heterogeneity might reflect the low energetic penalty for the incorporation of additional subunits into large oligomeric channels of the CALHM family. In this respect, the smaller size of CALHM1 channels could be responsible for its functional properties, which are manifested in electrophysiological recordings. Whereas CALHM1 in our hands showed the previously described functional hallmarks of a channel that is activated by depolarization and removal of extracellular calcium, we have not observed pronounced activity of CALHM2, 4 and 6 under the same conditions, despite their efficient targeting to the plasma membrane (***Figure 2***, ***Figure 2—figure supplement 1***). The low current response contrasts with the larger oligomeric organization of these proteins, which should lead to channels of even higher conductance than observed for CALHM1, and thus likely reflects their low open probability. Together our findings suggest that CALHM2, 4, and 6 are regulated by distinct, still unknown mechanisms. In that respect it remains puzzling how the large pores observed for the investigated structures (with diameters of CALHM4 decamers exceeding 40 Å within the membrane and 20 Å at the respective constriction, ***Figure 6A***) can be regulated to prevent leakage of substances under resting conditions, which would be deleterious to the cell. Despite the unknown activating stimuli, our study has provided insight into gating transitions of CALHM channels by showing two conformations with either a cylindrical pore of uniform large dimeter within the membrane that is constricted at the intracellular side as in case of CALHM4 and a conical pore that continuously

narrows from its extracellular entry towards the cytoplasm as in case of CALHM6 (**Figures 4** and **7**). The main difference in the pore geometry results from a large rearrangement of the pore-lining α-helix TM1 which is accompanied by a smaller change in TM3 (**Figure 7D**). Whereas in the cylindrical pore conformation of CALHM4, TM1 tightly interacts with TM3, which is a part of a densely packed outer rim of the pore consisting of TM2-4, the helix has dissociated from its interaction site and instead moved towards the symmetry axis to alter the pore geometry in the conical conformation of CALHM6. Similar conformational properties have previously been described for CALHM2 channels, although with a different orientation of TM1 in the conical pore conformation (**Choi et al., 2019**; **Figure 8—figure supplement 1A–C**). In this previous study, the cylindrical conformation was assigned to an open state and the conical conformation to a closed state of the pore, a proposal that is further supported by a structure of the bound blocker rubidium red which appears to stabilize the conical conformation (**Choi et al., 2019**; **Figure 8**). While, at first glance, the relationship between observed pore conformations and their corresponding functional states appears evident, there are still puzzling questions which prevent a definitive assignment at this stage. For example in light of the large diameter of the CALHM4 pore, the poor conductance properties in functional recordings remain mysterious. In that respect, the presence of lipids within the pore of large CALHM channels is noteworthy as it offers a potential alternative mechanism for regulation. In our structure of CALHM4, we find bound lipids inside the pore to stabilize the gap between non-interacting TM1 helices from different subunits (**Figure 6B**). Additionally, the bimodal diffuse residual cryo-EM density within the hydrophobic interior of CALHM4, which either originates form detergents or co-purified lipids that assemble as bilayers in the constrained environment of the pore are remarkable (**Figure 6D**). This distribution of density has changed markedly in the conical structure of CALHM6 (**Figure 7H**) and hints at a potential role of lipids in shaping the activation and permeation properties

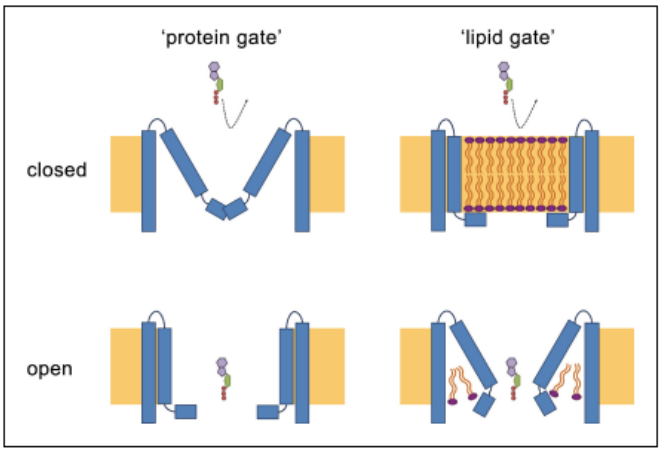

Figure 8. Hypothetical gating mechanisms. Schematic illustration of hypothetical gating mechanisms of large CALHM channels. Left, 'protein gate'. The gate impeding ion conduction of large CALHM channels (i.e. CALHM2, 4, 6) in the closed state is formed by the N-terminus of the protein, which closes the pore as observed in the modeled 'clogged' conformation of CALHM6 (top). In this case the conical conformation of CALHM6 would display a closed pore and the cylindrical conformation (bottom) an open pore. Right, 'lipid gate'. The gate impeding ion conduction of large CALHM channels in the closed state is formed by lipids assembling as a bilayer within the protein, which impedes ion conduction. Since bilayer formation is facilitated in the cylindrical conformation of CALHM4, this structure represents a closed pore (top) whereas the structure of the bilayer would be disturbed in the conical conformation of CALHM6 (bottom). Since both the 'kinked' and 'extended' pore conformations of CALHM6 show a large opening, these conformations could represent open pores.
The online version of this article includes the following figure supplement(s) for figure 8:

Figure supplement 1. Comparison of pore conformations.

of large CALHM channels, which is currently still not understood (**Figure 8**). We thus could envision two alternative scenarios which might underly regulation in large CALHM channels where the gate in the closed state could either be formed by part of the protein or by lipids (**Figure 8**, **Figure 8—figure supplement 1D**). Both models are at this stage hypothetical and it is still unclear how lipids in the pore would rearrange during activation. Another remarkable feature of large CALHM channels concerns their tendency to form pairwise assemblies upon extraction from the membranes (**Figure 3A,C**, **Figure 3—figure supplements 2**, **3** and **6**). This property has previously been observed for undecameric CALHM2 channels, which were described to dimerize on the extracellular side thus forming structures that resemble gap-junctions, and in the present study, where dimerization was found to some degree in all samples. In our data, the described behavior is most pronounced in case of CALHM4 where dimerization proceeds on the intracellular side mediated by interactions with the partly mobile C-terminus. Although intriguing, it is currently unclear whether any of the observed pairwise interactions is of relevance in a physiological context.

Thus, although our data have provided a large step forward towards the comprehension of CALHM channels, it has also opened many questions. An important area of future investigations relates to the characterization of the localization of CALHM channels in different placental cell types and the identification of their subcellular distribution. Knowledge of their localization would provide a first glimpse into potential roles of these large channels for transport processes in this organ and should provide answers on the potential relevance of intra- and extracellular interactions of channel pairs. Another question concerns the ability of the three paralogs to heteromerize and the potential relevance of such heteromeric channels in a physiological environment. Finally, it will be important to study the activation mechanism of the described channels and whether they are embedded in larger interaction networks, which shape their activation properties. These topics will be addressed in future studies for which our current data provide an important foundation.

Materials and methods

Placenta collection

Human placental tissues were collected from the Division of Obstetrics and Gynecology, Lindenhofgruppe Bern, Switzerland, under approval by the ethical commission of the Canton of Bern (approval No. Basec 2016–00250). Written informed consent was obtained from all participants. Placentas were collected from uncomplicated pregnancies following elective cesarean section beyond 37 weeks of gestation without prior labor upon patients request or due to breech presentation. All experiments were carried out in accordance with the relevant guidelines and regulations.

Expression analysis in placental tissue

RNA isolation, reverse transcription and quantitative RT-PCR

Approximately 50 mg of frozen placental tissue was subjected to RNA isolation as previously described (**Huang et al., 2012**; **Huang et al., 2013**). All RNA samples included in the study had an OD260/280 ratio >1.8. First-strand cDNA was synthesized from 2 µg of total RNA with oligo $(dT)_{15}$ primers and GoScript Reverse Transcriptase (Promega, Switzerland) according to the manufacturer's instructions. The qPCR reaction in SYBR Green reagent (10 µl) contained 0.5 µM primers, 2 x GoTaqqPCR Master Mix (Promega, Switzerland) and 1 µl cDNA. Primer nucleotide sequences and PCR efficiencies are shown in **Figure 1—figure supplement 1C and D**. Amplification reactions were performed in duplicates in 384-well plates with the ViiA7 system (Applied Biosystems, USA). To evaluate mRNA quantities, data were obtained as C_t values (describing the cycle number at which logarithmic plots cross calculated threshold lines). C_t values were used to determine ΔC_t values (ΔC_t = C_t value of the reference gene minus the C_t value of the target gene). The applied reference gene was Tyrosine 3-monooxygenase/tryptophan 5-monooxygenase activation protein, zeta polypeptide (YWHAZ). Comparative transcript data between undifferentiated (CTB) and differentiated (STB) cells were calculated as $2^{-\Delta\Delta Ct}$ values ($\Delta\Delta C_t$ = C_t value of CALHM gene – C_t value of YWHAZ) and are presented as x-fold difference. Data analysis and statistical evaluations were performed using paired 2-way ANOVA with Sidak's multiple comparisons test with GraphPad Prism software.

of large CALHM channels, which is currently still not understood (**Figure 8**). We thus could envision two alternative scenarios which might underly regulation in large CALHM channels where the gate in the closed state could either be formed by part of the protein or by lipids (**Figure 8**, **Figure 8—figure supplement 1D**). Both models are at this stage hypothetical and it is still unclear how lipids in the pore would rearrange during activation. Another remarkable feature of large CALHM channels concerns their tendency to form pairwise assemblies upon extraction from the membranes (**Figure 3A,C**, **Figure 3—figure supplements 2**, **3** and **6**). This property has previously been observed for undecameric CALHM2 channels, which were described to dimerize on the extracellular side thus forming structures that resemble gap-junctions, and in the present study, where dimerization was found to some degree in all samples. In our data, the described behavior is most pronounced in case of CALHM4 where dimerization proceeds on the intracellular side mediated by interactions with the partly mobile C-terminus. Although intriguing, it is currently unclear whether any of the observed pairwise interactions is of relevance in a physiological context.

Thus, although our data have provided a large step forward towards the comprehension of CALHM channels, it has also opened many questions. An important area of future investigations relates to the characterization of the localization of CALHM channels in different placental cell types and the identification of their subcellular distribution. Knowledge of their localization would provide a first glimpse into potential roles of these large channels for transport processes in this organ and should provide answers on the potential relevance of intra- and extracellular interactions of channel pairs. Another question concerns the ability of the three paralogs to heteromerize and the potential relevance of such heteromeric channels in a physiological environment. Finally, it will be important to study the activation mechanism of the described channels and whether they are embedded in larger interaction networks, which shape their activation properties. These topics will be addressed in future studies for which our current data provide an important foundation.

Materials and methods

Placenta collection

Human placental tissues were collected from the Division of Obstetrics and Gynecology, Lindenhofgruppe Bern, Switzerland, under approval by the ethical commission of the Canton of Bern (approval No. Basec 2016–00250). Written informed consent was obtained from all participants. Placentas were collected from uncomplicated pregnancies following elective cesarean section beyond 37 weeks of gestation without prior labor upon patients request or due to breech presentation. All experiments were carried out in accordance with the relevant guidelines and regulations.

Expression analysis in placental tissue

RNA isolation, reverse transcription and quantitative RT-PCR

Approximately 50 mg of frozen placental tissue was subjected to RNA isolation as previously described (**Huang et al., 2012**; **Huang et al., 2013**). All RNA samples included in the study had an OD260/280 ratio >1.8. First-strand cDNA was synthesized from 2 µg of total RNA with oligo $(dT)_{15}$ primers and GoScript Reverse Transcriptase (Promega, Switzerland) according to the manufacturer's instructions. The qPCR reaction in SYBR Green reagent (10 µl) contained 0.5 µM primers, 2 x GoTaqqPCR Master Mix (Promega, Switzerland) and 1 µl cDNA. Primer nucleotide sequences and PCR efficiencies are shown in **Figure 1—figure supplement 1C and D**. Amplification reactions were performed in duplicates in 384-well plates with the ViiA7 system (Applied Biosystems, USA). To evaluate mRNA quantities, data were obtained as C_t values (describing the cycle number at which logarithmic plots cross calculated threshold lines). C_t values were used to determine ΔC_t values (ΔC_t = C_t value of the reference gene minus the C_t value of the target gene). The applied reference gene was Tyrosine 3-monooxygenase/tryptophan 5-monooxygenase activation protein, zeta polypeptide (YWHAZ). Comparative transcript data between undifferentiated (CTB) and differentiated (STB) cells were calculated as $2^{-\Delta\Delta Ct}$ values ($\Delta\Delta C_t$ = C_t value of CALHM gene – C_t value of YWHAZ) and are presented as x-fold difference. Data analysis and statistical evaluations were performed using paired 2-way ANOVA with Sidak's multiple comparisons test with GraphPad Prism software.

Primary trophoblast isolation and characterization

Villous trophoblast cells were isolated from healthy human term placentas by enzymatic digestion and gravitational separation as previously described (**Nikitina et al., 2011**; **Huang et al., 2013**) with minor modifications. Briefly, villi-rich tissues were digested three times with 0.25% trypsin (Sigma, USA) and 300 IU/ml Deoxyribonuclease I (Sigma, USA), and then subjected to Percoll (Sigma, USA) density gradient centrifugation to isolate villous cytotrophoblast cells. In order to assure the purity of the cells, flow cytometry analysis was performed by using the trophoblast-specific epithelial cell marker cytokeratin 7 (**Maldonado-Estrada et al., 2004**) (anti-cytokeratin 7, Dako, Switzerland). Vimentin (anti-vimentin, Sigma, USA), which is only expressed in potentially contaminating cells (e.g. mesenchymal cells, fibroblasts, smooth muscle cells, stromal cells) served as a negative marker (**Soares and Hunt, 2006**).

Primary trophoblast cell culture

Isolated human trophoblast cells were cultured in Dulbecco's modified Eagle's medium containing 4.5 g/l glucose (DMEM-HG, Gibco, UK) supplemented with 10% fetal bovine serum (FBS, Seraglob, Switzerland) and Antibiotic-Antimycotic (Gibco, USA) in a humidified incubator under a 5% CO_2 atmosphere at 37˚C. Cells were seeded at a density of 0.2 10^6 cells/cm^2 in costar CellBIND six well plates (Corning, USA) and harvested after 24 hr (cytotrophoblast stage) or 48 hr (STB stage). The syncytialization process was confirmed by visualization under the microscope.

Expression cell lines

Adherent HEK293T cells used for protein expression and screening experiments were cultured in DMEM medium supplemented with 10% FBS and penicillin/streptomycin in a humidified incubator under a 5% CO_2 atmosphere at 37˚C. Suspension-adapted HEK293S GnTI$^-$ cells used for protein expression and purification were grown in HyClone TransFx-H media, supplemented with 2% fetal bovine serum (FBS), 4 mM L-glutamine, 1.5% Poloxamer 188 and penicillin/streptomycin in a humidified incubator under 5% CO_2 atmosphere at 37˚C. Both cell lines were tested negative for mycoplasma contamination.

For construct generation, cDNAs of human CALHM proteins, with SapI restriction sites removed, were obtained from GenScript. For expression in *X. laevis* oocytes, cDNAs of CALHM1, CALHM2, CALHM4 and CALHM6 were cloned into a pTLNX vector. For expression in mammalian cells, cDNAs of all human CALHM homologs were cloned into a pcDNA 3.1 vector which was modified to be compatible with FX cloning technology (**Geertsma and Dutzler, 2011**) and to encode a C-terminal 3C protease cleavage site followed by Venus-Myc-SBP tag.

Homolog screening

For overexpression studies of CALHM paralogs, adherent HEK293T cells were seeded on 10 cm dishes and grown to a density of 7 10^6 cells/well. Subsequently, cells were transiently transfected with mixtures of respective *CALHM* cDNA constructs and polyethylenimine with an average molecular weight of 25 kDa (PEI 25K, branched). As a preparative step, 12 µg of DNA and 48 µg of PEI were separately incubated in 0.5 ml of DMEM medium. After 5 min, both solutions were mixed, incubated for 15 min and added to respective cell cultures. 36 hr post transfection cells were washed with PBS, harvested by centrifugation at 400 g for 5 min, flash-frozen in liquid nitrogen and stored at −20˚C. For protein extraction, cells were thawed on ice, lysed with lysis buffer (25 mM HEPES, 150 mM NaCl, 0.5 mM $CaCl_2$, 2 mM $MgCl_2$, 2% GDN, protease inhibitors, RNase, DNase, pH 7.6) for 1 hr and clarified by centrifugation at 16,000 g for 10 min. The obtained supernatants were filtered through 0.22 µm centrifugal filters and injected onto a Superose 6 5/150 column equilibrated with elution buffer (10 mM HEPES, 150 mM NaCl, 50 µM GDN pH 7.6) and eluted in the same buffer. Proteins were identified by recording of the fluorescence of the attached Venus YFP.

Protein expression and purification

Suspension HEK293S GnTI$^-$ cells were grown in Bioreactor 600 vessels (TPP) and seeded to a density of 0.6 10^6 cells/ml a day prior to transfection. For protein expression, cells were transiently transfected with mixtures of *CALHM* cDNA constructs and PEI MAX 40K. For 300 ml of cell culture, 0.5 mg of DNA and 1.2 mg of PEI MAX were suspended in 20 ml volume of DMEM medium. After 5

min the DNA solutions were mixed with the PEI MAX solutions, incubated for 15 min and supplemented with 4 mM valproic acid. Transfection mixtures were subsequently added to cell cultures and expression proceeded for 36 hr. Afterwards, cells were harvested by centrifugation at 500 g for 15 min, washed with PBS and stored at −20˚C for further use. All following purification steps were carried out at 4˚C. For protein extraction, cells were suspended in lysis buffer (25 mM HEPES, 150 mM NaCl, 1% Lauryl Maltose Neopentyl Glycol (LMNG), 0.5 mM $CaCl_2$, 2 mM $MgCl_2$, protease inhibitors, RNase, DNase, pH 7.6) and incubated for 1 hr under constant stirring. For CALHM4 purification in Ca^{2+}-free conditions, Ca^{2+} was replaced by 5 mM EGTA after extraction. To clarify the extracts, lysates were centrifugated at 16,000 g for 15 min. Supernatants filtered through a 0.5 µm filter were applied to the StrepTactin Superflow affinity resin and incubated with the slurry for 2.5 hr under gentle agitation. Unbound proteins were removed and bound proteins were eluted with elution buffer (10 mM HEPES, 150 mM NaCl, 50 µM GDN, 2 mM $CaCl_2$ and 10 mM d-Desthiobiotin, pH 7.6). For purification in Ca^{2+}-free conditions, Ca^{2+} was replaced by 2 mM EGTA. For cleavage of fusion tags, eluates were incubated for 30 min with 3C protease. Subsequently, samples were concentrated, filtered through 0.22 µm filters and subjected to size exclusion chromatography on a Superose 6 10/300 GL column equilibrated with SEC buffer (10 mM HEPES, 150 mM NaCl, 50 µM GDN, 2 mM $CaCl_2$/2 mM EGTA, pH 7.6). Peak fractions were pooled and concentrated with 100 kDa MWCO centrifugal filters.

LC-MS analysis of co-purified lipids

For the analysis of lipids co-purified with CALHM4, the protein was prepared in the presence of Ca^{2+} in the same manner as described for structure determination. For lipid extraction, chloroform was added in a 1:1 ratio (v/v) to 200 µl of a CALHM4 sample with a protein concentration of 3.75 mg ml^{-1} or to 200 µl of SEC buffer as a control (blank). The samples were briefly vortexed and incubated for 5 min at ambient temperature until phases have separated. The lower organic phase was collected and used for liquid chromatography and mass spectrometry (LC-MS) analysis. Prior to analysis, 25 µl of chloroform extract was mixed with 475 µl of a 50% aqueous methanol solution. The suspension was vortexed and centrifuged at 20˚C for 10 min at 16,000 g. 100 µl of the supernatant were transferred to a glass vial with narrowed bottom (Total Recovery Vials, Waters) and subjected to LC-MS. Lipids were separated on a nanoAcquity UPLC (Waters) equipped with a HSS T3 capillary column (150 µm x 30 mm, 1.8 µm particle size, Waters), applying a gradient of 5 mM ammonium acetate in water/acetonitrile 95:5 (A) and 5 mM ammonium acetate in isopropanol/acetonitrile 90:10 (B) from 5% B to 100% B over 10 min. The following 5 min conditions were kept at 100% B, followed by 5 min re-equilibration to 5% B. The injection volume was 1 µl. The flow rate was constant at 2.5 µl/min. The UPLC was coupled to a QExactive mass spectrometer (Thermo) by a nano-ESI source. MS data were acquired using positive polarization and data-dependent acquisition (DDA). Full scan MS spectra were acquired in profile mode from 80 to 1,200 m/z with an automatic gain control target of 1 10^6, an Orbitrap resolution of 70,000, and a maximum injection time of 200 ms. The five most intense charged (z = +1 or +2) precursor ions from each full scan were selected for collision induced dissociation fragmentation. Precursor was accumulated with an isolation window of 0.4 Da, an automatic gain control value of 5 10^4, a resolution of 17,500, a maximum injection time of 50 ms and fragmented with a normalized collision energy of 20 and 30 (arbitrary unit). Generated fragment ions were scanned in the linear trap. Minimal signal intensity for MS2 selection was set to 500. Lipid datasets were evaluated with Progenesis QI software (Nonlinear Dynamics), which aligns the ion intensity maps based on a reference data set, followed by a peak picking on an aggregated ion intensity map. Detected ions were identified based on accurate mass, detected adduct patterns and isotope patterns by comparing with entries in the LipidMaps Data Base (LM). A mass accuracy tolerance of 5 mDa was set for the searches. Fragmentation patterns were considered for the identifications of metabolites. Matches were ranked based on mass error (observed mass – exact mass), isotope similarity (observed versus theoretical) and relative differences between sample and blank.

Cryo-EM sample preparation and data collection

For structure determination of human CALHM2, 4 and 6 in the presence of Ca^{2+} and of human CALHM4 in the absence of Ca^{2+} by cryo-EM, 2.5 µl samples of GDN-purified proteins at a concentration of 1.5–3 mg ml^{-1} were applied to glow-discharged holey carbon grids (Quantifoil R1.2/1.3 or

R0.6/1 Au 200 mesh). Excess liquid was removed in a controlled environment (4˚C and 100% relative humidity) by blotting grids for 4–6 s. Grids were subsequently flash frozen in a liquid propane-ethane mix using a Vitrobot Mark IV (Thermo Fisher Scientific). All samples were imaged in a 300 kV Tecnai G^2 Polara (FEI) with a 100 µm objective aperture. All data were collected using a post-column quantum energy filter (Gatan) with a 20 eV slit and a K2 Summit direct detector (Gatan) operating in counting mode. Dose-fractionated micrographs were recorded in an automated manner using SerialEM (**Mastronarde, 2005**) with a defocus range of –0.8 to –3.0 µm. All datasets were recorded at a nominal magnification of 37,313 corresponding to a pixel size of 1.34 Å/pixel with a total exposure time of 12 s (30 individual frames) and a dose of approximately 1.3 $e^-/Å^2$/frame. The total electron dose on the specimen level for all datasets was approximately between 32 $e^-/Å^2$ and 55 $e^-/Å^2$.

Cryo-EM image processing

Micrographs from all four datasets were pre-processed in the same manner. Briefly, all individual frames were used for correction of the beam-induced movement using a dose-weighting scheme in RELION's own implementation of the MotionCor2 algorithm available in version 3.0 (**Zivanov et al., 2018**). The CTF parameters were estimated on summed movie frames using CTFFIND4.1 (**Rohou and Grigorieff, 2015**). Low-quality micrographs showing a significant drift, ice contamination or poor CTF estimates were discarded resulting in datasets of 1,125 images of CALHM4 in the presence of Ca^{2+} (dataset 1), 717 images of Ca^{2+}-free CALHM4 (dataset 2), 1,059 images of CALHM6 (dataset 3) and 2,065 images of CALHM2 (dataset 4), which were subjected to further data processing in RELION (**Scheres, 2012**). Particles of CALHM4 and CALHM6 were initially picked using the Laplacian-of-Gaussian method and subjected to 2D classification. 2D class averages showing protein features were subsequently used as templates for more accurate auto-picking as well as input for generating an initial 3D model. From dataset one, 422,281 particles were extracted with a box size of 234 pixels, down-scaled three times and subjected to 2D classification. Having discarded false positives and particles of poor quality, the dataset was reduced to 201,782 particles. Two rounds of non-symmetrized 3D classification using the 60 Å low-pass filtered initial 3D model as a reference allowed to isolate two populations of homogenous particles representing dihedrally-related decameric and undecameric assemblies. These two subsets were refined separately with either D10 or D11 symmetry imposed followed by unbinning to an original pixel size and iterative rounds of 3D refinement, per-particle CTF correction and Bayesian polishing (**Zivanov et al., 2018**; **Zivanov et al., 2019**). Extra 3D classification without angular alignment showed increased flexibility within the dimerization interface of interacting intracellular regions in the decameric assembly while no such flexibility was observed for the undecameric population. In order to improve the resolution of the reconstructions, localized reconstruction was performed. For this purpose, the signal corresponding to the detergent belt and to one dihedrally-related monomer was subtracted from each particle followed by auto-refinement of merged in silico modified particles in the presence of a soft mask around the protein density with either C10 or C11 symmetry imposed. The final map of the decameric and undecameric assembly was improved to 4.07 Å and 3.92 Å, respectively. The maps were sharpened using isotropic b-factors of –200 $Å^2$ and –177 $Å^2$, respectively. Datasets of Ca^{2+}-free CALHM4 and Ca^{2+}-CALHM6 were processed in a similar manner. Briefly, from dataset two, 576,841 particles were extracted and cleaned by 2D classification. The pool, reduced to 97,978 particles, was subjected to non-symmetrized 3D classification that also yielded two populations of dihedrally-related decameric and undecameric assemblies. The final map of the decameric assembly at 4.07 Å and of the undecameric assembly at 3.69 Å was sharpened using isotropic b-factors of –169 $Å^2$ and –126 $Å^2$, respectively. From dataset three, 216,859 particles were extracted with a box size of 200 pixels and reduced to 201,761 particles after 2D classification. Non-symmetrized 3D classification also revealed decameric and undecameric populations, although no dihedrally-symmetrized dimers, as in case of CALHM4 in the presence and absence of Ca^{2+}, were observed. The final auto-refined map of the decameric assembly at 4.39 Å and of the undecameric assembly at 6.23 Å was sharpened using isotropic b-factors of –259 $Å^2$ and –435 $Å^2$, respectively. In all cases, resolution was estimated in the presence of a soft solvent mask and based on the gold standard Fourier Shell Correlation (FSC) 0.143 criterion (**Chen et al., 2013**; **Rosenthal and Henderson, 2003**; **Scheres, 2012**; **Scheres and Chen, 2012**). High-resolution noise substitution was applied to correct FSC curves for the effect of soft masking in real space (**Chen et al., 2013**). The local resolution was estimated using RELION (**Zivanov et al., 2018**).

Visual inspection of micrographs in dataset 4 (CALHM2) during pre-processing hinted at preferential orientation of particles. 2D class averages generated from the particles picked with the Laplacian-of-Gaussian method showed primarily views from the extracellular side with a small percentage of side or tilted views, similar to those found in CALHM4 datasets (dihedrally-related dimers) and the CALHM6 dataset (monomers). In order to recover projections at orientations other than from the extracellular side, representative 2D class averages of CALHM4 and 6 were combined and used as 2D templates for auto-picking. The pool of 417,612 particles was subjected to two rounds of 2D classification, after which the dataset was reduced to 71,555 particles. 2D class averages showed that the majority of the remaining particles comprised a view from the extracellular side with only a small fraction representing other orientations. As a consequence of this preferential orientation, projections from other angles were underpopulated and did not show high-resolution features. In other to separate monomeric and dimeric populations, non-symmetrized 3D classification was performed using low-pass filtered reconstructions of CALHM4 and CALHM6. However, both monomeric and dimeric 3D reconstructions of CALHM2 suffered from missing views and therefore were not able to converge to a reliable model during 3D auto-refinement. Additional 2D classification on particles classified either as CALHM2 monomers or dimers showed significant amount of remaining heterogeneity in form of undecameric and dodecameric assemblies, which together with the preferential orientation impeded obtaining a high-resolution reconstruction from this dataset.

Model building and refinement

The models of CALHM4 and CALHM6 were built in Coot (**Emsley and Cowtan, 2004**). CALHM4 was built de novo into the cryo-EM density of the dimer of undecameric channels at 3.82 Å. The slightly better resolved cryo-EM density of the unpaired undecameric channel at 3.69 Å obtained by localized reconstruction and a map blurred in Coot with a *b*-factor of 50 aided map interpretation. CALHM6 was built using the CALHM4 structure as a reference with the aid of modified cryo-EM maps of CALHM6 which were either low-pass filtered to 6 Å, blurred in Coot with a *b*-factor of 200 or sharpened in Coot with a *b*-factor of −50. The cryo-EM density of CALHM4 was of sufficiently high resolution to unambiguously assign residues 4–83 and 94–280. The cryo-EM density of CALHM6 allowed us to assign residues 20–82 and 94–282. The atomic models were improved iteratively by cycles of real-space refinement in PHENIX (**Adams et al., 2002**) with secondary structure and 22-fold (for CALHM4) and 10-fold (for CALHM6) NCS constraints applied followed by manual corrections in Coot. Validation of the models was performed in PHENIX. Surfaces were calculated with MSMS (**Sanner et al., 1996**). Figures and videos containing molecular structures and densities were prepared with DINO (http://www.dino3d.org), PyMOL (**DeLano, 2002**), Chimera (**Pettersen et al., 2004**) and ChimeraX (**Goddard et al., 2018**).

Analysis of the density inside the pore

For analysis of the density inside the pore, non-symmetrized final 3D reconstructions of CALHM4 and CALHM6 were opened as a stack in Fiji (**Schindelin et al., 2012**), where the mean density of the area inside the pore was quantified along the slices of each 3D reconstruction. The size of the measured area was chosen based on the 3D mask generated from the atomic models of CALHM4 and 6. In both cases, the area of 6 × 6 pixels centered around the pore axis was located outside the 3D mask ensuring that the procedure did not include density of CALHM4 or 6.

The 'experimental' reference profile was generated based on the electron density map of the MPEG-1 protein bound to a lipidic vesicle (EMD-20622) (**Pang et al., 2019**). The electron density corresponding to the protein was selected and subtracted in Chimera using the structure of MPEG-1 (PDBID 6U2W). Due to the membrane deformation, the central region of the bilayer was excluded from the measurement. The 'simulation' reference profile was generated using the atomistic model of a membrane obtained from the MemProtMD database (PDBID 2N5S) (**Mineev et al., 2015**; **Newport et al., 2019**). All atoms corresponding to protein, ions and water molecules were removed from the model and the remaining lipids were used to generate an electron density map with 1.34 Å pixel spacing at 6 Å resolution using Chimera (**Pettersen et al., 2004**). Electron density profiles were generated by measuring a mean pixel intensity of selected regions on map slices along the Z-axis using the Fiji software (**Schindelin et al., 2012**).

Two-electrode voltage-clamp recording

For preparation of cRNA coding for CALHM paralogs, *CALHM*-pTLNX DNA constructs were linearized with the FastDigest MluI restriction enzyme (ThermoFisher) purified, transcribed in vitro with the mMessage mMachine kit (Ambion) and purified with the RNeasy kit (Qiagen). The obtained cRNAs were either used immediately or aliquoted and stored at -20˚C. Defolliculated *X. laevis* oocytes obtained from Ecocyte Bioscience, were injected with mixtures containing either 1 ng of *CALHM1* cRNA or 5 ng of *CALHM 2, 4 and 6* cRNA and 10 ng of *X. laevis* connexin-38 antisense oligonucleotide (Cx38 ASO) to inhibit endogenous Cx38 currents (**Bahima et al., 2006**). Oocytes used as negative control (neg.) were injected with 10 ng of Cx38 ASO only. For protein expression, oocytes were kept in ND69 solution (96 mM NaCl, 2 mM KCl, 1.8 mM $CaCl_2$, 1 mM $MgCl_2$, 2.5 mM Na-pyruvate, 5 mM HEPES and 50 µg/ml gentamicin, pH 7.5) at 16˚C. Two-electrode voltage-clamp (TEVC) measurements were performed 48–60 hr after RNA injections at 20˚C. TEVC data were recorded on an OC-725B amplifier (Warner Instrument Corp.) Data recorded at 5 kHz and filtered at 1 kHz were and digitized using a Digidata interface board (1322A or 1440A, Axon Instruments) and analyzed with pCLAMP 10.3 software (Molecular Devices, Sunnyvale, CA). Microelectrodes with a resistance of 1–4 MΩ were filled with 3 M KCl. A VC-8 valve controller (Warner Instruments) was used for perfusion of different Ca^{2+} concentrations. Prior to recording, oocytes were additionally injected with a 50 nl of a mixture containing 20 mM BAPTA and 10 mM Ca^{2+} solution to minimize activation of Ca^{2+}-activated Cl^- currents. High Ca^{2+} bath solutions contained,100 mM Na^+, 5.4 mM K^+, 95 mM Cl^-, 1 mM Mg^{2+}, 3 mM Ca^{2+} and 10 mM HEPES, pH 7.2. Divalent cation-free solutions contained 0.5 mM EGTA and 0.5 mM EDTA instead of divalent cations. Intermediate Ca^{2+} concentrations were prepared from both stocks by mixing solution according to the volume calculated with WEBMAXC calculator.

Cell surface biotinylation

Surface biotinylation of proteins expressed in *X. laevis* oocytes was performed using the Pierce Cell Surface Protein Isolation kit. Oocytes (20-50), injected with *CALHM* cRNAs and incubated for 40–60 hr, were washed three times with ND96 solution, transferred to a white 6-well plate (NUNC) and biotinylated by 30 min incubation in 4 ml ND96 solution supplemented with 0.5 mg ml^{-1} EZ-link sulfo-NHS-SS biotin. After incubation, the biotinylation reaction was stopped by addition of quenching solution and oocytes were washed several times with ND96 solution to remove residual reagents. For protein extraction, oocytes were incubated in lysis buffer (25 mM HEPES, 150 mM NaCl, 0.5 mM $CaCl_2$, 1% LMNG, 2 mM $MgCl_2$, protease inhibitors, RNase, DNase, pH 7.6) for 1 hr at 4˚C and centrifuged at 10,000 g for 15 min. The supernatants were collected and incubated with NeutrAvidin agarose slurry for 1 hr at room temperature under constant mixing. After this step, agarose beads binding the biotinylated proteins were washed with wash solution (10 mM HEPES, 150 mM NaCl, 0.0058% GDN, 2 mM $CaCl_2$, protease inhibitors, RNase, DNase). Subsequently, the unbound material was discarded and biotinylated proteins were incubated with SDS-Page sample buffer containing 50 mM DTT for 1 hr at RT. Eluted protein fraction was obtained by centrifugation at 1,000 g for 2 min at RT. Membrane protein samples were stored at −20˚C. For western blot analysis, samples were loaded on a 4–20% SDS-polyacrylamide gel. After electrophoretic separation, the proteins were transferred to a polyvinylidene fluoride membrane by a semi-dry blotting procedure. The membranes were first blocked at room temperature for 2 hr with 5% non-fat milk in TBS-T buffer (50 mM Tris, 150 mM NaCl, 0.075% Tween20, pH 7.5) and then incubated with respective anti-CALHM primary antibodies overnight at 4˚C. To remove unbound primary antibodies, the membranes were washed with TBS-T buffer and subsequently blotted with goat anti-rabbit-HRP conjugated secondary antibody for 2 hr at 4˚C. The membranes were washed again with TBS-T buffer and chemiluminescent signals were developed with the Amersham ECL Prime Western Blotting Detection kit.

Statistics and reproducibility

Paired 2-way ANOVA with Sidak's multiple comparisons test was applied to detect differences in placental mRNA levels of CALHM isoforms between undifferentiated cytotrophoblast and differentiated syncytiotrophoblast cells. A p-value<0.05 was considered as statistically significant. Statistical comparisons were performed using GraphPad Prism (GraphPad). Electrophysiology data were repeated multiple times with different batches of cRNA and *X. laevis* oocytes with very similar

results. Conclusions of experiments were not changed upon inclusion of further data. In all cases, leaky oocytes were discarded. For Ca^{2+} concentration-response analysis using TEVC methods, statistical significance was determined by analysis of variance and by Student's t test. A p-value<0.05 was considered statistically significant. The number of independent experimental repetitions is represented by n.

Accession codes

The cryo-EM density maps of CALHM4 in absence of Ca^{2+} and CALHM4 and CALHM6 in presence of Ca^{2+} have been deposited in the Electron Microscopy Data Bank under following ID codes: EMD-10917, EMD-10919, EMD-10920, EMD-10921, EMD-10924 and EMD-10925. The coordinates of the corresponding atomic models of CALHM4 and CALHM6 have been deposited in the Protein Data Bank under ID codes 6YTK, 6YTL, 6YTO, 6YTQ, 6YTV and 6YTX.

Acknowledgements

This research was supported by a grant from the Swiss National Science Foundation (No. 31003A_163421) to RD. CA acknowledges support from the Swiss National Science Foundation through the National Centre of Competence in Research TransCure and from the Stiftung Lindenhof Bern. We thank O Medalia and M Eibauer, the Center for Microscopy and Image Analysis (ZMB) of the University of Zurich, and the Mäxi foundation for the access to electron microscopes, S Klauser and S Rast for their help in establishing the computer infrastructure. We are grateful to R Karahoda and S Shahnawaz for their expert help with qPCR and immunoblotting. The authors want to express their gratitude to the patients, physicians and midwives of the Lindenhofgruppe Bern, who participated in this study. Special thanks also to R Moser, Lindenhofgruppe Bern, for coordinating the placenta sampling process. Lipid analysis was performed with the help of the FGCZ of UZH/ETH Zurich. The support of Sebastian Streb and Endre Lacko is acknowledged. All members of the Dutzler lab are acknowledged for their help at various stages of the project.

Additional information

Funding

Funder	Grant reference number	Author
Schweizerischer Nationalfonds zur Förderung der Wissenschaftlichen Forschung	31003A_163421	Raimund Dutzler
Stiftung Lindenhof Bern		Christiane Albrecht
Schweizerischer Nationalfonds zur Förderung der Wissenschaftlichen Forschung	NCCR TransCure	Christiane Albrecht

The funders had no role in study design, data collection and interpretation, or the decision to submit the work for publication.

Author contributions

Katarzyna Drożdżyk, Conceptualization, Data curation, Formal analysis, Validation, Investigation, Visualization, Methodology, Writing - original draft, Writing - review and editing, Generated expression constructs, purified proteins and assisted with structure determination and functional experiments; Marta Sawicka, Conceptualization, Data curation, Formal analysis, Validation, Investigation, Visualization, Methodology, Writing - original draft, Writing - review and editing, Prepared the samples for cryo-EM, collected EM data and proceeded with structure determination; Maria-Isabel Bahamonde-Santos, Conceptualization, Data curation, Formal analysis, Validation, Investigation, Visualization, Methodology, Writing - original draft, Writing - review and editing, Recorded and analyzed electrophysiology data; Zaugg Jonas, Conceptualization, Data curation, Formal analysis, Validation, Investigation, Visualization, Methodology, Writing - original draft, Writing - review and editing, Carried out expression analysis in the placenta; Dawid Deneka, Investigation, Methodology,

Writing - review and editing, Generated and characterized initial constructs; Christiane Albrecht, Conceptualization, Data curation, Formal analysis, Supervision, Funding acquisition, Validation, Visualization, Writing - original draft, Project administration, Writing - review and editing, Carried out expression analysis in the placenta; Raimund Dutzler, Conceptualization, Data curation, Formal analysis, Supervision, Funding acquisition, Validation, Visualization, Writing - original draft, Project administration, Writing - review and editing

Author ORCIDs

Katarzyna Drożdżyk https://orcid.org/0000-0001-6288-4735
Marta Sawicka https://orcid.org/0000-0003-4589-4290
Raimund Dutzler https://orcid.org/0000-0002-2193-8129

Ethics

Human subjects: Human placental tissues were collected from the Division of Obstetrics and Gynecology, Lindenhofgruppe Bern, Switzerland, under approval by the ethical commission of the Canton of Bern (approval No Basec 2016-00250). Written informed consent was obtained from all participants.

Decision letter and Author response

Decision letter https://doi.org/10.7554/eLife.55853.sa1
Author response https://doi.org/10.7554/eLife.55853.sa2

Additional files

Supplementary files

- Supplementary file 1. Key resources table.

- Transparent reporting form

Data availability

Coordinates of the atomic models were deposited with the PDB and cryo-EM densities were deposited with the Electron Microscopy databank.

The following datasets were generated:

Author(s)	Year	Dataset title	Dataset URL	Database and Identifier
Sawicka M, Drozdzyk K, Dutzler R	2020	Cryo-EM structure of a dimer of decameric human CALHM4 in the absence of Ca2+	https://www.rcsb.org/structure/6YTK	RCSB Protein Data Bank, 6YTK
Sawicka M, Drozdzyk K, Dutzler R	2020	Cryo-EM structure of a dimer of undecameric human CALHM4 in the absence of Ca2+	https://www.rcsb.org/structure/6YTL	RCSB Protein Data Bank, 6YTL
Sawicka M, Drozdzyk K, Dutzler R	2020	Cryo-EM structure of a dimer of decameric human CALHM4 in the presence of Ca2+	https://www.rcsb.org/structure/6YTO	RCSB Protein Data Bank, 6YTO
Sawicka M, Drozdzyk K, Dutzler R	2020	Cryo-EM structure of a dimer of undecameric human CALHM4 in the presence of Ca2+	https://www.rcsb.org/structure/6YTQ	RCSB Protein Data Bank, 6YTQ
Sawicka M, Drozdzyk K, Dutzler R	2020	Cryo-EM structure of decameric human CALHM6 in the presence of Ca2+	https://www.rcsb.org/structure/6YTV	RCSB Protein Data Bank, 6YTV
Sawicka M, Drozdzyk K, Dutzler R	2020	Cryo-EM structure of undecameric human CALHM6 in the presence of Ca2+	https://www.rcsb.org/structure/6YTX	RCSB Protein Data Bank, 6YTX
Sawicka M, Drozdzyk K, Dutzler R	2020	Cryo-EM structure of a dimer of decameric human CALHM4 in the	https://www.ebi.ac.uk/pdbe/entry/emdb/EMD-	Electron Microscopy Data Bank, 10917

		absence of Ca2+	10917	
Sawicka M, Drozdzyk K, Dutzler R	2020	Cryo-EM structure of a dimer of undecameric human CALHM4 in the absence of Ca2+	https://www.ebi.ac.uk/pdbe/entry/emdb/EMD-10919	Electron Microscopy Data Bank, 10919
Sawicka M, Drozdzyk K, Dutzler R	2020	Cryo-EM structure of a dimer of decameric human CALHM4 in the presence of Ca2+	https://www.ebi.ac.uk/pdbe/entry/emdb/EMD-10920	Electron Microscopy Data Bank, 10920
Sawicka M, Drozdzyk K, Dutzler R	2020	Cryo-EM structure of a dimer of undecameric human CALHM4 in the presence of Ca2+	https://www.ebi.ac.uk/pdbe/entry/emdb/EMD-10921	Electron Microscopy Data Bank, 10921
Sawicka M, Drozdzyk K, Dutzler R	2020	Cryo-EM structure of decameric human CALHM6 in the presence of Ca2+	https://www.ebi.ac.uk/pdbe/entry/emdb/EMD-10924	Electron Microscopy Data Bank, 10924
Sawicka M, Drozdzyk K, Dutzler R	2020	Cryo-EM structure of undecameric human CALHM6 in the presence of Ca2+	https://www.ebi.ac.uk/pdbe/entry/emdb/EMD-10925	Electron Microscopy Data Bank, 10925

References

Adams PD, Grosse-Kunstleve RW, Hung LW, Ioerger TR, McCoy AJ, Moriarty NW, Read RJ, Sacchettini JC, Sauter NK, Terwilliger TC. 2002. *PHENIX*: building new software for automated crystallographic structure determination. *Acta Crystallographica Section D Biological Crystallography* **58**:1948–1954. DOI: https://doi.org/10.1107/S0907444902016657, PMID: 12393927

Bahima L, Aleu J, Elias M, Martín-Satué M, Muhaisen A, Blasi J, Marsal J, Solsona C. 2006. Endogenous hemichannels play a role in the release of ATP from *Xenopus* oocytes. *Journal of Cellular Physiology* **206**:95–102. DOI: https://doi.org/10.1002/jcp.20440, PMID: 15965959

Chen S, McMullan G, Faruqi AR, Murshudov GN, Short JM, Scheres SH, Henderson R. 2013. High-resolution noise substitution to measure overfitting and validate resolution in 3D structure determination by single particle electron cryomicroscopy. *Ultramicroscopy* **135**:24–35. DOI: https://doi.org/10.1016/j.ultramic.2013.06.004, PMID: 23872039

Choi W, Clemente N, Sun W, Du J, Lu W. 2019. The structures and gating mechanism of human calcium homeostasis modulator 2. *Nature* **576**:163–167. DOI: https://doi.org/10.1038/s41586-019-1781-3, PMID: 31776515

DeLano WL. 2002. Pymol: an open-source molecular graphics tool. *CCP4 Newsletter on Protein Crystallography* **40**:82–92.

Demura K, Kusakizako T, Shihoya W, Hiraizumi M, Nomura K, Shimada H, Yamashita K, Nishizawa T, Taruno A, Nureki O. 2020. Cryo-EM structures of calcium homeostasis modulator channels in diverse oligomeric assemblies. *bioRxiv*. DOI: https://doi.org/10.1101/2020.01.31.928093

Deneka D, Sawicka M, Lam AKM, Paulino C, Dutzler R. 2018. Structure of a volume-regulated anion channel of the LRRC8 family. *Nature* **558**:254–259. DOI: https://doi.org/10.1038/s41586-018-0134-y, PMID: 29769723

Dreses-Werringloer U, Lambert JC, Vingtdeux V, Zhao H, Vais H, Siebert A, Jain A, Koppel J, Rovelet-Lecrux A, Hannequin D, Pasquier F, Galimberti D, Scarpini E, Mann D, Lendon C, Campion D, Amouyel P, Davies P, Foskett JK, Campagne F, et al. 2008. A polymorphism in CALHM1 influences Ca2+ homeostasis, Abeta levels, and Alzheimer's disease risk. *Cell* **133**:1149–1161. DOI: https://doi.org/10.1016/j.cell.2008.05.048, PMID: 18585350

Edwards D, Jones CJ, Sibley CP, Nelson DM. 1993. Paracellular permeability pathways in the human placenta: a quantitative and morphological study of maternal-fetal transfer of horseradish peroxidase. *Placenta* **14**:63–73. DOI: https://doi.org/10.1016/S0143-4004(05)80249-8, PMID: 8456090

Emsley P, Cowtan K. 2004. *Coot*: model-building tools for molecular graphics. *Acta Crystallographica. Section D, Biological Crystallography* **60**:2126–2132. DOI: https://doi.org/10.1107/S0907444904019158, PMID: 15572765

Geertsma ER, Dutzler R. 2011. A versatile and efficient high-throughput cloning tool for structural biology. *Biochemistry* **50**:3272–3278. DOI: https://doi.org/10.1021/bi200178z, PMID: 21410291

Goddard TD, Huang CC, Meng EC, Pettersen EF, Couch GS, Morris JH, Ferrin TE. 2018. UCSF ChimeraX: meeting modern challenges in visualization and analysis. *Protein Science* **27**:14–25. DOI: https://doi.org/10.1002/pro.3235, PMID: 28710774

Huang X, Baumann M, Nikitina L, Wenger F, Surbek D, Kömer M, Albrecht C. 2013. RNA degradation differentially affects quantitative mRNA measurements of endogenous reference genes in human placenta. *Placenta* **34**:544–547. DOI: https://doi.org/10.1016/j.placenta.2013.03.011, PMID: 23623484

Huang X, Anderle P, Hostettler L, Baumann MU, Surbek DV, Ontsouka EC, Albrecht C. 2018. Identification of placental nutrient transporters associated with intrauterine growth restriction and pre-eclampsia. *BMC Genomics* **19**:173. DOI: https://doi.org/10.1186/s12864-018-4518-z, PMID: 29499643

Kasuya G, Nakane T, Yokoyama T, Jia Y, Inoue M, Watanabe K, Nakamura R, Nishizawa T, Kusakizako T, Tsutsumi A, Yanagisawa H, Dohmae N, Hattori M, Ichijo H, Yan Z, Kikkawa M, Shirouzu M, Ishitani R, Nureki O. 2018. Cryo-EM structures of the human volume-regulated anion channel LRRC8. *Nature Structural & Molecular Biology* **25**:797–804. DOI: https://doi.org/10.1038/s41594-018-0109-6, PMID: 30127360

Kawate T, Gouaux E. 2006. Fluorescence-detection size-exclusion chromatography for precrystallization screening of integral membrane proteins. *Structure* **14**:673–681. DOI: https://doi.org/10.1016/j.str.2006.01.013, PMID: 16615909

Kefauver JM, Saotome K, Dubin AE, Pallesen J, Cottrell CA, Cahalan SM, Qiu Z, Hong G, Crowley CS, Whitwam T, Lee WH, Ward AB, Patapoutian A. 2018. Structure of the human volume regulated anion channel. *eLife* **7**: e38461. DOI: https://doi.org/10.7554/eLife.38461, PMID: 30095067

Lager S, Powell TL. 2012. Regulation of nutrient transport across the placenta. *Journal of Pregnancy* **2012**:1–14. DOI: https://doi.org/10.1155/2012/179827

Lewis RM, Brooks S, Crocker IP, Glazier J, Hanson MA, Johnstone ED, Panitchob N, Please CP, Sibley CP, Widdows KL, Sengers BG. 2013. Review: modelling placental amino acid transfer–from transporters to placental function. *Placenta* **34 Suppl**:S46–S51. DOI: https://doi.org/10.1016/j.placenta.2012.10.010, PMID: 23187090

Ma Z, Siebert AP, Cheung KH, Lee RJ, Johnson B, Cohen AS, Vingtdeux V, Marambaud P, Foskett JK. 2012. Calcium homeostasis modulator 1 (CALHM1) is the pore-forming subunit of an ion channel that mediates extracellular Ca2+ regulation of neuronal excitability. *PNAS* **109**:E1963–E1971. DOI: https://doi.org/10.1073/pnas.1204023109, PMID: 22711817

Ma Z, Tanis JE, Taruno A, Foskett JK. 2016. Calcium homeostasis modulator (CALHM) ion channels. *Pflügers Archiv - European Journal of Physiology* **468**:395–403. DOI: https://doi.org/10.1007/s00424-015-1757-6

Ma J, Qi X, Yang C, Pan R, Wang S, Wu J, Huang L, Chen H, Cheng J, Wu R, Liao Y, Mao L, Wang FC, Wu Z, An JX, Wang Y, Zhang X, Zhang C, Yuan Z. 2018a. Calhm2 governs astrocytic ATP releasing in the development of depression-like behaviors. *Molecular Psychiatry* **23**:883–891. DOI: https://doi.org/10.1038/mp.2017.229, PMID: 29180673

Ma Z, Taruno A, Ohmoto M, Jyotaki M, Lim JC, Miyazaki H, Niisato N, Marunaka Y, Lee RJ, Hoff H, Payne R, Demuro A, Parker I, Mitchell CH, Henao-Mejia J, Tanis JE, Matsumoto I, Tordoff MG, Foskett JK. 2018b. CALHM3 is essential for rapid ion Channel-Mediated purinergic neurotransmission of GPCR-Mediated tastes. *Neuron* **98**:547–561. DOI: https://doi.org/10.1016/j.neuron.2018.03.043, PMID: 29681531

Maeda S, Nakagawa S, Suga M, Yamashita E, Oshima A, Fujiyoshi Y, Tsukihara T. 2009. Structure of the connexin 26 gap junction channel at 3.5 A resolution. *Nature* **458**:597–602. DOI: https://doi.org/10.1038/nature07869, PMID: 19340074

Maldonado-Estrada J, Menu E, Roques P, Barré-Sinoussi F, Chaouat G. 2004. Evaluation of cytokeratin 7 as an accurate intracellular marker with which to assess the purity of human placental villous trophoblast cells by flow cytometry. *Journal of Immunological Methods* **286**:21–34. DOI: https://doi.org/10.1016/j.jim.2003.03.001, PMID: 15087219

Mastronarde DN. 2005. Automated electron microscope tomography using robust prediction of specimen movements. *Journal of Structural Biology* **152**:36–51. DOI: https://doi.org/10.1016/j.jsb.2005.07.007, PMID: 16182563

Mineev KS, Panova SV, Bocharova OV, Bocharov EV, Arseniev AS. 2015. The membrane mimetic affects the spatial structure and mobility of EGFR transmembrane and juxtamembrane domains. *Biochemistry* **54**:6295–6298. DOI: https://doi.org/10.1021/acs.biochem.5b00851, PMID: 26440883

Newport TD, Sansom MSP, Stansfeld PJ. 2019. The MemProtMD database: a resource for membrane-embedded protein structures and their lipid interactions. *Nucleic Acids Research* **47**:D390–D397. DOI: https://doi.org/10.1093/nar/gky1047

Nikitina L, Wenger F, Baumann M, Surbek D, Körner M, Albrecht C. 2011. Expression and localization pattern of ABCA1 in diverse human placental primary cells and tissues. *Placenta* **32**:420–430. DOI: https://doi.org/10.1016/j.placenta.2011.03.003

Oshima A, Tani K, Fujiyoshi Y. 2016. Atomic structure of the innexin-6 gap junction channel determined by cryo-EM. *Nature Communications* **7**:13681. DOI: https://doi.org/10.1038/ncomms13681, PMID: 27905396

Pang SS, Bayly-Jones C, Radjainia M, Spicer BA, Law RHP, Hodel AW, Parsons ES, Ekkel SM, Conroy PJ, Ramm G, Venugopal H, Bird PI, Hoogenboom BW, Voskoboinik I, Gambin Y, Sierecki E, Dunstone MA, Whisstock JC. 2019. The cryo-EM structure of the acid activatable pore-forming immune effector Macrophage-expressed gene 1. *Nature Communications* **10**:4288. DOI: https://doi.org/10.1038/s41467-019-12279-2, PMID: 31537793

Pettersen EF, Goddard TD, Huang CC, Couch GS, Greenblatt DM, Meng EC, Ferrin TE. 2004. UCSF chimera–a visualization system for exploratory research and analysis. *Journal of Computational Chemistry* **25**:1605–1612. DOI: https://doi.org/10.1002/jcc.20084, PMID: 15264254

Rohou A, Grigorieff N. 2015. CTFFIND4: fast and accurate defocus estimation from electron micrographs. *Journal of Structural Biology* **192**:216–221. DOI: https://doi.org/10.1016/j.jsb.2015.08.008, PMID: 26278980

Rosenthal PB, Henderson R. 2003. Optimal determination of particle orientation, absolute hand, and contrast loss in single-particle electron cryomicroscopy. *Journal of Molecular Biology* **333**:721–745. DOI: https://doi.org/10.1016/j.jmb.2003.07.013, PMID: 14568533

Sanner MF, Olson AJ, Spehner JC. 1996. Reduced surface: an efficient way to compute molecular surfaces. *Biopolymers* **38**:305–320. DOI: https://doi.org/10.1002/(SICI)1097-0282(199603)38:3<305::AID-BIP4>3.0.CO;2-Y, PMID: 8906967

Scheres SH. 2012. RELION: implementation of a bayesian approach to cryo-EM structure determination. *Journal of Structural Biology* **180**:519–530. DOI: https://doi.org/10.1016/j.jsb.2012.09.006, PMID: 23000701

Scheres SHW, Chen S. 2012. Prevention of overfitting in cryo-EM structure determination. *Nature Methods* **9**: 853–854. DOI: https://doi.org/10.1038/nmeth.2115

Schindelin J, Arganda-Carreras I, Frise E, Kaynig V, Longair M, Pietzsch T, Preibisch S, Rueden C, Saalfeld S, Schmid B, Tinevez JY, White DJ, Hartenstein V, Eliceiri K, Tomancak P, Cardona A. 2012. Fiji: an open-source platform for biological-image analysis. *Nature Methods* **9**:676–682. DOI: https://doi.org/10.1038/nmeth.2019, PMID: 22743772

Siebert AP, Ma Z, Grevet JD, Demuro A, Parker I, Foskett JK. 2013. Structural and functional similarities of calcium homeostasis modulator 1 (CALHM1) ion channel with connexins, pannexins, and innexins. *Journal of Biological Chemistry* **288**:6140–6153. DOI: https://doi.org/10.1074/jbc.M112.409789, PMID: 23300080

Smart OS, Neduvelil JG, Wang X, Wallace BA, Sansom MS. 1996. HOLE: a program for the analysis of the pore dimensions of ion channel structural models. *Journal of Molecular Graphics* **14**:354–360. DOI: https://doi.org/10.1016/S0263-7855(97)00009-X, PMID: 9195488

Soares MJ, Hunt JS. 2006. Placenta and trophoblast: methods and protocols: overview II. *Methods in Molecular Medicine* **122**:3–7. DOI: https://doi.org/10.1385/1-59259-989-3:1, PMID: 16511972

Syrjanen JL, Michalski K, Chou TH, Grant T, Rao S, Simorowski N, Tucker SJ, Grigorieff N, Furukawa H. 2020. Structure and assembly of calcium homeostasis modulator proteins. *Nature Structural & Molecular Biology* **27**:150–159. DOI: https://doi.org/10.1038/s41594-019-0369-9, PMID: 31988524

Taruno A, Matsumoto I, Ma Z, Marambaud P, Foskett JK. 2013a. How do taste cells lacking synapses mediate neurotransmission? CALHM1, a voltage-gated ATP channel. *BioEssays* **35**:1111–1118. DOI: https://doi.org/10.1002/bies.201300077, PMID: 24105910

Taruno A, Vingtdeux V, Ohmoto M, Ma Z, Dvoryanchikov G, Li A, Adrien L, Zhao H, Leung S, Abernethy M, Koppel J, Davies P, Civan MM, Chaudhari N, Matsumoto I, Hellekant G, Tordoff MG, Marambaud P, Foskett JK. 2013b. CALHM1 ion channel mediates purinergic neurotransmission of sweet, bitter and umami tastes. *Nature* **495**:223–226. DOI: https://doi.org/10.1038/nature11906, PMID: 23467090

Zivanov J, Nakane T, Forsberg BO, Kimanius D, Hagen WJ, Lindahl E, Scheres SH. 2018. New tools for automated high-resolution cryo-EM structure determination in RELION-3. *eLife* **7**:e42166. DOI: https://doi.org/10.7554/eLife.42166, PMID: 30412051

Zivanov J, Nakane T, Scheres SHW. 2019. A bayesian approach to beam-induced motion correction in cryo-EM single-particle analysis. *IUCrJ* **6**:5–17. DOI: https://doi.org/10.1107/S205225251801463X, PMID: 30713699

Figures and figure supplements

Cryo-EM structures and functional properties of CALHM channels of the human placenta

Katarzyna Drożdżyk *et al*

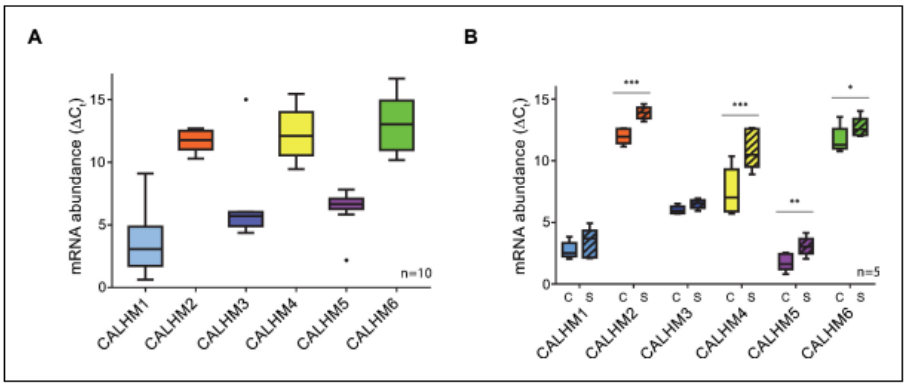

Figure 1. Expression analysis of CALHM genes in the human placenta. mRNA abundances of different CALMH paralogs in (A), human placental tissues (n = 10) and (B), human trophoblasts isolated from healthy term placentae (n = 5) was assessed by quantitative RT PCR and normalized to the reference gene YWHAZ. The relative amounts of the different CALHM genes are shown as ΔC_t values (ΔC_t = C_t value of YWHAZ – C_t value of CALHM gene). Comparative transcript data are presented as mRNA abundance ($\Delta Ct = Ct_{\text{reference gene}} - Ct_{\text{target gene}}$) between undifferentiated cytotrophoblasts (C) and differentiated syncytiotrophoblast (S) cells. Data analysis and statistical evaluations were performed using paired 2-way ANOVA with Sidak's multiple comparisons test; *p<0.05; **p<0.01; ***p<0.001.

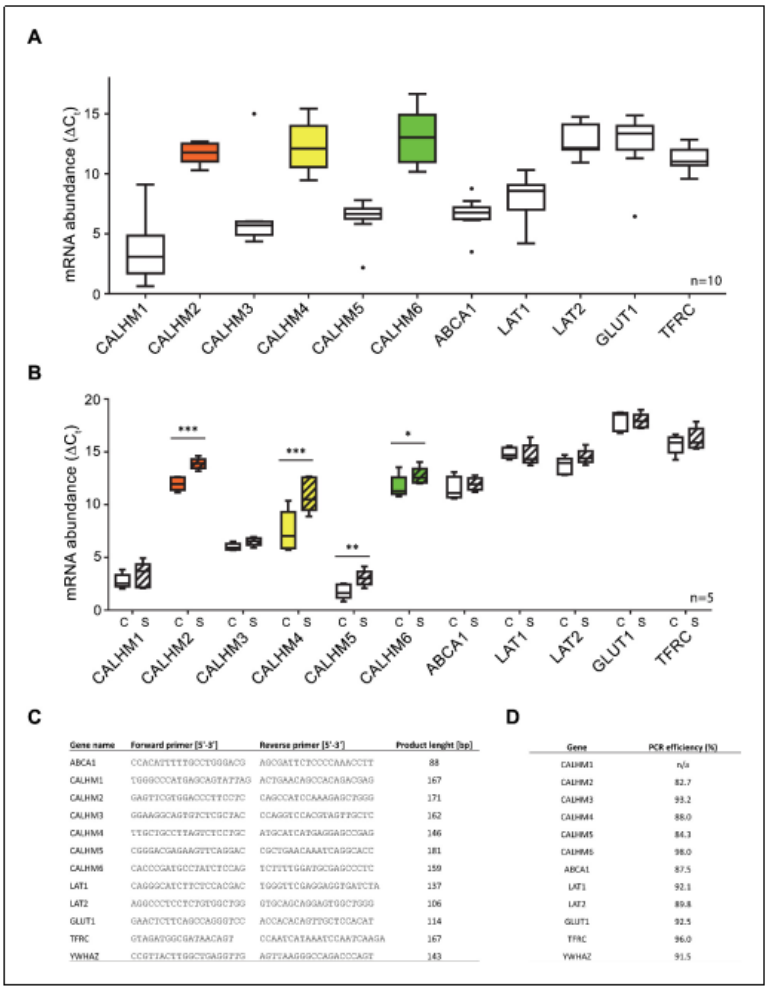

C

Gene name	Forward primer [5'-3']	Reverse primer [5'-3']	Product lenght [bp]
ABCA1	CCACATTTTTGCCTGGGACG	AGCGATTCTCCCCAAACCTT	88
CALHM1	TGGGCCCATGAGCAGTATTAG	ACTGAACAGCCACAGACGAG	167
CALHM2	GAGTTCGTGGACCCTTCCTC	CAGCCATCCAAAGAGCTGGG	171
CALHM3	GGAAGGCAGTGTCTCGCTAC	CCAGGTCCACGTAGTTGCTC	162
CALHM4	TTGCTGCCTTAGTCTCCTGC	ATGCATCATGAGGAGCCGAG	146
CALHM5	CGGGACGAGAAGTTCAGGAC	CGCTGAACAAATCAGGCACC	181
CALHM6	CACCCGATGCCTATCTCCAG	TCTTTTGGATGCGAGCCCTC	159
LAT1	CAGGGCATCTTCTCCACGAC	TGGGTTCGAGGAGGTGATCTA	137
LAT2	AGGCCCTCCTCTGTGGCTGG	GTGCAGCAGGAGTGGCTGGG	106
GLUT1	GAACTCTTCAGCCAGGGTCC	ACCACACAGTTGCTCCACAT	114
TFRC	GTAGATGGCGATAACAGT	CCAATCATAAATCCAATCAAGA	167
YWHAZ	CCGTTACTTGGCTGAGGTTG	AGTCAAGGGCCAGACCCAGT	143

D

Gene	PCR efficiency (%)
CALHM1	n/a
CALHM2	82.7
CALHM3	93.2
CALHM4	88.0
CALHM5	84.3
CALHM6	98.0
ABCA1	87.5
LAT1	92.1
LAT2	89.8
GLUT1	92.5
TFRC	96.0
YWHAZ	91.5

Figure 1—figure supplement 1. Comparative mRNA expression data for other physiologically relevant transporters/receptors in the human placenta. Y-axis and statistical analysis are according to *Figure 1*. mRNA concentrations of different CALMH paralogs and of other transport proteins in (A), human placental tissues (n = 10) and (B), human trophoblasts isolated from healthy term placentae (n = 5) were assessed by quantitative RT PCR and normalized to the reference gene YWHAZ. Abbreviations: ABCA1, ATP-binding cassette transporter A1; CALHM, calcium homeostasis modulator; LAT1 (SLC7A5), L-type amino acid transporter 1; LAT2 (SLC7A8), L-type amino acid transporter 2; GLUT1 (SLC2A1), Glucose transporter 1; TFRC, transferrin receptor complex 1; YWHAZ, Tyrosine 3-monooxygenase/tryptophan 5-monooxygenase activation protein, zeta polypeptide. (C) Primer sequences used for PCR amplification. (D) Calculated amplification efficiencies for the indicated genes.

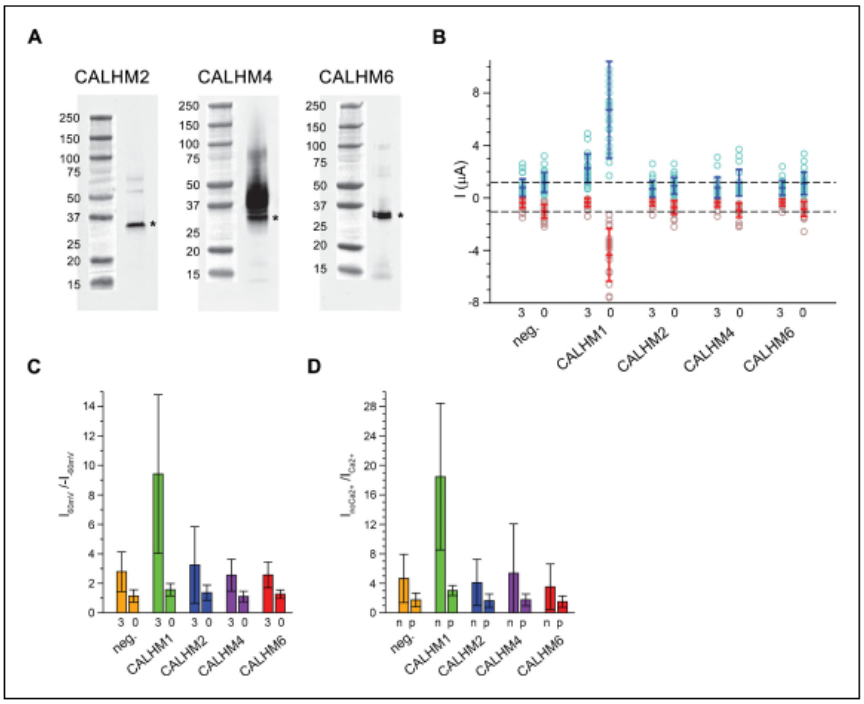

Figure 2. Functional characterization of CALHM channels expressed in *X. laevis* oocytes. (A) Western blot of proteins located in the plasma membrane of *X. laevis* oocytes heterologously expressing the indicated CALHM channels. Protein was isolated after surface-biotinylation by binding to avidin-resin. The proteins are detected with specific antibodies recognizing the respective CALHM paralog. Left, CALHM2, center CALHM4, right CALHM6. The blot demonstrates the targeting of all three paralogs to the plasma membrane. Bands corresponding to the respective CALHM paralogs are indicated by asterisk. (B) Electrophysiological characterization of *X. laevis* oocytes heterologously expressing the paralogs CALHM1, CALHM2, CALHM4 and CALHM6 in comparison to control oocytes (neg.) recorded at extracellular solutions either containing 3 mM Ca^{2+} (3) or 0.5 mM EDTA and 0.5 mM EGTA (Ca^{2+}-free, 0). Data show currents of individual oocytes (circle) recorded by two-electrode voltage-clamp (TEVC) at 60 (light blue) and −60 mV (light red). In each case, currents were tabulated at the end of a 5 s voltage step. Averages are shown as bars in red (−60 mV) and blue (60 mV), respectively. Dashed lines indicate mean current levels of control oocytes (neg.) recorded in Ca^{2+}-free extracellular solutions at 60 and −60 mV. Currents measured for all investigated channels, except CALHM1, are not significantly different from control oocytes (as judged by a Student t-test). (C), Rectification of steady-state currents of oocytes displayed in (B) expressed as I_{60mV}/I_{-60mV} calculated for individual oocytes at 3 mM Ca^{2+} (3) and in Ca^{2+}-free solutions (0) and averaged. The large value of CALHM1 reflects the activation of the protein at positive voltage in presence of Ca^{2+}. (D) Ca^{2+}-dependence of activation. Change of steady-state currents of oocytes displayed in (B) after Ca^{2+}-removal expressed as I_{noCa2+}/I_{Ca2+} calculated from individual oocytes at −60 mV (n) and 60 mV (p) and averaged. The large value of CALHM1 at −60 mV reflects the strong activation of currents at negative voltages upon Ca^{2+}-depletion. C, D, The difference between the corresponding values of the CALHM paralogs 2, 4, and 6 and neg. are statistically insignificant (as judged by a Student t-test). B-D, Data show averages of 27 (neg.), 21 (CALHM1), 26 (CALHM2), 19 (CALHM4) and 21 (CALHM6) oocytes respectively. Errors are standard deviations.

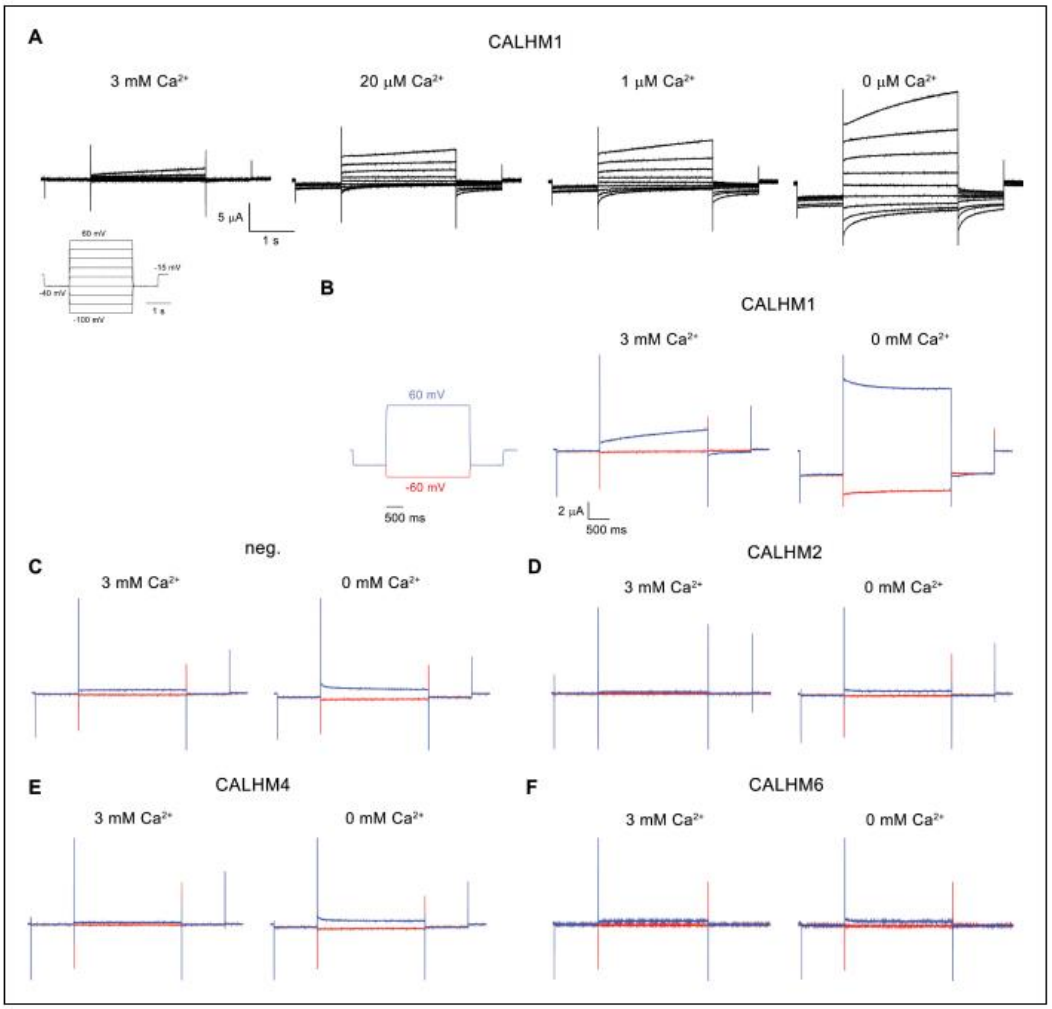

Figure 2—figure supplement 1. Electrophysiology traces. (A) Representative current traces of CALHM1 recorded at indicated extracellular Ca^{2+} concentrations. The voltage protocol is shown as inset (left). (B–F) Representative currents of CALHM paralogs (B), CALHM1, (D), CALHM2, (E), CALHM4 and (F), CALHM6 in comparison to (C), control oocytes (neg.). The current protocol is shown left. Traces including a step to −60 mV are colored in red, traces including a step to 60 mV in blue. A-F, Data were recorded 40–60 hr after injection of cRNA.

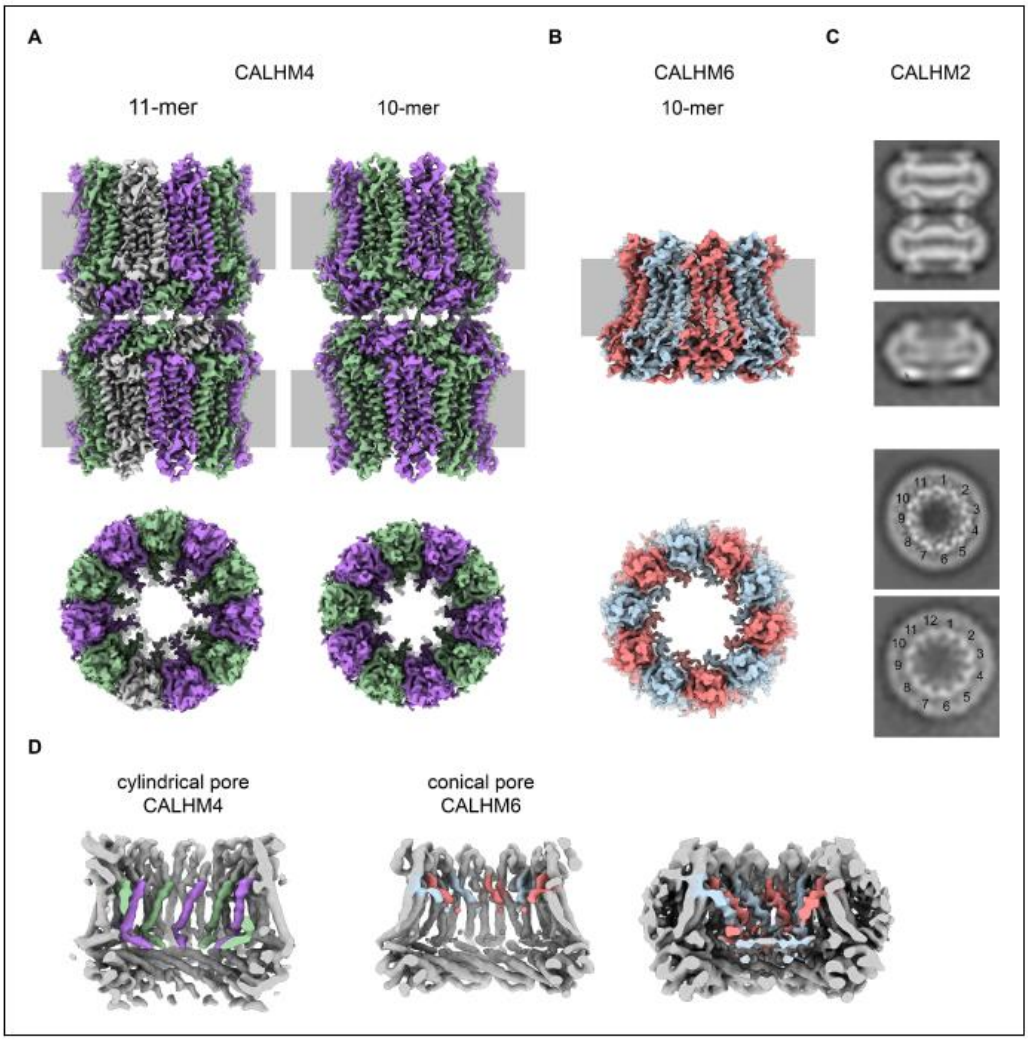

Figure 3. Cryo-EM analysis. (A) Cryo-EM density of undecameric (11-mer) and decameric (10-mer) pairs of CALHM4 channels at 3.8 and 4.1 Å respectively. Data were recorded from a Ca^{2+}-free sample. Subunits are colored in lilac and green, respectively. (B) Cryo-EM density of decameric CALHM6 channels at 4.4 Å. Subunits are colored in red and light-blue, respectively. A, B, Views are from within the membrane with membrane indicated as grey rectangle (top) and from the outside (bottom). (C) Selected 2D classes of the CALHM2 data showing interacting channel pairs and single channels viewed from within the membrane (top) and views of undecameric and dodecameric channels with subunits numbered (bottom). (D) Slices through the CALHM4 (left) and the CALHM6 (right) channels illustrating the distinct features of the cylindrical and conical pore conformations. View of CALHM6 at lower contour (right) shows extended density for the mobile TM1. Maps are low-pass filtered at 6 Å. Colored features refer to density corresponding to TM1 and NH.

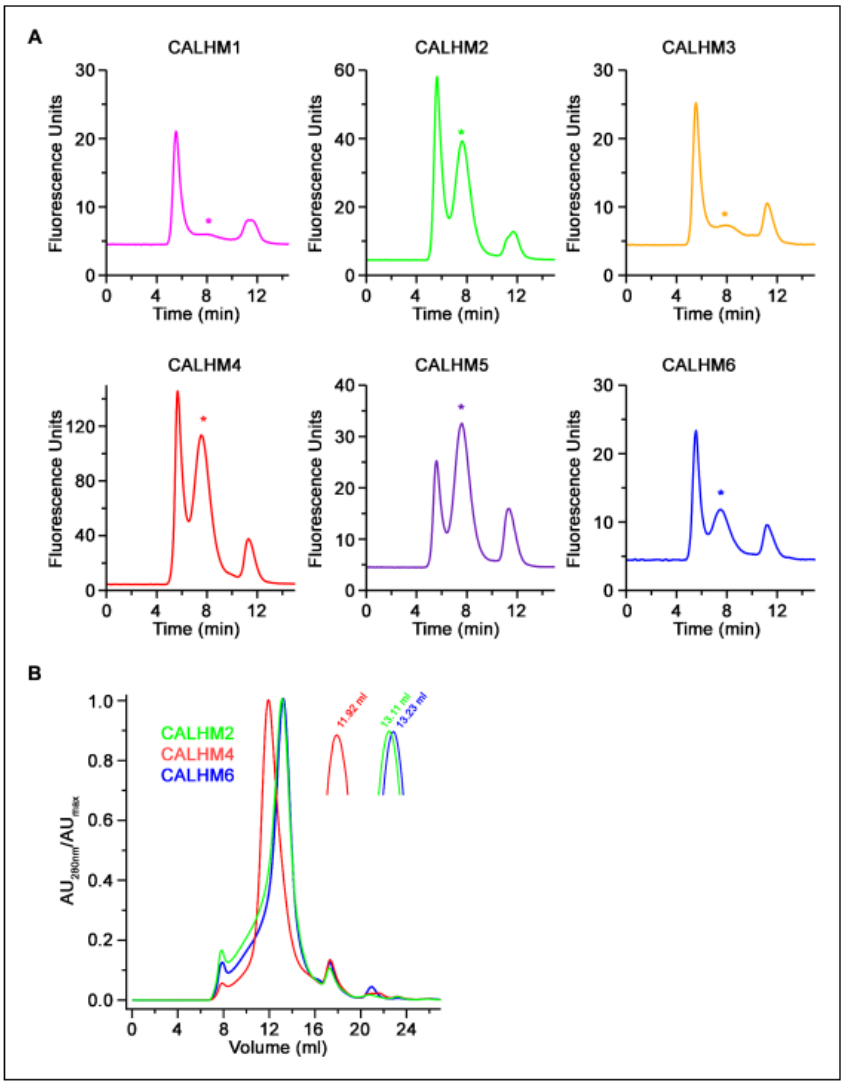

Figure 3—figure supplement 1. Biochemical characterization. (A) Size-exclusion chromatograms recorded from fluorescently tagged CALHM subunits from a whole-cell extract in the detergent GDN on a Superose 6 5/150 column at a flow rate of 0.2 ml/min. Asterisks indicate elution times for each paralog. (B) Overlay of size-exclusion chromatograms recorded from purified CALHM paralogs after cleavage of the fusion peptide used for cryo-EM analysis on a Superose 6 10/300 column. Inset shows magnified peak region with respective elution volumes indicated.

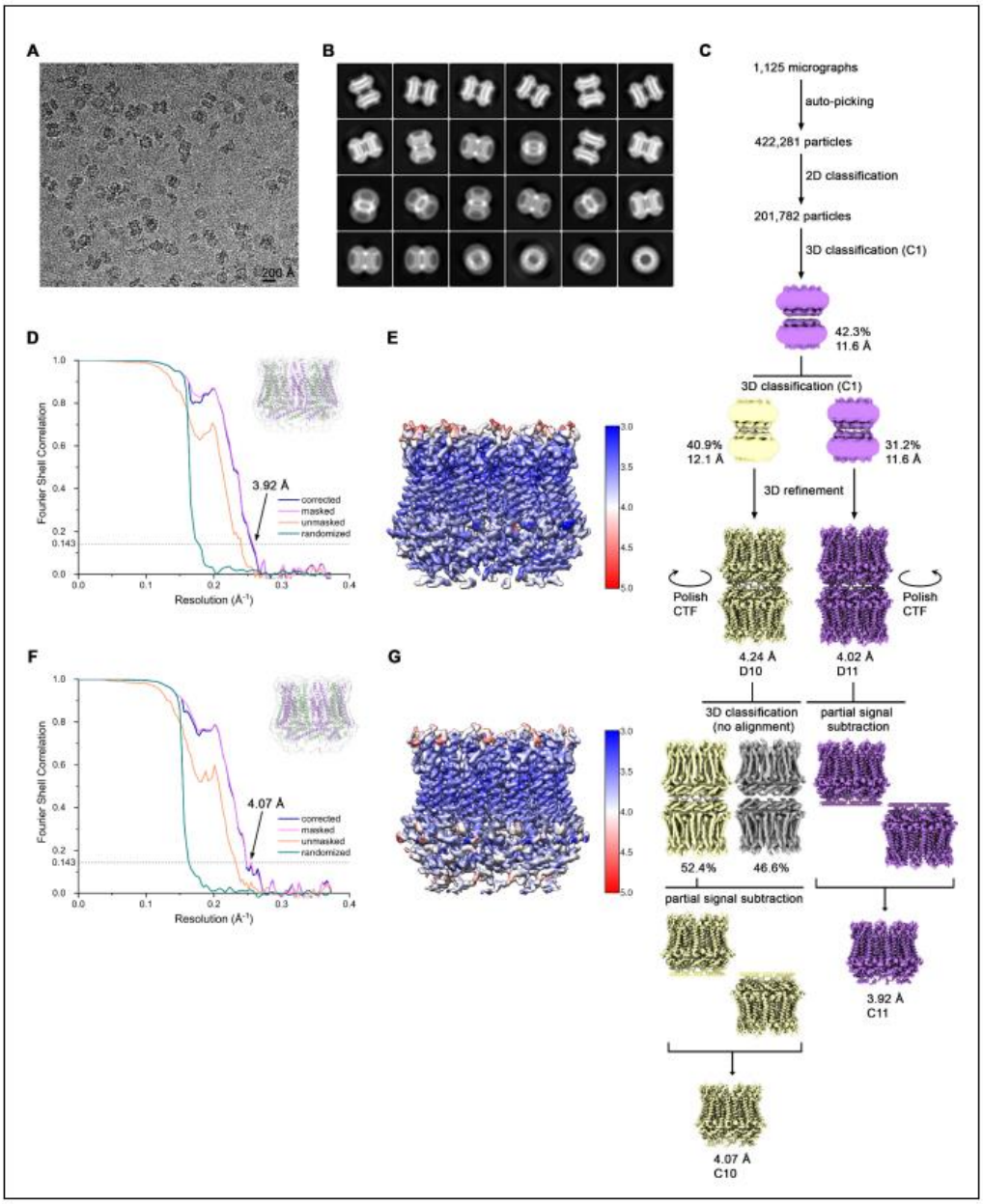

Figure 3—figure supplement 2. Cryo-EM reconstruction of CALHM4 in presence of Ca^{2+}. (A) Representative cryo-EM micrograph acquired with a Tecnai G^2 Polara microscope. (B) 2D class averages of CALHM4 in presence of Ca^{2+}. (C) Data processing workflow. Two rounds of non-symmetrized 3D

Figure 3—figure supplement 2 continued on next page

Figure 3—figure supplement 2 continued

classification allowed to isolate two populations representing decameric and undecameric assemblies. The particles were further refined with either D10 or D11 symmetry imposed. After performing per-particle CTF refinement and Bayesian polishing, the remaining structural heterogeneity in decamers was segregated by performing the final 3D classification, where the orientations were kept fixed as in the consensus model. To further improve the resolution of each reconstruction, partial signal subtraction followed by 3D refinement was applied. Particles with the symmetry relaxed to either C10 or C11 were merged and subjected to a final round of auto-refinement. The distribution of all particles (%) and the resolution of each class is indicated. (D) FSC plot of the final refined undecameric unmasked (orange), masked (pink), phase-randomized (green) and corrected for mask convolution effects (blue) cryo-EM density map of CALHM4. The resolution at which the FSC curve drops below the 0.143 threshold is indicated. The inset shows the atomic model within the mask that was applied for calculations of the resolution estimates. (E) Final 3D reconstruction of undecameric CALHM4 colored according to local resolution. (F) FSC plot of the final refined decameric unmasked (orange), masked (pink), phase-randomized (green) and corrected for mask convolution effects (blue) cryo-EM density map of CALHM4. The resolution at which the FSC curve drops below the 0.143 threshold is indicated. The inset shows the atomic model within the mask that was applied for calculations of the resolution estimates. (G) Final 3D reconstruction of decameric CALHM4 colored according to local resolution.

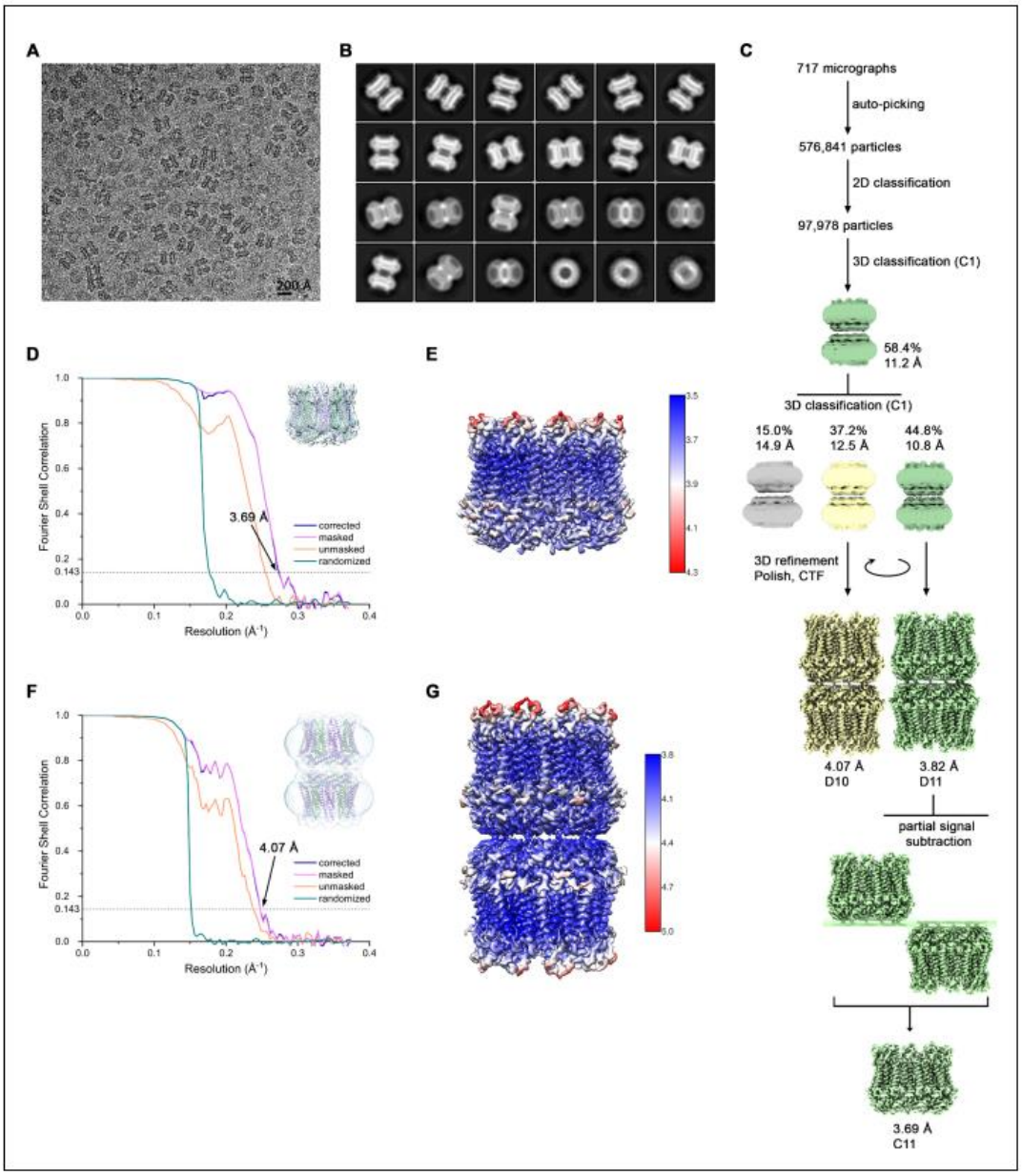

Figure 3—figure supplement 3. Cryo-EM reconstruction of CALHM4 in absence of Ca^{2+}. (A) Representative cryo-EM micrograph acquired with a Tecnai G^2 Polara microscope. (B) 2D class averages of CALHM4 in absence of Ca^{2+}. (C) Data processing workflow. Two rounds of non-symmetrized

Figure 3—figure supplement 3 continued on next page

Figure 3—figure supplement 3 continued

3D classification allowed to isolate two populations representing decameric and undecameric assemblies. The particles were further refined with either D10 or D11 symmetry imposed and iterative per-particle CTF refinement and Bayesian polishing. The resolution of the undecameric assembly was further improved by partial signal subtraction followed by 3D refinement with C11 symmetry applied. The distribution of all particles (%) and the resolution of each class is indicated. (D) FSC plot of the final refined undecameric unmasked (orange), masked (pink), phase-randomized (green) and corrected for mask convolution effects (blue) cryo-EM density map of CALHM4. The resolution at which the FSC curve drops below the 0.143 threshold is indicated. The inset shows the atomic model within the mask that was applied for calculations of the resolution estimates. (E) Final 3D reconstruction of undecameric CALHM4 colored according to local resolution. (F) FSC plot of the final refined decameric unmasked (orange), masked (pink), phase-randomized (green) and corrected for mask convolution effects (blue) cryo-EM density map of CALHM4. The resolution at which the FSC curve drops below the 0.143 threshold is indicated. The inset shows the atomic model within the mask that was applied for calculations of the resolution estimates. (G) Final 3D reconstruction of decameric CALHM4 colored according to local resolution.

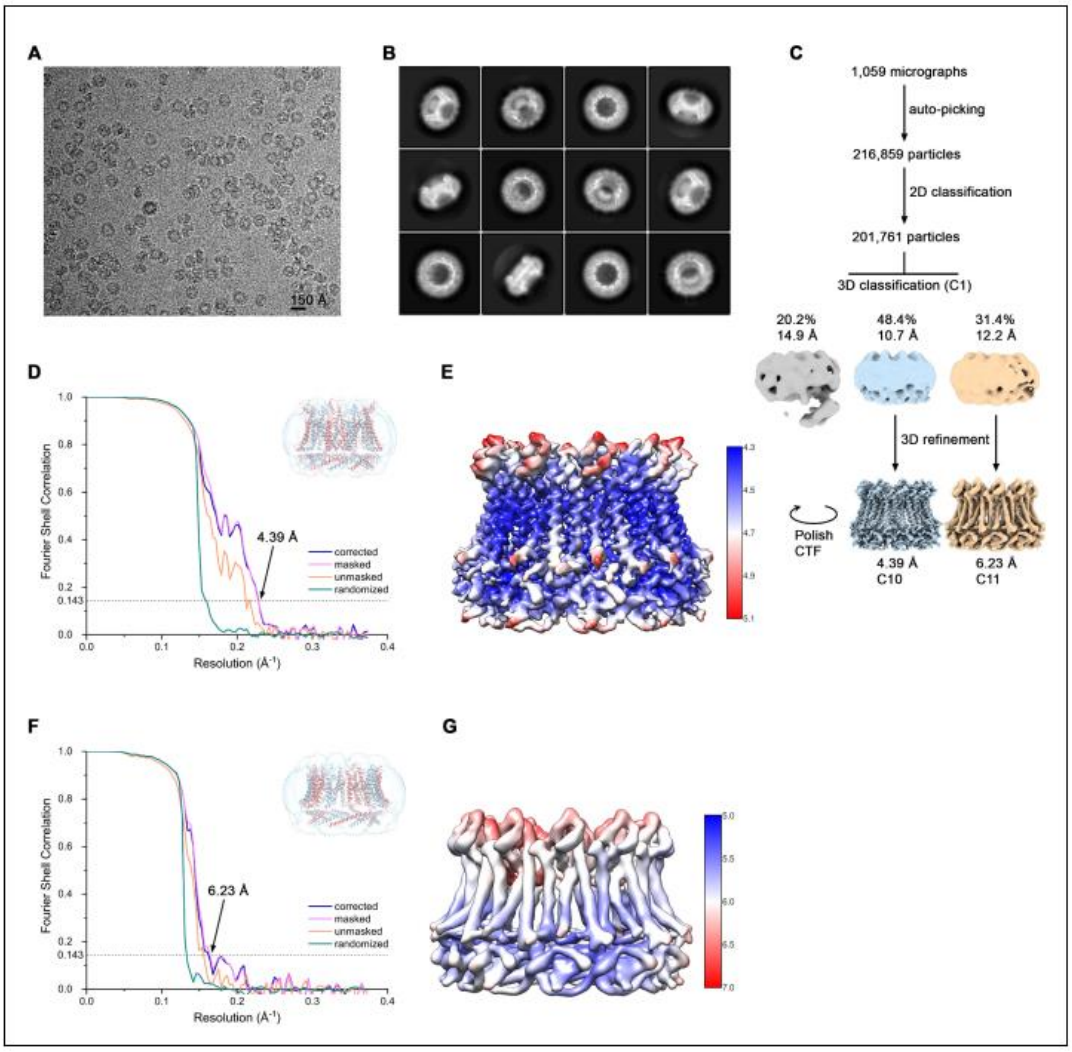

Figure 3—figure supplement 4. Cryo-EM reconstruction of CALHM6 in presence of Ca^{2+}. (A) Representative cryo-EM micrograph acquired with a Tecnai G^2 Polara microscope. (B) 2D class averages of CALHM6 in presence of Ca^{2+}. (C) Data processing workflow. Non-symmetrized 3D classification allowed to isolate two populations representing decameric and undecameric assemblies. The particles were further refined with either C10 or C11 symmetry imposed and iterative per-particle CTF refinement and Bayesian polishing. The distribution of all particles (%) and the resolution of each class is indicated. (D) FSC plot of the final refined decameric unmasked (orange), masked (pink), phase-randomized (green) and corrected for mask convolution effects (blue) cryo-EM density map of CALHM6. The resolution at which the FSC curve drops below the 0.143 threshold is indicated. The inset shows the atomic model within the mask that was applied for calculations of the resolution estimates. (E) Final 3D reconstruction of decameric CALHM6 colored according to local resolution. (F) FSC plot of the final refined undecameric unmasked (orange), masked (pink), phase-randomized (green) and corrected for mask convolution effects (blue) cryo-EM density map of CALHM6. The resolution at which the FSC curve drops below the 0.143 threshold is indicated. The inset shows the atomic model within the mask that was applied for calculations of the resolution estimates. (G) Final 3D reconstruction of undecameric CALHM6 colored according to local resolution.

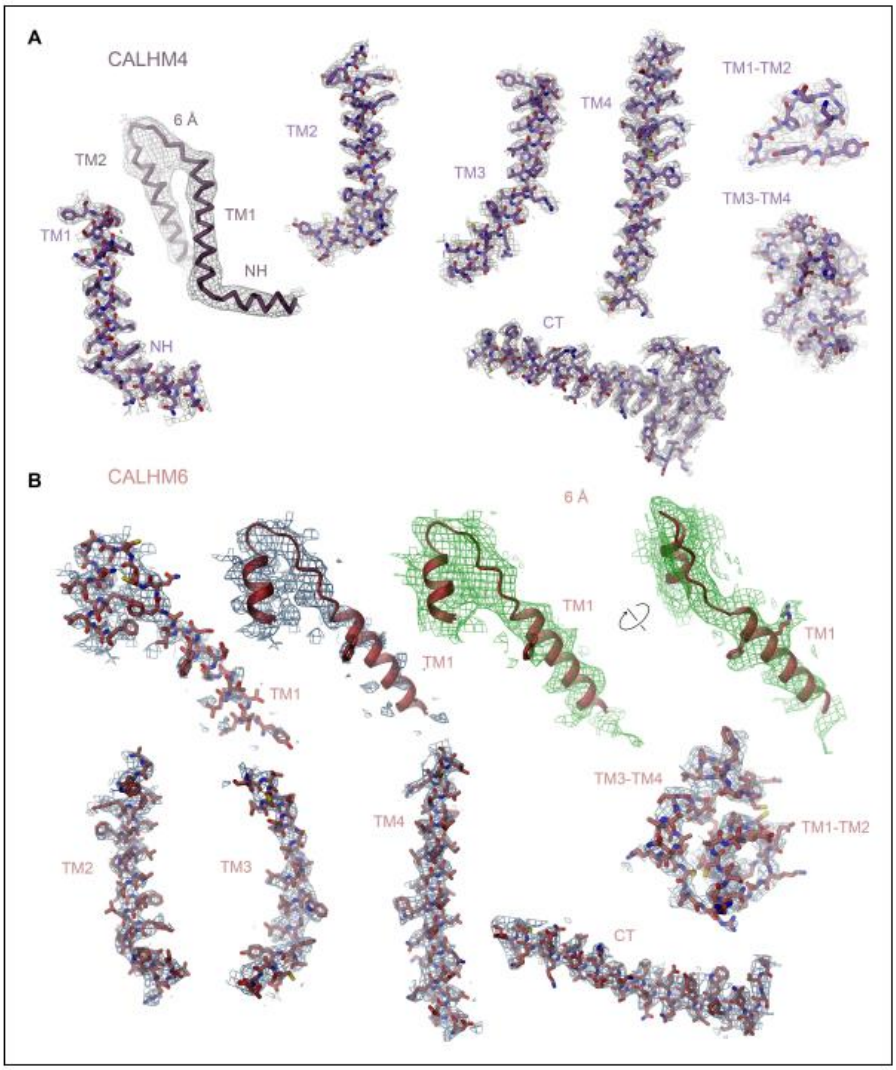

Figure 3—figure supplement 5. Cryo-EM density of CALHM4 and CALHM6. (A) Cryo-EM density at 3.7 Å of selected regions of the undecameric CALHM4 structure recorded from a sample obtained in the absence of Ca^{2+} superimposed on the model. Structural elements are indicated. '6 Å' marks cryo-EM density low-pass filtered to 6 Å superimposed on a Cα trace of NH and TM1, which illustrates the helicity of the entire NH region that is partly not defined in the density at higher resolution due to its intrinsic mobility. (B) Cryo-EM density at 4.4 Å of selected regions of the decameric CALHM6 structure superimposed on the model. Structural elements are indicated. '6 Å' marks cryo-EM density low-pass filtered to 6 Å superimposed on a ribbon of TM1 and parts of TM2, which displays extended density for the entire TM1 region that is partly not defined in the density at higher resolution due to its intrinsic mobility. Density is shown from two different views with indicated relationship. Large side chains that are recognizable in the low-pass filtered map are displayed as sticks.

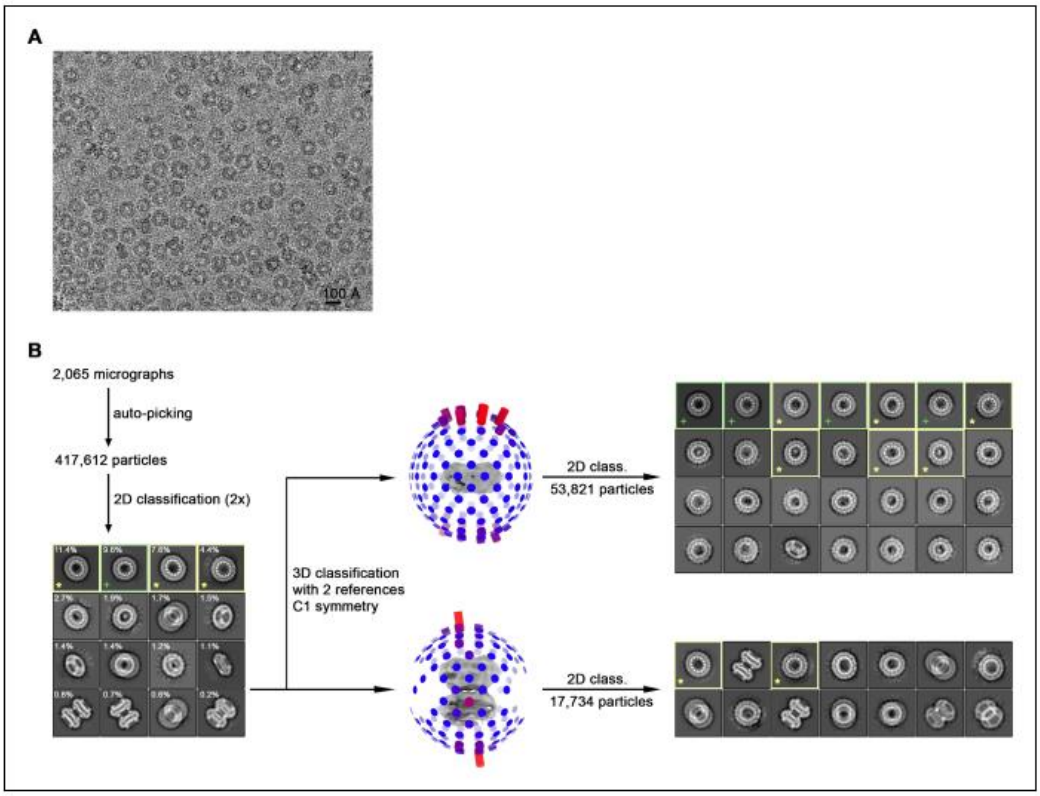

Figure 3—figure supplement 6. Cryo-EM reconstruction of CALHM2 in presence of Ca^{2+}. (A) Representative cryo-EM micrograph acquired with a Tecnai G^2 Polara microscope. (B) Data processing workflow. Non-symmetrized 3D classification with two reference models representing monomeric and dihedrally-related dimeric architectures as observed for CALHM6 and CALHM4, respectively, allowed to separate CALHM2 particles into two respective subsets. However, preferential orientation of the particles on a grid together with the presence of compositional heterogeneity in form of undecameric and dodecameric assemblies within each subset hindered generation of a high-resolution 3D reconstruction. 2D class averages calculated separately from monomeric and dimeric subsets highlight the predominance of views from the extracellular side. Green boxes and '+' mark representative views of undecameric and yellow boxes and '*' of dodecameric assemblies.

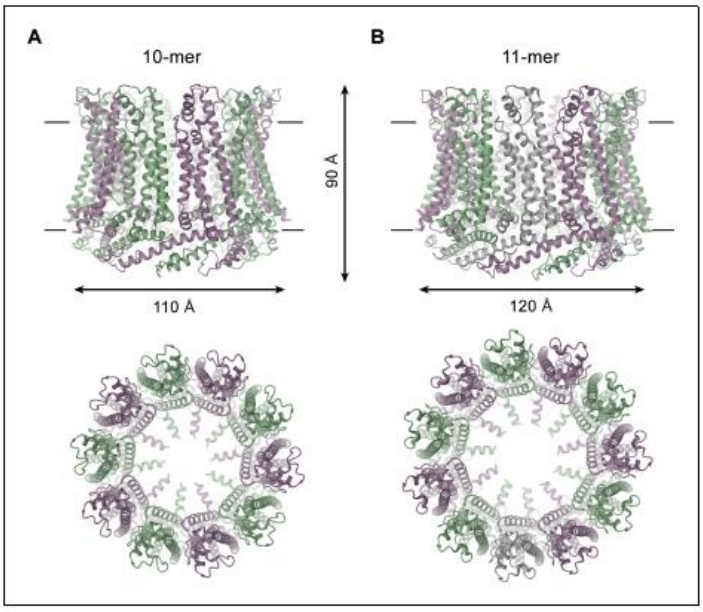

Figure 4. CALHM4 structure. Ribbon representation of (A), decameric and (B), undecameric CALHM4 channels. Top views are from within the membrane with membrane boundaries indicated, bottom views are from the extracellular side. The approximate dimensions are indicated. Subunits are colored in lilac and green.

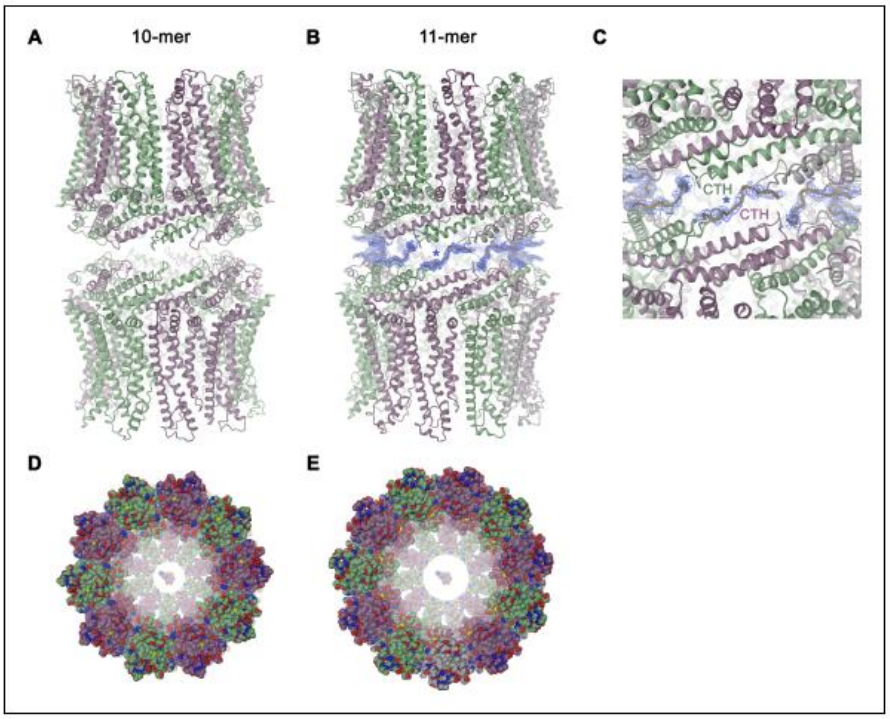

Figure 4—figure supplement 1. Features of the CALHM4 structure. Ribbon representation of (A), decameric and (B), undecameric channel pairs as observed in the CALHM4 dataset. In both cases, the proteins interact via their intracellular regions. Residual density at the C-terminus connecting both channels is shown as blue mesh and modeled as a poly-glycine chain. (C) Close-up of the interface between channel pairs shown in B. Space-filling models of the decameric (D), and undecameric (E) CALHM4 channel viewed from the extracellular side with ATP molecules shown a space-filling models for reference. Subunits are colored in lilac and green.

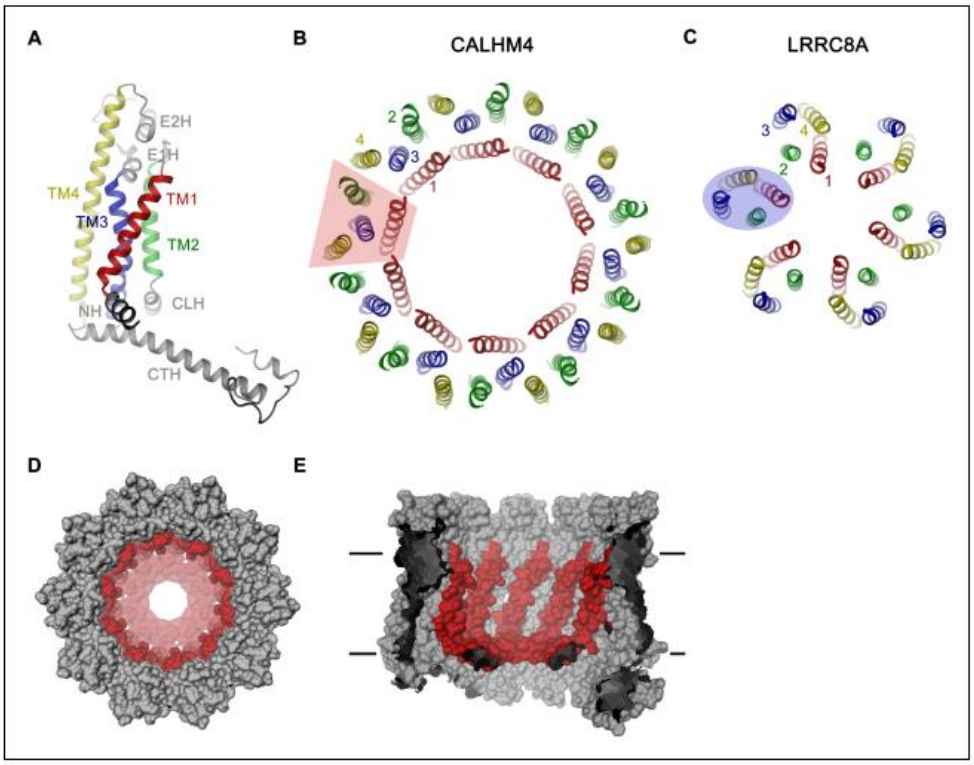

Figure 5. CALHM4 subunit and oligomeric arrangement. (A) Ribbon representation of the CALHM4 subunit. Secondary structure elements are labeled and transmembrane α-helices are shown in unique colors. View of the transmembrane α-helices of (B), the CALHM4 decamer and (C), the volume regulated anion channel LRRC8A from the extracellular side. B-C, color code is as in A, transmembrane segments of one subunit are numbered. The general shape of a single subunit is indicated (B, trapezoid, C, oval). (D) Surface representation of the CALHM4 decamer. The view is from the outside. (E) Slice through the CALHM4 pore viewed from within the membrane. D, E, TM1 and the N-terminal α-helix NH are colored in red.

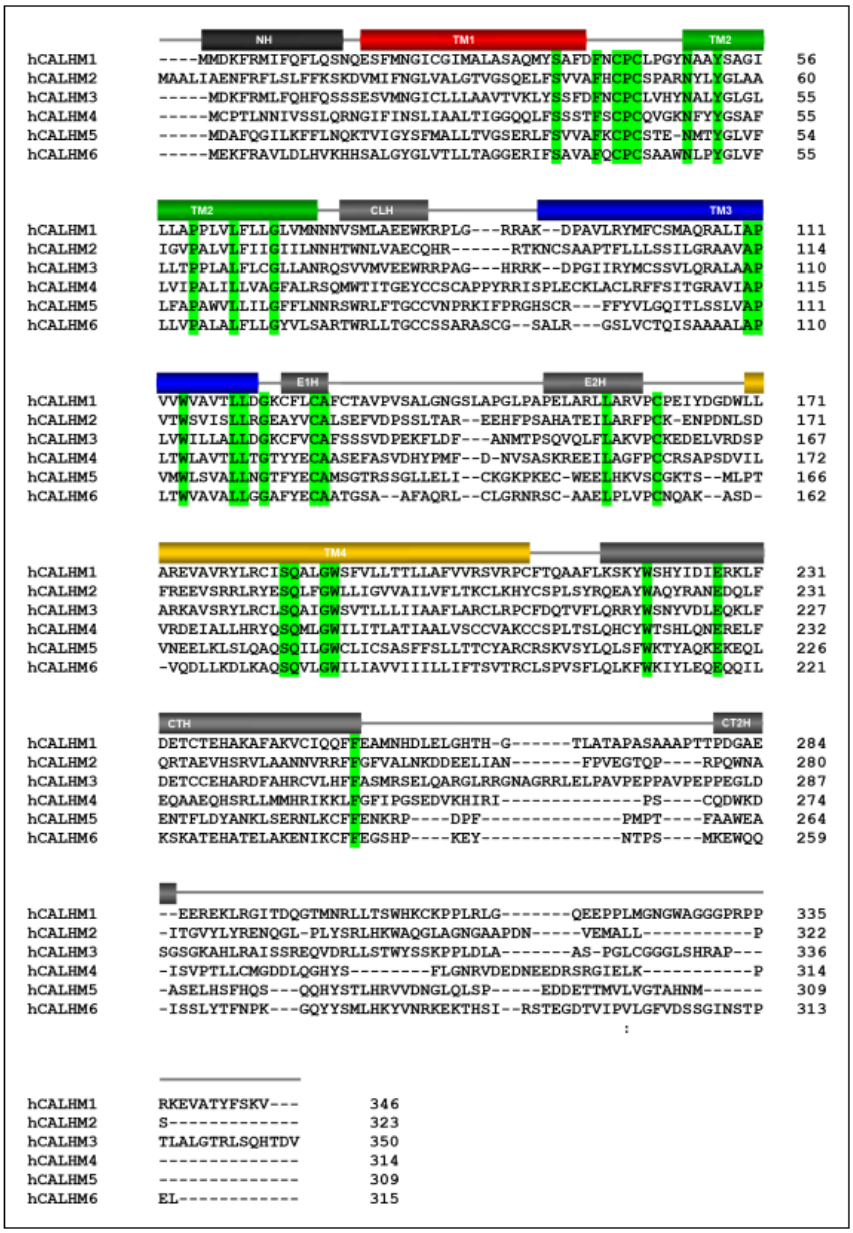

Figure 5—figure supplement 1. Sequence and topology. Sequence alignment of the human CALHM paralogs CALHM1 (NP_001001412.3), CALHM2 (NP_057000.2), CALHM3 (NP_001123214.1), CALHM4 (NP_001353007.1), CALHM5 (NP_714922.1) and CALHM6 (NP_001010919.1). Identical residues are highlighted in green, secondary structure elements of CALHM4 are indicated above.

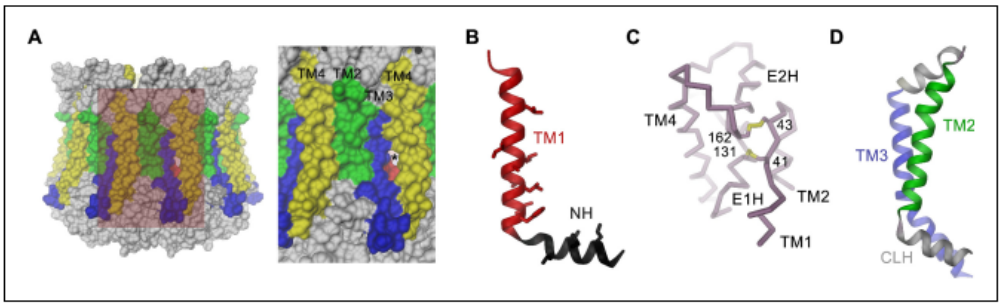

Figure 5—figure supplement 2. Features of the CALHM4 structure. (A) Molecular surface of the CALHM4 decamer viewed from within the membrane (left) and zoom into the highlighted region showing the interface between two subunits (right). Asterisk indicates location of a small fenestration on the surface between TM3 and TM4 of the same subunit. (B) Ribbon representation of TM1 and the N-terminal α-helix NH with side chains of hydrophobic residues facing the pore displayed as sticks. (C) Cα-trace of the extracellular region of CALHM4 with disulfide bridges shown as sticks and labeled. (D) Ribbon representation of TM2, the intracellular α-helix CLH and TM3. A, B, D, Transmembrane segments are colored as in ***Figure 5A*** and labeled.

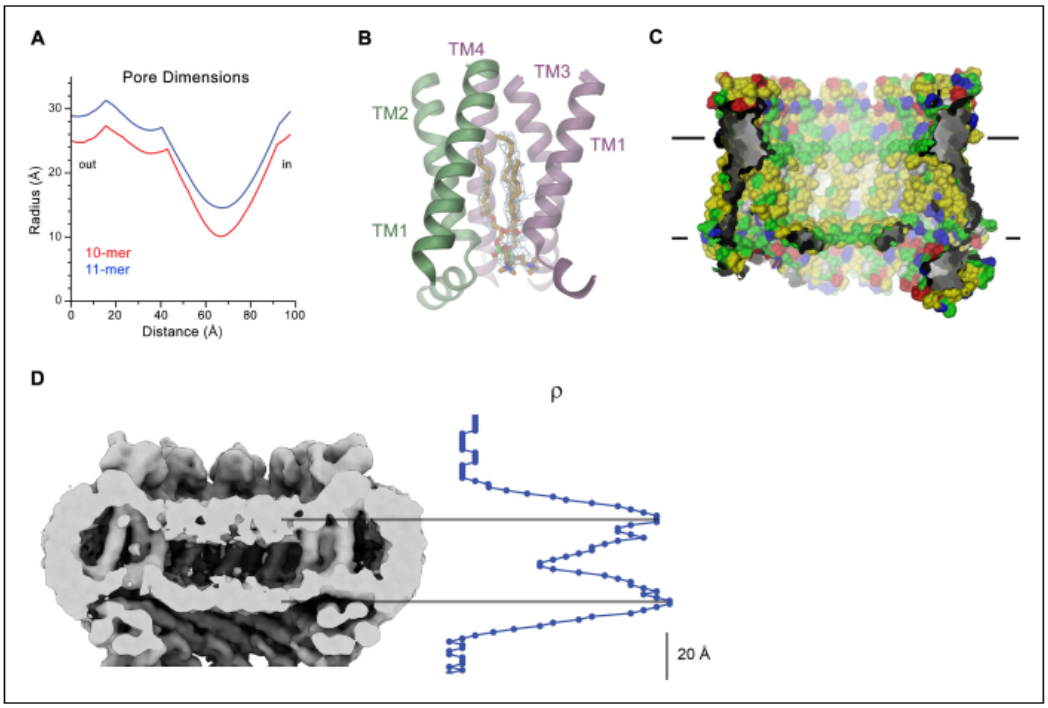

Figure 6. CALHM4 pore properties and lipid interactions. (A), Pore radius of the CALHM4 decamer (red) and undecamer (blue) as calculated in HOLE (*Smart et al., 1996*). (B) Two phosphatidylcholine molecules modeled into residual cryo-EM density (blue mesh) in a cavity at the interface between neighboring α-helices TM1. Secondary structure elements are indicated. (C) Chemical properties of residues lining the pore of the CALHM4 channel. Shown is a slice through the pore viewed from within the membrane. The protein is displayed as molecular surface. Hydrophobic residues are colored in yellow, polar residues in green, acidic residues in red and basic residues in blue. (D) Slice through the pore region of the CALHM4 undecamer viewed from within the membrane. Shown is non-averaged density in a single copy of the undecameric CALHM4 channel pair at low contour to highlight the location of increased density within the pore corresponding to a bilayer of either phospholipids or detergents. A plot of the density along the pore axis showing two maxima that are separated by the expected distance between the headgroup regions of a lipid bilayer is shown right. B, D, Displayed cryo-EM density refers to data from the undecameric channel in presence of Ca^{2+}.

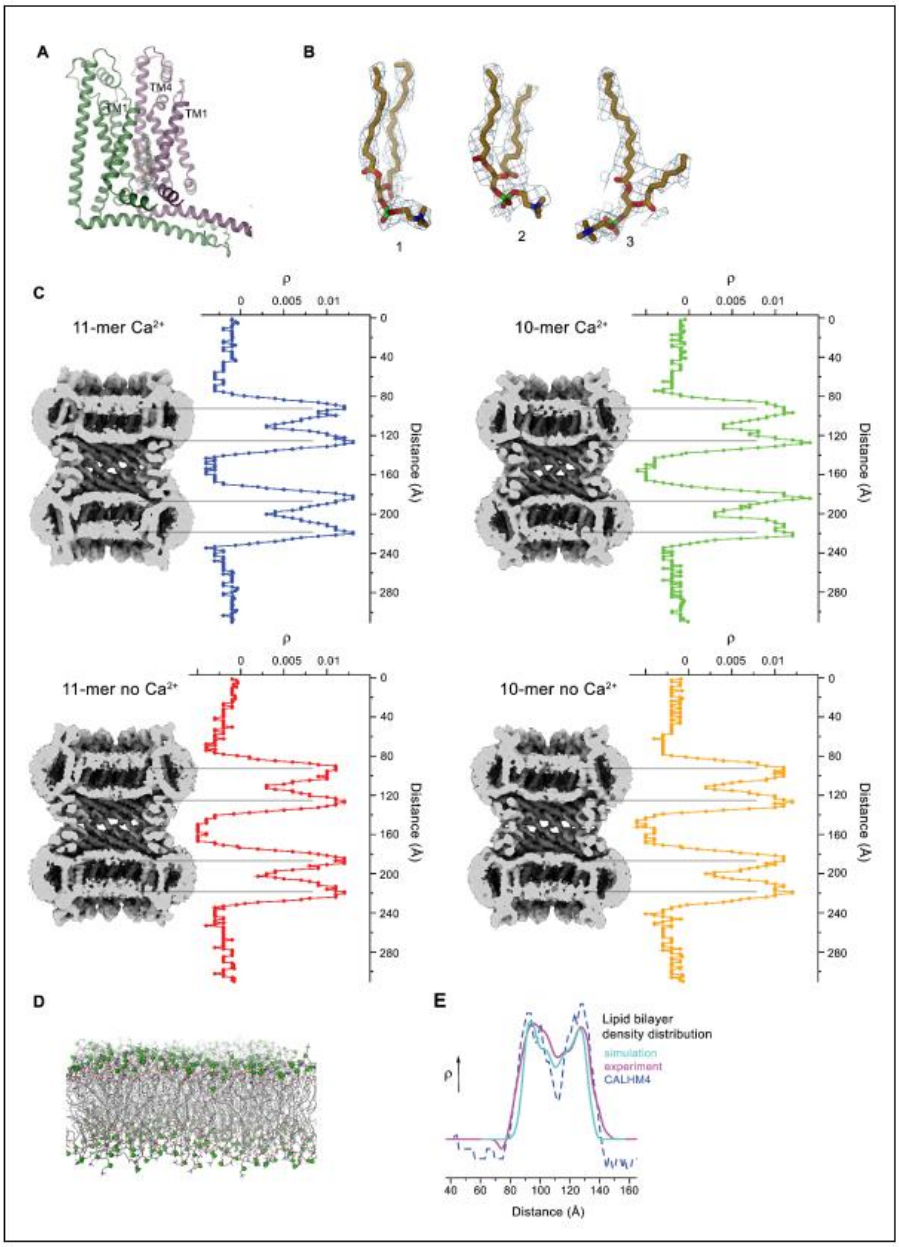

Figure 6—figure supplement 1. Lipid interactions in the pore of CALHM4. (A) Interface between α-helices TM1 of two neighboring subunits with two bound lipid molecules. View is similar as in *Figure 6A*. (B) Lipids modeled into residual electron density at the interface displayed in A. Lipids 2 and 3

Figure 6—figure supplement 1 continued on next page

Figure 6—figure supplement 1 continued

could occupy the cavity at the same time. I shows alternative interpretation of the density with a single lipid. A, B, Displayed cryo-EM density refers to data from the undecameric channel in presence of Ca^{2+}. (C) Slices through the pore regions of interacting CALHM4 channel pairs as observed in different datasets. Proteins are viewed from within the membrane. Shown is non-averaged density at low contour (left). The distribution (right) shows two equivalent regions of increased density corresponding to bilayers of ether phospholipids or detergents residing in each channel. The pore-density displays very similar features in CALHM4 decamers and undecamers irrespective of the presence or absence of Ca^{2+}. (D) Model membrane obtained from MD simulations shown as stick models with the phosphate atoms highlighted as green spheres. (E) Comparison of the observed pore density distribution (dashed blue line, CALHM4) to equivalent distributions obtained from membrane simulations (cyan, simulation) and cryo-EM data of liposomes (magenta, experiment). All distributions display equivalent features.

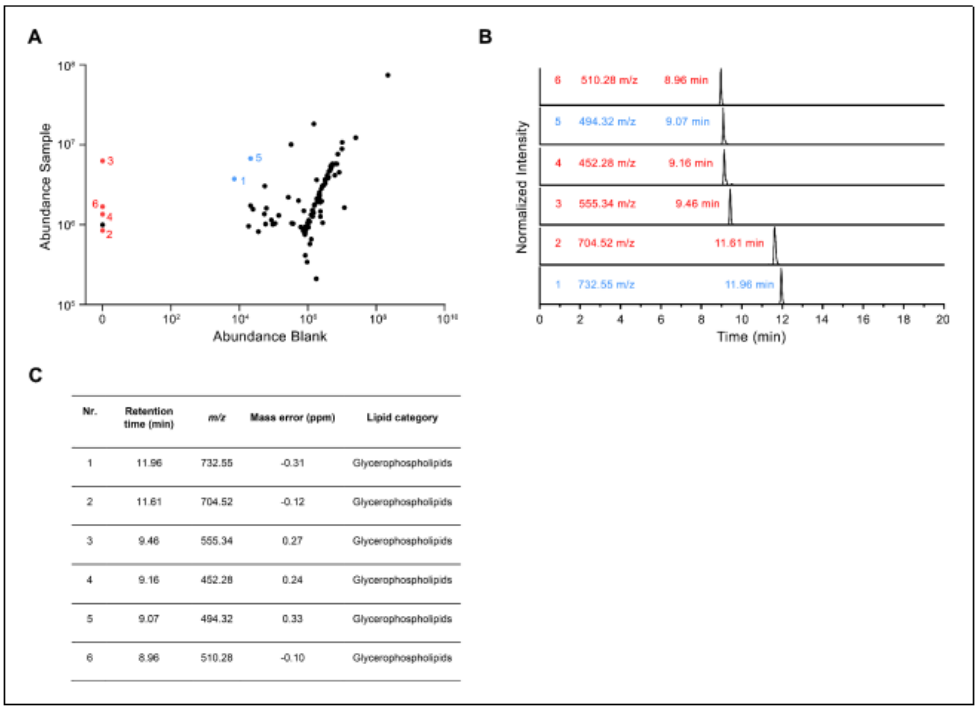

C

Nr.	Retention time (min)	m/z	Mass error (ppm)	Lipid category
1	11.96	732.55	-0.31	Glycerophospholipids
2	11.61	704.52	-0.12	Glycerophospholipids
3	9.46	555.34	0.27	Glycerophospholipids
4	9.16	452.28	0.24	Glycerophospholipids
5	9.07	494.32	0.33	Glycerophospholipids
6	8.96	510.28	-0.10	Glycerophospholipids

Figure 6—figure supplement 2. LC-MS analysis of co-purified lipids. (A) Scatter plot depicting the relative amounts of the 100 most abundant hydrophobic compounds detected in the LC-MS analysis of the CALHM4 sample compared to the blank. Red dots represent compounds that are detected in the CALHM4 sample only and blue dots represent compounds that are highly enriched in the CALHM4 sample compared to the blank (fold change >100). (B) TIC chromatograms of compounds indicated in A, with assigned mass to charge ratio (m/z) and retention time. (C) Table summarizing the properties of compounds isolated from the CALHM4 sample. The chemical identity was identified in a search against the LipidMaps (LM) library with matching tolerances of 1 ppm in mass accuracy and >90% in isotope similarity.

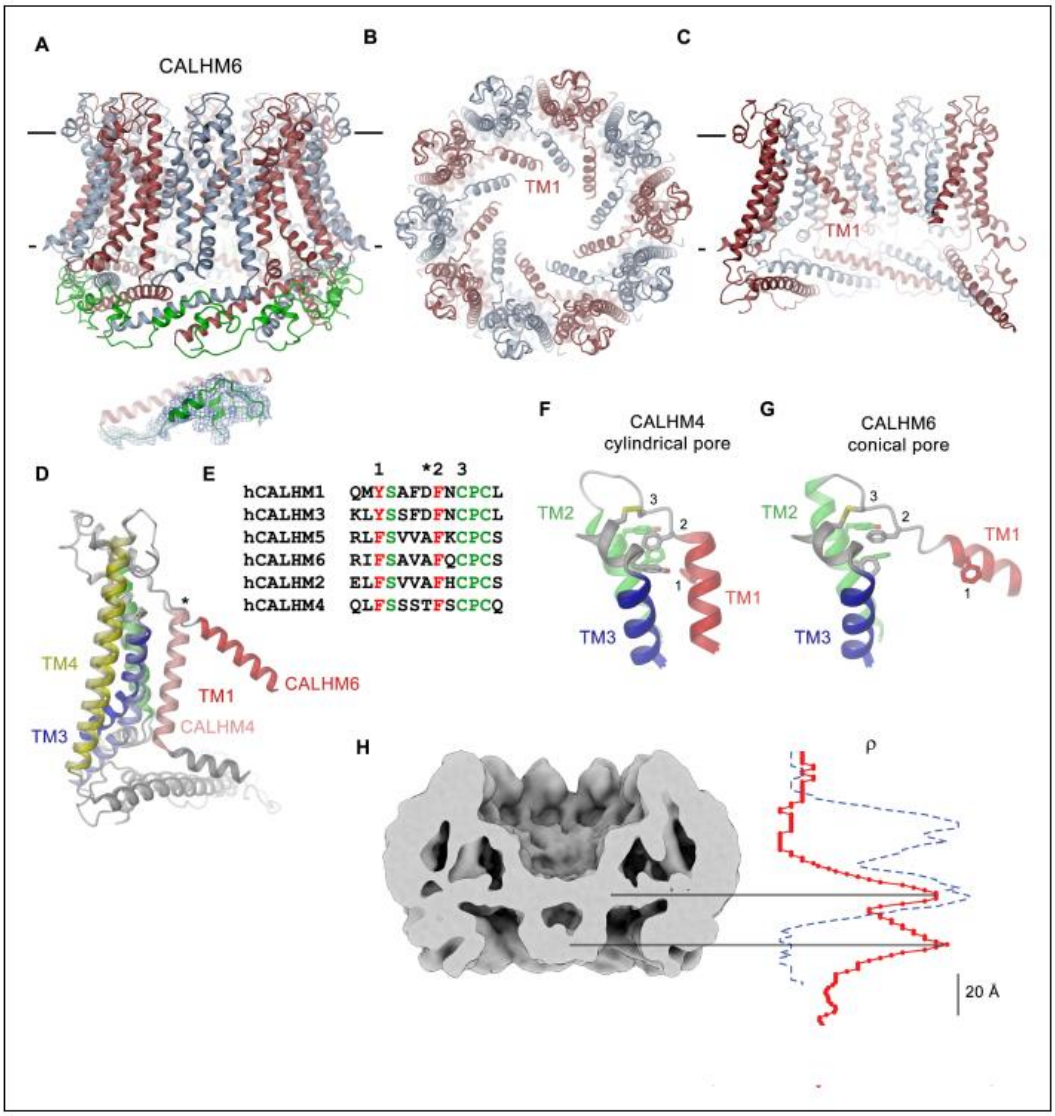

Figure 7. CALHM6 structure. (A) Ribbon representation of the decameric CALHM6 structure viewed from within the membrane. Subunits are colored in red and light blue. The C-terminus following CTH is colored in green. Inset (below) shows a close-up of this region with cryo-EM density superimposed. (B) View of the CALHM structure from the extracellular side. (C) Slice through the pore of the CALHM6 structure. B, C, TM1, which has moved towards the pore axis is labeled. A, C, the membrane boundary is indicated. (D) Superposition of single subunits of the CALHM4 and CALHM6 structures illustrating conformational changes. Coloring is as in *Figure 5A* with CALHM4 shown in brighter shades of the same color. Secondary structure elements are labeled and the hinge for the movement of TM1 is indicated by an asterisk. (E) Sequence alignment of the end of TM1 and the following loop of CALHM paralogs. Selected conserved residues are colored in green and red. Numbering corresponds to residues indicated in panels F and G. Asterisk marks the hinge region displayed in D. Close-up of the extracellular region involved in conformational changes in (F), the cylindrical

Figure 7 continued on next page

Figure 7 continued

conformation displayed in CALHM4 and (G), the conical conformation displayed in CALHM6. Residues contributing to a cluster of aromatic residues on TM1-3 and a conserved disulfide bridge are shown as sticks. Selected positions highlighted in E are labeled. F, G, Coloring is as in ***Figure 5A***. (H) Slice through the pore region of the CALHM6 decamer viewed from within the membrane. Shown is non-averaged density at low contour to highlight the location of diffuse density within the pore. A plot of the density along the pore axis of CALHM6 is shown in red, the corresponding density in CALHM4 is shown as a dashed blue line for comparison. The two maxima in the CALHM6 density are shifted towards the intracellular side. The density corresponding to the headgroups of the outer leaflet of the bilayer in CALHM4 is absent. Density at the location of the headgroup region at the inner leaflet of the bilayer and further towards the intracellular side could correspond to either lipids or to the poorly ordered N-terminus.

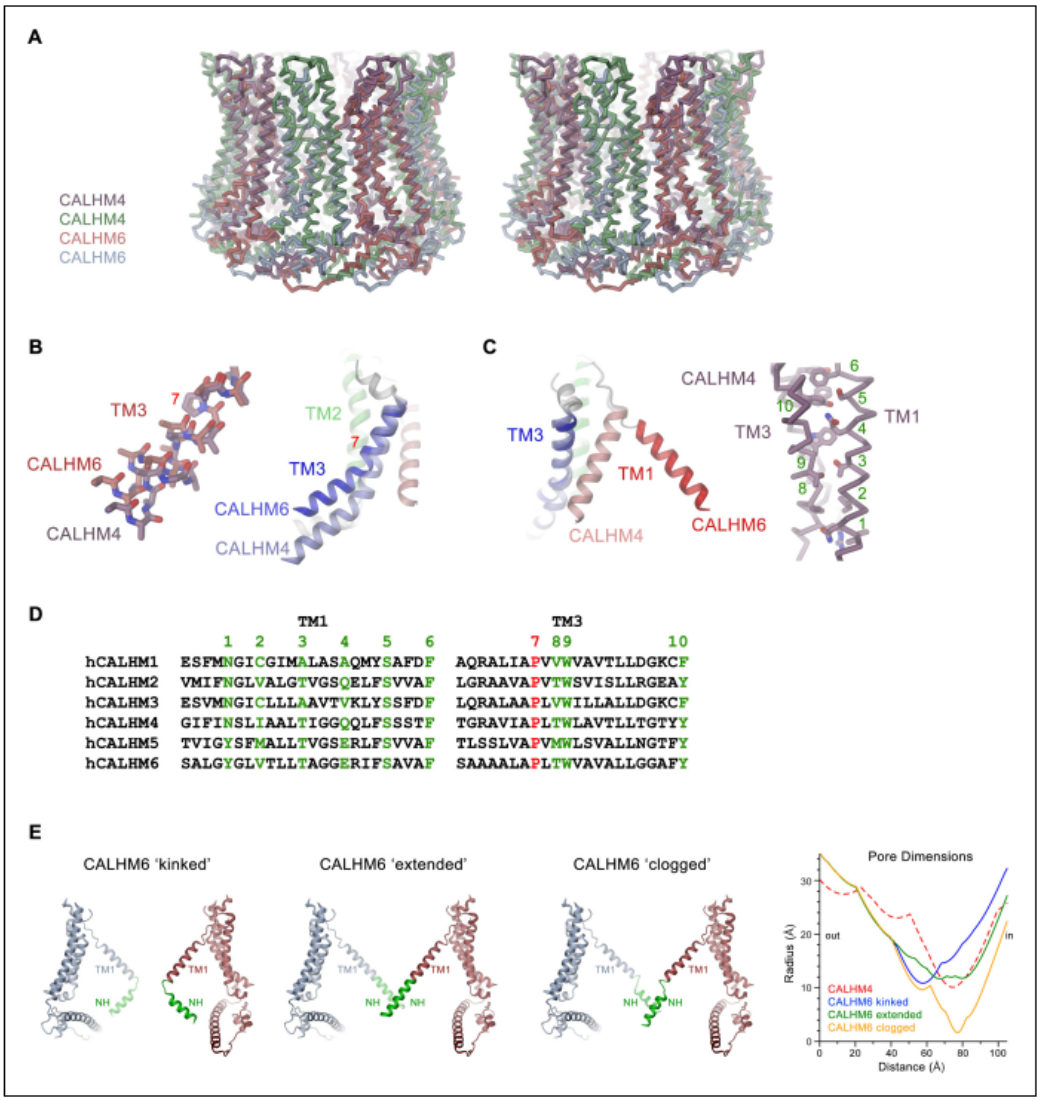

Figure 7—figure supplement 1. Features of the CALHM6 structure. (A) Stereo view of a superposition of the CALHM4 and CALHM6 decamers. The proteins are shown as Cα-traces. Coloring is as in *Figures 4* and *6*. (B) Close-up of the conformational change in TM3 from the cylindrical conformation displayed in CALHM4 to the conical conformation displayed in CALHM6. Right panel shows ribbon, left panel a stick model of TM3 with side chains truncated to their Cβ position except for a conserved proline at the site of conformational changes where the entire side chain is displayed. (C) Close-up of the conformational change of TM1 with molecules displayed as ribbons (left) and interaction region of TM1 and TM3 in the CALHM4 structure with the protein shown as Cα trace and side chains of interacting residues as sticks (right). B and C, coloring of ribbons is as in *Figure 7D* with secondary structure elements in CALHM4 shown in brighter shades of the same color. (D) Sequence alignments of TM1 and TM3 of different CALHM paralogs. The conserved proline displayed in B is colored in red, selected residues at the TM1 TM3 interaction interface displayed in C are colored in

Figure 7—figure supplement 1 continued on next page

Figure 7—figure supplement 1 continued

green. B, C, Numbering corresponds to positions labeled in D. (E) Hypothetical pore shapes of the conical conformation displayed in the CALHM6 structure. The disordered N-terminal helix NH (green) was modeled in different conformations. Left, 'kinked' conformation where the mutual relationship between TM1 and NH is as in CALHM4, center left, 'extended' conformation where NH has changed its conformation to extend the TM1 helix. Center right, 'clogged' conformation where the mobile NH helix has moved towards the pore axis. The 10-fold symmetry is maintained in the 'kinked' and 'extended' conformations and broken for NH in the 'clogged' conformation to improve protein interactions. Opposite subunits of the decameric structures are displayed. Right, pore dimensions of the different modeled conformations of CALHM6 calculated with HOLE (***Smart et al., 1996***) compared to the CALHM4 decamer (red dashed) display similar constricting pore radius as for CALHM4 for 'kinked' and 'extended' conformations and an occluded pore in case of the 'clogged' conformation.

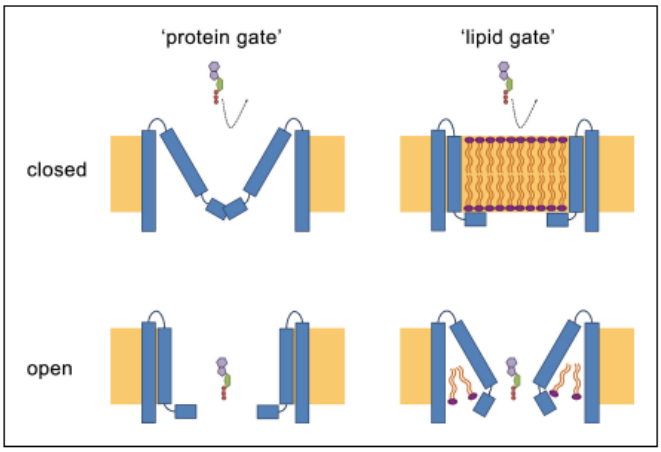

Figure 8. Hypothetical gating mechanisms. Schematic illustration of hypothetical gating mechanisms of large CALHM channels. Left, 'protein gate'. The gate impeding ion conduction of large CALHM channels (i.e. CALHM2, 4, 6) in the closed state is formed by the N-terminus of the protein, which closes the pore as observed in the modeled 'clogged' conformation of CALHM6 (top). In this case the conical conformation of CALHM6 would display a closed pore and the cylindrical conformation (bottom) an open pore. Right, 'lipid gate'. The gate impeding ion conduction of large CALHM channels in the closed state is formed by lipids assembling as a bilayer within the protein, which impedes ion conduction. Since bilayer formation is facilitated in the cylindrical conformation of CALHM4, this structure represents a closed pore (top) whereas the structure of the bilayer would be disturbed in the conical conformation of CALHM6 (bottom). Since both the 'kinked' and 'extended' pore conformations of CALHM6 show a large opening, these conformations could represent open pores.

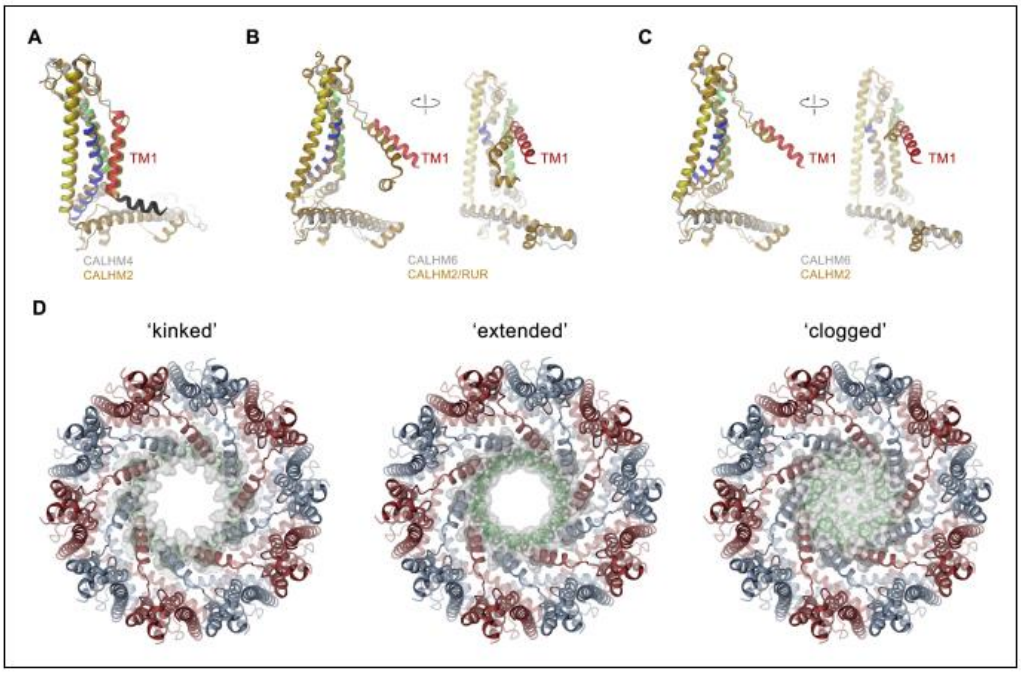

Figure 8—figure supplement 1. Comparison of pore conformations. (A) Comparison of the structures of subunits determined in this study to recent structures of CALHM2. Left, structure of the cylindrical conformation of CALHM4 superimposed on the equivalent conformation of CALHM2 (PDBID 6UIV). Superposition of the conical CALHM6 conformation with (B), the CALHM2 structure in complex with the putative inhibitor ruthenium red (RUR) (PDBID 6UIW) and (C), an equivalent conformation in the absence of RUR (PDBID 6UIX), both showing a different orientation of TM1. A-C, CALHM4 and 6 structures are colored as in ***Figure 5A***, CALHM2 structures are colored in beige. B and C show two views of the subunit with indicated mutual relationship. (D) View of the three potential conformations of CALHM6 with modeled N-termini (green) as defined in ***Figure 7—figure supplement 1E***. The molecular surface at the pore constriction is shown superimposed on the structure. A-D, proteins are displayed as ribbons.

Curriculum vitae

Katarzyna Drożdżyk

Nationality: Polish
Address: Scheuchzerstrasse 14, 8006 Zurich, Switzerland
E-mail: k.drozdzyk@bioc.uzh.ch
Phone: +41 76 377 92 91

Research experience

Jan. 2019 – Present	**PhD student, Group of Prof. Raimund Dutzler, University of Zurich**, Zurich, Switzerland
Aug. 2018 – Dec. 2018	**Junior Scientist, Group of Protein Biochemistry, Selvita Company**, Cracow, Poland
Feb. 2017 – Jul. 2018	**Master's Student, Group of Dr. Sebastian Glatt, Max Planck Research Group in Malopolska Centre of Biotechnology**, Cracow, Poland
Oct. 2015 – Jun. 2016	**Bachelor's Student, Virogenetics Group, Jagiellonian University in Cracow**, Cracow, Poland

Education

Jan. 2019 – Present	**PhD in Biochemistry,** University of Zurich, Raimund Dutzler group, Department of Biochemistry, Faculty of Science, Zurich Switzerland
2016 – 2018	**MSc in Molecular Biotechnology**, Jagiellonian University, Cracow, Poland
Sep, 2016 – Jan. 2017	**Exchange Student in Biomedical Sciences**, University of Amsterdam, Amsterdam, Netherlands
2013 – 2016	**BSc in Biotechnology**, Jagiellonian University, Cracow, Poland

Publications

Lehmann, E.F., Liziczai, M. et al., *Structures of ferroportin in complex with its specific inhibitor vamifeport*. Elife 12, e83053 (2023); doi: 10.7554/eLife.83053.sa2

Kojic, M., Gawda, T., Gaik, M. et al. *Elp2 mutations perturb the epitranscriptome and lead to a complex neurodevelopmental phenotype*. Nat Commun 12, 2678 (2021); doi:10.1038/s41467-021-22888-5

Drożdżyk, K., Sawicka, M. et al. *Cryo-EM structures and functional properties of CALHM channels of the human placenta*. Elife 9 (2020); doi:10.7554/eLife.55853

References

1 Ma, Z., Tanis, J. E., Taruno, A. & Foskett, J. K. Calcium homeostasis modulator (CALHM) ion channels. *Pflugers Arch* **468**, 395-403, doi:10.1007/s00424-015-1757-6 (2016).

2 Ma, Z. *et al.* Calcium homeostasis modulator 1 (CALHM1) is the pore-forming subunit of an ion channel that mediates extracellular Ca2+ regulation of neuronal excitability. *Proc Natl Acad Sci U S A* **109**, E1963-1971, doi:10.1073/pnas.1204023109 (2012).

3 Siebert, A. P. *et al.* Structural and functional similarities of calcium homeostasis modulator 1 (CALHM1) ion channel with connexins, pannexins, and innexins. *J Biol Chem* **288**, 6140-6153, doi:10.1074/jbc.M112.409789 (2013).

4 Alberts B, J. A., Lewis J, et al. Molecular Biology of the Cell. 4th edition. *New York: Garland Science* (2002).

5 Al-Awqati, Q. One hundred years of membrane permeability: does Overton still rule? *Nature Cell Biology* **1**, E201-E202, doi:10.1038/70230 (1999).

6 Stein, W. D. & Litman, T. in *Channels, Carriers, and Pumps (Second Edition)* (eds Wilfred D. Stein & Thomas Litman) 1-36 (Elsevier, 2015).

7 Stillwell, W. in *An Introduction to Biological Membranes (Second Edition)* (ed William Stillwell) 423-451 (Elsevier, 2016).

8 Armstrong, C. M. The Na/K pump, Cl ion, and osmotic stabilization of cells. *Proceedings of the National Academy of Sciences* **100**, 6257-6262, doi:doi:10.1073/pnas.0931278100 (2003).

9 Wright, S. H. Generation of resting membrane potential. *Advances in Physiology Education* **28**, 139-142, doi:10.1152/advan.00029.2004 (2004).

10 Lewis, R. *et al.* The role of the membrane potential in chondrocyte volume regulation. *Journal of Cellular Physiology* **226**, 2979-2986, doi:https://doi.org/10.1002/jcp.22646 (2011).

11 Abdul Kadir, L., Stacey, M. & Barrett-Jolley, R. Emerging Roles of the Membrane Potential: Action Beyond the Action Potential. *Front Physiol* **9**, 1661, doi:10.3389/fphys.2018.01661 (2018).

12 Hille, B. Ion Channels of Excitable Membranes *Sinauer, Sunderland, Mass* (2001).

13 Gouaux, E. & MacKinnon, R. Principles of Selective Ion Transport in Channels and Pumps. *Science* **310**, 1461-1465, doi:doi:10.1126/science.1113666 (2005).

14 Di Resta, C. & Becchetti, A. Introduction to ion channels. *Adv Exp Med Biol* **674**, 9-21, doi:10.1007/978-1-4419-6066-5_2 (2010).

15 Aryal, P., Sansom, M. S. P. & Tucker, S. J. Hydrophobic Gating in Ion Channels. *Journal of Molecular Biology* **427**, 121-130, doi:https://doi.org/10.1016/j.jmb.2014.07.030 (2015).

16 Lam, A. K. M. & Dutzler, R. Calcium-dependent electrostatic control of anion access to the pore of the calcium-activated chloride channel TMEM16A. *eLife* **7**, e39122, doi:10.7554/eLife.39122 (2018).

17 Katta, S., Krieg, M. & Goodman, M. B. Feeling Force: Physical and Physiological Principles Enabling Sensory Mechanotransduction. *Annual Review of Cell and Developmental Biology* **31**, 347-371, doi:10.1146/annurev-cellbio-100913-013426 (2015).

18 Josselyn, S. A. The past, present and future of light-gated ion channels and optogenetics. *eLife* **7**, e42367, doi:10.7554/eLife.42367 (2018).

19 Lamas, J. A., Rueda-Ruzafa, L. & Herrera-Pérez, S. Ion Channels and Thermosensitivity: TRP, TREK, or Both? *International Journal of Molecular Sciences* **20** (2019).

20 Harris, A. L. Connexin channel permeability to cytoplasmic molecules. *Prog Biophys Mol Biol* **94**, 120-143, doi:10.1016/j.pbiomolbio.2007.03.011 (2007).

21 Beyer, E. C. & Berthoud, V. M. Gap junction gene and protein families: Connexins, innexins, and pannexins. *Biochim Biophys Acta Biomembr* **1860**, 5-8, doi:10.1016/j.bbamem.2017.05.016 (2018).

22 Strange, K., Yamada, T. & Denton, J. S. A 30-year journey from volume-regulated anion currents to molecular structure of the LRRC8 channel. *J Gen Physiol* **151**, 100-117, doi:10.1085/jgp.201812138 (2019).
23 Whyte-Fagundes, P. & Zoidl, G. Mechanisms of pannexin1 channel gating and regulation. *Biochimica et Biophysica Acta (BBA) - Biomembranes* **1860**, 65-71, doi:https://doi.org/10.1016/j.bbamem.2017.07.009 (2018).
24 Dahl, G. & Muller, K. J. Innexin and pannexin channels and their signaling. *FEBS Letters* **588**, 1396-1402, doi:https://doi.org/10.1016/j.febslet.2014.03.007 (2014).
25 Scemes, E., Spray, D. C. & Meda, P. Connexins, pannexins, innexins: novel roles of "hemi-channels". *Pflügers Archiv - European Journal of Physiology* **457**, 1207-1226, doi:10.1007/s00424-008-0591-5 (2009).
26 Maeda, S. *et al.* Structure of the connexin 26 gap junction channel at 3.5 A resolution. *Nature* **458**, 597-602, doi:10.1038/nature07869 (2009).
27 Oshima, A., Tani, K. & Fujiyoshi, Y. Atomic structure of the innexin-6 gap junction channel determined by cryo-EM. *Nat Commun* **7**, 13681, doi:10.1038/ncomms13681 (2016).
28 Deneka, D., Sawicka, M., Lam, A. K. M., Paulino, C. & Dutzler, R. Structure of a volume-regulated anion channel of the LRRC8 family. *Nature* **558**, 254-259, doi:10.1038/s41586-018-0134-y (2018).
29 Ruan, Z., Orozco, I. J., Du, J. & Lu, W. Structures of human pannexin 1 reveal ion pathways and mechanism of gating. *Nature* **584**, 646-651, doi:10.1038/s41586-020-2357-y (2020).
30 Maeda, S. *et al.* Structure of the connexin 26 gap junction channel at 3.5 Å resolution. *Nature* **458**, 597-602, doi:10.1038/nature07869 (2009).
31 Güiza, J., Barría, I., Sáez, J. C. & Vega, J. L. Innexins: Expression, Regulation, and Functions. *Frontiers in Physiology* **9**, doi:10.3389/fphys.2018.01414 (2018).
32 Goodenough, D. A. & Paul, D. L. Beyond the gap: functions of unpaired connexon channels. *Nature Reviews Molecular Cell Biology* **4**, 285-295, doi:10.1038/nrm1072 (2003).
33 Oshima, A., Matsuzawa, T., Nishikawa, K. & Fujiyoshi, Y. Oligomeric structure and functional characterization of Caenorhabditis elegans Innexin-6 gap junction protein. *J Biol Chem* **288**, 10513-10521, doi:10.1074/jbc.M112.428383 (2013).
34 Giuliani, A. L., Sarti, A. C. & Di Virgilio, F. Extracellular nucleotides and nucleosides as signalling molecules. *Immunol Lett* **205**, 16-24, doi:10.1016/j.imlet.2018.11.006 (2019).
35 Dreses-Werringloer, U. *et al.* A polymorphism in CALHM1 influences Ca2+ homeostasis, Abeta levels, and Alzheimer's disease risk. *Cell* **133**, 1149-1161, doi:10.1016/j.cell.2008.05.048 (2008).
36 Beecham, G. W., Schnetz-Boutaud, N., Haines, J. L. & Pericak-Vance, M. A. CALHM1 Polymorphism is not Associated with Late-onset Alzheimer Disease. *Annals of Human Genetics* **73**, 379-381, doi:https://doi.org/10.1111/j.1469-1809.2009.00509.x (2009).
37 Minster, R. L., Demirci, F. Y., DeKosky, S. T. & Kamboh, M. I. No association between CALHM1 variation and risk of Alzheimer disease. *Human Mutation* **30**, E566-E569, doi:https://doi.org/10.1002/humu.20989 (2009).
38 Sleegers, K. *et al.* No association between CALHM1 and risk for Alzheimer dementia in a Belgian population. *Human Mutation* **30**, E570-E574, doi:https://doi.org/10.1002/humu.20990 (2009).
39 Nacmias, B. *et al.* Lack of Implication for CALHM1 P86L Common Variation in Italian Patients with Early and Late Onset Alzheimer's Disease. *Journal of Alzheimer's Disease* **20**, 37-41, doi:10.3233/JAD-2010-1345 (2010).
40 Lambert, J. C. *et al.* The CALHM1 P86L polymorphism is a genetic modifier of age at onset in Alzheimer's disease: a meta-analysis study. *J Alzheimers Dis* **22**, 247-255, doi:10.3233/JAD-2010-100933 (2010).
41 Lu, Y. *et al.* Genetic association of CALHM1 rs2986017 polymorphism with risk of Alzheimer's disease: a meta-analysis. *Neurological Sciences* **37**, 525-532, doi:10.1007/s10072-015-2451-3 (2016).

42 Moreno-Ortega, A. J., Ruiz-Nuno, A., Garcia, A. G. & Cano-Abad, M. F. Mitochondria sense with different kinetics the calcium entering into HeLa cells through calcium channels CALHM1 and mutated P86L-CALHM1. *Biochem Biophys Res Commun* **391**, 722-726, doi:10.1016/j.bbrc.2009.11.127 (2010).
43 Tanis, J. E., Ma, Z. & Foskett, J. K. The NH2 terminus regulates voltage-dependent gating of CALHM ion channels. *Am J Physiol Cell Physiol* **313**, C173-C186, doi:10.1152/ajpcell.00318.2016 (2017).
44 Ma, Z. *et al.* CALHM3 Is Essential for Rapid Ion Channel-Mediated Purinergic Neurotransmission of GPCR-Mediated Tastes. *Neuron* **98**, 547-561 e510, doi:10.1016/j.neuron.2018.03.043 (2018).
45 Taruno, A. *et al.* CALHM1 ion channel mediates purinergic neurotransmission of sweet, bitter and umami tastes. *Nature* **495**, 223-226, doi:10.1038/nature11906 (2013).
46 Kashio, M., Wei-Qi, G., Ohsaki, Y., Kido, M. A. & Taruno, A. CALHM1/CALHM3 channel is intrinsically sorted to the basolateral membrane of epithelial cells including taste cells. *Sci Rep* **9**, 2681, doi:10.1038/s41598-019-39593-5 (2019).
47 Segal, M. Calcium stores regulate excitability in cultured rat hippocampal neurons. *Journal of Neurophysiology* **120**, 2694-2705, doi:10.1152/jn.00447.2018 (2018).
48 Gover, T. D., Moreira, T. H. & Weinreich, D. in *Sensory Nerves* (eds Brendan J. Canning & Domenico Spina) 563-587 (Springer Berlin Heidelberg, 2009).
49 Workman, A. D. *et al.* CALHM1-Mediated ATP Release and Ciliary Beat Frequency Modulation in Nasal Epithelial Cells. *Sci Rep* **7**, 6687, doi:10.1038/s41598-017-07221-9 (2017).
50 Romanov, R. A. *et al.* Chemical synapses without synaptic vesicles: Purinergic neurotransmission through a CALHM1 channel-mitochondrial signaling complex. *Sci Signal* **11**, doi:10.1126/scisignal.aao1815 (2018).
51 Sana-Ur-Rehman, H., Markus, I., Moore, K. H., Mansfield, K. J. & Liu, L. Expression and localization of pannexin-1 and CALHM1 in porcine bladder and their involvement in modulating ATP release. *American Journal of Physiology-Regulatory, Integrative and Comparative Physiology* **312**, R763-R772, doi:10.1152/ajpregu.00039.2016 (2017).
52 Sana-Ur-Rehman, H., Markus, I., Moore, K. H., Mansfield, K. J. & Liu, L. Expression and localization of pannexin-1 and CALHM1 in porcine bladder and their involvement in modulating ATP release. *Am J Physiol Regul Integr Comp Physiol* **312**, R763-r772, doi:10.1152/ajpregu.00039.2016 (2017).
53 Jessica, E. T. *et al.* CLHM-1 is a Functionally Conserved and Conditionally Toxic Ca²⁺-Permeable Ion Channel in <em>Caenorhabditis elegans</em&gt. *The Journal of Neuroscience* **33**, 12275, doi:10.1523/JNEUROSCI.5919-12.2013 (2013).
54 Jun, M. *et al.* Calhm2 governs astrocytic ATP releasing in the development of depression-like behaviors. *Molecular Psychiatry* **23**, 883-891, doi:10.1038/mp.2017.229 (2018).
55 Kasamatsu, J. *et al.* INAM plays a critical role in IFN-gamma production by NK cells interacting with polyinosinic-polycytidylic acid-stimulated accessory cells. *J Immunol* **193**, 5199-5207, doi:10.4049/jimmunol.1400924 (2014).
56 Ebihara, T. *et al.* Identification of a polyI:C-inducible membrane protein that participates in dendritic cell-mediated natural killer cell activation. *J Exp Med* **212**, 1337, doi:10.1084/jem.2009157307012015c (2015).
57 Drozdzyk, K. *et al.* Cryo-EM structures and functional properties of CALHM channels of the human placenta. *Elife* **9**, doi:10.7554/eLife.55853 (2020).
58 Ehrnstorfer, I. A., Manatschal, C., Arnold, F. M., Laederach, J. & Dutzler, R. Structural and mechanistic basis of proton-coupled metal ion transport in the SLC11/NRAMP family. *Nature Communications* **8**, 14033, doi:10.1038/ncomms14033 (2017).
59 Uhlén, M. *et al.* Tissue-based map of the human proteome. *Science* **347**, 1260419, doi:10.1126/science.1260419 (2015).

60 Maier, T., Güell, M. & Serrano, L. Correlation of mRNA and protein in complex biological samples. *FEBS Letters* **583**, 3966-3973, doi:https://doi.org/10.1016/j.febslet.2009.10.036 (2009).
61 Liu, Y., Beyer, A. & Aebersold, R. On the Dependency of Cellular Protein Levels on mRNA Abundance. *Cell* **165**, 535-550, doi:10.1016/j.cell.2016.03.014 (2016).
62 Assur, Z., Hendrickson, W. A. & Mancia, F. in *Protein Expression in Mammalian Cells: Methods and Protocols* (ed James L. Hartley) 173-187 (Humana Press, 2012).
63 Rutz, S., Deneka, D., Dittmann, A., Sawicka, M. & Dutzler, R. Structure of a volume-regulated heteromeric LRRC8A/C channel. *Nat Struct Mol Biol* **30**, 52-61, doi:10.1038/s41594-022-00899-0 (2023).
64 Kern, D. M. *et al.* Structural basis for assembly and lipid-mediated gating of LRRC8A:C volume-regulated anion channels. *Nat Struct Mol Biol* **30**, 841-852, doi:10.1038/s41594-023-00944-6 (2023).
65 Flores, J. A. *et al.* Connexin-46/50 in a dynamic lipid environment resolved by CryoEM at 1.9 Å. *Nature Communications* **11**, 4331, doi:10.1038/s41467-020-18120-5 (2020).
66 Myers, J. B. *et al.* Structure of native lens connexin 46/50 intercellular channels by cryo-EM. *Nature* **564**, 372-377, doi:10.1038/s41586-018-0786-7 (2018).
67 Zimmermann, I. *et al.* Generation of synthetic nanobodies against delicate proteins. *Nat Protoc* **15**, 1707-1741, doi:10.1038/s41596-020-0304-x (2020).
68 Zimmermann, I. *et al.* Synthetic single domain antibodies for the conformational trapping of membrane proteins. *eLife* **7**, e34317, doi:10.7554/eLife.34317 (2018).
69 Scheres, S. H. W. RELION: Implementation of a Bayesian approach to cryo-EM structure determination. *Journal of Structural Biology* **180**, 519-530, doi:https://doi.org/10.1016/j.jsb.2012.09.006 (2012).
70 Noble, A. J. *et al.* Reducing effects of particle adsorption to the air–water interface in cryo-EM. *Nature Methods* **15**, 793-795, doi:10.1038/s41592-018-0139-3 (2018).
71 Syrjanen, J., Michalski, K., Kawate, T. & Furukawa, H. On the molecular nature of large-pore channels. *Journal of molecular biology* **433**, 166994, doi:10.1016/j.jmb.2021.166994 (2021).
72 Syrjanen, J. L. *et al.* Structure and assembly of calcium homeostasis modulator proteins. *Nat Struct Mol Biol*, doi:10.1038/s41594-019-0369-9 (2020).
73 Choi, W., Clemente, N., Sun, W., Du, J. & Lu, W. The structures and gating mechanism of human calcium homeostasis modulator 2. *Nature* **576**, 163-167, doi:10.1038/s41586-019-1781-3 (2019).
74 Danielli, S. *et al.* The ion channel CALHM6 controls bacterial infection-induced cellular cross-talk at the immunological synapse. *Embo J* **42**, e111450, doi:10.15252/embj.2022111450 (2023).
75 Geertsma, E. R. in *Enzyme Engineering: Methods and Protocols* (ed James C. Samuelson) 133-148 (Humana Press, 2013).
76 Michalski, K. *et al.* The Cryo-EM structure of pannexin 1 reveals unique motifs for ion selection and inhibition. *Elife* **9**, doi:10.7554/eLife.54670 (2020).
77 Kuzuya, M. *et al.* Structures of human pannexin-1 in nanodiscs reveal gating mediated by dynamic movement of the N terminus and phospholipids. *Sci Signal* **15**, eabg6941, doi:10.1126/scisignal.abg6941 (2022).
78 Kefauver, J. M. *et al.* Structure of the human volume regulated anion channel. *Elife* **7**, doi:10.7554/eLife.38461 (2018).
79 Nakamura, R. *et al.* Cryo-EM structure of the volume-regulated anion channel LRRC8D isoform identifies features important for substrate permeation. *Commun Biol* **3**, 240, doi:10.1038/s42003-020-0951-z (2020).
80 Ambrosi, C. *et al.* Pannexin1 and Pannexin2 channels show quaternary similarities to connexons and different oligomerization numbers from each other. *J Biol Chem* **285**, 24420-24431, doi:10.1074/jbc.M110.115444 (2010).

81 Lee, S. N. *et al.* Cryo-EM structures of human Cx36/GJD2 neuronal gap junction channel. *Nat Commun* **14**, 1347, doi:10.1038/s41467-023-37040-8 (2023).
82 Bennett, B. C. *et al.* An electrostatic mechanism for Ca(2+)-mediated regulation of gap junction channels. *Nat Commun* **7**, 8770, doi:10.1038/ncomms9770 (2016).
83 Demura, K. *et al.* Cryo-EM structures of calcium homeostasis modulator channels in diverse oligomeric assemblies. *Sci Adv* **6**, eaba8105, doi:10.1126/sciadv.aba8105 (2020).
84 Ren, Y. *et al.* Cryo-EM structure of the calcium homeostasis modulator 1 channel. *Sci Adv* **6**, eaba8161, doi:10.1126/sciadv.aba8161 (2020).
85 Bhat, E. A., Sajjad, N., Banawas, S. & Khan, J. Human CALHM5: Insight in large pore lipid gating ATP channel and associated neurological pathologies. *Mol Cell Biochem* **476**, 3711-3718, doi:10.1007/s11010-021-04198-y (2021).
86 Ren, Y. *et al.* Cryo-EM structure of the heptameric calcium homeostasis modulator 1 channel. *J Biol Chem* **298**, 101838, doi:10.1016/j.jbc.2022.101838 (2022).
87 Yang, W. *et al.* Cryo-electron microscopy structure of CLHM1 ion channel from Caenorhabditis elegans. *Protein Sci* **29**, 1803-1815, doi:10.1002/pro.3904 (2020).
88 Catacuzzeno, L. & Franciolini, F. The 70-year search for the voltage-sensing mechanism of ion channels. *The Journal of Physiology* **600**, 3227-3247, doi:https://doi.org/10.1113/JP282780 (2022).
89 Penkov, N. V. & Penkova, N. Key Differences of the Hydrate Shell Structures of ATP and Mg.ATP Revealed by Terahertz Time-Domain Spectroscopy and Dynamic Light Scattering. *J Phys Chem B* **125**, 4375-4382, doi:10.1021/acs.jpcb.1c02276 (2021).
90 Syrjanen, J. L., Epstein, M., Gomez, R. & Furukawa, H. Structure of human CALHM1 reveals key locations for channel regulation and blockade by ruthenium red. *Nat Commun* **14**, 3821, doi:10.1038/s41467-023-39388-3 (2023).
91 Liu, J. *et al.* Cryo-EM structures of human calcium homeostasis modulator 5. *Cell Discov* **6**, 81, doi:10.1038/s41421-020-00228-z (2020).
92 Burendei, B. *et al.* Cryo-EM structures of undocked innexin-6 hemichannels in phospholipids. *Sci Adv* **6**, eaax3157, doi:10.1126/sciadv.aax3157 (2020).
93 Mastronarde, D. N. Automated electron microscope tomography using robust prediction of specimen movements. *Journal of Structural Biology* **152**, 36-51, doi:https://doi.org/10.1016/j.jsb.2005.07.007 (2005).
94 Zivanov, J. *et al.* New tools for automated high-resolution cryo-EM structure determination in RELION-3. *eLife* **7**, e42166, doi:10.7554/eLife.42166 (2018).
95 Rohou, A. & Grigorieff, N. CTFFIND4: Fast and accurate defocus estimation from electron micrographs. *Journal of Structural Biology* **192**, 216-221, doi:https://doi.org/10.1016/j.jsb.2015.08.008 (2015).
96 Zivanov, J., Nakane, T. & Scheres, S. H. W. A Bayesian approach to beam-induced motion correction in cryo-EM single-particle analysis. *IUCrJ* **6**, 5-17, doi:doi:10.1107/S205225251801463X (2019).
97 Chen, S. *et al.* High-resolution noise substitution to measure overfitting and validate resolution in 3D structure determination by single particle electron cryomicroscopy. *Ultramicroscopy* **135**, 24-35, doi:https://doi.org/10.1016/j.ultramic.2013.06.004 (2013).
98 Rosenthal, P. B. & Henderson, R. Optimal Determination of Particle Orientation, Absolute Hand, and Contrast Loss in Single-particle Electron Cryomicroscopy. *Journal of Molecular Biology* **333**, 721-745, doi:https://doi.org/10.1016/j.jmb.2003.07.013 (2003).
99 Scheres, S. H. W. & Chen, S. Prevention of overfitting in cryo-EM structure determination. *Nature Methods* **9**, 853-854, doi:10.1038/nmeth.2115 (2012).
100 Punjani, A., Rubinstein, J. L., Fleet, D. J. & Brubaker, M. A. cryoSPARC: algorithms for rapid unsupervised cryo-EM structure determination. *Nature Methods* **14**, 290-296, doi:10.1038/nmeth.4169 (2017).

101 Kimanius, D., Dong, L., Sharov, G., Nakane, T. & Scheres, S. H. W. New tools for automated cryo-EM single-particle analysis in RELION-4.0. *Biochemical Journal* **478**, 4169-4185, doi:10.1042/BCJ20210708 (2021).

102 Emsley, P. & Cowtan, K. Coot: model-building tools for molecular graphics. *Acta Crystallographica Section D* **60**, 2126-2132, doi:doi:10.1107/S0907444904019158 (2004).

103 Adams, P. D. *et al.* PHENIX: building new software for automated crystallographic structure determination. *Acta Crystallographica Section D* **58**, 1948-1954, doi:doi:10.1107/S0907444902016657 (2002).

104 Sanner, M. F. A Component-Based Software Environment for Visualizing Large Macromolecular Assemblies. *Structure* **13**, 447-462, doi:https://doi.org/10.1016/j.str.2005.01.010 (2005).

105 DeLano, W. L. Unraveling hot spots in binding interfaces: progress and challenges. *Current Opinion in Structural Biology* **12**, 14-20, doi:https://doi.org/10.1016/S0959-440X(02)00283-X (2002).

106 Pettersen, E. F. *et al.* UCSF ChimeraX: Structure visualization for researchers, educators, and developers. *Protein Science* **30**, 70-82, doi:https://doi.org/10.1002/pro.3943 (2021).